Characterising honeys *in situ* by spectral methods

A thesis presented in partial fulfilment of the

requirements for the degree of

Doctor in Philosophy

in

Food Technology

At Massey University, Manawatu, New Zealand

Hien Thi Dieu Truong

September 2022

"Love bears all things, believes all things, hopes all things, endures all thing. Do everything in love."

1 Corinthians 13:7 & 16:14

Acknowledgments

I have started to write acknowledgement a year before submitting my thesis. Each day I add additional gratitude to the day before.

I think I have received many blessings during my three-year Ph.D. journey at Massey University, New Zealand. I have met great people and learned beautiful things even in challenging situations.

At the beginning, I thought doing a Ph.D. would be a job, but now I know that doing a PhD is a part of my life journey. On this journey, I have met great-hearted people, in particular my supervisors and colleagues, who supported my research at Massey University and AgResearch. Without their support, I do not think that I can achieve all my research objectives on time. Therefore, I would like to write down my sincere gratitude to all the people who have companied me on this Ph.D. journey. I know that words cannot express how grateful I am, but I will try. Praise God for His blessings and for letting me work on the honey project with the great support of my three supervisors. The success of this Ph.D. research is fulfilled with the teaching of all my supervisors. I feel I am very lucky, and I would like to send my gratitude to my supervisors: Richard Archer, Marlon M. Reis and P. Reddy who are very supportive and kind.

First, I would like to express my gratitude to my chief supervisor, Richard Archer. I do not know how to say thank you but let me describe my memories of Richard. Richard, in my eyes, is a Santa Claus who has white hair and a big smile. I called him Santa Claus since he gave me an opportunity to do research at Massey just after the first interview. With this opportunity, I could do what I am passionate about as a spectral analysis researcher. For three years, I have learned a lot from Richard. I think I admire his intelligence, open mind, straight-forward thinking, and mindset for future perspectives. Honestly, I would like to learn more from him, but three years have flown by very fast. During these years, I have also learned to improve my English writing skills with Richard. He is very patient in telling me when I write wrongly and adds new words (i.e., comprehensive phrases) to improve my writing style. I really like the way he contacts students and lets students develop themselves in a good way. Indeed, I see myself grow up in many ways. Richard is also a good listener. He listens to me, although we sometimes have disagreements during discussion. But eventually, disagreements become good ideas so that the research moves forward. I think I have learned what is good for an argument. For all of these, I would like to say a big thanks to him. The most beautiful time I

had with Richard was when he taught me how to do pruning at his farm in Whanganui in 2021. I think we pruned 60 trees in two hours. I enjoyed it very much.

Companying me on the progress of my Ph.D. research is my co-supervisor, Marlon M. Reis. Many thanks to him for supervising me from limited understanding to enlightenment. Marlon showed me his kindness, support, and intelligence, which he always shares with all his students and his colleagues. I think I have learned from him: “To be kind, not to be right.” Overall, I overcame research challenges, and Marlon is always there for his students when they need him. He is a helping hand to me. Thousands of thanks wouldn’t be enough, but my heartfelt gratitude would be sent to him. The nicest memory I have with Marlon is that I stayed in his house when he and his family were away. I played with Luna, a beautiful dog. I had a good time enjoying myself before the final Ph.D. year kicked off.

Another co-supervisor I would like to thank you is Reddy Pullanagari. I think in my first year, Reddy helped me a lot. Reddy is an open-minded and charming supervisor. He is very talented at modelling. I would like to learn to be good at modelling like he is. The best memory I remember of Reddy is that we were on a trip to visit the honey extraction plant near Hawkes Bay in 2020. This trip recalled my previous colleague, Abhimanyu Garhwal. I also would like to give thanks to him, who helped me when I just started my research in 2019. Abhimanyu sent me a book on hyperspectral imaging systems. With this book, I began to develop my interest in what it would be like to have a camera that could capture images in continuous wavelengths. Enlightenment! Later, I have many books I need to read.

On this Ph.D. journey, I would like to express my gratitude to two other colleagues at AgResearch. Thank you very much, Mahmoud Al-Sarayreh, who supported me a lot in coding one of my thesis chapters. I believe he is an excellent teacher because our discussions have improved my understanding of coding. Mahmoud is also very patient and helpful. Although he is in Jordan, a completely different time zone, and his schedule is quite busy, he still gives me time to teach convolutional neural network models. Because of this, I cannot say enough “thank you” to him. Another colleague I want to express my gratitude to is Yash Dixit, who supported me in setting up a hyperspectral imaging system and always carried a heavy camera for me. Many thanks to Yash for this kindness.

My previous supervisors at KU Leuven in Belgium, Wouter Saeys and Nghia Nguyen Do Trong, will always have a special place in my heart. Although I work in New Zealand far away from Belgium, they always keep in touch and give me advice when I need it. I am very thankful for this.

Next, I would like to say thank you to Comvita® Ltd., in particular, to Cameron Walker, Tony Wright, Jackie Evans, and Jennae O'Donnell, with whom I have collaborated on the development of this Ph.D. project. I have gained knowledge of honey from production and industrial perspectives. Therefore, I am very thankful.

The list is still long. To many people, I want to say thank you, but I cannot write here in detail. From my heart, I want to thank you all for your help and kindness to me, including technicians and colleagues at Massey. Once again, thank you very much.

Finally, I would like to give thanks to my beloved family: my grandma, my parents, my aunt and uncles, my siblings, and my love, Bartje. All your support, prayers, and love for me have encouraged me a lot to do my research. All of you always give me chances to do what I like and respect and love me for who I am. For all of that, I am very grateful. My soul praises God for all of His blessings on me, my family, and everyone I care about.

Every day, I pray to God to shower His blessings on everyone, who has helped me including people I have just met. I think that I am blessed since my life is fulfilled with your help, your support, and your kindness. I pray that God will bless you, be with you, and strengthen you in your life.

Thank you very much in Vietnamese: "Cảm ơn rất nhiều".

Sincerely,

Hien Thi Dieu Truong

Abstract

New Zealand mānuka honey is derived mainly from *Leptospermum scoparium* nectar and is valuable through accumulation of antibacterial methyl glyoxal (MGO). Mānuka honey also has a strong polyphenolic profile. Some phenolics act as chemical markers aiding verification of botanical origin as *Leptospermum scoparium*. A total of eight key chemical markers (DHA, MGO, 3-PLA, 4-HPLA, 2'-MAP, 2-MBA, Leptosperin and Lepteridine^{TM}) are found at higher levels in mono-mānuka honey than in multi-mānuka honey, with little or none in other floral honeys. These key markers signify mānuka honey quality and purity (i.e., monoflorality of *L. scoparium*). The quality and purity of mānuka honeys depend on multiple factors, largely determined by botanical source, which define the value of the final honey product. Available nectar is, in turn, influenced by geographic district and season.

Wild harvest honey is naturally a mixture from different nectars. Honey quality varies among apiaries, between beehives and even in a honey frame. Current industry practice lumps all frames of the same apiary together for extraction. Potentially, "good" quality frames of mānuka honey could be mixed with "bad" quality frames. This bulked process can limit the monetary value of mānuka honey.

Quality assessment of honey while still in the frame before bulk extraction is of great of interest to the honey industry to preserve the value of mānuka honey at source and to ensure authenticity. The current study used rapid and non-destructive methods such as NIR and fluorescence combined with chemometrics, machine learning and deep learning to evaluate mānuka honey in the frame. The study focuses on assessment of mānuka honey quality in two ways: 1) direct measurement of levels of eight key chemical makers; 2) indirect measurement of potency (based on UMF^{TM} score) and purity (verification of botanical origin as *L. scoparium*) that are built from key chemical markers.

Honey samples (n ~ 1656) representing 200 L drums, each extracted from multiple frames, spanning eight geographic districts across New Zealand, were scanned with NIR non-imaging (350 - 2500 nm) and imaging (547 – 1701 nm) sensors. A sub-dataset of 100 honey samples was scanned in excitation-emission matrix mode (250 - 400/300 - 600 nm) under in-line geometry by a fluorescence sensor. Once techniques were verified, freshly uncapped seven honey frames were scanned and modelled to evaluate the current optical methods used.

Overall, the research showed the capability of NIR methods for measurement of honey potency and purity in the frame, achieving 70 - 80 % accuracy. However, NIR methods showed

limited ability to measure levels of individual key chemical markers, giving 60 - 70 % accuracy, due to the complexity of the honey matrix. This study has calculated the economic benefit of using NIR methods for sorting honey frames into different quality buckets (UMF™ buckets and MPI honey buckets) before lumped extraction. The greatest revenue increase is found for apiaries with large variation between frames and in seasons with high curvature in the price-quality curve. Later, this study employed fluorescence-based methods that further improved prediction of almost all key chemical markers, in particular two polyphenolic fluorescence markers, Leptosperin and Lepteridine™, to above 80 % accuracy. Moreover, the fusion of NIR and fluorescence data further enhanced predictability of chemical markers, potency and purity of mānuka honey to 90 - 100 % accuracy.

In conclusion, this study confirms the fusion of NIR and fluorescence methods has great potential for at-line/on-line assessment of New Zealand mānuka honey while still in the frame. This research provides basic scientific guidance for future application of NIR and fluorescence methods for quality assessment of honey in general and has implications for other wild harvest foods.

Table of contents

List of abbreviations

AGEs	Advanced glycation end-products
ARPs	Amadori-rearrangement products
DNA	Deoxyribonucleic acid
DOF	Depth of field
EEM	Excitation emission matrix
ELISA	Enzyme-linked immunosorbent assay
eq.	Equation
FOV	Field of view
GA	Genetic algorithm
GC	Gas chromatography
GC-MS	Gas chromatography-mass spectroscopy
HMF	5-hydroxymethylfurfural
HPLC	High performance liquid chromatography
HPLC-MS	High performance liquid chromatography-mass spectroscopy
HPP	High-pressure processing
4-HPLA	4-hydroxyphenyllactic acid
HSI	Hyperspectral imaging
LC	Liquid chromatography
LC-MS	Liquid chromatography-mass spectroscopy
LVs	Latent variables
2'-MAP	2'-methoxyacetophenone
2-MBA	2-methoxybezoic acid
MIC	Minimum inhibitory concentration
MC	Moisture content
MM1	Leptosperin
MM2	Lepteridine^{TM} 3,6,7-trimethyllumazine
MPI	Ministry for Primary Industries
MSC	Multiplicative scatter correction
NIR	Near infrared
NPA	Non-peroxide activity
PARAFAC	Parallel factor analysis
3-PLA	3-phenyllacticacid
PCs	Principal components
PCA	Principal component analysis
PCR	Polymerase chain reaction
rtPCR	Real time polymerase chain reaction
PLS	Partial least squares
PLSDA	Partial least squares discrimination analysis
iPLS	Interval partial least squares
n-PLS	Multi-way partial least squares

rbf	Radial basic function
RMSECV	Root mean square error cross-validation
RMSEP	Root mean square error prediction
RPD	Ratio of prediction to deviation
OSC	Orthogonal signal correction
SEP	Standard error of prediction
SD	Standard deviation
SDS-PAGE	Sodium dodecyl sulphate polyacrylamide gel electrophoresis
SNV	Standard normal variates
SSTO	Total sum of squares
SSE	Error sum of squares
SVM	Support vector machine
SVR	Support vector machine regression
SVMDA	Support vector machine discriminant analysis
UV	Ultraviolet
UMF^{TM}	Unique mānuka factor trademark
UMFHA	Unique mānuka factor honey association
WD	Working distance
VIP	Variable important in projection
Vis/VIS	Visible

List of symbols

$^{-1}$	Inverting operator
^{t}	Transpose operator
b, β	Beta coefficient
c	Absorbing component
C	Regularization parameter
ξ_i	Slack variable
C, γ	Cost and gamma hyperparameters of the rbf kernel
f	Mathematical function
k	Absorption coefficient
I_o	Incident intensity
I	Transmitted intensity
L	The optical pathway
λ_{ex}	Excitation wavelength, nm
λ_{em}	Emission wavelength, nm
A	Absorbance
A’	Pseudo-absorbance
M	Mānukaness
Po	Potency
Pu	Purity
T	Transmittance
Id (λ)	Reflectance spectrum of the dark reference at wavelength λ nm
Ir (λ)	Reflectance spectrum of the white reference at wavelength λ nm
Is (λ)	Raw reflectance spectrum measured at wavelength λ nm
Rs (λ)	Relevant reflectance spectrum corrected
r^2	Coefficient of determination (simple linear regression)
R^2	Coefficient of determination (multivariate linear regression)
vs	versus
w/v	Weight per volume
x_i	Spectrum of the i-th sample
E	Residual error matrix
P	Loading matrix
T	Score matrix
X	Spectral data matrix
Y	Reponses matrix

List of terminology

Purity	explaining the botanical origin as *L. scoparium*. Another term which can be used to describe purity is monoflorality
Mānukaness	a spectral quality mark used to measure quality and purity of mānuka honey
UMF™	being a trademarked quality standard for unique mānuka factor that is used to measure mānuka honey quality
Apiary	a location where several beehives of bees are kept
Beehive	a box containing several honey frames in which bees store nectar after foraging
Honey frame	a structural element in a beehive having hexagonal cell or comb in which bees put the nectar in. In New Zealand, honey frame is often made of virgin food grade polypropylene in black or yellow colour
Lepteridine™	being a trademarked chemical abbreviated from Lepteridine™ 3,6,7-trimethyllumazine

List of figures

List of tables

Chapter 1 Introduction

1.1. Project Overview

This project is aimed at using non-invasive methods (non-imaging spectroscopy & hyperspectral imaging) combined with chemometrics and machine learning algorithms to estimate the quality and identity of honey in-frame immediately after uncapping, and before extraction to enable mānuka honey to be graded by imputed quality. A non-imaging sensor was also used in this study as a way of benchmarking benefits or limitations of hyperspectral imaging.

New Zealand mānuka honey is mainly derived from nectar of *Leptospermum scoparium* (commonly known as mānuka plant) that is rich in dihydroxyacetone (DHA). The DHA compound found in the nectar is the key precursor for transforming the antibacterial activity in mānuka honey (Williams et al., 2014). During honey ageing, DHA decomposes into 1,2-dicarbonyl methylglyoxal (MGO) following the kinetics typical of Maillard reactions (Hellwig et al., 2017). MGO is the main antibacterial compound conferring the non-peroxide activity (NPA) in the mānuka honey (Hellwig et al., 2017; Owens et al., 2019). However, bee defense-1 and poly-phenolic compounds also play a role for the NPA within mānuka honey (Johnston et al., 2018; Roberts et al., 2015).

In addition to DHA and MGO, other phytochemicals are also distinctive for mānuka honey (Oelschlaegel et al., 2012; Smallfield et al., 2018). According to the Ministry for Primary Industries (MPI) criteria (2017), four chemicals from the group of flavonoids and phenolic acids are identified as chemical markers in mānuka honey: 3-phenyllacticacid (3-PLA), 2′-methoxyacetophenone (2'-MAP), 2-methoxybenzoic acid (2-MBA) and 4-hydroxyphenyllactic acid (4-HPLA) (MPI, 2017b; Oelschlaegel et al., 2012; Smallfield et al., 2018). However, 3-PLA and 4-HPLA are also found in *Kunzea ericoides* (kānuka) nectar which is a member of the myrtaceous family like *Leptospermum scoparium* (Bong et al., 2018).

Mānuka honey is mainly graded by two different scales: one is based on MGO concentration (mg/kg mānuka honey) and the other uses Unique Mānuka Factor (UMF^{TM}), which indicates the NPA value (Roberts et al., 2015). In 1990, the UMF^{TM} number was established by testing mānuka honey against *Staphylococcus aureus* bacteria (Combarros-Fuertes et al., 2019; Roberts et al., 2015). The UMF^{TM} score was determined to be the equivalent percentage of phenol concentration (w/v) producing the same inactivation effect

against *S. aureus* as a mānuka honey sample (Johnston et al., 2018; Roberts et al., 2015). Currently, the UMF™ is mainly predicted by MGO concentration (Georgescu et al., 2017) and is widely used in the quality rating system for trading mānuka honey around the world (UMFHA, 2021).

Previous studies showed that mānuka honey possesses a distinctive fluorescence profile (Johnston et al., 2018; Lin et al., 2017). Leptosperin (MM1) and Lepteridine™ 3,6,7-trimethyllumazine (MM2) were to be unique fluorescence markers for mānuka honey (Bong et al., 2018; Bong et al., 2017; Lin et al., 2017; Smallfield et al., 2018). According to Bong et al. (2018 &2017) the fluorescence markers MM1 & MM2 exhibit fluorescence in the UV (ultraviolet)/Vis (visible) region at $\lambda_{ex/em}$ 270/365 nm and $\lambda_{ex/em}$ 330/470 nm, respectively (Bong et al., 2017; Lin et al., 2017). Other fluorophores of the flavonoid group also display fluorescence emission in Vis region in response to UV excitation wavelengths (Chan et al., 2013).

Seasons, geographic districts, and the presence of other floral nectars influence the quality and purity of mānuka honey (Burns et al., 2018; Williams et al., 2014). Intuitively, honey in cells across frames in the same beehive or among beehives could be inhomogeneous since honeybees could collect different nectar during foraging. Therefore, the quality of mānuka honey potientally varies among apiaries, beehives and frames, or even within a frame. During the extraction process for an apiary, frames are usually pooled, which can reduce the quality of the bulked extracted mānuka honey below its potential. The assessment of honey frames prior to extraction is concerned. However, the current methods (e.g. the UMF™ ratings, MGO measurement) are mostly applied after bulk extraction in which all frames from an apiary are lumped together (Johnston et al., 2018; Roberts et al., 2015). UMF™ ratings or measurement of MGO concentration by wet-lab analysis is too time-consuming for on-line and at-line applications in the extraction process.

In the search of a new method for evaluation of mānuka honey's quality and identity, up-to-date non-invasive methods, and the eight key chemical markers (DHA, MGO, 3-PLA, 2'-MAP, 4-HPLA, 2-MBA, MM1 & MM2) which are largely unique to mānuka honey are studied. Based on these key chemical makers, this work has developed a term in relation to their concentrations, so-called "mānukaness". We assume the "mānukaness" is a function of eight chemical makers:

$$[\text{mānukaness}] = f\,(DHA, MGO, 3-PLA, 2'-MAP, 2-MBA, 4-HPLA, MM1, MM2)$$

1.2. Research objectives

A rapid grading tool requires a predictive model for quality and identity of mānuka honey in-frames. The prediction of mānukaness for potency (UMF^{TM} scores) and for purity (MPI identity of mānuka honeys) will be indirectly measured from spectral data carrying signatures of mānuka honey key chemical markers. Different non-destructive methods: NIR and fluorescence and their combinations will be studied to measure honey potency and purity "mānukaness". Three main objectives are outlined as follows:

[1] Estimation of eight key chemical markers in mānuka honey using a non-imaging Vis-NIR sensor (350 - 2500 nm) and hyperspectral imaging sensor (547 - 1701 nm) in combination with chemometrics and machine learning algorithms.

[2] Developing a tool to capture unique fluorescence signatures in undiluted mānuka honey using fluorescence spectroscopy and chemometrics.

[3] Combining fluorescence and Vis-NIR spectral data extracted from hyperspectral imaging data to estimate "mānukaness" in commercial honey frames immediately after uncapping (removing the wax on honey frames).

The overall research objective is to find and prove in principle a non-destructive and rapid grading tool for estimating potency and purity "mānukaness" in honey frames prior to the bulk extraction to sort honey frames having poor quality out of those of good quality. In this study, non-imaging and hyperspectral imaging combined with chemometrics and machine learning algortihms were employed to estimate mānukaness. The prediction of "mānukaness" in frames based on unique mānuka properties could measure the potency quality (UMF^{TM} score) and the purity of floral source (MPI criteria for grading of mānuka honey from multi-floral mānuka and non- mānuka honeys).

1.3. Food Industry Enabling Technology and Comvita® partnership

This study is one of 14 industrial projects under Food Industry Enabling Technology (FIET) research program funded by New Zealand Ministry of Business, Innovation and Employment (MBIE). FIET was a six-year collaborative programme of technology development of six New Zealand leading research institutes and universities (AgReseach, Massey University, The University of Auckland, University of Otago, Plant and Food Research, and the Riddet Institute) to enhance the benefit of export for New Zealand food processing companies. The FIET projects spanned dairy, meat, horticulture, and prepared food sectors. This study belongs to the project 14, namely Spectral Separations, which is

collaborated with Massey University, AgResearch, Comvita® and Potatoes New Zealand. The Spectral Separations project focuses on (a) recognising *psyllid* damage in whole potato tubers at grading and (b) optimising the extraction frames of honey to enhance New Zealand mānuka honey's export values. Total funding for spectral separation on honey is about NZ $400,000.

Comvita® is one of the pioneering companies in exporting mānuka honeys to other countries and is also one of the best equipped of New Zealand honey companies to benefit from export values. It is listed on the NZ stock exchange (about $300 million market cap). Comvita® has branches in several countries (Japan, South Korea, USA, Hong Kong, Australia, UK and China). The company has produced many famous products originated from honeys such as Mānuka Honey (with different level of UMF), Medihoney (a high-graded mānuka honey certified for medical purposes), and from propolis. This study is a close collaboration with Comvita® who provided large sets of fully analysed honey samples from across the North Island of New Zealand. In addition, we also have shared research progress, research results, modelling applications and honey expertise to make the work become specific. The output of this study could bring great benefit for honey industry.

The projected endpoint of this study is proof of principle of a spectral inspection method. Potentially, fusion of NIR and UV-VIS fluorescence techniques combined in the reflectance mode will be shown suitable for use on undiluted honey in recently uncapped honey frames. The method must include robust models tunable by seasons and regions. The study will include an analysis of factors impacting financial returns from the technology where it was implemented.

Figure 1.1. *Four main products from Comvita® company*

Chapter 2 Literature review

This literature review aims to describe essential information of three critical components for this work: (a) mānuka honey, (b) non-destructive tools (spectroscopy/non-imaging & imaging spectroscopy/hyperspectral imaging), and (c) chemometrics and machine learning algorithms.

Section 1: Mānuka honey

The demand for New Zealand mānuka honey has been growing around the world (News, 2019). Its high unit value makes people concerned how mānuka honey becomes distinctive to other honeys and how to be sure what they purchase is a good quality honey. To answer these questions, this chapter unveils mānuka honey's chemical profiles that are distinctive to those of traditional honeys. In addition, this section also covers the extraction process, honey applications and current quality measurements of mānuka honeys before selling in the market.

2.1. Mānuka honey: valued components

New Zealand mānuka honey is mainly derived from *Leptospermum scoparium* nectar (Smallfield et al., 2018; Williams et al., 2014). Before the 1980s, it was used as food for bees since this honey (dark in colour, strong in flavor and lowly value) was difficult to extract in comparison with other local honeys. Early 1990s, Peter Molan, a researcher from the University of Waikato, Hamilton, New Zealand, discovered the antibacterial activity in mānuka honeys, which can inactivate microbes, including pathogens, better than traditional honeys (Van Eaton, 2014; White, 2018). Ten years later, Thomas Henle, a professor of University of Dresden (Germany) found the primary antibacterial activity in mānuka honey originated from methylglyoxal or MGO (Elvira et al., 2008). MGO is gradually formed during honey ripening and storage by facile dehydration of dihydroxyacetone (DHA) which is a three-carbon sugar compound uniquely hyperaccumulated in *Leptospermum scoparium* nectar (Hellwig et al., 2017; Owens et al., 2019; Williams et al., 2018). In addition, mānuka honey purity is reckoned with a diverse polyphenolic profile (flavonoids, phenolic acids, methyl syringate) which also adds value to mānuka honey's quality and signature (Bong et al., 2017; Wang, 2011; Yiuchung et al., 2019). After the antibacterial MGO agent was first discovered in 2008, mānuka honey has become a "gold" liquid honey since it has benefit for ulcer healing, human consumption, cosmetics, and other applications.

❖ *Therapeutic*

Mānuka honey has been used as a therapeutic agent for ulcer treatment and burn healing (Combarros-Fuertes et al., 2019; Johnston et al., 2018; Kwakman et al., 2011). MGO and other antibacterial compounds are able to compete against several pathogens (*Staphylococcus aureus, Escherichia coli* and *Pseudomonas aeruginosa*), which potentially replace synthetic antibacterial drugs (Elvira et al., 2008; Kwakman et al., 2011). With a certain amount of MGO in mānuka honey, external pathogens are inactivated before entering ulcer injuries (Johnston et al., 2018). According to Combarros-Fuertes et al. (2019), *S. aureus* and *E. coli* are significantly reduced in bacterial growth at the minimum inhibitory concentration (MIC) 10 % (w/v) and 20 % (w/v) of mānuka honey MGO 550+, respectively. Similarly, Lu et al. (2013 & 2014) reported that the growth of *Staphylococcus* spp. and *Bacillus subtilis* was decreased at just MIC 4 % (w/v) (Johnston et al., 2018). In addition to pathogenic inactivation, MGO can also stimulate cellular macrophages in infected tissues to produce mediators for healing wound cells (Johnston et al., 2018). In 2007, the U.S. Federal Drug Administration (FDA) accepted mānuka honey as an alternative approach for treating wounds (burns, ulcers and non-healing ulcers) (Johnston et al., 2018). However, ulcers caused by diabetes should not be treated with mānuka honey for healing since the degradation of advanced glycation end products (AGEs) derived from MGO could produce detrimental effects (Juraj, 2011) .

❖ *Functional ingredient*

Food used as a functional ingredient to cure a certain disease must demonstrate safety for human consumption (Dominguez, 2013). Mānuka honey has been studied as a functional ingredient for stomach ulcer (Rosendale, 2009). There is little scientific evidence proving impact of mānuka honey against *Helicobacter pylori* bacteria after human consumption. The study of Rosendale (2009) reported that mānuka honey has little value for inactivation of *H. pylori* at normal consumption. This is because mānuka honey could not travel far to reach the colon at concentrations giving the significant effect (Rosendale, 2009). Further research is suggested for a formulation of mānuka honey to protect its degradation from digestion.

❖ *Cosmetic ingredient*

The cosmetic industry nowadays aims to use natural preservatives instead of synthetic chemicals following the trend of using natural ingredients (Claudia & Giovanni Antonio, 2018). The abundant profile of antibacterial and antioxidant compounds (MGO, Leptosperin, antioxidants) found in mānuka honeys are potentially useful as cosmetic ingredients. The compounds in cosmetic products must follow the European Pharmacopoeia's criteria (Claudia

& Giovanni Antonio, 2018). In the market, skincare and body care products have employed antimicrobial and anti-inflammatory agents from mānuka honeys (Patel & Cichello, 2013). For example, anti-microbial creams (e.g., Ampule energy) containing propolis and mānuka honey are claimed to inactivate ringworm and fungal pathogens on skin infections (Patel & Cichello, 2013). Propolis is not a single compound, but a mixture made by bees as a glue (Betances-Salcedo et al., 2017). Lotions deodorants and face-care products (facial cleanser, face masks, anti-wrinkle cream and lip balm) containing antibacterial and antioxidant agents from mānuka honey are currently available in New Zealand pharmacies and supermarkets (Patel & Cichello, 2013).

2.2. New Zealand mānuka honey exports

Before the 1980s, New Zealand (NZ) honey industry was stuck in both domestic and foreign markets. The value of mānuka honey was low. Few domestic consumers bought mānuka honey from beekeepers. Honey exporters faced many obstacles with governmental export regulations. NZ beekeepers struggled to remain in the honey business at that time (Van Eaton, 2014). Discoveries of the antibacterial activity by Peter Molen (1998) and the unique antibacterial agent MGO by Thomas Henle (2008) has increased interest in mānuka honey in New Zealand and around the world (Elvira et al., 2008; Stephens et al., 2005). Early NZ honey entrepreneurs such as Comvita®, Airbone Honey and Arataki had engaged in mānuka honey production despite the export challenge (Van Eaton, 2014). Since the Unique Mānuka Factor Honey Association (UMFHA) was established in 1998, it has facilitated mānuka honey trading from NZ to other countries (UMFHA, 2022; Van Eaton, 2014). A few years ago, the top five honey manufacturers in NZ who benefited the greatest revenue and global market share of mānuka honey were Comvita®, Mānuka Health, Arataki Honey, Watson & Son and Streamland (Newswire, 2019; Van Eaton, 2014).

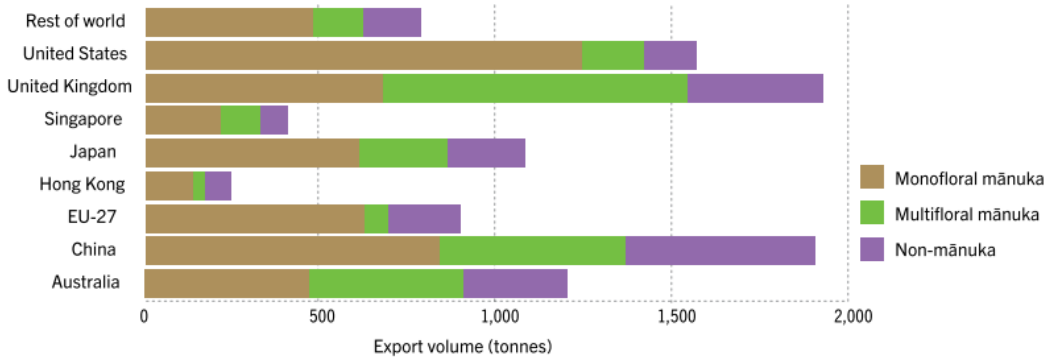

Figure 2.1. *New Zealand pure honey exports by floral type and by destination (Source: Statistics New Zealand, June/2020) (Ministry for Primary Industries, 2020)*

The main export markets for NZ mānuka honey are United Kingdom, China, United States, Europe, Singapore, Japan, Hong Kong, China and Australia (Ministry for Primary Industries, 2020). The value of New Zealand honey exports has been continuously increasing every year. In 2019/2020, the export value increased by 20 % with worth of NZ $425 million due to good weather. Mānuka honey contributed 76 % of export volume of all honey types and 88 % of export revenue (Ministry for Primary Industries, 2020). The increasing in export of mono-floral mānuka honey is significant compared to other floral honey (Figure 2.1). In 2019, the average price of mono-floral mānuka honey was NZ$ 54.67/kg almost double that of multi-floral mānuka honey (NZ$ 29.57/kg) and nearly three times higher than that of non-mānuka honey (NZ$ 20.46) (Ministry for Primary Industries, 2020).

In response to global demand, mānuka honey production has attracted investment. The number of registered beekeeping enterprises and beehive numbers are 9000 and 900,000 respectively, tripling over two decades (Ministry for Primary Industries, 2020). Domestic mānuka plantations and honey production have both increased. Large-scale plantation projects have been developed by myFarm, HoneyBros, Tweeddale and others (Archer, 2022; Gerard, 2018). For example, MyFarm has joint venture with Comvita in the Waimarie Mānuka Limited Partnership project which owns 1800 hectares to plant mānuka trees (myFarm, 2022).

In global markets, the authenticity of mānuka honey is of concern since reports of fraudulence were increasing (Creasey, 2014). Thousand tons of fake mānuka honey products were sold annually over the world according to UMFHA (Creasey, 2014; Times, 2013). Labelling of mānuka honey with UMF^{TM} score sometimes confuses consumers (Creasey, 2014). For example, mānuka honeys were labeled “Active” sold in UK and online market, but the “Active” definition is occasional. UMF^{TM} score are labeled higher than the antimicrobial

activity measured. However, according to Creasey (2014), mānuka honey is valued more highly if the antibacterial activity UMF^{TM} score is above 5 or MGO ≥100 mg /kg honey (Creasey, 2014). Overall, the authenticity of mānuka honey has been a main focus of supply chains (Creasey, 2014). To avoid honey fraud, NZ MPI has released rules for identification of mānuka honey, chemical tests to ensure NZ beekeepers and honey companies to follow the international food safety legislations before export (MPI, 2017a, 2017b).

2.3. The growing demand of high-grade mānuka honeys

The demand for high-grade mānuka honey (e.g., UMF^{TM} score 15+, 20+, 25+) has been increasing. Consumers likely purchase these high-grade mānuka honeys as gifts for medicinal purposes. Comvita® has recently produced 4 % of its harvest as "medical grade" honeys which are applied in hospitals. These medical-grade honeys are packed and sold by United States firm Derma Sciences (Gerard, 2016).

A high-grade mānuka honey is dependent on *Leptospermum* nectar content which varies with geographic district, and season. In New Zealand, although mānuka honey is primarily derived from *L. scoparium* specie, there are several varieties (e.g., *var. scoparium*, *var. incanum*, *var. myrtifolium*, *var. linofolium*, …) across NZ regions (Stephens, 2006). Each variety of *L. scoparium* differs somewhat in the nectar quality for biochemical attributes.

NZ honey industry sells honey in different bands of UMF^{TM}: UMF^{TM} 5+ (for honey with UMF^{TM} value in 5 - 10 range); UMF^{TM} 10+ (for honey with UMF^{TM} value 10 - 15 range); UMF^{TM} 15+ (for honey with UMF^{TM} value in 15 - 20 range) and UMF^{TM} 20+ (for honey with UMF^{TM} value >20). This strategy aims to ensure honey is true to label at the time of purchase. To achieve the demands of accurate analysis, samples are drawn from 300 kg drums of honey allowing blending decision to be made.

2.4. Mānuka honey operation

In New Zealand, harvest seasons of mānuka honey are typically in spring and early summer each year (Bicknell & Jaksons, 2018; Van Eaton, 2014). Thousands of foraging bees could fly up to 5 km to collect nectar, pollen, water and resin to support 1500 - 2000 eggs laid per day by a queen bee (Van Eaton, 2014). Bee workers generally gather nectar in a sac, while others gather pollen and make pellets to carry in front of the abdomen (Van Eaton, 2014). To both nectar and pollen are added enzymes (typically invertase and glucose oxidase) to transform them into honey and beebread in wax cells, respectively. Bees consume mostly beebread, which provides protein, vitamins and minerals while they keep honey for their winter

food (Van Eaton, 2014). Resin from plants is also collected to combine with their own beeswax to form propolis which is used for building their colonies or to fill gaps in hives (Van Eaton, 2014).

Honey ripening in combs undergoes two phases. At the first phase, the fresh nectar will be evaporated to 30 - 50 % moisture content by young bee workers in the colony (Van Eaton, 2014). This process can be called half-ripening. In second phase, small droplets of the half-ripened honey are deposited on the cell floor with a filling rule: a quarter to a third in the comb (Van Eaton, 2014). Bees fully fill honey liquid into cells when the moisture content of honey is less than 20 %, then capped those cells in the comb with wax (Van Eaton, 2014). Then, beekeepers will harvest honey frames if honey combs are almost filled with a rule of three fourths of wax cover capped on the frame surface (Van Eaton, 2014).

A mānuka honey operation requires much effort in terms of extraction and filtration (Van Eaton, 2014). In general, the extraction process of mānuka honey can be divided into three steps. Firstly, honey frames after harvesting from apiaries are uncapped by removing the thin wax layer on the top of cells. After uncapping, honey frames are passed through the HonninglØsner honey-loosener to create holes through combs. The principle of this loosener is based on movements of honey frames towards two solid metal frames having fiber glass and nylon needles. Needles will pierce holes in comb to loosen honey liquid inside, but still remain hexagon cells (Van Eaton, 2014). Mānuka honey liquid possesses a shear thinning characteristic which requires agitation in the cell (e.g., needling) exceeding honey's yield stress to reduce the apparent viscosity ready for the extraction. After needling, honey frames are put in a barrel centrifugator with high speed rotation to collect honey liquid (Van Eaton, 2014). Coarse filtration is applied to remove wax capping pieces dislodged in previous steps. Finally, mānuka honey liquid is collected from a faucet located at the bottom of the barrel, and is drummed off typically into 200 L drums containing just over 300 kg of honey (Van Eaton, 2014).

2.5. Mānuka honey characteristics

2.5.1. Physical properties

- *Rheology*

Mānuka honey is a non-Newtonian *thixotropic* solution, which is very viscous like gel under static conditions (Fauzi et al., 2014; Van Eaton, 2014). *Thixotropic* fluids show time-dependent shear thinning characteristic, which means the viscosity reducing over time by

introducing external force (agitation, shaking or shearing) (Fauzi et al., 2014; Van Eaton, 2014). When this external force is halted, thixotropic mānuka honey liquid will gradually return to a gel state. Viscosity is an important rheological variable of a solution, and is temperature-dependent (Pascual-Mate et al., 2018). Honey viscosity should be measured at constant temperature without the presence of foreign objects (Waite, 2016). Air bubbles, crystals and other impurities will influence on the accuracy of viscosity measurement (Waite, 2016).

- *Hygroscopic structure and fermentation*

Native honey is a hygroscopic food, which can absorb moisture from the surrounding environment. When moisture content exceeds 17 %, yeast can grow and fermentation can occur (Kretavičius et al., 2010; Lucília Carolina Vardenski et al., 2015). Changing moisture content in honey solution can alter physical properties of the honey matrix. Therefore, honey products should be stored in jars with tightly sealed caps (minimum head space) to avoid the absorption of moisture from the external environment. Fermentation is checked carefully prior to exporting mānuka honeys since it will influence on the final quality of honeys when they reach other continents.

- *Optical properties and electrical conductivity*

Honey fluid is a polarised solution which can absorb and refract electromagnetic radiation. The refractive index of honey depends on sugar composition and moisture content (Pascual-Mate et al., 2018). A refractometer can be used to measure degrees Brix which describes the sugar content in honey solution (1^o Brix = 1g sucrose/100g solution) (Waite, 2016). From degrees Brix, moisture content can also be calculated following the Weber formula (Waite, 2016). In addition, honey is known as an electrical solution. The electrical conductivity reflects the mineral content in honey, which can be measured by the conductivity meter or by NIR spectroscopy (Pascual-Mate et al., 2018). The conductivity parameter only displays mineral or ash content in honey (Pascual-Mate et al., 2018).

2.5.2. Chemical properties

Mānuka honey contains over 80 % carbohydrates mainly monosaccharides such as fructose and glucose (Nickless, 2015). Fructose/glucose ratio is approximately 1.5:1 (Nickless, 2015). Moisture content (MC) in mānuka honey varies among floral nectar sources (Nickless, 2015). It can be around 17 - 20 % by mass in the fresh mānuka honey after extracting from beehives (Grainger et al., 2014; Kretavičius et al., 2010). The pH of mānuka honey is in the range at 3.5 - 4.5 compared to other native honeys at pH 4.5 - 5 (Alvarez-Suarez et al., 2014).

Protein and free amino acids are about 0.3 - 3 g/kg mānuka honey (Hellwig et al., 2017). c are two major amino acids found in mānuka honey. They easily join Maillard reactions with carbonyl compounds to form intermediate-Maillard products. Other amino proteins or protein residues could also join Maillard reactions (Hellwig et al., 2017). Mānuka honey contains royal jelly, which is a specific protein released by honeybees for feeding larvae. Royal jelly often binds to glucose, fructose and water creating a jelly matrix, which contributes to the thixotropic property (Van Eaton, 2014). In addition, mānuka honey also contains unique arabinogalactan protein which provides the immunostimulatory properties (Gannabathula et al., 2012).

2.5.3. Phytochemicals and kinetics of reactions in mānuka honeys

- *Dihydroxyacetone*

Dihydroxyacetone (DHA) is abundant in *L. scoparium* nectar (Williams et al., 2014). During honey ripening and storage, DHA decomposes into MGO based on the kinetics of Maillard reactions (Hellwig et al., 2017). The ratio of DHA to total sugar in floral nectar can be divided into three groups: low (< 0.001 mg/mg), moderate (0.001 - 0.002mg/mg) and high (> 0.002 mg/mg) (Williams et al., 2014). DHA content is hyperaccumulated in NZ mānuka nectar and later presents in mānuka honeys at up to 3 µg/mg of total sugars (Hellwig et al., 2017). Compared to *Leptospermum* genus in Australia, the DHA/total sugar ratio of NZ mānuka nectar is approximately double (Williams et al., 2014). DHA content apparently differs with *L. scoparium* varieties, regions, and harvest years (Alvarez-Suarez et al., 2014; Hellwig et al., 2017; Williams et al., 2014).

- *Methylglyoxal*

The 1,2-dicarbonyl methylglyoxal (MGO) is a primary antibacterial component in mānuka honey (Elvira et al., 2008; Goss, 2009; Hellwig et al., 2017; Owens et al., 2019). While all honeys contain the antimicrobial compound hydrogen peroxide, mānuka honey derives additional antibacterial characteristics via MGO. MGO mainly contributes to the non-peroxide activity (NPA) within mānuka honey (Alvarez-Suarez et al., 2014; Hellwig et al., 2017; Roberts et al., 2015; Snow & Manley-Harris, 2004). As with DHA, MGO content also varies from nectar sources, geographical lands, processing conditions and storage time (Alvarez-Suarez et al., 2014). NZ mānuka honey can reach up to 725 mg MGO per kg honey (Roberts et al., 2015).

In mānuka nectar, DHA is present as a dimer that rapidly dissociates into monomers in the aqueous environment (Grainger et al., 2016a). Figure 2.2 describes the dissociation of DHA dimer into DHA monomers. With the presence of phenolic compounds and amino acids

and water, the process of DHA dissociation is facilitated (Stephens et al., 2010; Hermosín, Chicón, & Dolores Cabezudo, 2003; Grainger et al., 2016).

Figure 2.2. *DHA dimer dissociated into two DHA monomers in acidic environment (:BH- phenolic compounds and/ amino acids act as proton donors and/or acceptors) (Grainger et al., 2016a)*

In honey solution, MGO is directly formed from DHA and from Maillard reaction chains. In Maillard reactions, MGO is formed as an intermediate compound (Hellwig et al., 2017; Nickless, 2015). According to Hellwig et al. (2017), Maillard reactions in mānuka honey are divided into three stages. The first stage forms Amadori- rearrangement products (ARPs) by reactions between reducing sugars and amino acids (Hellwig et al., 2017). Reducing sugars such as glucose and maltose react with free lysine to form N-Ɛ-fructosyllysine and N-Ɛ-maltulosyllysine, respectively (Hellwig et al., 2017). ARPs are unstable compounds and so degrade to form MGO, glyoxal (GO) and 3-deoxyglucose (3-DG) known as the second stage of Maillard reactions (Hellwig et al., 2017). In addition, caramelisation-based reactions also proceed due to the interactions of reducing sugars in the absence of amino compounds (Hellwig et al., 2017). The final stage of the Maillard reaction sequence produces advanced glycation end-products (AGEs) and protein cross-linking (Hellwig et al., 2017). AGEs are products of the reaction between di-carbonyl compounds and amino proteins or protein residues (Hellwig et al., 2017). Protein cross-links are formed by interactions between AGEs and other protein residues, and can have pathological effects. However, limited literature indicates the formation of AGEs and protein cross-linking from 1,2 di-carbonyl compounds in mānuka honey (Hellwig et al., 2017).

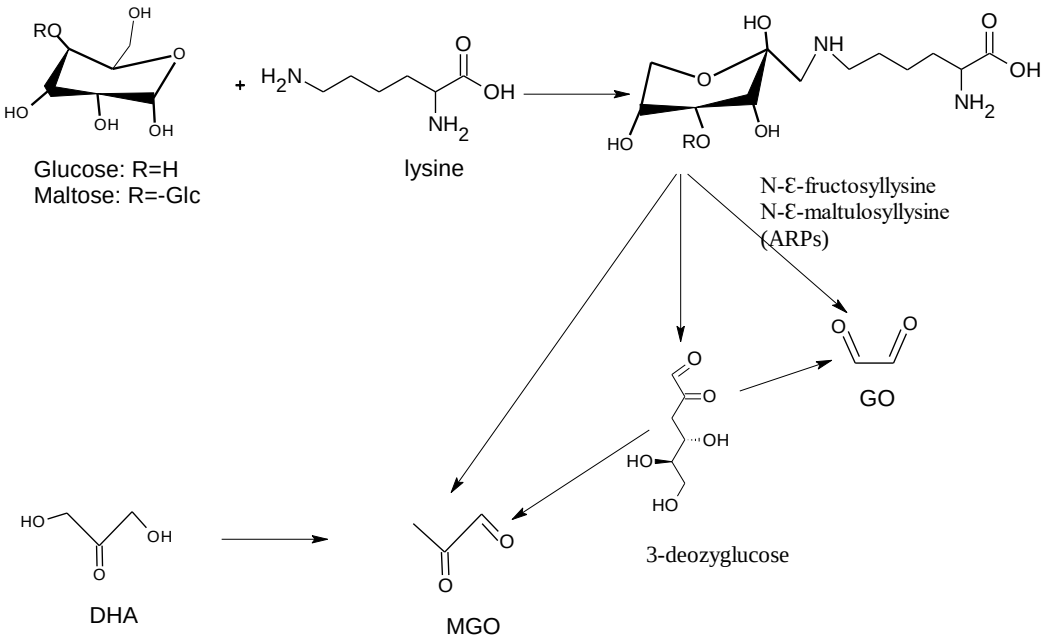

Figure 2.3. *The reaction scheme of the formation of the antibacterial MGO compound from DHA and from Maillard reactions (Hellwig et al., 2017)*

Besides, Maillard-side reactions can occur and form active compounds. MGO can react with amino acid proline to produce 2-acetyl-1-pyrroline, which is an aroma compound in mānuka honey (Grainger et al., 2016a; Grainger et al., 2017; Rueckriemen et al., 2015). Side reactions can cause the loss of DHA and MGO. According to Grainger et al. (2016a), DHA loss and the MGO formation were slow at 37^{o} C, 0.006 ± 0.0007 mmol/kg/day and 0.0037 ± 0.0010 mmol/kg/day, respectively (Grainger et al., 2016a). The loss of DHA is not just because of the MGO formation, but also because of Maillard-based side reactions (Grainger et al., 2016a). The Maillard side reactions in the presence of amino acid asparagine and reactive 1,2-dicarbonyl compounds will form the carcinogen acrylamide (Grainger et al., 2016a). However, only lysine and proline are major amino acids in mānuka honey, and the formation of acrylamide requires high temperature above 120^{o} C (Ghent, 2016; Grainger et al., 2016a). Thanks to the absence of asparagine and ambient temperature during honey storage, carcinogenic acrylamide compound cannot be generated in mānuka honey.

- *5-hydroxymethylfurfural*

The 5-hydroxymethylfurfural (HMF) component is formed in honey by two different pathways: caramelisation-based and Maillard-based procedures (Grainger et al., 2017). On the one hand, fructose and glucose are degraded into an intermediate 3-deoxyosone in the acidic honey environment following the caramelisation pathway, and then form HMF. Fructose is considered less stable than glucose, so easily fractures at pH 4.6 (Grainger et al., 2017). On the

other hand, HMF is also produced by degradation of ARPs in the complex Maillard reaction chain (Grainger et al., 2017). The accumulation of HMF in honey principally depends on temperature (Grainger et al., 2017). At 37^{o} C storage condition, the amount of HMF increases markedly, which couples with the formation of 2-acetyl-1-pyrroline due to the reaction of MGO and amino acid proline (Grainger et al., 2017). HMF is considered as a quality indicator for assessing heat exposure and storage condition of honey (Grainger et al., 2017). According to the international food standard (CODEX, 2001), the amount of HMF accumulating in honey should not exceed 40 mg/kg (Grainger et al., 2014; Grainger et al., 2017; Thrasyvoulou et al., 2018). Over 40 mg/kg, honey would be discarded. Several factors influence HMF accumulation including pH, sugar compositions, fructose/glucose ratio, temperature, mineral and water content (Grainger et al., 2017). Grainger et al. (2017) showed that the formation of HMF in mānuka honey at 37^{o}C is about 0.005 ± 0.001 mmol/kg/day. Of optical interest, HMF is a chromophore which independently absorbs in ultra-violet and visible (UV-Vis) region and induces maximal luminescence around 590 nm (Grainger et al., 2017).

- *Phenolic and polyphenolic compounds*

Mānuka honey contains diverse phenolic and polyphenolic compounds (Burns et al., 2018; Chan et al., 2013; Inoue et al., 2005; Yao et al., 2003). Methyl syringate, flavonoids and phenolic acids display bioactive properties important for mānuka honey (Burns et al., 2018; Van Eaton, 2014). While methyl syringate performs the scavenging property of superoxide anion radicals, flavonoids contribute to the antioxidant activity and color for mānuka honey (Burns et al., 2018; Van Eaton, 2014). In addition, phenolic acids dissociate at lower pH, which also contributes to the antibacterial effect along with MGO (Patel & Cichello, 2013; Van Eaton, 2014).

- *Methyl syringate residues*

Two important glycosides of methyl syringate are Lepstoperin (or Leptosin) and Lepteridine^{TM} 3,6,7-trimethyllumazine, which are both unique to mānuka nectar. These compounds are also found in Australian leptospermum-based honeys (Bong et al., 2017; Lin et al., 2017). However, they have not been identified in non-leptospermum-derived nectar yet (Bong et al., 2017; Daniels et al., 2016; Fearnley et al., 2012; Lin et al., 2017).

According to Bong et al. (2017 & 2018), Leptosperin and Lepteridine^{TM} 3,6,7-trimethyllumazine termed MM1 and MM2 respectively, produce fluorescence emission which can be used as mānuka honey chemical markers (Bong et al., 2018; Bong et al., 2017; Johnston et al., 2018; Lin et al., 2017; Smallfield et al., 2018). MM1 produces fluorescence at the

excitation - emission wavelengths at $\lambda_{ex/em}$ 270/365nm, while MM2 fluoresces at $\lambda_{ex/em}$ 330/470 nm (Lin et al., 2017). With diluted honey, MM1 & MM2 fluorescence emissions were easily detected, but with undiluted honey fluorescence signals can be distorted or quenched by the highly concentrated honey matrix (Bong et al., 2017; Kumar Panigrahi & Kumar Mishra, 2019; Lin et al., 2017). Both MM1 and MM2 are stable over prolonged storage at 37^{o} C within honey (Bong et al., 2017; Lin et al., 2017).

❖ *Flavonoids and phenolic acids*

Mānuka honey contains idiosyncratic flavonoid and phenolic acid profiles (Chan et al., 2013; Yao et al., 2003). Pinobanksin, pinocembrin (flavanone), luteolin and chrysin typically represent about 61 % of the flavonoids (Alvarez-Suarez et al., 2014; Chan et al., 2013). Yao et al. (2003) showed that quercetin, isorhamnetin, luteolin and an unknown flavanone are also principal flavonoids in mānuka honey. Phenolic acids dominated by gallic acid are present at up to 14.0 mg per 100 g mānuka honey (Yao et al., 2003). According to MPI (2017), four flavonoids and phenolic acids are considered as chemical makers for mānuka honey: 3-phenyllacticacid (3-PLA), 2′-methoxyacetophenone (2'-MAP), 2-methoxybenzoic acid (2-MBA) and 4-hydroxyphenyllactic acid (4-HPLA) (MPI, 2017b; Oelschlaegel et al., 2012; Smallfield et al., 2018). Four fingerprinting phytochemicals: MM1, MM1, 2′-MAP, 2-MBA are unique in mānuka nectar, with no presence in kanuka nectar (Bong et al., 2018). In contrast, lumichrome metabolite is unique for kanuka nectar (Bong et al., 2018). Nevertheless, 3-PLA and 4-HPLA are found in both mānuka and kanuka nectar (Bong et al., 2018). In general, flavonoids possess antibacterial and antioxidant activities (Chan et al., 2013). However, Chan et al. (2013) considered that flavonoids in mānuka honey correspond only to the antioxidant capacity rather than the antimicrobial activity (Bundit et al., 2016). Meanwhile, phenolic acids may contribute to the defensive capacity against pathogens, but are not principal antibacterial compounds in mānuka honey (Van Eaton, 2014).

Fluorescence properties of flavonoids in mānuka honey may be useful in gauging authenticity next to fluorescence makers MM1 & MM2 (Alvarez-Suarez et al., 2014; Bong et al., 2018; Bong et al., 2017). According to Chan et al. (2013), most flavonoids and phenolic acids absorb the light in Ultra-violet (UV) region at 290 - 390 nm and release fluorescence signals in Visible (Vis) region.

In summary, there are eight key phytochemicals representing the quality and monoflorality of mānuka honeys. Table 2.1 displays these key markers, their chemical structures and spectral information in UV-Vis and infrared range. Overall, almost all eight key

markers absorb in the UV range, but only MM1 and MM2 release fluorescence signals strong enough to represent as fluorescence markers for mānuka honey. In the infrared, these key markers could strongly absorb between 1900 and 1600 cm^{-1} due to the stretching of carbonyl group (C=O) that are consistent with their chemical structures (PubChem, 2022; Smith, 2017). The carbonyl group in all eight key chemical markers interacts readily with water in the honey matrix (Iwamoto, 2010).

Table 2.1. The eight chemical markers in mānuka honey and their spectral information in UV-Vis and infrared ranges

Chemical markers	Chemical structure	UV-Vis range	Infrared range	References
DHA	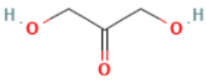	DHA-brown pigments absorb at 490 nm and fluorescence emission at 550 nm	Carbonyl (C=O) stretching between 1900 and 1600 cm^{-1}	(Nguyen & Kochevar, 2003; PubChem, 2022; Smith, 2017)
MGO	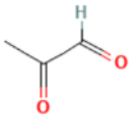	Photolysis in UV range < 420 nm to form CH_3CO + HCO radicals	1900 and 1600 cm^{-1} due to C=O	(PubChem, 2022; Staffelbach et al., 1995)
3-PLA	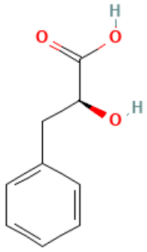	Absorb in UV range	1900 and 1600 cm^{-1} due to C=O group	(Chaudhari, 2016; PubChem, 2022; Smith, 2017)
4-HPLA	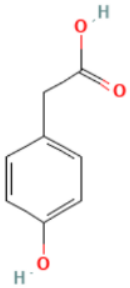	Absorb in UV around 277 nm	Stretching of C=O group at 3030, 2896, 1692 cm^{-1}	(Ohtani et al., 2011; PubChem, 2022)
2'-MAP	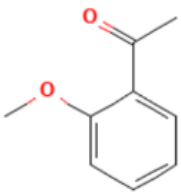	Absorb in UV range 315-400 nm →Fluorescence emission: 400-440 nm at λ_{ex} 320 nm	Strong absorb around 1663 cm^{-1} due to C=O group	(Liu et al., 2015; PubChem, 2022)

2-MBA	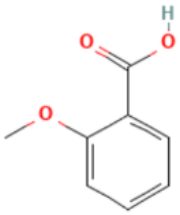	Absorb in UV range 250-260 nm	1900 and 1600 cm^{-1} due to C=O group	(PubChem, 2022; SpectraBase, 2022)
Leptosperin	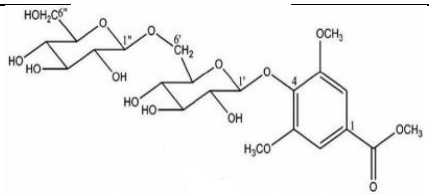	Fluorescence marker $\lambda_{ex/em}$ 270/365 nm	1900 and 1600 cm^{-1} due to C=O group	(Bong et al., 2017; PubChem, 2022)
Lepteridine™ 3,6,7-trimethyllumazine	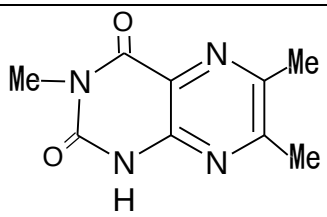	Fluorescence maker $\lambda_{ex/em}$ 330/470 nm	1900 and 1600 cm^{-1} due to C=O group	(Lin et al., 2020; PubChem, 2022)

Note: Me is methyl group (-CH_3)

2.6. Challenges of high-quality-grade mānuka honeys in production

Mānuka honey quality could be affected through natural crystallisation and by incorporating inferior honeys during the bulk extraction process.

2.6.1. Crystallisation

Crystallisation is a natural phenomenon occurring in the supersaturated solution (honey) (Dettori et al., 2018). Mānuka or non-mānuka honey contains a high amount of carbohydrates up to 80 %, mainly monosaccharides glucose and fructose (Lucília Carolina Vardenski et al., 2015; Nickless, 2015). Glucose is less soluble in water than is fructose. As a result, glucose displays a primary role of crystallisation during honey process and storage (Dettori et al., 2018; Lucília Carolina Vardenski et al., 2015).

Crystallisation can be an undesirable process in honey products (Dettori et al., 2018; Lucília Carolina Vardenski et al., 2015) because it increases water activity and favours for yeast growth and fermentation (Kretavičius et al., 2010; Lucília Carolina Vardenski et al., 2015). The formation of crystals in honey can affect honey rheological sensory and changes in optical properties (Dettori et al., 2018; Lucília Carolina Vardenski et al., 2015).

2.6.2. Bulk extraction

Currently, honey frames from the beehives within an apiary are generally lumped for extraction together. Mānuka honey quality and identity differ between and within geographic districts due to different *L. scoparium* varieties and other floral sources, which influence the nectar quality. In addition, in a frame, bees could move nectar around to fill up cells. Intuitively, there can be quality variability across apiaries, across beehives and even in a honey frame. At the same beehive, the quality of honey could vary cell by cell and frame by frame. When frames with poor quality are extracted with good quality ones, the final quality of mānuka honeys in drums could be devalued. Further, when the good frames go into poor drums, these good frames will be wasted.

Figure 2.4. *From mānuka nectar to apiary/hives and bulk extraction*

The quality and identity of mānuka honeys is generally evaluated after the extraction process. There is a paucity of measurement prior to extraction. Traditional methods (wet analysis) are inconvenient to apply directly on frames and are relatively expensive. This study aims to find a suitable method for quality measurement of honey in frames. In the next sections (2.7 & 2.8), the current quality measurement systems, and a new approach that this study aims to apply are described.

2.7. Current quality measurements of mānuka honeys

2.7.1. Sensory evaluation

Quality of mānuka honey had been evaluated by sensory methods and by measuring physicochemical properties for composite honeys after extraction at least 10 years ago (MPI, 2017b; Van Eaton, 2014). Colour and flavour are tested by sensory experts (Van Eaton, 2014). Mānuka honey's colour varies across geographic districts. Mānuka honey from New Zealand South Island is lighter than that from the North Island. According to the Honey Marketing Authority, mānuka honey having light colour is sold for a better price than that of dark colour

with the same MGO concentration (Van Eaton, 2014). In addition, flavour is also very important, which is the combination of taste from the mouth and aroma from the nose. Colour and flavour often need experts to evaluate. Fresh mānuka honey is different in flavour from aged honey (Van Eaton, 2014).

2.7.2. Quality and identity measurement

❖ *The Unique Mānuka Factor (UMF™) rating system*

The UMF™ rating system is used to measure mānuka honey quality. Mānuka honey contains a significant level of non-peroxide activity (NPA) which Peter Molan measured via the UMF™ unit (Stephens, 2006; Van Eaton, 2014). Early in the 1990s, Allen et al. (1991) established measurement of UMF™ units based on the equivalence to the concentration of phenol (w/v %) effective against *Staphylococcus aureus* using the radial agar diffusion assay (Combarros-Fuertes et al., 2019; Roberts et al., 2015; Stephens, 2006). In 2008, MGO was discovered to be the main agent responsible for the NPA in mānuka honey (Elvira et al., 2008; Hellwig et al., 2017; Owens et al., 2019; Snow & Manley-Harris, 2004), but Roberts et al. (2015) and Matthew et al. (2018) held that the overall NPA arises from a complex mixture of diversified antibacterial components within mānuka honey. Currently, the NPA value can be measured by two different scalings: UMF™ units and MGO concentration (mg/kg mānuka honey) (Roberts et al., 2015). In general, UMF™ represents for the overall NPA of mānuka honey rather than merely MGO concentration (Johnston et al., 2018; Roberts et al., 2015).

Despite other influences, the UMF™ score is strongly indicated by MGO concentration. The relationship between UMF™ score and MGO is non-linear (Georgescu et al., 2017; Roberts et al., 2015). Table 2.2 shows the relationship between UMF™ and MGO concentration defined by the UMFHA.

Table 2.2. The UMF™ rating system with MGO and Leptosperin concentrations required

UMF™ value	***5+***	***10+***	***15+***	***20+***	***25+***
MGO required	*83 mg/kg*	*263 mg/kg*	*514 mg/kg*	*829 mg/kg*	*1200 mg/kg*
Minimum Leptosperin required	*≥ 100 mg/kg*	*≥ 150 mg/kg*	*≥ 200 mg/kg*	*≥ 200 mg/kg*	*≥ 200 mg/kg*

In addition, K-factor 16 unit is also introduced to mānuka honey grading system. This unit was accepted by NZ MPI (UMFHA, 2022). K-factor 16 unit does not quantify MGO concentration but measures biochemical properties of mānuka honey including the purity, live enzymes, DHA, the number of pollens, pH and phenolic compounds (UMFHA, 2022). Generally, UMF^{TM} and MGO units are commonly used to measure antibacterial activity for commercial mānuka honey products while K-factor 16 measures biochemical properties within mānuka honey and is mostly for company usage.

Mānuka honeys with different UMF^{TM} scales display different antibacterial effects against gram-positive and gram-negative's growth and cell morphology (Johnston et al., 2018). Gram-positive organisms such as *S. aureus and Bacillus subtili*s are inhibited at UMF^{TM} just above 10+ (Johnston et al., 2018; Roberts et al., 2015). The action on gram-positive strains is because of the 1,2-dicarbonyl MGO compound interfering with their cell division process (Combarros-Fuertes et al., 2019; Roberts et al., 2015). By contrast, gram-negative bacteria (*E. coli* and *P. aeruginosa)* are inactivated by metabolic disruption (Combarros-Fuertes et al., 2019; Roberts et al., 2015). In general, gram-negative organisms are more resistant than gram-positive strains, requiring higher antibacterial activity than do gram-positives (Johnston et al., 2018; Roberts et al., 2015).

- *Ministry for Primary Industries (MPI) criteria*

MPI criteria are employed to determine mānuka honey identity. NZ MPI has regulated methods to authenticate mono-floral and multi-floral mānuka honeys. The main method used is high-performance liquid chromatography (HPLC) to measure concentrations of four key chemical markers (2-MAP, 3-PLA, 4-HPLA and 2-MBA). In addition, a pollen DNA test is required for *Leptospermum scoparium* < Cq 36 (approximately 3 fg/µL) (Table 2.3) (MPI, 2017b).

Table 2.3. The MPI criteria for definition and identity standards of New Zealand mānuka honeys (MPI, 2017b)

New Zealand mānuka honey definition	Mānuka honey: - 2'-MAP ≥ 1 mg/kg - 2-MBA ≥ 1 mg/kg - 4-HPLA ≥ 1 mg/kg - 3-PLA ≥ 20 mg/kg - DNA test from pollen: required < Cq 36 (approximately 3 fg/µL)
	Multi-mānuka: - All levels are met in as the definition of mānuka honeys - But 3-PLA ≥ 20 mg/kg and < 400 mg/kg
	Mono-mānuka: - All levels are met in as the definition of mānuka honey - But 3-PLA ≥ 400 mg/kg and 2'-MAP > 5 mg/kg

2.8. Introduction of in-house measurement approach "mānukaness"

Mānuka honeys contain biochemical compounds which are unique to *L. scoparium*. The eight chemical markers are important to define the quality and identity of mānuka honeys. In this study, the new term "mānukaness" is introduced as a spectral quality mark for estimating mānuka honey quality and purity based on spectral analysis. Assessment of mānukaness reflects both the quality and purity of mānuka honey measured from the current UMF™ rating system and MPI criteria. The quality and purity of mānuka honey are spectrally predicted as so-called potency mānukaness and purity mānukaness, respectively. Chemometric methods (regression and classification) will be applied to spectral data to predict UMF™ scores as a proxy for potency mānukaness. Meanwhile, the classification approach was employed to distinguish between mono-, multi-, and non-mānuka honeys as a proxy measure of purity mānukaness. Potency and purity mānukaness predictions given together could allow honey companies degrees of freedom in decision-making.

The general equation of mānukaness (M) can be explained as follows:

$$M = f([DHA], [MGO], [2' - \text{MAP}], [2 - \text{MBA}], [4 - \text{HPLA}], [3 - \text{PLA}], [\text{MM1}], [\text{MM2}])$$

(eq. 2.1)

Based on the study of laboratory data, potency mānukaness is measured as a function of DHA, MGO and MM1.

$$\text{Po} = f([DHA], [MGO], [MM1]) \quad \text{(eq. 2.2)}$$

By contrast, purity mānukaness is a function of DHA, MGO, PLA-3, HPLA-4, MAP-2', MBA-2, MM1 and MM2, which were identified in PCA analysis (Appendix).

$$Pu = f([2' - \text{MAP}], [2 - \text{MBA}], [4 - \text{HPLA }], [3 - \text{PLA}], [MM1], [MM2]) \quad \text{(eq. 2.3)}$$

Section 2: Spectroscopy and hyperspectral imaging

Spectroscopy is a branch of science that studies the interaction of electromagnetic radiation (light) and matter (e.g., food). The extension of spectroscopy known as hyperspectral imaging is based on multiple spectroscopic measurements. In general, light illuminates the sample and the outcoming light is detected as a result of the interaction. The detection can be arranged for the light transmitted through the sample or for the light that has travelled back towards the illumination side. The detection is usually focused on a specific area of the sample, where it is possible to collect one spectrum representing the scanned area (so-called non-imaging spectroscopy) or collect a spectrum per pixel in the scanned area (so-called hyperspectral imaging) (Saeys et al., 2019).

2.9. Visible-Near Infrared spectroscopy

Visible-Near Infrared covers the visible (Vis) range of 400 - 700 nm and near-infrared (NIR) 800 - 2500 nm (Krzysztof & Christian, 2019; Yukihiro Ozaki, 2018). Spectroscopy measures the interaction of light with matter (e.g., food) as a result of changes in intramolecular energy. Where light is absorbed, molecular energy is shifted to a higher level. In the Vis, the energy in the electronic state of the molecules is lifted, while in the NIR there is a change in the molecular vibration status.

In the NIR region molecules containing a covalent hydrogen bond X-H (e.g., C-H, O-H, N-H) are indicated through characteristic molecular vibrations and interactions (Krzysztof & Christian, 2019). In addition, molecules consisting of carbon groups (C=O, C=C, C=N or C≡N) also absorb in the NIR (Krzysztof & Christian, 2019). This provides the possibility of interpreting the presence of target molecular compounds in a specific medium (Krzysztof & Christian, 2019; Saeys et al., 2019).

Two common types of spectroscopic measurement are transmittance and reflectance. The selection of the measurement mode depends on several factors such as the type of material (liquid/solid), the aim of the measurement (e.g., non-invasive or invasive) and others. If

samples are clear liquid, transmittance mode is often used. Here, the sample is placed between the light source and the detector. If samples are turbid, containing many particles, the transmittance mode is inappropriate since these suspended particles prevent light transmission through the sample, so the reflectance mode is suggested. In reflectance mode the detector is placed at the same side of the light source to capture diffuse reflectance intensity.

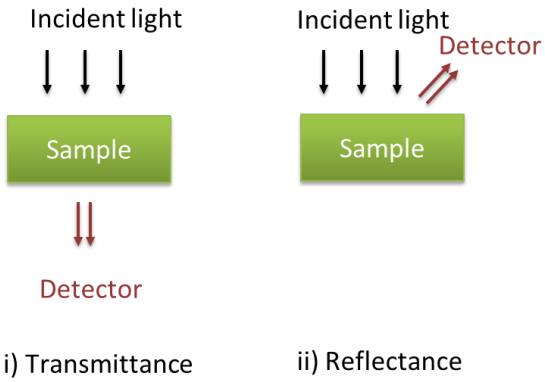

Figure 2.5. *Optical pathways of transmittance and reflectance* (Saeys, 2006)

2.9.1. The interaction between radiation and molecular species

As the light beam reaches the surface of the sample, part of light will reflect from the surface to the original environment and so it does not interact with the sample, resulting in specular reflectance (Weik, 2001). The other part of the light beam will travel through the sample. Depending on the structure of the medium, scattering events can occur which cause the changes in direction of light. As a result, a component of the light beam may travel back and leave the sample leading to diffuse reflectance (Weik, 2001). As the light travels through the sample, absorption events are expected in which the energy of the light is absorbed by the sample. Eventually, a part of the incident light beam might reach the opposite side of the sample (so-called transmittance) or be completely absorbed. Following the absorption events, chemical molecules which accumulate the energy can release light with lower energy (higher wavelength), known as fluorescence. Multiple types of scattering can be induced. In general, two types exist: elastic where the energy of light is similar before and after scattering (e.g., Rayleigh); and inelastic which the light energy is different before and after the scattering event (e.g., Raman) (Kruppa & Strube, 1994). All these processes of light interactions are dependent of the incoming light energy (excitation wavelength). However, not all processes have the same chance to occur. Both inelastic scattering and the chemical absorption are the prominent events. As a result, when the incident light is polychromatic (multiple wavelengths), the light of each

wavelength will follow a unique series of interactions with the sample. Then the outcoming light (either diffuse reflectance or transmitted) will have a unique distribution of intensity according to the specific excitation wavelength. This distribution forms the spectrum and is closely linked to the chemical and structural characteristics of the sample *(Lu et al., 2020).*

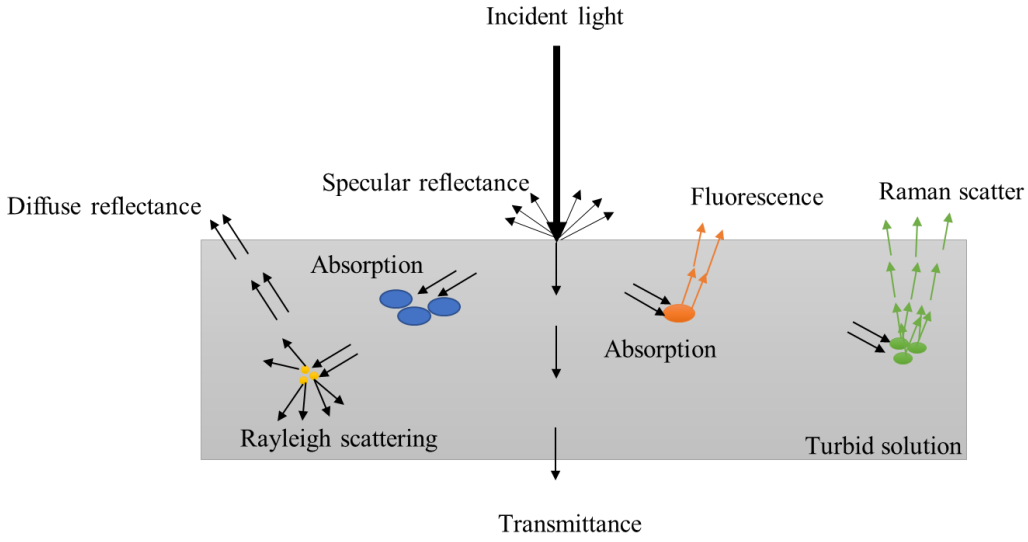

Figure 2.6. *Common events during the interaction between molecular species and electromagnetic radiation in a medium (after Lu et al., 2020)*

2.9.2. Lambert-Beer's law

The Lambert-Beer's law states that for transparent solutions (with few particles), where scatterings are assumed absent, the light transmittance is linear to the concentration of the absorbing component *(c)*, which possesses an absorbtion coefficient (*k)* for an optical pathway distance (*L)*:

$$T = \frac{I}{I_o} = exp\,(-kcL) \quad \text{(eq. 2.4)}$$

where T, I_o and I are transmittance, the incident intensity and the transmitted intensity, respectively.

According to equation 2.4, the transmittance depends on the optical pathway distance in which sample container and sample thickness contribute to this pathlength (Saeys, 2018).

2.9.3. Absorbance vs pseudo-absorbance

Rearranging the equation 2.4 statement of Lambert-Beer's law, the absorbance *A* of an absorbing specie is linear to its concentration that can be calculated by taking the logarithm of the reciprocal of transmittance *T*:

$$A = Log\left(\frac{1}{T}\right) = kcL \quad \text{(eq. 2.5)}$$

For a transparent liquid, the pathway L is assumed constant. Thus, the absorbance is calculated by transmittance measurement following the formula 2.5. However, most samples are turbid containing suspended particles, specially solid species. In this case, the pathway L is not constant because of scattering effects. So, diffuse reflectance is suggested for unclear solutions since reflectance signals are independent of the optical pathway distance. The pseudo-absorbance *A'* can be calculated by taking the logarithm of the reversed diffuse reflectance *Log (1/R)*. The pseudo-absorbance is still linear to the concentration of absorbing species (Saeys et al., 2019).

2.10. Fluorescence spectroscopy

2.10.1. Fluorescence phenomenon

Fluorescence is an illumination phenomenon when absorbers, so-called fluorophores, absorb the energy from electromagnetic radiation at a certain excitation band, and after about 10 ns, those compounds release fluorescence signals with lower energy of a longer wavelength than the incident light (Lakowicz, 2006). Fluorescence phenomena often occur very fast with an average lifetime of 8 - 10 ns. The emission of fluorescence can be either in UV-Vis or NIR regions and it is independent from the incoming light. For instance, an intrinsic tryptophan-protein absorbs in the UV range (λ_{ex} = 280 nm) and releases fluorescence in in the UV-Vis region (λ_{em} = 300 - 400 nm) (Moller & Denicola, 2002).

2.10.2. Fluorophores

Fluorophores are fluorescent molecules often having a chemical structure containing conjugated bonds with available *p* orbitals. When receiving energy, free electrons from *p* orbitals can localise within and between other adjacent orbitals. The transit of electrons corresponds to the energy difference between the two orbitals. As the results, they move from the ground state to a high energy state. In the higher state, energised electrons are unstable and tend to come back to the ground state. When they return to the ground state, they release weak energy at long wavelengths. The process of releasing energy is named fluorescence emission. In general, fluorophores often possess higher quantum yield than those of non-fluorescent compounds. Quantum yield means the ratio between the number of photons emitted to the number of photons absorbed (Lakowicz, 2006).

The process of light absorption for fluorescent compounds will follow the same principle (section 2.9.1), but the fluorescence emission will depend on unique characteristics of each molecule (Lakowicz, 2006). As a result, the chemical footprints could be detected or identified based on fluorescence emission at a certain excitation wavelength. For example, common fluorophores in biological samples include tryptophan, chlorophyl and haemoglobin (Hb). These compounds have indole groups or benzoic rings with a branch of conjugated bonds in their chemical structures. In mānuka honey, two unique fluorophores are Leptosperin and Lepteridine^{TM} (Bong et al., 2018; Bong et al., 2017). Other fluorescent compounds are also present in mānuka honeys (flavonoids, DHA-brown pigments) (Nguyen & Kochevar, 2003).

2.10.3. Fluorescence spectroscopy

Fluorescence spectroscopy is an optical technique which works based on the principle of the fluorescence phenomenon. In applications of fluorescence spectroscopy, detection of biochemical signatures from fluorescence emission has been widely applied to evaluate food quality and safety. For instances, fluorescence spectroscopy has been used to measure the changes of protein structure, lipid and carbohydrate content during processing and storage (Hassoun et al., 2019). In addition, fluorescence spectroscopy was also used to detect contamination by pathogenic microorganisms (e.g., *Pseudomonas aeruginosa*) (Lewis et al., 2013) and the presence of carcinogenic aflatoxins in maize (Smeesters et al., 2015). In general, fluorescence spectroscopy works with aqueous samples rather than solid matter. The fluorescence intensity and fluorophore concentration are in a linear relationship if the solution has the absorption ≤ 0.1 and accords with Lambert-Beer's law. However, in the case of turbid solutions (Absorbance > 0.1), non-linearity is observed between the fluorescence intensity and concentration due to inner filter effects (Chen et al., 2018; Kumar Panigrahi & Kumar Mishra, 2019).

Currently, three configurations are known in fluorescence spectroscopy. Right-angle is standard and often uses cuvettes for containing samples. The incoming light (excitation) excites the sample with the angle 90^{o} (Figure 2.7 (1)). Meanwhile, front-face fluorescence has the incoming light exciting the sample at 45^{o} (Figure 2.7 (2)). In-line geometry fluorescence spectroscopy often utilises micro-plates for containing samples. The incoming light and the emission are in-line (Figure 2.7 (3)). If the excitation and emission are on the same side of the sample, fluorescence measurement is "top reading". If the excitation and emission come from different sides of the sample, fluorescence measurement is "bottom reading" (ThermoScientific, 2022).

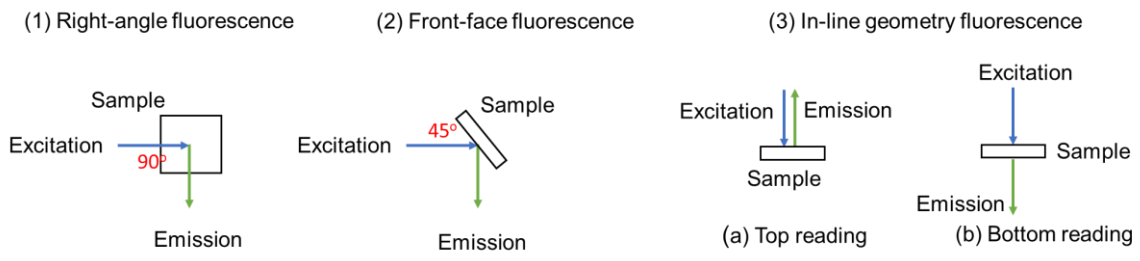

Figure 2.7. *Three different configurations of fluorescence spectroscopy: (1) Right-angle fluorescence, (2) front-face fluorescence, (3) in-line geometry fluorescence with (a) top reading and (b) bottom reading (Latchoumane et al., 2022; ThermoScientific, 2022)*

2.10.4. Scattering interference during fluorescence measurements

During fluorescence measurements, Rayleigh and Raman scatterings are often undesirable. The presence of those scattering processes can influence and obstruct fluorescence signatures of a excitation-emission matrix (EEM) (Murphy et al., 2013). Ideally, these scatterings should be eliminated during collection of fluorescence data. Rayleigh scattering can be reduced by removing particles from the sample. The presence of Rayleigh effect in the spectra can be also mitigated after subtracting the blank for the raw intensity (Murphy et al., 2013). Moreover, this scattering can also be removed by optimising the excitation-emission range of interest. For example, each emission wavelength is measured 30 - 50 nm higher than the default excitation wavelength (Lakowicz, 2006; Truong et al., 2021). This cut-off strategy can minimise first and second order Rayleigh scatterings (1st order: Rayleigh scattering has the same frequency as the incident light; 2nd order: Rayleigh scattering has double the frequency of the incident light). By contrast, Raman scattering cannot not be totally eliminated due to the presence of particles. However, it can be minimised by diluting samples to have the absorbance less than 0.1 (Vandenabeele, 2013). For unclear solutions, fluorescence measurement will be strongly affected by Raman scattering at high energy wavelengths (e.g., UV) (Engelen et al., 2007).

2.10.5. Quenching phenomenon

Quenching is an interference phenomenon that happens when a fluorophore interacts with another species (quencher) causing energy loss of the excited state (Albani, 2004; Algar & Massey, 2019). As a result, the fluorescence intensity of a fluorescent substance decreases. Several types of quenching exist: collisional, static, thermal and energy transfer. Collisional

quenching happens between a fluorophore and another molecule during collision without the formation of a complex. This collision could arise between two fluorophores or a fluorophore with another non-fluorescent molecule (Alimova et al., 2006; Lakowicz, 2006; Moller & Denicola, 2002). Fluorophores with high quantum yield could collide or quench molecules with low quantum yield (Moller & Denicola, 2002). By contrast, static quenching appears to involve formation of a molecular complex. For example, the interaction of aromatic acid amines with carbonyl compounds (Albani, 2004). Several factors trigger fluorescence quenching such as temperature and pH. High temperature can increase the reactions between fluorophores and other active compounds causing thermal quenching meanwhile pH can influence fluorescence decay that decreases fluorescence yield (Beechem & Brand, 1985). Energy transfer is a dynamic quenching (e.g, Forster resonance energy transfer) which interferes with the emission of a fluorophore at the excited state. The energy is transferred through space without collision (Algar & Massey, 2019). In general, quenching phenomena are undesired during fluorescence measurements, but it is not easy to eliminate this issue (Albani, 2004; Lakowicz, 2006).

In some cases, quenching could be used to detect non-fluorescent compounds. Dairy manufacture has employed the quenching principle to measure melamine, which migrates from the plastic package into food. A fluorescent compound Triton X-114 is used as a standard. Triton X-114 reacts with melanin forming a complex compound which does not produce a fluorescence signature. Measuring the difference of fluorescence intensity added and fluorescence intensity remained will reflect the concentration of Triton reacted with melamine. From that, qualitative and quantitative of melamine can be measured (Shaikh & O'Donnell, 2017).

2.11. Hyperspectral imaging

Hyperspectral imaging is an advanced technique that combines spectroscopy and imaging. A hyperspectral image is represented by hypercubes (x*y*z) having the spatial information (x*y) captured in multi-continuous spectral bands z. The spatial dimension is constructed by individual pixels that carry the spectral information. Figure 2.8 illustrates a three-dimensional hyperspectral image where x and y illustrate the image dimension and z is the spectral dimension. At each ‘x’ and ‘y’ represent a pixel in the image and carries a spectrum (Sun & ElMasry, 2010).

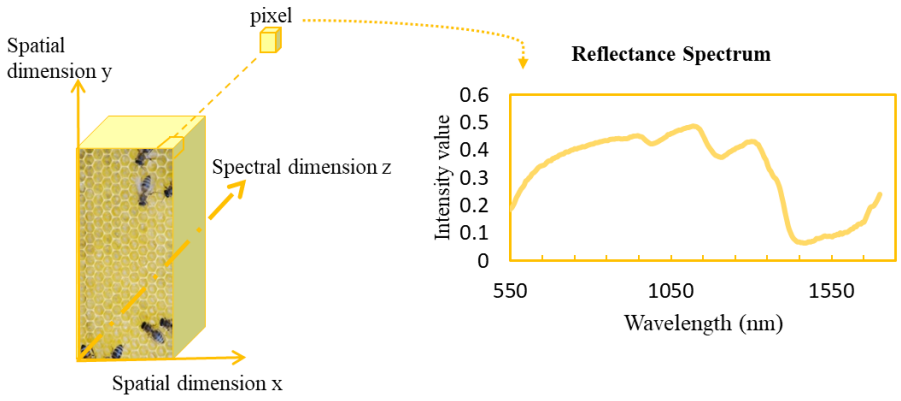

Figure 2.8. *The scheme of a hyperspectral image obtained at the pixel level (Sun & ElMasry, 2010)*

2.11.1. Hyperspectral acquisitions

Four main hyperspectral acquisition techniques are currently known such as whiskbroom (point-scanning), push-broom (line-scanning), staring (area-scanning) and snapshot. Point-scanning collects spectra pixel by pixel in a mapping process. By contrast, the line-scanning collect 'n' spectra along a line simultaneously, and the image is obtained by translating the samples or detector. Area scanning captures an image one wavelength at time. Snapshot collects the whole hyperspectral image at once. At the end, all acquisitions seize a hyperspectral image with three dimensions (x*y*z). Point-scanning produces high pixel-resolution meanwhile line-scanning obtains good spectral information. Staring and snapshot are not very often used in the food industry since their configurations are complicated and expensive. Besides, some spectral information might be lost when using snapshot and staring acquisitions (Arthur, 2016; Qin, 2010). In this study, line-scanning acquisition was used to capture the spectral images of honeys (Figure 2.9).

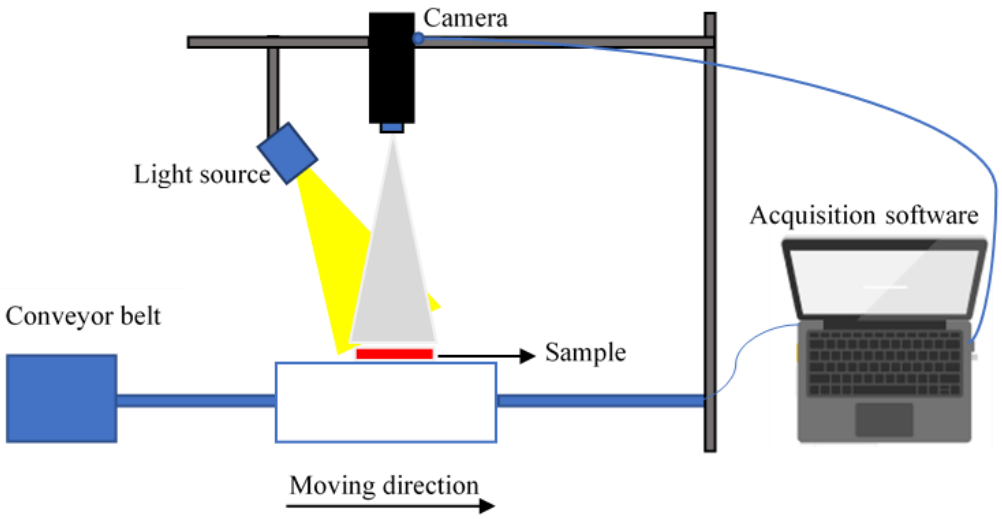

Figure 2.9. *The reflectance line-scanning hyperspectral imaging system (after Al-Sarayreh, Reis, Yan & Klette, 2020)*

2.11.2. Hyperspectral components

A hyperspectral imaging system consists of two key components: the illumination (light source) and a detection system. The illumination is chosen based on phenomena of interest. For examples, halogen is used on applications involving Vis-NIR since it has a broad spectrum across these spectral ranges. LED and lasers are also used but are better for specific applications, such as imaging scattering (Qin, 2010).

The detector system known as the wavelength dispersion device consists of diffraction gratings allowing multiple wavelengths to be detected by an array of detectors to obtain spectral information. Then, the spectral information is synchronised into the spatial dimension to obtain a spectral image (Qin, 2010).

According to Qin (2010), diffraction gratings were quite different in transmittance and reflectance modes. In transmittance mode, the incident light enters the entrance slit and travels through the prism components (Figure 2.10a). Before projecting into the detector, the incident light is dispersed into different bands. By contrast, in the reflectance mode, the excitation light is guided by a lower mirror to be dispersed into different bands through reflecting gratings and then reflected via the upper mirror before detected by the detector (Figure 2.10b) (Qin, 2010).

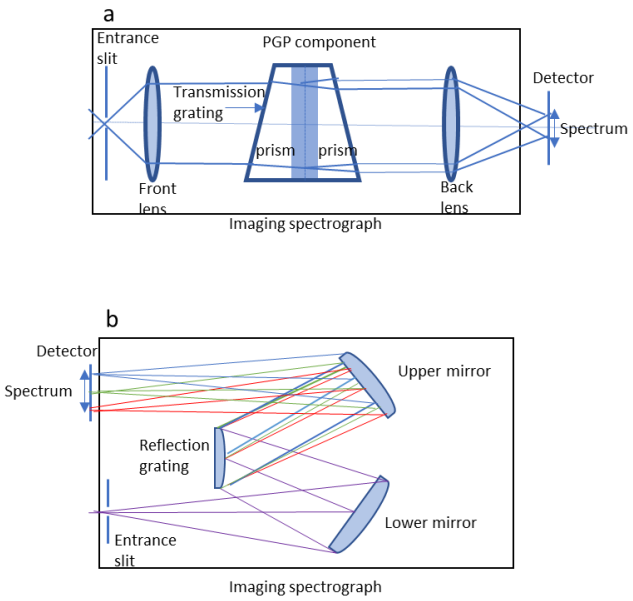

Figure 2.10. *The configuration of transmitting (a) and reflective (b) gratings in imaging spectrograph (after Qin, 2010)*

2.11.3. Imaging system parameters

Figure 2.11 illustrates some fundamental parameters in a hyperspectral imaging system including field of view, working distance, sensor size, resolution, pixel size, depth of field, and magnification.

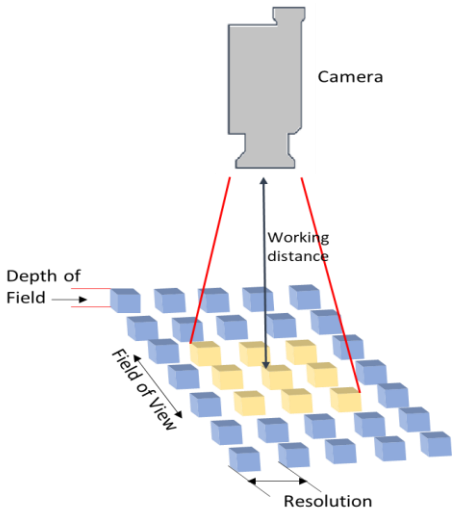

Figure 2.11. *An illustration of imaging parameters of a hyperspectral imaging system (after Gregory & Nicholas, 2020)*

Field of view (FOV) is the camera view which covers the scanning area (usually expected as a diameter) while working distance (WD) is the distance between the camera lens and the object. By contrast, sensor size is the camera's active area which is important in determining the FOV. Resolution (spatial resolution) is the minimum size of object which the camera can detect. Analogous to resolution, pixel size is the dimension of a tile square (pixel) measured by metric units (e.g., mm, μm). Depth of field (DOF) is the maximum object depth that gives an acceptable focus meanwhile magnification is the ratio between the sensor size and the FOV (Centre for Remote Imaging, 2020; Gregory & Nicholas, 2020).

2.11.4. Instrumental correction

In hyperspectral imaging, several sources of instrumental variation are recognised such as the variation in light intensity and distribution over the sample, variations in optical collection and in the sensor. To mitigate the presence of these instrumental variations, a common strategy is the utilisation of reference materials. These reference materials allow cancelation of variation over time. As a result, the instrumental variation of hyperspectral data from this type of material is assumed mostly to originate from the hyperspectral system. This allows the data to be corrected for reproducible information.

White and dark references are used for the correction of raw reflectance spectra following the equation below:

$$Rs(\lambda) = \frac{Is(\lambda) - Id(\lambda)}{Ir(\lambda) - Id(\lambda)} * Rr(\lambda) \quad \text{(eq. 2.7)}$$

where Rs (λ) is the relevant reflectance spectrum corrected for analysis; Is (λ) is the raw reflectance spectrum measured at the wavelength of λ nm; Id (λ) is the reflectance spectrum of the dark reference captured by using a black opaque cap to cover the whole camera lens. Ir (λ) is the reflectance spectrum of the white reference captured by using the white panel. Rr (λ) is the reflectance factor of the white reference which assumes more than 99 % of the light is reflected (Arthur, 2016; Qin, 2010).

Section 3: Modelling methods

2.12. Chemometrics and machine learning

Chemometrics and machine learning are utilised to handle the multivariate nature of the spectroscopic data and the particular property of a high correlation among the variables. This section describes the definition and algorithms of all chemometrics, and machine learning methods employed in this study.

2.12.1. Definition

Chemometrics is an application of statistical methods to improve the understanding of chemical information generated from different instruments. According to the International Chemometrics Society, "Chemometrics is the science of relating measurements made on a chemical system or process to the state of the system via application of mathematical or statistical methods" (Saeys, 2018).

Machine learning (ML) is a computational learning process which uses specific algorithms to train models and by this process the learning algorithm is used for prediction of attributes associated with a set of variables. Machine learning models extract relevant information contained in the data for predictions (Murdoch et al., 2019).

Both chemometrics and machine learning methods create predictive models, which are used to estimate responses of new circumstances (Shalev-Shwartz & Ben-David, 2014).

2.12.2. Multivariate analysis

❖ *Principal Component Analysis*

Principal Component Analysis (PCA) is an unsupervised method, which compresses the high dimensional data (**X**) into a low dimensional data space of principal components (PCs). PCA-PCs capture maximal variance from the raw data and minimise the correlation among variables. Principal components are formed in a decreasing order of significant importance. The first PCA-PC captures the most variance in the data and then the next-order PCs are formed by the same principle. Following that, all PCs are set orthogonal to each other and carry relevant information from the original data. For spectral data collected from spectroscopy or hyperspectral imaging, the matrix **X** (n x m) contains n samples and m spectral variables. Each sample n has a spectral response at each variable p. The PCA algorithm decomposes the original data (**X**) into the score matrix (**T**), the loading matrix (**P**) and the residual modelling error (**E**) (Saeys et al., 2019).

$$\mathbf{X} = \mathbf{T} \times \mathbf{P^t} + \mathbf{E}$$

Spectral data | Scores | Loadings | Residues

Where 't' is the transpose operator in the unfold PCA algorithm.

Each column vector of the **T** matrix represents the scores of principal components. Meanwhile, each column vector of the **P** matrix displays the loadings of principal components (Saeys et al., 2019). The information not explained by PCA-PCs is characterised as noise and contained within the modelling error (**E**).

PCA method is often used to explore multivariable data before applying other chemometrics methods since PCA helps to observe clusters, trends and outliers which supports to understand the relationship between samples and variables (Saeys et al., 2019).

❖ *Principal Component Regression*

Principal Component Regression (PCR) works based on the PCA principle. The spectral data (**X**) are decomposed into the score matrix (**T**) and the loading matrix (**P**) (eq. 2.8). Similar to PCA, the score matrix $\mathbf{T_{PCR}}$ contains variance values captured by principal components while the loading matrix $\mathbf{P_{PCR}}$ measures the distance of PCs to the mean-center of the X-data that indicate the weight value of each X-variable.

$$\mathbf{X_{PCR}} = \mathbf{T_{PCR}}\mathbf{P^t}_{\mathbf{PCR}} + \mathbf{E_{PCR}} \quad \text{(eq. 2.8)}$$

The PCR matrix of responses ($\mathbf{Y_{PCR}}$) is regressed into the score matrix ($\mathbf{T_{PCR}}$) and the loading matrix ($\mathbf{Q_{PCR}}$) which is gerneralised from the true values. The unfitted information is contained in the residuals $\boldsymbol{F_{PCR}}$ (Naes et al., 2004; Saeys et al., 2019).

$$\mathbf{Y_{PCR}} = \mathbf{T_{PCR}}\mathbf{Q_{PCR}} + \mathbf{F_{PCR}} \quad \text{(eq. 2.9)}$$

From equation 2.9, the score $\mathbf{T_{PCR}}$ contains score values which are linear with predicted values. When a PCR model is established, the PCR regression coefficient vector $\boldsymbol{\hat{b}_{PCR}}$ is determined as follows (Naes et al., 2004; Saeys et al., 2019).

$$\boldsymbol{\hat{b}_{PCR}} = \boldsymbol{\hat{P}_{PCR}}\ \boldsymbol{\hat{q}_{PCR}} \qquad \text{(eq. 2.10)}$$

To apply a PCR model for a new dataset, the new estimated response can be calculated: (Naes et al., 2004; Saeys et al., 2019).

$$y_{new} = \bar{y} + x_{new}\,\hat{b}_{PCR} \qquad \text{(eq. 2.11)}$$

❖ *Partial Least Squares Regression*

Partial Least Squares (PLS) regression is a supervised multivariate regression method which is different from unsupervised PCR. PLS regression maximises the covariance between **X** and **Y**, instead of capturing the variance from only the X-data (a PCR model). As with PCR, PLS transforms the matrix **X** into the dimensionless space of latent variables (LVs) which maximises the covariance between **X** and **Y** (Saeys et al., 2019). A basic PLS model can be written as follows:

$$\mathbf{X_{PLS}} = \mathbf{T_{PLS}} \cdot \mathbf{P^t}_{\mathbf{PLS}} + \mathbf{E_{PLS}} \quad \text{(eq. 2.12)}$$

$$\mathbf{Y_{PLS}} = \mathbf{U_{PLS}Q_{PLS}} + \mathbf{F_{PLS}} \quad \text{(eq. 2.13)}$$

where $\mathbf{X_{PLS}}$ is the data matrix (n x m); $\mathbf{Y_{PLS}}$ is the matrix of responses (n x p); $\mathbf{T_{PLS}}$ is the X-score matrix (n x l); $\mathbf{P_{PLS}}$ is the X-loading matrix (m x l); $\mathbf{U_{PLS}}$ is the Y-score matrix (n x l); $\mathbf{Q_{PLS}}$ is the Y-loading matrix (p x l) and $\mathbf{E_{PLS}}$ and $\mathbf{F_{PLS}}$ carry the regression noise.

When the PLS model is built, the regression coefficient vector b_{PLS} can be computed by minimising the squares of residual errors (Naes et al., 2004; Saeys et al., 2019).

$$\widehat{\boldsymbol{b}}_{\boldsymbol{PLS}} = \widehat{\boldsymbol{W}}_{\boldsymbol{PLS}}\left(\widehat{\boldsymbol{P}}^{\boldsymbol{t}}_{\boldsymbol{PLS}}\widehat{\boldsymbol{W}}_{\boldsymbol{PLS}}\right)^{-1}\widehat{\boldsymbol{q}}_{\boldsymbol{PLS}} \quad \text{(eq. 2.15)}$$

To apply a PLS model for a new dataset, the new response can be estimated:

$$y_{new} = \bar{y} + x_{new}\,\hat{b}_{PLS} \quad \text{(eq. 2.14)}$$

where $\bar{y}$ is the intercept from the PLS calibration model; x_{new} represents data obtained from new samples.

❖ *Partial Least Squares Discriminant Analysis*

Partial Least Squares Discriminant Analysis (PLSDA) is a supervised classifier driven by the principle of Partial Least Squares Regression. PLSDA maximises the covariance between **X** and dummy variables **Y**. Dummy variables **Y** are categorical classes, which are often converted into binaries. Similar to PLS regression, PLSDA extracts sequential latent variables (LVs) which capture maximal variance.

The choice of number of LVs is important for PLS prediction/classification. The number of LVs is chosen based on the lowest root mean square error (RMSE). However, the trade-off point between RMSE calibration and cross-validation must be determined (Naes et al., 2004; Saeys et al., 2019). The regression coefficient vector $\boldsymbol{b_{PLS\text{-}DA}}$ is also estimated by minimising least squares of residual errors from a PLSDA model.

$$\widehat{\boldsymbol{b}}_{\boldsymbol{PLSDA}} = \widehat{\boldsymbol{W}}_{\boldsymbol{PLSDA}}\left(\widehat{\boldsymbol{P}}^{\boldsymbol{t}}_{\boldsymbol{PLSDA}}\widehat{\boldsymbol{W}}_{\boldsymbol{PLSDA}}\right)^{-1}\widehat{\boldsymbol{q}}_{\boldsymbol{PLSDA}} \quad \text{(eq. 2.16)}$$

❖ *Support Vector Machine*

Suport Vector Machine (SVM) is a binary classification technique often applied to separate two classes by support vectors. For multi classes, the pairwise "one versus one" classification approach is driven (Deepa & Thilagavathi, 2015; Saeys, 2018; Su et al., 2017). The SVM discriminant function is driven by lines (linear) or hyperplanes (non-linear).

➢ *Linear SVM*

A linear SVM model is expressed by the equation:

$$f(x_i) = w^t x_i + b \quad \text{(eq. 2.17)}$$

where w is the weight vector of each class i = 1,…, n; the superscript 't' is the transform operator; x_i is sample of that class and b is the bias (Sontag, 2020).

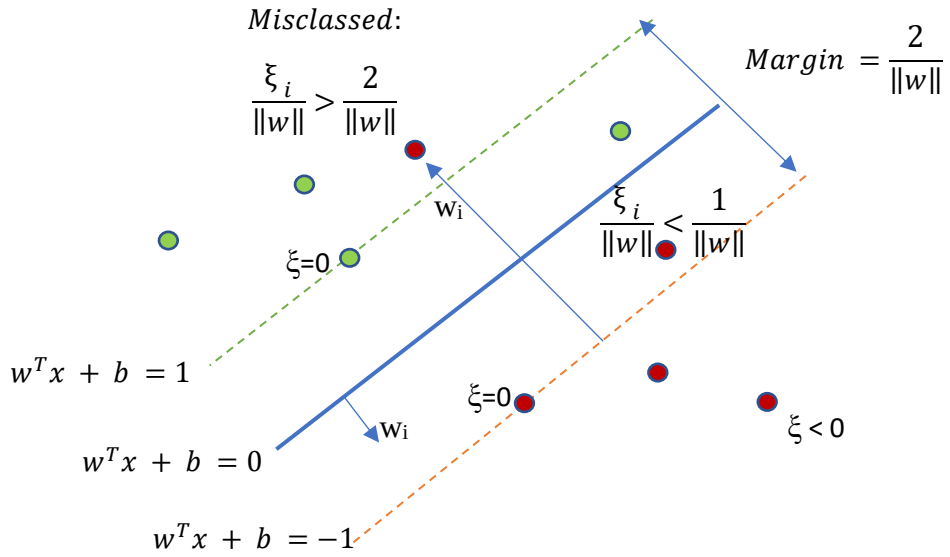

Figure 2.12. *The classification scheme of a linear SVM classifier (after Sontag, 2020)*

The linear SVM classifier classifies classes by both positive support vectors: $w^T x_i + b$ = +1 and negative support vectors: $w^T x_i + b = -1$. The margin of the discriminant line is determined by the slack variable ξ_i , which is the distance between positive or negative support vectors ($w^T x_i + b = \pm 1$) and the mean vector ($w^T x_i + b = 0$). The slack variable ξ_i measures the error of each point (x_i, y_i) between the margin and the correct side of discriminant lines. Based on the equation 2.17, a linear SVM classification model is optimised by minimising classification error.

$$\min_{w,\xi i} \|w\|^2 + C \sum_i^N \xi i \quad \text{with } y_i(w^T x_i + b) \geq 1 - \xi_i$$

where *C* is a regularization parameter. *C* is expected to be as small as possible, so the discriminant line has a large margin to display good classification. If *C* is large or infinite, the discriminant line will have a small margin or hard margin, which is difficult for class discrimination. The optimal linear SVM model is defined by the maximum of the margin between 2 support vectors of $\frac{2}{\|w\|}$ and the mininum of classification errors.

According to the SVM algorithm, all classes are classified when the slack variable is equal to or smaller than 0 ($\xi_i \leq 0$). If a class is in the range (0,1) or $0 < \xi_i < 1$, that class will be located between the margin and the correct side of the discriminant line. By contrast, if the slack variable is larger than 1 ($\xi_i > 1$), that sample will be missclassed (Su et al., 2017).

- ***Non-linear SVM***

Non-linear SVM with a radial basic function (*rbf*) kernel is often employed for non-linear data. SVM (*rbf*) works with the Gaussian function $G(x_i, x_j) = e^{(-\|x_i - x_j\|^2)}$ that transforms the input data into the high dimensional kernel space for modelling. The *rbf* kernel was defined by Cost (*C*) and gamma (γ) hyperparameters, which determine the number of support vectors needed. The support vectors create the kernel margin or hyperplane which separates the target class from another by minimising the misclassification error. A larger kernel margin or more support vectors mean a target class could be discriminated more easily, but it also drives over-estimation and low classification accuracy. Optimising *C* & γ hyperparameters is suggested to avoid overfitting.

❖ *Artificial Neural Network*

Artificial Neural Network (ANN) is a machine learning method, which was inspired by the principle of human neural systems. ANN is constructed by several neural layers in which the input data will be the first layer, and the output or the result displays at the final layer. Between the input and output layers are hidden layers by which the data are transformed and activiated by the ANN algorthrim. The previous ANN layer links to the next layer via nodes having associated weights and bias values. The weights and biases in every layer are calculated to determine values for nodes of the next layer. In ANN, hidden layers can be one or more (Kwon, 2011; Patrício & Rieder, 2018).

- ***FeedForward Back-Propagation Neural Network***

A FeedForward Back-Propagation Neural Network (FF-BPNN) is a common ANN method in which neural layers are input and ouput in one direction (Figure 2.13). The weights in each layer are optimised by the gradient-descent algorithm to reduce the predictive error.

The ANN function activates the learning process across layers to produce the output. After that, the back-propagation function returns the output to the neural network to optimise the prediction by minimising the predictive error. This cycle can iterate more than 1000 times of back-proparation in a FF-BPNN model (Wikieigenvector, 2019).

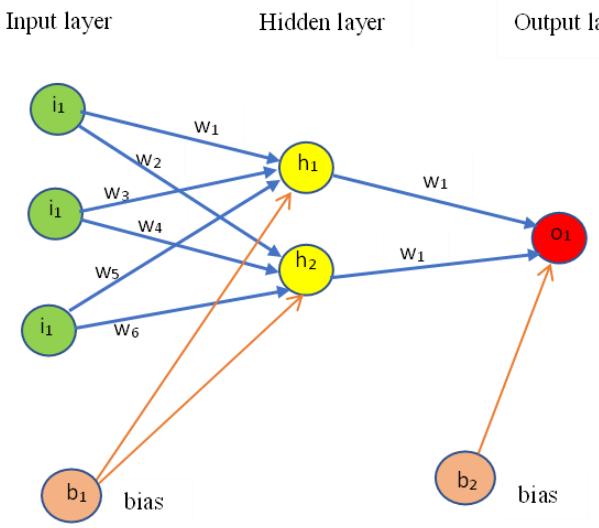

Figure 2.13. *The illustration of feed forward back-propagation neural network with i: the input, w: the associated weight, h: hidden, o: output and b: bias (Kwon, 2011)*

- ***Convolutional neural network***

Convolutional neural network (CNN) is an advanced artificial neural network known as an AI deep learning method, which is popular for object recognition and classification. Deep CNN recently became popular in agricultural and food safety fields (Al-Sarayreh et al., 2020; Pullanagari et al., 2021; Soni et al., 2021). Similar to ANN, CNN contains the input, convolutional layers (hidden layers) and the output. CNN algorithm activates in convolutional blocks which are defined by convolutional layers. Each convolutional layer has the kernel size and the feature nodes of the previous layer, which allows features to be recognized and detected.

Deep CNN is quite flexible for analysing three dimensional images (hyperspectral images) or two dimensional images (RBG images, 2D-hyperspectral images) or one dimensional data (spectral data) (Soni et al., 2021). CNN's principle is the same for 3D, 2D and 1D data, but the complexity of CNN structure in 3D & 2D is more than in 1D. In this study, deep 1D-CNN is applied to analyse spectral data extracted from hyperspectral images.

❖ *PARAFAC method*

Parallel Factor Analysis (PARAFAC) is a multiway method, often applied to three or more-dimensional data, such as three-way excitation emission matrix (EEM) fluorescence data. The traditional fluorescence two-way data consists of **J** measurements from **I** samples collected into a matrix of $\mathbf{X_{IxJ}}$. By contrast, three-way fluorescence data consists of **I** samples, **J** emission wavelengths and **K** excitation bands (Bro, 1997; Bro & Gallagher, 2022).

In general, the three-way data are constructed in a **X** data cube of I x J x K before modelling with the PARAFAC method. Principally, PARAFAC is driven by estimating the uniqueness of chemical components contained in the original data. The PARAFAC algorithm searches for a likely match of a certain fluorescence signal based on a binary of excitation-emission channels using alternating least squares. This algorithm works in a decreasing order match allowing identification of the unknown chemical component. This procedure is repeated until all components are identified. A trilinear PARAFAC model can be performed as follows.

$$\mathbf{X_K} = \mathbf{A D_K B^T} + \mathbf{E_K} \quad \text{for k} = 1,\ldots,\text{K (eq. 2.18)}$$

where $\mathbf{X_K}$ is the emission spectrum for the k^{th} excitation. For a model with P components, **A** is the score matrix of I x P in the sample mode. $\mathbf{D_K}$ is the diagonal matrix of P x P which contains scores of the excitation loading matrix K x P for the k^{th} row. **B** is the loading matrix of J x P in the emission mode, "*T*" is the transpose operator and $\mathbf{E_K}$ is the model error for the k^{th} sample (Bro & Gallagher, 2022).

According to Engelen & Hubert, (2011), PARAFAC works well with an optimal sample subset that adequately represents the whole population but cleaned of outliers to help achieve convergence. This subset often lies over a half of the total observations (samples). Although a larger sample size can increase the power of statistics, it could compromise the robustness of a PARAFAC model since the PARAFAC algorithm is most suited for a small and clean dataset (Engelen & Hubert, 2011; Frosch et al., 2009).

❖ *Multi-way PLS regression*

Multi-way PLS or n-PLS is an extension of two-way PLS for the analysis of high order array datasets (e.g., fluorescence excitation-emission matrices). The PLS-1 algorithm approach (modelling for each analyte separately) is used in a three-way dataset which contains a group of samples (Faber & Bro, 2002). The independent three-way fluorescence EEM data contained excitation-emission spectral variables and fluorescence intensity of samples. Similar to standard two-way PLS, tri-PLS also searches for a few latent variables (LVs) maximising the covariance between fluorescence data (**X**) and the response (**y**). In the standard PLS model,

two-way **X** data is decomposed into a matrix of scores (**T**) and a matrix of weights or loading scores (**W**) where **T** and **W** are orthogonal. By contrast, tri-PLS decomposes the **X** cube data for a matrix of scores (**T**) and matrices of weights ($\mathbf{W_1}$, $\mathbf{W_2}$) which are not orthogonal (Bro, 1996; Dinç et al., 2017; Faber, 2015). According to Bro et al. (1996), a tri-PLS model for a matrix **X** (I x J x K) is written as follows.

$$x_{ijk} = \mathrm{t}_i w_j^J w_k^K + e_{ij} \quad \text{(eq. 2.19)}$$

Where x_{ij} and e_{ij} are elements of **X** data and $\mathbf{E_x}$ error matrices, $w_j^J \ and \ w_k^K$ are elements of loading matrices $\mathbf{W_1}$ and $\mathbf{W_2}$, and t_j is an element of the score matrix. I is the number of samples (first dimension); J is the number of measurements at emission bands (second dimension) and K is the number of measurements at excitation bands (third dimension).

According Bro (1996), tri-PLS analyses fold three-way data directly without unfolding in two-way PLS that copes effectively with noisy data to increase the interpretability for better predictions (Bro, 1996).

2.12.3. Calibration, validation, and test sets

The predictive model represents a given sample population. Thus, model parameters are estimated based on a sample set of that population (so-called calibration dataset). The procedure of estimating the parameters is called training. To assess the fitness of model parameters, an independent test set which also comes from the same population but has not been used in the training process is used to generate a set of predicted values. The test dataset is also assessed by a reference method so the predicted values from the model can be compared.

❖ ***Sample population***

The quality and identity of honey is affected by geographic districts, seasons, *L. scoparium* varieties, and other floral sources. Principally, a good honey dataset would consist of diverse honey samples from different districts and seasons. A large sample dataset which is collected from different districts and seasons intuitively gives more freedom of predictability. It is not always possible to collect a broad dataset due to high expense but having a dataset to enable an approximation of normal distribution for statistical prediction brings benefit. This study has worked with a large dataset of 1656 honey samples which were harvested in 2019-early 2020 spanning eight different districts across the North Island of New Zealand. Samples were randomised before experiments in order to avoid confounding between scanning effects and honey districts.

❖ ***Cross-validation***

Cross-validation technique is introduced during training a model to avoid overfitting. Several different cross-validation techniques are introduced such as venetian blind, leave-one-out, contiguous block, random selection, and costume (groupwise). In general, the cross-validation algorithm splits the calibration dataset into training and validation sets. The sub-model is trained on (n-1) subsets and leave-one-out at each training iteration. Then, that trained model was applied on a leave-out subset to obtain the prediction accuracy for that iteration. This process is repeated for all iterative runs. Eventually, the cross-validation accuracy is calculated by averaging all predictive values of all sub-models.

Cross-validation also helps the balance between complexity and simplicity of a model. The complexity of a model is determined by tuning parameters chosen to minimize the estimated error. For example, in a PLS model, the selection of the number of latent variables can result in a complex model (high number of latent variables) or a simple model (low number of latent variables). Where the error function (e.g., RMSECV) against the number of latent variables is monotone, then if adding more latent variables to 'n' no longer significantly decreases the error, these 'n' latent variables are chosen as optimal for the corresponding PLS model. PLS software routines may suggest an ideal number of latent variables by searching for a "knee" in the error function (e.g., RMSECV). Meanwhile, the box constraints, and regularization C, are important hyperparameters in a SVM model (Chapter 6, section 6.3.2). Convolutional layers, number of nodes, kernel size and other hyperparameters determine the complexity of a CNN model. These hyperparameters are further discussed in section 9.3.4 of the Chapter 9 (Table 9.1 & 9.3).

To select a cross-validation technique for modelling, it is necessary to know how data are collected (number of samples in data, the absence and presence of replicates in the data). The trap of replicates needs to be avoided. If a sample is measured in replicates with the same instrument, these replicates often have the same errors. So, replicates should be put together in the calibration model or test set. If different replicates are collected in different days which causes different errors, these replicates should be present in both calibration and validation sets (Wikieigenvector, 2022).

❖ ***Model validation***

Evaluation of a model is essential to assess the model's robustness. This is done by applying the model to the independent test set which has not been employed during training the model. In this validation step, all modelling information including preprocessing and cross-

validation algorithms remain on the test set. The prediction results of the test set are expected to exhibit the same trends as the original model. Otherwise, that model is not robust.

2.12.4. Spectral pre-processing techniques

Spectral data often bear multiplicative or/and additive effects due to scattering issues. When light excites samples, the light can change direction when passing through different environments. During scanning samples, the turnabout of light generates the multiplicative effect of light scatterings due to unequal optical pathlengths among samples. In addition, if samples are turbid solutions, the presence of small particles causes Raman scattering so-called additive effects (section 2.10.4). Therefore, it is often suggested to correct or pre-process spectral data before further analysis. Several common techniques are used to remove these scattering effects (Naes et al., 2004).

- ***Baseline correction***

Baseline correction uses a first or second order polynomial to remove scattering effects by selecting two points from the background spectra (baseline) or noise but avoiding the spectral signal. A baseline is fitted for each spectrum to subtract this line from that spectrum. By this way, scattering effects could be removed. The weighted least squares (WLS) algorithm is often used in baseline correction. WLS baseline can remove the spectral background automatically and avoid negative peaks. However, the WLS baseline can also remove some valuable information (Saeys et al., 2019).

- ***Detrend***

The detrend technique aims to remove a constant, linear or curve offset in the spectral data. Detrend will fit a polynomial of a given order to all points including the baseline and signals, and then subtract the spectrum to that polynomial line. Detrend only works well for the spectral datasets containing background interference due to the presence of a large signal variation (Barnes, 1989). If the variation of signal interest (net analyte signal) is significant, detrend can also remove useful variations. It is noticeable that detrend technique can even create non-linear responses from the linear ones (Saeys, 2018).

- ***Derivatives***

Derivatives is a pre-processing technique which allows removal of the baseline effects (or low frequency noise) in the raw spectra and resolution of overlapping spectra. First and second derivatives are often employed in analytical chemistry (Clark et al., 1990). The first

derivative captures the slope of the raw spectrum while the second derivative captures the slope of the first derivative spectra at each wavelength. The peak of the first derivative spectrum is the maximum slope, and the zeros corresponds to the maxima or minima of the original spectrum. So, the first derivative removes the additional baseline in the spectral data. By contrast, the second derivative measures the curvature of the original spectrum. By this way, the second derivative eliminates both the additional and multiplicative baseline due to scattering effects. In addition, if the spectral signals overlap, derivatives with narrow bandwidths relatively enhance the amplitude of overlapping spectra and this increases with higher derivative order (Clark et al., 1990). Derivative spectra often employ the Savitzky-Golay method as a differentiation filter that uses polynomial functions fitted over certain bandwidth intervals to smooth noisy data (Naes et al., 2004; Saeys et al., 2019).

- ***Smoothing***

Smoothing is a filter pre-processing technique used to remove high-frequency noise in a signal. A Savitzky-Golay algorithm is typically applied to smooth the spectra. Two steps are applied in Smooth technique. First a subset is selected of adjacent data points with a low-degree polynomial (e.g., order 0) in the filter window. Second, the filter window is fitted into the spectra. A filter is generally chosen to accommodate an odd number of data points, centered on the data points of current interest. Since selected data points are equally spaced, the method of linear squares generates convolution coefficients to smooth spectra, in particular coherent spectra. The smooth filter significantly removes noise without losing necessary signals (Gallagher, 2021; Naes et al., 2004; Saeys et al., 2019).

- ***Multiplicative Scatter Correction***

Multiplicative Scatter Correction (MSC) is a pre-processing technique applied to remove multiplicative scattering effects embedded in raw spectra. MSC algorithm fits a regression line for the individual i-th spectrum at the k wavelength variables described as follows:

$$x_{ik} = a_i + b_i \bar{x}_k + e_{ik} \quad \text{(eq. 2.20)}$$

where i is the sample of i-th, k is the number of wavelength variables; x_{ik} is the individual spectrum of the i-th sample for k wavelengths, a_i is the intercept and b_i is the slope of regression line, and e_{ik} is the MSC model error. Therefore, every i-th spectrum is corrected:

$$x_{ik}^{*} = \frac{x_{ik} - \hat{a}_i}{\hat{b}_i} \quad \text{(eq. 2.21)}$$

From equation 2.21, MSC corrects each spectrum over spectral data, but also changes intercept and slope from the regression line. Potentially, subtle absorptions in spectral data might be lost (Saeys et al., 2019).

- ***Standard Normal Variates***

Standard Normal Variates (SNV) was first described by Barnes et al. (1989) to correct spectral data having scattering effects. SNV removes the additive and multiplicative scatters from the raw spectra. Differing from MSC, SNV calculates the subtraction of each wavelength variable x_{ik} from the mean-centered value m_i and then divides the difference by the standard deviation s_i of that spectrum:

$$x_{ik}^{*} = \frac{x_{ik} - m_i}{s_i} \quad \text{(eq. 2.22)}$$

This equation is applied for each sample over all variables. When the SNV pre-processes with the mean zero, the standard deviation value of s_i will become 1. Compared to MSC, SNV can overcome the loss of spectral information from MSC algorithm since SNV algorithm corrects the individual spectrum of a sample just based on the spectral data of that sample (Saeys et al., 2019).

- ***Orthogonal Signal Correction***

Orthogonal Signal Correction (OSC) preprocessing technique is employed for spectral data that contain much variation due to different time measurements or sample preparation. OSC removes the variation from the spectral **X**-data that is orthogonal to the response of **y**. By input of the spectral data into the space of few latent variables, OSC defines a first latent variable which captures the most variation of **X** uncorrelated with **y**. Then, the second latent variable is generated after subtracting the contribution of the first latent variable. The same procedure is continued for sequential latent variables. OSC works well for data having many spectral variables exceeding the number of samples. For two different datasets measured with different instruments, OCS can also help to remove instrumental variation that is not related to the predicted variables. Compared to other techniques, OSC can compensate for the risk of removing relevant information which most pre-processing techniques bear when applied scatter correction (Saeys, 2018).

2.12.5. Variable selection techniques

The spectral data contain many spectral variables. Variables nearby are often correlated. This is known as multicollinearity. When the number of variables in the spectral data are larger

than the number of samples, multicollinearity can impair the robustness of a predictive model (Wilcox, 2019). Since several variables in a dataset given may be unnecessary, they can complicate the prediction results due to the attachment of irrelevant compounds. A robust model often contains few variables, only those related to the target chemicals (Saeys, 2018; Saeys et al., 2019). This section describes three variable selection techniques used in this study.

- ***Variable Important in Projection***

Variable Important in Projection (VIP) is often used along with the PLS model to estimate the importance of each projected variable. VIP calculates the weighted sum of squares of PLS scores that account for the explained y variance at each latent variable (Farrés et al., 2015). The bands with larger VIP score or close to 1 are considered as being important, while bands with a VIP score less than 1 are considered as being less important. Low score variables will be excluded from the final model. VIP technique is often applied after modelling to improve the predictive model (Saeys, 2018; Saeys et al., 2019).

- ***Genetic Algorithm***

Genetic Algorithm (GA) technique is used through a cross-validation regression method (i.e., PLS) to select a subset of variables which will give superior prediction. First, GA selects a random subset of variables as an individual window and generates the gene for that window. At each gene, the prediction error (i.e., RMSECV) is calculated. Then, the GA algorithm uses the fitness function to describe the fitness of the window in the population. Finally, GA chooses windows with the greatest fit or which give the smallest prediction error (Saeys, 2018; Saeys et al., 2019; WikiEigenvector, 2020).

Figure 2.14 illustrates the output of a diagnostic plot during GA running (a) and the selection of variables (b). The plot of fitness and number of windows (Figure 2.14 a, top left) shows the fitness and number of variable windows of the whole population. The evolution of average and best fitness plot (Figure 2.14 a, top right) indicates the trend of the average fitness (blue line) and the best fitness (red line) at each generation number. The evolution of number of windows plot (Figure 2.14 a, bottom left) shows the trend in number of variable windows required. Models with window plot (Figure 2.14 a, bottom right) presents the frequency of each variable window is used. The higher the frequency of variables is, the more importance those variables have in the final model selection (WikiEigenvector, 2020).

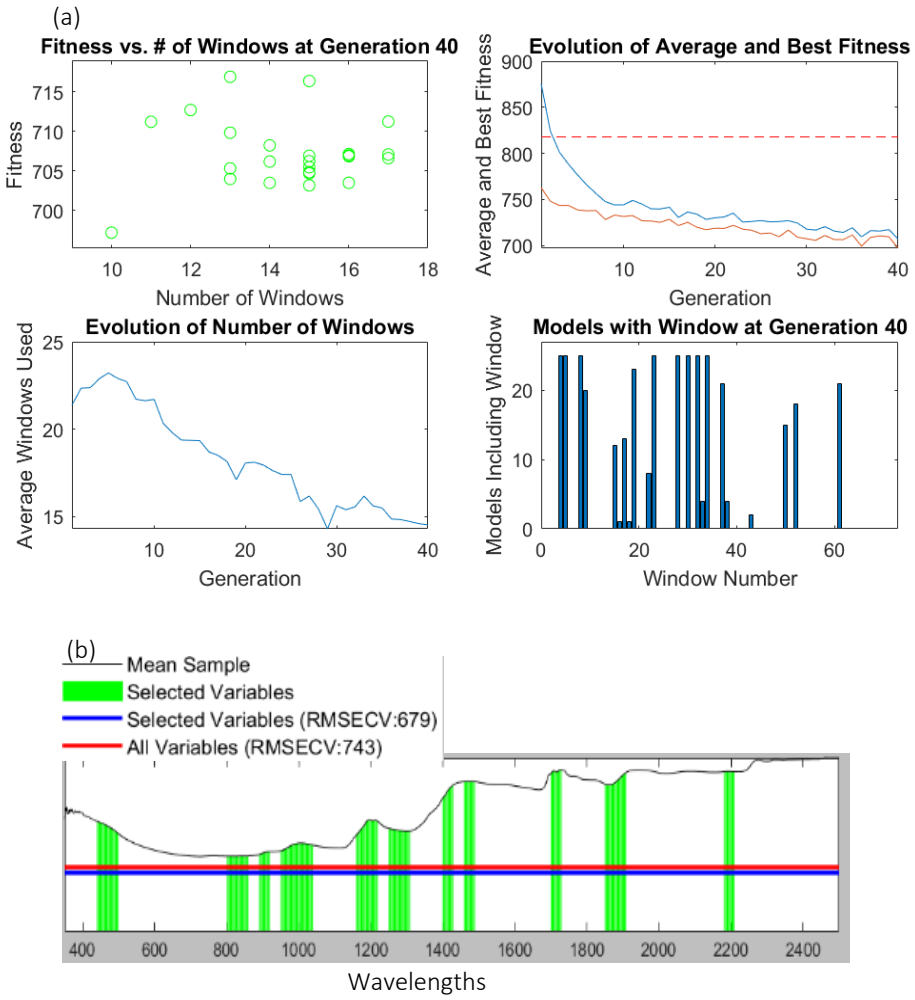

Figure 2.14. *The output of diagnostic plots during GA running (a) in a PLS model over NIR spectral range 370 – 2500 nm and selection of variables (b). GA stopped at generation 40 giving the best fitness (Honey data, 2020)*

- ***Interval Partial Least Squares***

Analogous to GA, Interval Partial Least Squares (iPLS) also collects a subset of variables, but the variable selection works for a variable interval rather than the variable window as in the GA algorithm. For a given variable interval, iPLS sequentially searches for the best combination of variable intervals giving good prediction (Figure 2.15). The forward procedure is implemented by adding the best interval while the backward is done by excluding unnecessary bands (Saeys, 2018; Saeys et al., 2019; Xiaobo et al., 2010).

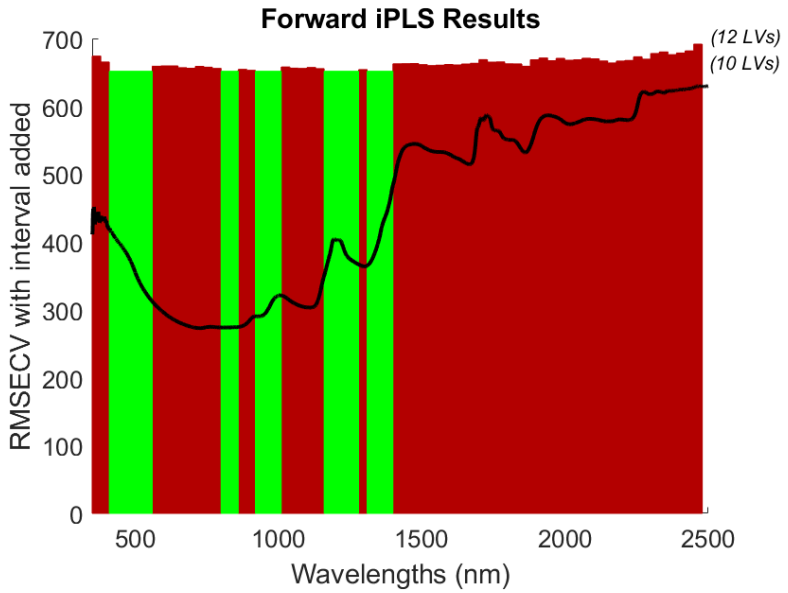

Figure 2.15. *Variable selection (green bars) of a forward iPLS which was run with 30 intervals over NIR spectral range 370 – 2500 nm. The iPLS plot showed a relationship between cross-validation prediction errors (RMSECV) and selected variables. The green interval illustrated the selected variables (Honey data, 2020)*

2.12.6. Statistical measures

Most linear regression methods are quantified from the regression coefficient **β** when the sum of square of residuals (**e**) is minimised to predict the **y** value from the **X** variable data (Saeys et al., 2019).

$$\mathbf{y} = \mathbf{X\beta} + \mathbf{e} \text{ (eq. 2.23)}$$

When the equation is established, linear regression models are evaluated by statistical parameters to assess how well the models are generalised. Important statistical parameters are used for diagnostics of the predictive model performance as follows.

- ***Goodness-of-fit metrics***
  - *Root mean square error*

Root mean square error (RMSE) is the absolute error which is computed from a linear model. Root Mean Square Error of Calibration (RMSEC), Root Mean Square Error of Cross-Validation (RMSECV) and Root Mean Square Error of Prediction (RMSEP) are calculated for evaluating the model for calibration, cross-validation and on test sets, respectively. A good model performs a trade-off where RMSEP achieves as a low value as that of RMSECV.

$$RMSE = \sqrt{\frac{1}{n}\sum_{i=1}^{n}(\hat{y} - y_i)^2} = \sqrt{\frac{1}{n}\sum_{i=1}^{n}(x_i b - y_i)^2} \quad \text{(eq. 2.24)}$$

In which *n* is the number of samples; *y* & y_i are the estimated and measured values for the sample *i* with spectral vector x_i.

In comparison with other models for different sample size, the normalised Root Mean Square Error (nRMSE) is used.

$$nRMSE = \frac{RMSE}{\bar{y}}$$ where $\bar{y}$ is the mean of the measured values.

In addition, other statistical parameters are also checked together with RMSE since RMSE does not indicate clear information about the systematic (average) error of the predicted values or random error.

- *Bias*

In contrast to RMSE, bias value represents the average difference between the predicted values and the measured values.

$$Bias = \frac{1}{n}\sum_{i=1}^{n}(\hat{y} - y_i) = \frac{1}{n}\sum_{i=1}^{n}(x_i b - y_i) \quad \text{(eq. 2.25)}$$

- *Standard error of prediction*

Standard error of prediction (SEP) is also calculated to measure the estimation errors or the accuracy of predictions.

$$SEP = \sqrt{\frac{1}{n-1}\sum_{i=1}^{n}(\hat{y} - y_i - Bias)^2} = \sqrt{\frac{n}{n-1}(RMSE^2 - Bias^2)} \quad \text{(eq. 2.26)}$$

where *n-1* is the number of degrees of freedom with *n* being the number of samples

- *Ratio of prediction to deviation*

Ratio of prediction to deviation (RPD) is the ratio of standard error of performance (RMSECV) to standard deviation (SD). It calculates how accurate the model is estimated by comparing the predicted *y* to the average measured value $\bar{y}$. Table 2.4 shows the interpretation of RPD value for a predictive model performance.

$$RPD = \frac{SD}{RMSEP} = \frac{\sqrt{\frac{1}{n-1}\sum_{i=1}^{n}(y_i - \bar{y})^2}}{\sqrt{\frac{1}{n-1}\sum_{i=1}^{n}(y_i - \hat{y}_i)^2}} = \frac{\sqrt{\frac{1}{n-1}SSTO}}{\frac{1}{n}SSE} \quad \text{(eq. 2.27)}$$

where SSTO is total sum of squares and SSE is the error sum of squares.

Table 2.4. Explanation of RPD value ranges indicating utility of a calibration model (Saeys et al., 2005)

RPD value	*Explanation*
RPD ≤1.5	The calibration model is not usable
1.5 < RPD ≤ 2	The calibration model can distinguish between high and low values
2 < RPD ≤ 2.5	The calibration model can give approximate quantitative predictions
2.5 < RPD ≤ 3	Predictions by the calibration model are classified as good
RPD >3	Predictions by the calibration model are classified as excellent

- *Coefficient of determination*

Coefficient of determination (R^2) is calculated to evaluate the fit between predicted and measured values in a linear regression model. The R^2 value represents the variance in the predicted y response that is explained by X-data from the model. The RPD is related to R^2 in that it also expresses which fraction of the variation in y response captured in the model.

$$R^2 = 1 - \frac{SSE}{SSTO} = 1 - \frac{n}{(n-1)\,RPD^2} \quad \text{(eq. 2.28)}$$

From equation 2.28, the R^2 value ranges from 0 to 1 (±0.05). The predictive model is linear when the SSE value is 0 or R^2 equals to 1. In practice, SSE never goes to 0 since the model always contains errors. SSE expresses the variance that is not explained by the model.

To summarise statistical measures, R^2 is often used to determine how well the model fits the data. A higher R^2 value indicates better fit to the data. Depending on the application, R^2 value in some certain range can be accepted. Two or more statistical parameters are often combined to examine how well the model performs. For example, R^2 and RMSECV, R^2 and Bias, R^2 and SSE, R^2 and RPD or three combinations of these statistical parameters.

➢ ***Statistical comparison between models***

To compare models with different selected variables, some common statistical parameters are often used.

- *Coefficient of determination $R^2_{adjusted}$*

$R^2_{adjusted}$ number is calculated to compensate for models with different variables.

$$R^2_{adjusted} = \frac{RSS}{N-p-1} \quad \text{(eq. 2.29)}$$

Where *N* is the number of samples; *p* is the number of variables and RSS is residual sum of squares. Both RSS and (N-p-1) will decrease when the number of variables *p* increases.

- *RMSECV/RMSEP*

Different models with different numbers of variables *p* can be compared based on RMSEP/RMSECV. Ideally, RMSEP/RMSECV will first decrease with increasing *p* and stabilize around an optimal value. When RMSEP/RMSECV value increases, the model starts

over-fitting. A model should be chosen when p variables minimise RMSEP/RMSECV. Where two models give a similar value of RMSEP/RMSECV that with the smaller p is preferable. In addition, models processed with different pre-processing can also be evaluated by RMSEP/RMSECV.

- *Mallow's C_p*

Mallow's C_p is useful in selecting between competing models using different subsets of the available variables. A lower C_p value is generally preferable.

$$C_p = \frac{RSS}{s^2} + 2p - N \quad \text{(eq. 2.30)}$$

where RSS is residual sum of squares; s^2 is the estimated value of the residual variance of the model; p is the number of variables; and N is the number of samples.

- *Evaluating overfitting*

The complexity of a model is determined by the number of degrees of freedom. For simple multiple regression, the degrees of freedom df = k which is the number of predictors (i.e., slope, intercept). For multiple regression, the df=N-k-1 where k is the number of latent variables, regression coefficients or the number of factors); N is the number of total observations (Workman & Mark, 2016). Therefore, the k factor in multivariate regression PCA/PLS model equals the number of latent variables chosen. when many variables or latent variables are used, the degree of freedom of a model is high which risks model over-fit. A trade-off should be chosen between underfitting and overfitting. Generally, the RMSECV value decreases when increasing the number of PCs/LVs. The rule of thumb for the trade-off selection is the first local minimum RMSECV versus principal components (PCs) or latent variables (LVs). The lowest number of PCs or LVs is selected in which the prediction error is not significantly worse than the error of RMSECV. It is better not to increase the number of PCs/LVs if the reduction in error is less than 2 %. Using factor signal to noise ratio (SNR) to select factors (PCs/LVs) is more accurate for avoiding overfitting (Saeys, 2018).

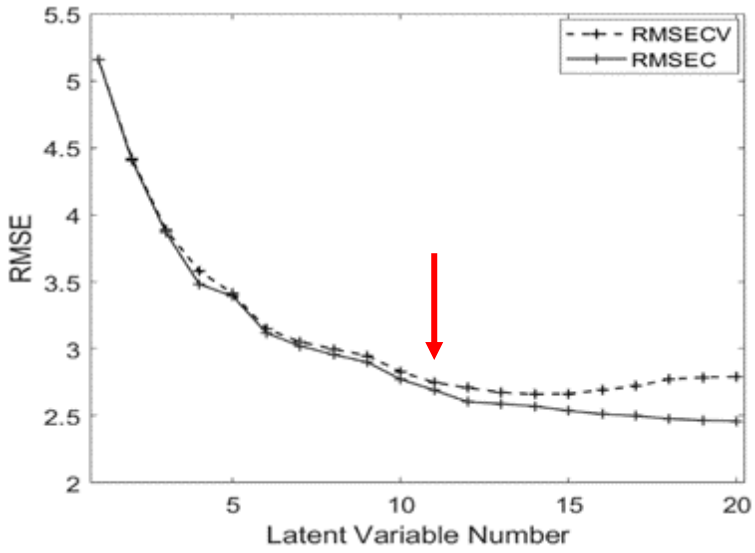

Figure 2.16. *Trade-off point for selection of a good PLS model in which both RMSEC and RMSECV are low with a small number of latent variables*

This chapter unfolded principles of non-imaging and imaging sensor systems combined with chemometrics and machine learning methods. In the next chapter, the state of the art will be described for non-invasive systems and analytical methods reported in recent studies for analysing honeys, in particular mānuka honeys.

2.12.7. Detection of outliers

Detection of outliers is an essential step during data analysis or modelling. The presence of outliers can obscure the true relationship and patterns in the data observed (Saeys, 2018). During interpretation of data, outliers could skew the results and lead to inaccurate conclusion and poor prediction (Hadi et al., 2009). Therefore, removing outliers is often suggested to ensure informative and accurate results. However, some outliers could indicate important information in the data. It is necessary to observe data and check outliers carefully.

There are several techniques used such as residual analysis, Hotelling's T^2 statistic, Mahalanobis distance, Cook's distance, and leverage analysis (Hadi et al., 2009; Saeys, 2018). This study mainly uses Hotelling's T^2 combined with residual analysis to detect outliers. Hotelling's T^2 shows how far each datapoint is from the mean of the data while residual analysis indicates how difference between the true value of each datapoint and its predicted value (Wikieigenvector, 2023). The plot between Hotelling's T^2 and Q residuals shows the potential of outliers, which have high scores of Hotelling's T^2 and Q residuals and lie outside 95 % confidence limit (dash lines) (Figure 2.17a) compared to the remaining population. In addition,

Leverage analysis is also observed to confirm outliers detected. Leverage calculates the distance of each datapoint in the dataset to the mean of the whole population (Saeys, 2018). Datapoints have high leverage which indicates outliers. The plot between Leverage score and standard deviation of residuals is observed to detect outliers. For example, Figure 2.17 showed two outliers detected in the 1650-honey dataset observed by the Hotelling T^2 vs Q-residuals plot (Figure 2.17a). These two outliers showed high leverage scores compared to remaining datapoints (Figure 2.17b).

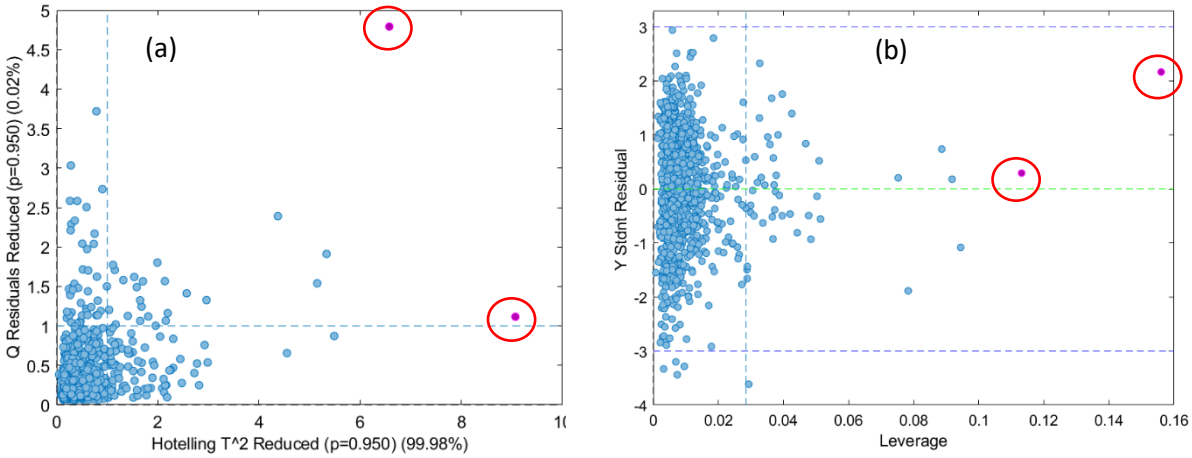

Figure 2.17. *Detection of outliers (pink datapoints in red circles) in the HSI 1650-honey dataset for PLS prediction of DHA.*

2.12.8. Software

This study mainly used PLS Toolbox 9.0 (Eigenvector Research, Inc., Manson, WA 98831, USA) in a MATLAB environment for almost chemometric methods.

In addition, R x 64 4.1.2 (library: ggplot2, matplot, dplyr, tidyr, ggraph, caret, dplyr, tidyverse, plotly) and Python 3.9 (packages: skimage, scipy, matplotlib, and spectral python) were also used to visualize data and to segment hyperspectral images for extraction of spectral data.

Chapter 3
State of the art and research gap

3.1. Introduction

Quality assessment of mānuka honey is necessary for regulatory compliance and process control purposes to ensure its value. In the past ten years, several studies have been conducted to authenticate mānuka honey, to detect honey fraud and to determine botanical origin as *L. scoparium* (Goss, 2009; Noviyanto & Abdulla, 2020; Stephens et al., 2010; Yang et al., 2020). These studies have employed both conventional and non-invasive methods. However, according to our knowledge, assessment of mānuka honey quality and purity based on the changes of chemical markers using non-destructive methods has not been reported. In addition, no report anticipates the grading of mānuka honey non-invasively before the extraction process, while honey is still in comb form in the frame.

This chapter describes the state of the art of most current analytical methods used to characterise mānuka honey. Google Scholar and Scopus were used to discover studies relevant to assessment of honey quality, determination of its botanical origin and verification of authenticity as mānuka honey. This summary covers basic methodology, benefits, and limitations of each analytical method. Based on the summary of state of the art and industry needs, the research gap was then identified to guide the current study.

3.2. Conventional analytical methods

3.2.1. Melissopalynology

Melissopalynology is the scientific field of studying pollen and spores in bee-honey to investigate botanical origin (Dinkov, 2015). Melissopalynology was codified by the International Commission for Bee Botany in 1978 (Louveaux et al., 1978) and validated in 2004 (von der Ohe et al., 2004) to verify botanical origin of honeys (Dinkov, 2015; Guzelmeric et al., 2020). This method first identifies spores morphologically by microscopy and then counts the number of pollens present in honey. The count indicates botanical sources. When bees collect nectar, it is usually randomly contaminated with pollen particles. Pollens of large size are often removed by the bee, but small pollens can remain in the nectar (Van Eaton, 2014). The relative abundance of pollens in honey allows the origin of floral sources to be

estimated. Ministry for Primary Industries (MPI) of New Zealand has used melissopalynology to classify mono-floral and multi-floral honeys for supporting the export of honeys. The honey sample needs to be prepared before counting. Firstly, a 10g-honey sample is dissolved in distilled water having sulfuric acid solution 5 % and then centrifuged (e.g., 4000 rpm, 30 mins) to remove supernatant. Secondly, pollens in the pellet are washed with distilled water twice and then centrifuged (e.g., 3500 rpm, 20 mins) to collect pollens (Bobis et al., 2013). In the next step, the washed pollens were counted and classified under light microscopy (magnitude 400x). Total count of pollen grains in a sample can be up to 1000, enough to generate a pollen spectrum which reflects the locality, floral origin and characteristics (e.g., flavour, odour, and colour) of that honey sample. Relative frequencies of pollens in a total count of pollens and other particles are expressed based on a nomenclature reference table (Moar, 1985). A floral honey having the frequency of a specific pollen at least 45 % of total pollen count is considered as a mono-floral honey (Guzelmeric et al., 2020). For mono-mānuka honeys, the total count of *L. scoparium* pollen grains needs to reach at least 70 % frequency (McDonald et al., 2018). Otherwise, honeys are classified as multi-floral mānuka honeys due to mixing with other floral sources.

Currently, the standard method of quantitative melissopalynology has been updated by using a Burker chamber (Dinkov, 2015). The new method gives more rapid results of counting the number of pollen grains in 10 g honey than the previous method of Louveaux et al. (1978) and von der Ohe et al. (2004). With development of technology, the Classifynder™, a digital microscope was developed at Massey University in 2013 and is now available from Veritaxa Limited. This Classifynder™ scans pollens as objects at up to 2000x magnification. The images collected by microscope are compared with reference images in a database and then a 'Neural Net' algorithm used to classify pollens based on shape, histogram, moment, and texture parameters. The Classifynder™ microscope automates counting pollens which helps reduce time and eye strain compared to traditional counting techniques (Flenley, 2013; Li et al., 2022; Pedersen et al., 2018).

Melissopalynology plays an important role for beekeepers to identify bee-honey origin. It is a simple but time-consuming. The technique requires considerable training and comprehensive knowledge of pollen morphology (Bobis et al., 2013; Mildenhall & Tremain, 2005). The results of melissopalynology are often inconsistent with high standard errors since pollen grains can be lost during the extraction or can be limited in the honey due to vegetation issues. Mānuka pollens have size and shape similar to those of kanuka. Kanuka (Kunzea

ericoides) is a plant in the myrtle family which has flowers and pollens similar to those of mānuka (Stephens et al., 2005; Van Eaton, 2014). Discrimination between mānuka and kanuka pollen grains could pose a challenge if only using morphological characteristics. Overall, melissopalynology requires more time and effort than is appropriate for use at-line in the honey industry (Guzelmeric et al., 2020).

3.2.2. Molecular biological techniques

Molecular biological techniques analyse pollen DNA and protein in honeys. About 0.03 - 0.3 % (w/w) protein is contained in honeys which depends on the origin of nectar sources and bee species (Chin & Sowndhararajan, 2020; Hellwig et al., 2017). Enzymes (amylase, invertase and glucose oxidase, …) from honeybees appear in most honeys but some honeys may not have catalase or acid phosphatase (Chin & Sowndhararajan, 2020). Some honey proteins come directly from nectar sources. For example, arabinogalactan protein is uniquely originated from *L. scoparium* nectar (Gannabathula et al., 2012). Therefore, protein analysis could be useful to help identify the origin of floral sources.

Compared to protein analysis, DNA-based methods are more reliable since DNA from pollen is very specific to botanical origins (Zábrodská & Vorlová, 2014). Enzyme-linked immunosorbent assay (ELISA) and real time polymerase chain reaction (rtPCR) are common techniques for DNA analysis. ELISA aims to detect DNA meanwhile PCR amplifies DNA before detecting. PCR is more sensitive but less qualitative than ELISA. In addition, sodium dodecyl sulphate polyacrylamide gel electrophoresis (SDS–PAGE) is also used for DNA analysis and has recently been used to authenticate honeys (Chin & Sowndhararajan, 2020; McDonald et al., 2018).

Molecular methods often give correct results, but they are laborious and time-consuming due to the laboratory extraction process. The extraction process of DNA from pollen has been optimised by automated methods which shortens the waiting time. However, the technique requires highly-skilled and well-trained lab-workers, and laboratory-based equipment and laboratory clean rooms. It is not suited to industrial use at-line.

New Zealand MPI has recently included the pollen DNA test as one of the official technical criteria to characterise mānuka against non-mānuka honeys. *Leptospermum scoparium* pollens are usually found in mānuka honey because the size of pollen grains is relatively small (7 µm in diameter). Depending on floral regions, pollen size differs from 10-35 µm (Waite, 2016). In general, DNA technique is accurate enough to distinguish pollens

from different nectars but is destructive. In addition, the chance of *Leptospermum scoparium* pollens being present in mānuka honey is not always 100 % (Alvarez-Suarez et al., 2014).

3.2.3. Chromatography-based techniques

Phytochemicals in mānuka honey are currently measured by chromatography-based methods. High Performance Liquid Chromatography (HPLC), Liquid Chromatography (LC)- and Gas Chromatography (GC), often coupled with mass spectroscopy, have been used to quantify phenolic compounds in mānuka honeys (Chan et al., 2013; Elvira et al., 2008; Inoue et al., 2005; Oelschlaegel et al., 2012; Ruiz-Matute et al., 2007; Wang, 2011). HPLC & LC-MS methods were employed to determine MGO concentration (Elvira et al., 2008) and four chemical markers (2-MAP, 3-PLA, 4-HPLA and 2-MBA) of MPI criteria with 100 % accuracy (MPI, 2017b).

The authentification of mānuka honey has been studied using HPLC/LC-MS methods. Rueckriemen & Henle (2018) used HPLC-MS to differentiate between commercial New Zealand (NZ) mānuka honeys, *Leptospermum* honeys from Australia and other non-mānuka honeys, by quantifying concentrations of MGO and phytochemical markers in honey samples. Their results showed a significant amount of MGO and four chemical markers (2'-MAP, 3-PLA, 4-HPLA and 2-MBA) in *Leptospermum* honeys, but MGO was not found in non-*Leptospermum* honeys. In addition, NZ mānuka honeys contained a remarkably high average amount of 2'-MAP (11.8 mg/kg), 3-PLA (795.5 mg/kg) and 4-HPLA (11.8 mg/kg), whereas *Leptospermum* honeys from Australia showed no 2'-MAP compound and small amounts of 3-PLA and 4-HPLA. However, 2-MBA in Australia's *Leptospermum* honeys was more abundant than that in NZ mānuka honey (Rueckriemen & Henle, 2018). Similarly, Daniels et al. (2016) and Bong et al. (2017) applied HPLC-MS to identify Leptosperin (MM1) and Lepteridine^{TM} 3,6,7-trimethyllumazine (MM2). Their results indicated that MM1, MM2 and their fluorescence signals are unique to mānuka honey.

Characterising honey adulteration based on carbohydrate compositions has been also reported using HPLC/GC-MS techniques (Ruiz-Matute et al., 2007; Wang et al., 2015). Merchants in floating markets often mix raw honeys with sugar syrups (high fructose corn syrup or invert sugar syrup) which contain a product of caramelization reactions, so-called difructose anhydrides (DFAs). This modified honey has changes in the carbohydrate profile compared to that of the original honey (Ruiz-Matute et al., 2007). Ruiz-Matute et al. (2007) analysed carbohydrate profile in fake honeys by GC-MS along with yeast treatment. Firstly, major monosaccharides in honey were removed by introducing yeast since yeast consume

monosaccharides to produce carbon dioxide and water. Yeast cannot digest any DFA present. After 24 hours, honey treated with yeast at 30^{o} C was analysed by GC-MS to detect DFAs (Ruiz-Matute et al., 2007). By contrast, Wang et al. (2015) detected honey adulteration by HPLC without prior yeast fermentation. Their study aimed to determine the degree of polymerization (DP) of oligosaccharides (Wang et al., 2015). Oligosaccharides shorter than 5 DP are common in authentic honey. When honey is mixed with starch syrups or other syrups, the modified honey may possess more and larger oligosaccharides, residue of starch hydrolysis syrup. HPLC methods can detect aduterated honeys having starch-derived syrup at > 10 % concentration (w/w) (Wang et al., 2015). MPI has used HPLC to measure concentrations of key chemical markers (2-MAP, 3-PLA, 4-HPLA and 2-MBA) which helps to authenticate mono-floral and multi-floral mānuka honeys (MPI, 2017b).

HPLC-/LC-/GC-MS and the pollen DNA test are now the official standard methods to characterize New Zealand mānuka honey for sale. These two-suite analyses on honey samples are expensive, prohibitively so if testing individual frames. Beekeepers and honey companies can only afford to apply these techniques to evaluate the quality of mānuka honey after the extraction process in which multiple frames are lumped into large drums. Potentially, poor and good honey frames could be mixed when extracted together meaning the resulting mānuka honey could be devalued.

3.2.4. Non-invasive methods

Spectroscopy and hyperspectral imaging technologies have been recently applied to characterise honeys (Yang et al., 2020; Zhang & Abdulla, 2022). They are rapid, accurate and non-destructive. Several spectroscopic methods including Near Infrared (NIR), fluorescence and Raman spectroscopy have been used to discriminate honey adulteration (Bazar et al., 2016; Bong et al., 2018; Dramicanin et al., 2018; Gan et al., 2016; Nickless, 2015; Oroian et al., 2017).

NIR spectroscopy has been widely employed at line in the food industry for over 25 years (Bazar et al., 2016; Pu et al., 2020). NIR methods use the electromagnetic radiation in the short infrared (1300 - 2500 nm), mid-wave (2500 - 15000 nm) and long infrared (15000-25000 nm) ranges to interpret chemical signatures based on absorption signals (Bazar et al., 2016; Gan et al., 2016). Gan et al. (2016) successfully classified botanical origins of honey samples and distinguished raw honeys from adulterated honeys containing rice/corn syrup using Fourier Transform (FT) NIR and Mid-infrared (MR) spectroscopy. They used a total of 105 samples and scanned with NIR and MIR illumination across the 10000 - 4000 cm^{-1} and

4000 - 650 cm^{-1} ranges, respectively. The spectral data were optimised by Interval Partial Least Squares (iPLS) technique to obtain regions 6310 – 5847 cm^{-1} (NIR) and 3397 - 3298 cm^{-1}, 2893 - 2592 cm^{-1} & 1381 - 980 cm^{-1} (MIR) corresponding to the absorptions of O-H and C-H in NIR, C-H, O-H for H_2O and C-O & C-C stretching bands in MIR. These optimised regions were then modelled by Partial Least Squares Discriminant Analysis (PLSDA) resulting in 100 % and 96 % accuracy for separating floral origins and the detection of adulterated honeys, respectively (Gan et al., 2016). Similarly, Bazar et al. (2016) investigated detecting adulteration of honeys in the NIR region (1300 – 1800 nm) based on the absorption differences between raw and foreign water molecules associated with polymeric materials (protein, vitamins, minerals, fibres) in a honey matrix. Authentic honeys contain well-structured water molecules in the honey matrix, but once diluted with other simple carbohydrates, water molecules are less highly structured. The differentiation of water spectra between original and fake honeys was identified in the NIR range of 1300 - 1800 nm (Bazar et al., 2016). The NIR models could detect the adulteration rate in honeys with the lowest cross-validation error of 1.48 % (Bazar et al., 2016).

Fluorescence spectroscopy is a noteworthy technique recently used for quality assessment of food (Karoui & Blecker, 2011). It analyses fluorescence emission from sample-fluorophores. When fluorescent compounds absorb electromagnetic energy of the right wavelength, they release unique fluorescence signals at the low electromagnetic energy (longer wavelength) than the incident energy (Lakowicz, 2006). Fluorescence spectroscopy was used to detect distinctive fluorescence profiling in genuine honeys, which can be discriminated from adulterated honeys (Bong et al., 2018; Dramicanin et al., 2018). Dramicanin et al. (2018) applied fluorescence excitation-emission matrices to measure 99 native and 15 adulterated honey samples in five different spectral regions across the excitation 240 - 375 nm and the emission 370 - 520 nm ranges. The fluorescence data were analysed by statistical tools (PCA & LDA), which can detect adulterated honeys with 100 % accuracy (Dramicanin et al., 2018). In addition, fluorescence spectroscopy has been also used to classify honeys based on botanical origins. Lenhardt et al. (2015) applied synchronous front-face fluorescence spectroscopy to capture fluorescence spectra of honeys in the excitation 240 - 500 nm range. Since honeys from different botanical and geographic origins contain a large variety of physical and chemical information, the analysis of honey fluorescence data using chemometrics was able to distinguish geographic districts of honeys (Lenhardt et al., 2015). New Zealand honeys (mānuka and kanuka honeys) also exhibit unique fluorescence markers that potentially can be detected to identify signatures of floral local geography (Bong et al., 2018; Dramicanin et al.,

2018). Although fluorescence spectroscopy has been used to characterise honeys in the laboratory and use in the field has been anticipated, fluorescence spectroscopy employed to characterise NZ mānuka honeys at-line in industry has not been reported.

Raman spectroscopy is also considered as a powerful detection technique, which can find tiny molecules contained in adulterated honeys (Oroian et al., 2017). Similar to NIR and fluorescence spectroscopies, Raman spectroscopy captures footprints of molecules of interest through Raman scatter induced when exposed to laser light (Larkin, 2018; Nickless, 2015). Oroian et al. (2017) used Raman spectroscopy along with multivariate statistics to determine levels of adulterant agents (fructose, glucose, invert sugar, hydrolysed inulin sugar and malt) added to several native honeys (acacia, sunflower, tilia, polyfloral, and honeydew). Their results showed fake honeys were discriminated by classification technique PLSDA, and the adulterant concentration was also predicted by statistical tools PLS regression & PCR. Li et al. (2012) used Raman spectroscopy combined with chemometrics (PLSDA) to detect adulterants (high fructose corn syrup and maltose syrup) in honeys with an accuracy of 84.4 %. In respect to mānuka honeys, Nickless et al. (2015) applied Fourier transform (FT) Raman spectroscopy coupled with chemometrics to measure the concentration of DHA in *Leptospermum scoparium* nectar from various NZ cultivars. Their results predicted DHA well with an R^2 at 0.85 when using HPLC data as standard. In general, Raman spectroscopy has not been employed to authenticate of mānuka honeys and nor has its application to honey at-line in industry been reported.

Hyperspectral imaging along with chemometrics and machine learning methods have been used to authenticate honeys (Minaei et al., 2017; Shafiee et al., 2016). Shafiee et al. (2016) and Minaei et al. (2017) applied line-scanning hyperspectral imaging in the laboratory in the VIS/NIR region to determine the authenticity of raw honeys (acacia, buckwheat, tilia and rapeseed). Genuine honeys and mixtures of fructose/glucose (1:1) adulterated with native honeys were scanned with a hyperspectral sensor in transmittance mode. By using supervised classification methods, authentic and adulterated honeys were discriminated with high statistical accuracy (> 90 %). Employing a heatmap to visualise adulterated components in a 2D image, these authors were able to identify their positions mixed in raw honeys. Although hyperspectral imaging requires computational efforts to interpret data, the potential of using it to authenticate New Zealand mānuka honeys is clear. Noviyanto & Abdulla (2020) and Zhang & Adulla (2022) differentiated commercial monofloral New Zealand honeys including mānuka honeys using reflectance line scanning hyperspectral imaging in the range from 399.40 to

1063.79 nm. They obtained high accuracy (> 90 %) among commercial mānuka honeys with different UMF^{TM} level, and between clover, mānuka blend and mono-mānuka honeys. However, their study was only applied on retail honey products against the label identity (Noviyanto & Abdulla, 2020; Zhang & Abdulla, 2022). Applications of hyperspectral imaging to honey in comb before extraction for the frame has not been reported.

3.2.5. Summary

Both conventional and non-invasive methods have been employed to characterise NZ mānuka honeys. Recently, the demand for non-destructive technologies (NIR spectroscopy and hyperspectral imaging) has grown. The previous findings indicated that various spectral techniques give good predictions of chemical compositions in honeys in comparison with conventional methods (HPLC, GC-MS, molecular biological analysis and melissopalynology). Using chemometrics and machine learning to analyse spectroscopic and hyperspectral data has resulted in good classifications of authentic mānuka honey against adulterated honey. However, no report yet discovered has mentioned applying non-destructive methods to evaluate mānuka honey while in comb form in the frame.

3.3. Research gap

The eight chemical makers (DHA, MGO, 2'-MAP, 3-PLA, 4-HPLA, 2-MBA, Leptosperin and Lepteridine^{TM}) are important to define the quality and identity of mānuka honey (Bong et al., 2018; MPI, 2017b). Quality assessment of mānuka honeys is officially based on these chemical markers using chromatography-based techniques (MPI, 2017b). However, such techniques are destructive and inconvenient for evaluating frame by frame. No studies have been reported to measure these markers using non-invasive methods while honey is still in the frame and undiluted. The current study aims to develop scientific guidance and methods for estimation of the eight chemical markers using non-destructive methods. Measurement of concentration of chemical markers is a direct way to assess honey quality. However, the complexity of the honey matrix due to variation in botanical sources could impact prediction. So, this study introduces an additional way to measure quality and purity of mānuka honey, so-called mānukaness (Chapter 2). Potency mānukaness is function of levels of DHA, MGO and Leptosperin. Purity mānukaness was built from combination of 2'-MAP, 3-PLA, 4-HPLA, 2-MBA, Leptosperin and Lepteridine^{TM}. Potency mānukaness is closely related to the UMF^{TM} score since UMF^{TM} is primarily estimated from MGO concentration

although Leptosperin also contributes to the UMF^{TM} value (Hellwig et al., 2017; Owens et al., 2019; Snow & Manley-Harris, 2004; UMFHA, 2022).

Honey quality varies across apiaries, beehives and in a honey frame. This depends on geographic districts and seasonal temperature which changes every year (Burns et al., 2018; Williams et al., 2014). The value of mānuka honey changes yearly due to variation in botanical sources. Blind extraction of multiple frames together could devalue mānuka honey since the UMF^{TM} score decreases if good frames are mixed with poor frames. The value of mānuka honey is often represented by the UMF^{TM}/$$ curve (i.e., pricing curve) that is generally concave upwards but could change every year. Quality assessment of honey frames before lumped extraction could preserve mānuka honey value at source. This study also aims to calculate the dollar benefit of using non-destructive methods to separate the rich mānuka frames from the lean frames.

Line-scanning hyperspectral imaging was able to discriminate mānuka honeys from other honeys when applied to commercial honey samples in the laboratory (Noviyanto & Abdulla, 2020). Noviyanto and Abdulla (2020) showed that line-scanning hyperspectral imaging along with chemometrics could classify mānuka honeys with different UMF^{TM} but their study did not predict UMF^{TM} scores. Zhang et al. (2022) used deep learning to improve the classification of mānuka honey from Noviyanto and Abdulla's hyperspectral data. Their results also did not predict UMF^{TM} scores nor identify chemicals relevant to classifying mānuka honeys from other honeys.

Fluorescence spectroscopy has been used to detect two unique fluorescence markers in mānuka honey (Bong et al., 2018; Bong et al., 2017; Lin et al., 2020). Their methods used fluorescence mode to detect Leptosperin and Lepteridine^{TM} in diluted honey samples to avoid scattering effects and fluorescence self-quenching by other compounds in the complex honey matrix. Detecting fluorescence signatures of Leptosperin and Lepteridine^{TM} in raw mānuka honey in frames without dilution has not been studied before. Line-scanning hyperspectral imaging coupled with chemometrics, and machine learning could be a powerful technique for characterising mānuka honey. However, there are still several gaps which must be filled if key chemical markers and "mānukaness" are to be predicted for uncapped honey frames at line speed in a mānuka honey extraction plant.

- Research gap 1: No continuously variable statistic for codifying potency and purity of "mānukaness" from eight measured quantities, and suitable for grading at line, has been reported.

- Research gap 2: Characterising mānuka honey in honey frames immediately after uncapping using optical technology has not been reported.
- Research gap 3: The economic benefit in return if quality of honey frames can be evaluated before bulk extraction has not yet been reported.
- Research gap 4: The matrix effect of undiluted mānuka honey on fluorescence emission of Leptosperin and Lepteridine^{TM} has not been investigated.
- Research gap 5: The combination of fluorescence and NIR reflectance data to assess multiple honey compounds has not been examined.

Based on these research gaps, four research questions or hypotheses for answering in this PhD could be identified. The overall objective is to examine the potential of rapid, non-destructive hyperspectral imaging and supporting chemometrics to predict "mānukaness" and chemical markers in honey frames before bulk extraction to permit real-time grading at line. Research hypotheses were identified to test as follows:

- Hypothesis 1: That the optical signals of eight key chemical makers in mānuka honey associated with potency and purity "mānukaness" are detectable by Vis-NIR spectroscopy and hyperspectral imaging enabling a non-invasive proxy for scoring "mānukaness".
- Hypothesis 2: That honey frames can be sorted by quality before lumped extraction using Vis-NIR methods and that this brings commercial benefit over the current extraction method in which all frames from an apiary are lumped together.
- Hypothesis 3: That it is possible to develop chemometric methods to eliminate the effect of the undiluted honey matrix on fluorescence emission to detect fluorescence signatures associated with mānuka honey.
- Hypothesis 4: That in-frame potency and purity "mānukaness" can be predicted more accurately by combining fluorescence and Vis-NIR hyperspectral imaging systems.

Chapter 4
Estimation of chemical markers using NIR methods

4.1. Introduction

Mānuka honey contains the eight key chemical markers which represent mānuka honey quality and identity (MPI, 2017b; UMFHA, 2021). Chemical structures of these markers (described in Chapter 2 (Literature review)) contain hydrogen bonds X-H exhibiting characteristic molecular vibrations and interactions in the NIR range (Krzysztof & Christian, 2019). Therefore, the current chapter is aimed at research hypothesis 1: assessment of the capability of non-destructive Near Infrared Spectroscopy (NIRS) combined with chemometrics to estimate concentrations of key chemical markers in mānuka honey. The key knowledge gaps are: 1) can the signals of key markers be distinguished from the bulked signal of the honey matrix? 2) if the premise 1) is true, can spectral signals of honey be used to measure concentrations of key markers in mānuka honey? Both non-imaging (350 - 2500 nm) and hyperspectral imaging (547 - 1701 nm) techniques were used to assess honeys. This chapter describes the methodology of these two techniques in capturing the complex signals of honey spectra. Then, modelling methods (chemometrics) were employed to extract chemical information from spectra for prediction of key chemical markers.

Section 1. NIR non-imaging system (350 - 2500 nm)

4.2. Materials & methods

4.2.1. Materials

A total of 1451 honey samples drawn from a set of 1656 samples (205 samples were mismatched during scanning with the non-imaging system), collected from eight geographic districts of the North Island of New Zealand, along with standard laboratory analytical data for each sample. Samples and data were provided by Comvita® Ltd. for use in this work. All honey samples were harvested between December 2019 and April 2020. The samples were scanned within one year of chemical analysis. Some chemical markers (e.g., DHA and MGO) could change slightly in concentrations over the time span of the research, but Leptosperin and Lepteridine™ are stable during storage (Bong et al., 2018; Stephens et al., 2017).

Each honey sample was a single composite of honey which had been extracted from many frames from several hives usually from the same apiary. Each sample was stored in a 50 mL polypropylene plastic container and kept at ambient temperature until scanned. A clover honey with UMF^{TM} 0 was introduced as a sample control (non-mānuka honey) in the dataset. Some honey samples in the 1451-datasheet were also rated UMF^{TM} 0, but none was devoid of all compounds of interest. Samples were randomly grouped into 24-honey sample sets and were scanned in the darkroom laboratory at Agresearch, Te Ohu building, Palmerston North, New Zealand.

4.2.2. Statistical overview

The 1451 honey samples had a large distribution of chemical compositions having been drawn from eight geographic districts (Figure 4.1), but the dataset was unbalanced in that a majority group was mono-mānuka honeys due to good weather that season. Overall, mono-mānuka honey typically contains higher levels of key chemical markers than multi- mānuka and non-mānuka honeys. Figure 4.1 shows a cumulative probability distribution plot, also known as a cumulative distribution function (CDF) plot of 10 chemical parameters in the current dataset. The CDF plots of almost all key markers (DHA, MGO, Leptosperin, Lepteridine^{TM}, 4-HPLA, 2'-MAP, 2-MBA, 3-PLA, and UMF^{TM}) are curved lines, skewed to the left and having long tails to the right. This indicates the data of these markers are non-uniformly distributed, having more samples with low values than high values. However, the data are still considered as if normally distributed. The mean concentration of these parameters can be seen in the CDF plot. For example, the mean UMF^{TM} is 10 and the mean DHA is around 1500 mg/kg. There are few samples with UMF^{TM} score above 17 but many samples have UMF^{TM} 0. There is a paucity of samples with DHA above 2500 mg/kg. These are also found in other chemical markers.

The intercorrelation matrix of eight key chemical markers in the 1451-honey dataset was calculated for pairs of markers using Origin software (version 2020, OriginLab Corporation, Massachusetts, USA) and Pearson's r values were obtained indicating the linear correlation between each pair of markers (Table 4.1). Leptosperin and Lepteridine^{TM} are highly correlated with DHA, MGO, 2'-MAP and 2-MBA. The UMF^{TM} score is likely correlated to almost all chemical markers, but least with 3-PLA. However, 3-PLA is highly correlated ($r^2 = 0.90$) with 4-HPLA. The colour parameter is not significantly correlated to any key chemicals or to UMF^{TM} value.

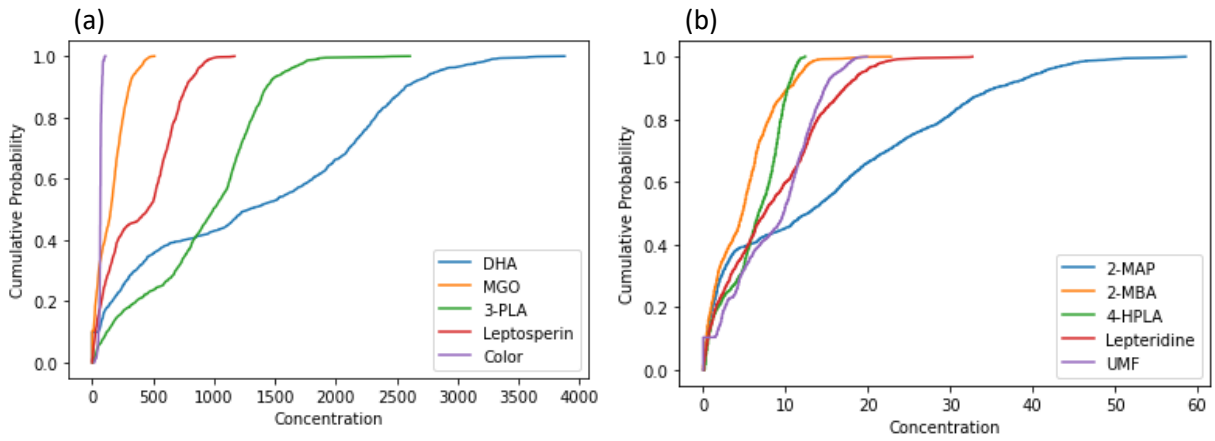

Figure 4.1. Cumulative probability distribution plot of 10 chemical parameters in the 1451-honey dataset (a): CDF for DHA (mg/kg), MGO (mg/kg), 3-PLA (mg/kg), Leptosperin (mg/kg) and color (pfund) (b): CDF for 2'-MAP (mg/kg), 2-MBA (mg/kg), 4-HPLA (mg/kg), Lepteridine (mg/kg) and UMF™

Table 4.1. Matrix of square Pearson's r correlation coefficients for eight chemical markers (as determined by lab-based analysis) from a 1451-sample dataset.

Chemicals	DHA	MGO	2'-MAP	3-PLA	2-MBA	4-HPLA	Lepteridine™	Leptosperin	Colour	UMF™
DHA	1.00									
MGO	**0.92**	1.00								
MAP-2	**0.91**	**0.82**	1.00							
PLA-3	0.55	0.57	0.52	1.00						
MBA-2	**0.85**	**0.73**	**0.82**	0.46	1.00					
HPLA-4	**0.70**	0.69	0.69	**0.90**	0.63	1.00				
Lepteridine™	**0.86**	**0.88**	**0.80**	0.63	0.66	**0.73**	1.00			
Leptosperin	**0.92**	**0.86**	**0.80**	0.55	**0.73**	0.67	**0.85**	1.00		
Colour	0.02	0.09	0.00	0.55	0.10	0.45	0.14	0.05	1.0	
UMF™	**0.92**	**0.98**	**0.82**	0.62	**0.77**	**0.74**	**0.88**	**0.88**	0.15	1.00

Note: bold numbers mean significantly correlated

4.2.3. NIR spectroscopy

The NIR range (800 - 2500 nm) was investigated, extending into the visible (Vis) region (350 - 700 nm), to search for footprints of chemical markers in mānuka honeys. A NIR Analytical Spectral Devices (ASD) spectroradiometer (Model NIRLS408, ASD Inc., Boulder, CO, USA) was used in the 350 - 2500 nm range. This is a non-imaging instrument as shown in Figure 4.2, the spectral reflectance of each sample was captured through the transparent base of the polypropylene sample container neglecting any material influence (polypropylene's

absorption maxima lies in 2 - 400 cm^{-1}). The spectral data were collected by acquisition software LabSpec 4 (ASD Inc., Boulder, CO, USA).

Figure 4.2. *Scanning of reflectance spectral data of 1451 honey samples through the container transparent base using ASD spectroradiometer*

4.2.4. Modelling method

Linear partial least squares (PLS) regression was employed to model and predict concentrations of eight chemical markers from the spectral data. For modelling, the spectral data (n = 1451 samples) of eight districts were divided into calibration and validation sets using the Kennard-Stone technique. This technique was applied to split the sample set 70:30 calibration to validation samples. The PLS model was optimised using the 10-fold venetian blind cross-validation procedure. Ten sub-models were formed during one-fold of calibration dataset leave-out. The output of a calibration model was obtained by the average of all sub-models' prediction results. The calibration model performance was tested on validation data and goodness-of-fit was evaluated.

The PLS method searches a small number of independent linear combinations of latent variables that maximises the covariance between the spectral data (**X**) and the reference (**y**) to enhance prediction accuracy. Several pre-processing techniques: SNV; area normalised, MSC; first and second derivatives and their combinations were investigated on the mean of spectral data. For feature selection, two methods iPLS and VIP were employed to discard irrelevant spectral bands. Since some chemical interferents from different botanical sources could absorb at wavelengths close to key markers that could affect prediction, variable selection helps to improve prediction of key markers. The 30-interval iPLS was first operated on the full spectral data to select subsets of 30 spectral bands giving optimal prediction. Then, automatic VIP was applied to select important spectral features with a cut-off of 1, which removed wavelengths

having PLS projection scores smaller than 1 (Saeys et al., 2019; Xiaobo et al., 2010). A PLS model was selected based on the relationship between the number of latent variables (LVs) and root mean square error of cross-validation (RMSECV). When the number of LVs increases, the value of RMSECV decreases. However, a large number of LVs could lead to overestimation. The optimal number of LVs was chosen that would significantly improve the modelling predictive accuracy (R^2 CV) and obtain a low value of RMSECV. During PLS modelling, outliers were detected and removed using the plot of Q residuals and Hotelling T^2.

For each PLS model, the prediction to deviation (RPD) and model bias were calculated. The RPD number is used to evaluate the model predictive capability towards a new sample (Table 2.4, Chapter 2). RPD is calculated by the ratio between standard deviation (STD) and standard error of performance or RMSECV (Saeys et al., 2019; Saeys et al., 2005). Model bias was also expected to be close to 0 since it reflects a small variation between the prediction and true reference (Aleixandre-Tudo et al., 2018).

This section investigated two modelling approaches: global and region-based models. The PLS global model was built from a whole dataset of 1451 samples spanning all eight geographic districts. Meanwhile, a PLS region-based model was built from the dataset of each geographic district alone. Between and within districts there are different floral sources contributing to honey. This results in a complex matrix of spectral signals of mānuka honey. These two approaches would help to assess the effect of chemical variation from nectar sources among geographic districts on ability to detect the signals of key markers.

4.3. Results

4.3.1. Honey reflectance and absorbance spectra

All honey samples were scanned in the spectral range from 350 to 2500 nm. Figure 4.3 shows the mean spectra of 1451 honey samples collected from eight districts. Figure 4.3 A and C show the mean reflectance and absorbance honey spectra of each district while Figure 4.3 B and D display those of three MPI classes (non-mānuka, multi-mānuka and mānuka honeys). The absorbance spectra of honeys from each geographic district are visibly different in the 600 - 1400 nm range. By contrast, the absorbance spectra of non-mānuka, mono-mānuka and multi-mānuka honeys are quite separable in the spectral range of 1500 - 2500 nm. Overall, the absorbance spectra of multi-mānuka and non-mānuka honeys were quite similar except beyond 1500 nm.

The absorption intensity is low in the Vis range between 650 - 850 nm and then slightly increases after 900 nm. The absorption intensity continues to rise and finally drops after 1600 nm. The absorption peaks around 1000 and 1450 nm are relevant to 2nd overtone and 1st overtone of O-H of water molecules in the honey matrix (Xiaobo et al., 2010). Meanwhile, the absorption peak around 1200 nm could be relevant to 1st overtone of C-H combination of carbon groups (-CH_3, -CH_2, -CH) (Xiaobo et al., 2010).

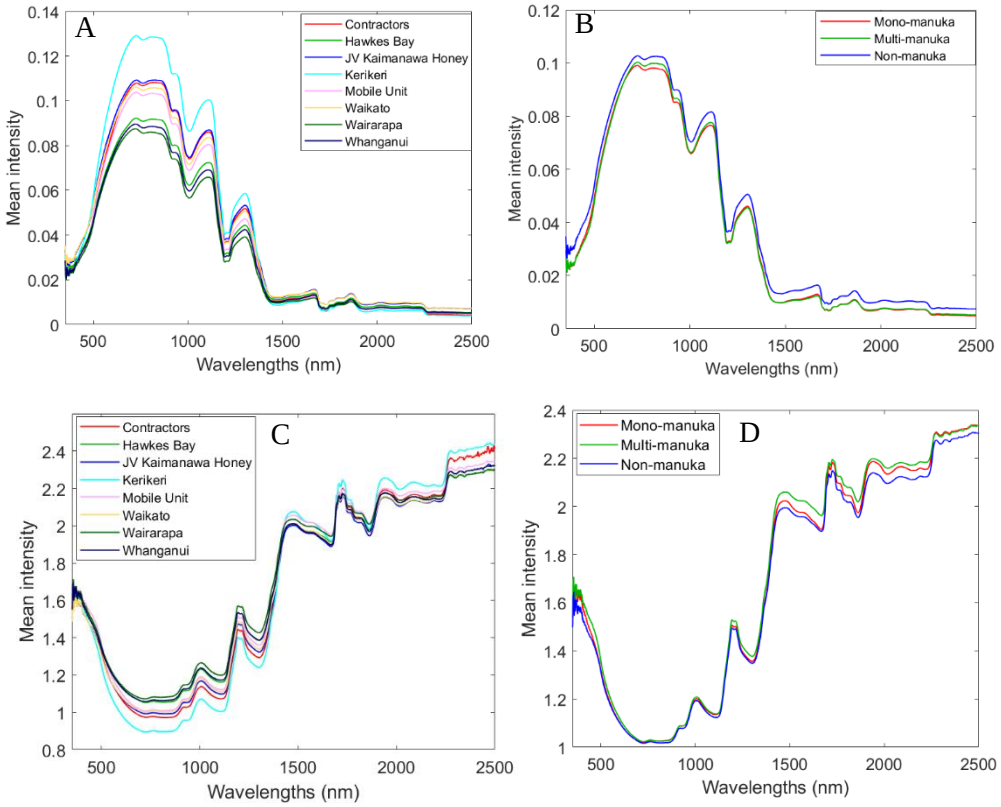

Figure 4.3. *The mean reflectance and absorbance spectra of averaged 1451-honey samples across eight geographical districts (A) & (C) and the mean reflectance and absorbance spectra for mono-mānuka, multi-mānuka and non-mānuka honeys (B) & (D) in 350 - 2500 nm range, respectively*

4.3.2. Development of global models

The NIR non-imaging data described in Figure 4.3 were analysed by PLS regression to derive models to predict concentrations of chemical markers and colour. The best PLS-calibration models derived are displayed in the Table 4.2 as follows.

Table 4.2. The best PLS regression models of NIR non-imaging 1451-sample data for prediction of eight chemical markers (calibration = 1016, test = 435)

PLS models	Pre-processing	LVs	R^2 (CV)	RMSE CV	Bias (CV)	R^2 (Pred.)	RMSEP	Bias (Pred)	RPD
DHA	SNV	13	0.60	640.75	0.45	0.53	688.58	-22.48	**1.59**
MGO	SNV	13	0.47	83.84	0.16	0.41	88.89	-10.32	1.39
3-PLA	SNV	13	0.60	319.08	0.25	0.45	316.70	-26.34	**1.53**
4-HPLA	SNV	12	0.56	2.39	0	0.40	2.49	-0.10	1.48
2'-MAP	Normalised	13	0.49	0.49	-0.01	0.40	10.87	-0.97	1.41
2-MBA	Normalised	12	0.50	2.75	0	0.51	2.48	-0.19	1.38
Leptosperin	SNV	13	0.56	194.92	-0.49	0.49	203.27	7.35	**1.51**
Lepteridine™	SNV	12	0.45	4.67	-0.38	0.43	4.85	-0.38	1.39
Colour	MSC	7	0.67	7.34	-0.02	0.53	5.75	-0.13	**1.63**

Overall, PLS-calibration global models did not perform well with all eight geographic districts lumped together. None of the PLS cross-validation and prediction models of eight markers gave R^2 (CV) and (Pred.) coefficients exceeding 60 % model accuracies. MGO and Lepteridine™ were predicted least accurately. Only DHA, 3-PLA and Leptosperin gave predictive determination (RPD) scores ≥ 1.5 signalling ability to discriminate between high and low values.

In general, prediction of eight chemical markers and colour by global models built from NIR non-imaging data was highly impacted by regional variation. This became obvious when plotting global models across geographic districts for each chemical prediction (Figures 4.4-7). Overall, Wairarapa and Kerikeri and Whanganui data gave greater linearity in the prediction for most markers than other districts (Hawkes Bay, Waikato, Mobile Unit, JV Kaimanawa Honey). There looked to be considerable sample variability within some districts, in particular Hawkes Bay, Mobile Unit and Waikato. The presence of high sample variability could impact overall performance of global models as mentioned in Table 4.2. These results indicated that some districts may be better served by region-specific models, while others may suit the global model better, drawn from all the data available.

Much of the limitation in prediction of chemical markers likely derives from variability native to the honey samples. Few districts will be dominated by a single sub-variety of mānuka, nor show the same mix of non-mānuka nectar sources. Many chemicals deriving from non-mānuka nectars could absorb at the same wavelength interfering with signals of the eight target chemical markers characteristic of mānuka honey. The impact of chemical interference could cause the matrix effect of regional variability on modelling which obscures the information of chemical markers to be extracted.

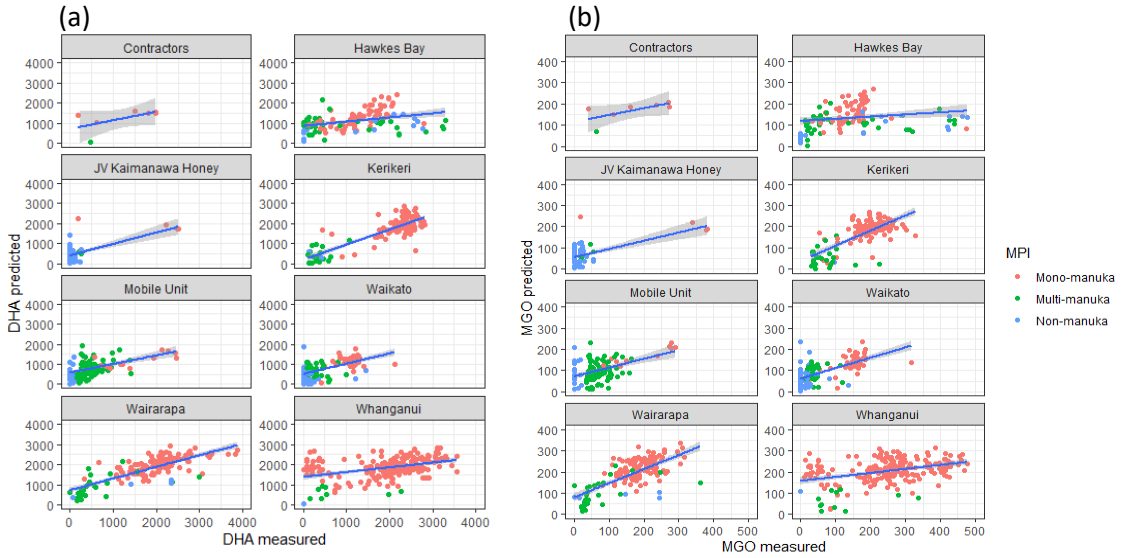

Figure 4.4. *Prediction of DHA (a), MGO (b) plotted across eight geographic districts coloured by mono-mānuka (red), multi-mānuka (green) and non-mānuka (blue) honeys*

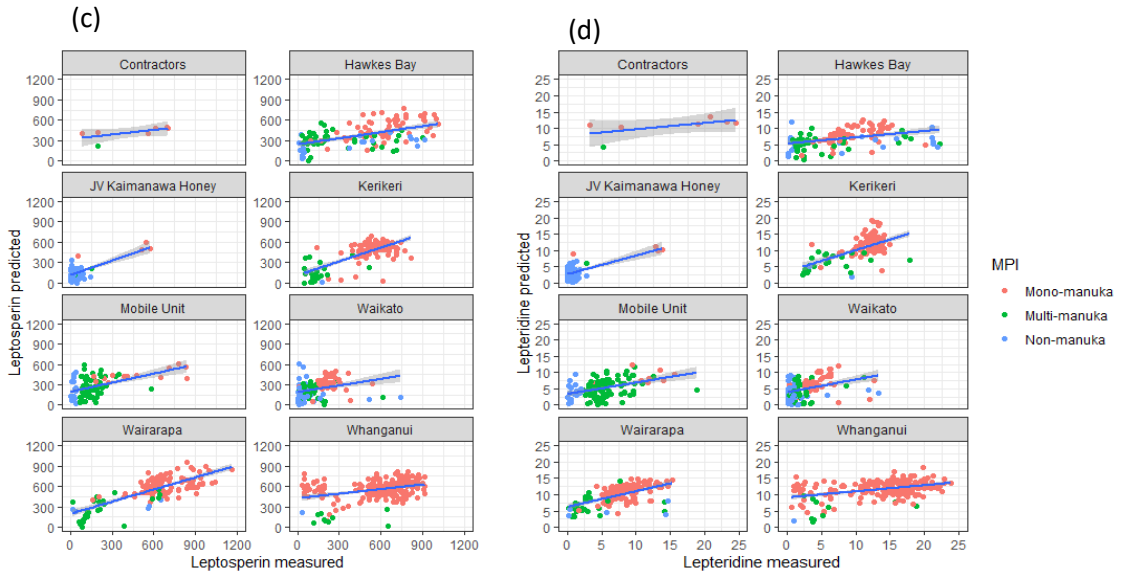

Figure 4.5. *Prediction of Leptosperin (c), Lepteridine™ (d) plotted across eight geographic districts coloured by mono-mānuka (red), multi-mānuka (green) and non-mānuka (blue) honeys*

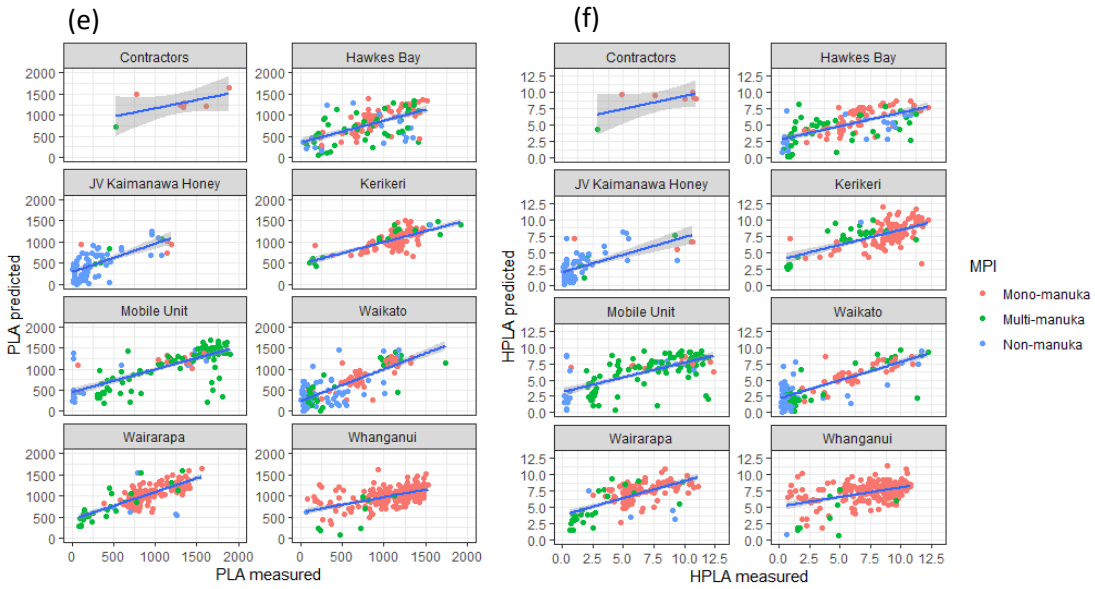

Figure 4.6. *Prediction of 3-PLA (e), 4-HPLA (f) plotted across eight geographic districts coloured by mono-mānuka (red), multi-mānuka (green) and non-mānuka (blue) honeys*

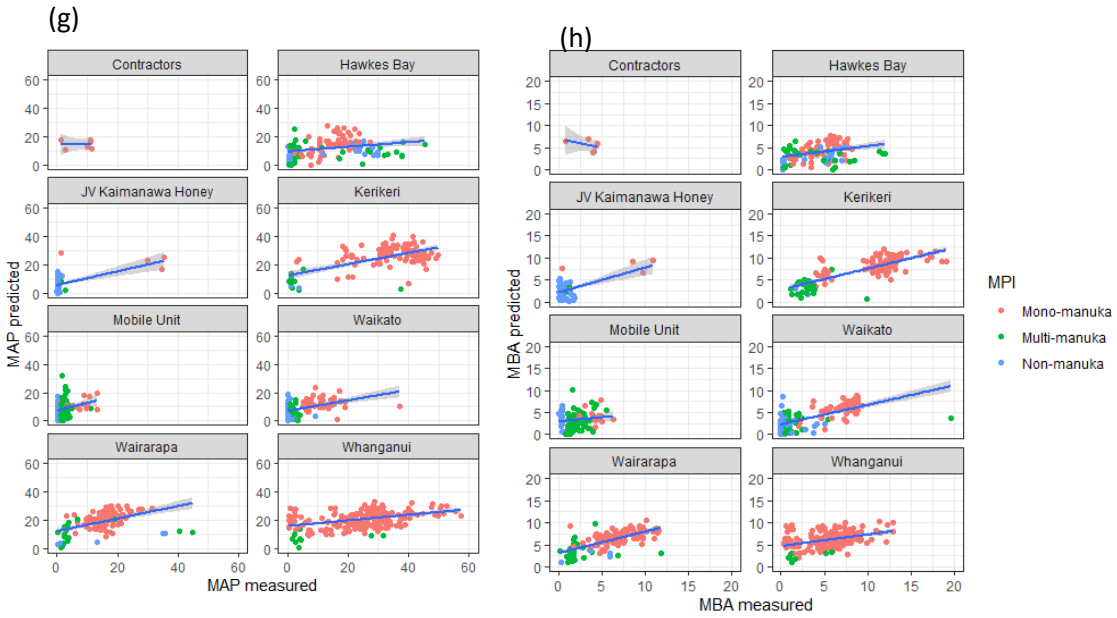

Figure 4.7. *Prediction of 2'-MAP (g), 2-MBA (h) plotted across eight geographic districts coloured by mono-mānuka (red), multi-mānuka (green) and non-mānuka (blue) honeys*

4.3.3. Understanding region-based models

The NIR non-imaging data in the 350 - 2500 nm range were modeled with SNV pre-processing for each district, using district level data. After discarding irrelevant bands by iPLS & VIP, the best performed PLS models, selected with the lowest RMSECV with small number of LVs, are shown in Table 4.3. Kerikeri, Wairarapa and Whanganui provided good predictive regional PLS models over all chemical markers, which was in line with the regional observation from the findings mentioned in the global models. The calibration models from Kerikeri district resulted the best model performances at over 72 % accuracy (R^2 CV) across seven chemicals (DHA, MGO, 3-PLA, 2'-MAP, 2-MBA, Leptosperin and Lepteridine™); For 4-HPLA only 67 % accuracy was achieved, but the predictability was high with RPD > 3. The 3-PLA and 2-MBA calibration models were good enough for quantitative predictions since the RPD score was around 2 – 2.5, while the DHA, Leptosperin and 2'-MAP showed RPD close to 3.

All calibration models obtained from Wairarapa, and Whanganui regions could discern high concentration from low, for almost all key chemicals (RPD number 1.5 - 2) with accuracy over 60 % (R^2-CV > 0.60). However, the Leptosperin and Lepteridine™ calibration models from Whanganui district seemed unable to predict Leptosperin and Lepteridine™ concentrations well since the RPD scores were less than 1.5. These markers appear especially variable in Whanganui honeys.

Hawkes Bay, Waikato, Mobile Unit and JV Kaimanawa did not result in as good calibration models. JV Kaimanawa showed most models got an RPD number above 1.5, but RMSECV and bias values were quite large compared to those of other districts. So, JV Kaimanawa did not rate as a well-predicted district. The Mobile Unit seemed the worst "district" to develop a specific model for, presumably implying greater heterogeneity in the sample set.

Table 4.3. Summary of calibration models for each chemical prediction at each district

Districts	Kerikeri (n=171)		Wairarapa (n= 211)		Whanganui (n= 392)		Hawkes Bay (n= 187)		Waikato (n= 218)		JV Kaimanawa (n=103)		Mobiles Unit (n= 169)	
PLS models	R^2 CV	RPD	R^2 CV	RPD	R^2 CV	RPD	R^2 CV	RPD	R^2 CV	RPD	R^2 CV	RPD	R^2 CV	RPD
DHA	0.88	**2.86**	0.72	**1.86**	0.71	**1.76**	0.62	**1.64**	0.51	1.47	0.51	**1.52**	0.52	1.41
MGO	0.74	**1.92**	0.63	**1.91**	0.62	**1.59**	0.61	**1.58**	0.67	**1.84**	0.61	**1.68**	0.5	1.36
3-PLA	0.81	**2.48**	0.76	**1.97**	0.67	**1.71**	0.75	**2.08**	0.59	**1.57**	0.51	1.45	0.48	1.34
4-HPLA	0.67	**3.77**	0.61	**1.71**	0.61	**1.58**	0.69	**1.84**	0.67	**1.76**	0.52	**1.51**	0.47	1.36
2'-MAP	0.86	**2.60**	0.71	**1.78**	0.60	**1.55**	0.56	1.49	0.61	**1.74**	0.71	**1.90**	0.45	1.29
2-MBA	0.79	**2.19**	0.77	**2.09**	0.72	**1.78**	0.57	**1.54**	0.44	1.30	0.69	**1.98**	0.35	1.24
Leptosperin	0.86	**2.68**	0.66	**1.57**	0.56	1.49	0.51	1.42	0.29	1.12	0.61	**1.67**	0.53	1.41
Lepteridine™	0.72	**1.87**	0.63	**1.65**	0.48	1.42	0.54	1.47	0.26	1.10	0.57	**1.60**	0.53	1.39
Colour	0.89	**2.90**	0.53	1.45	0.75	**1.80**	0.45	1.21	0.82	**2.20**	0.66	**1.64**	0.54	1.42

Note: CV means cross-validation

4.3.4. Discussion

Performance of the global models, using data from all eight districts, was poor for most markers. Only for DHA and 3-PLA were calibration models able to discern high from low levels of concentration. The limitation of prediction of eight chemical markers was likely due to the varying floral nectar sources across different districts. This complexity of the honey matrix regarding variation in botanical sources become high when all districts are lumped together. This made it difficult for PLS modelling to extract the information of chemicals of interest since other chemicals may be present and absorb at the same wavelengths as key markers.

When eight district-specific models were developed and evaluated, Kerikeri gave the best-performed model followed by Wairarapa and Whanganui districts. These three districts were better served by region-specific models than by the global model. In general, these districts had the highest levels of the eight chemical markers. Thus, Kerikeri, Wairarapa and Whanganui districts justify having their own prediction models to estimate the values of chemical markers. For other districts, the global model looks more promising regardless of its weakness.

In conclusion, the signals of key markers can be detected and quantified at the acceptable level of accuracy in the Vis-NIR range (350 - 2500 nm) using NIRS (for example models for Kerikeri). However, regional variation in botanical sources influences the prediction of chemical markers at global levels and even at some other region-based models. Districts with a small number of samples (e.g., Mobile Units, JV Kaimanawa) offered insufficient variation to generate a robust model. The complex matrix of honey signals varies among geographic districts and seasons that impacts the detection of chemical markers for assessment of honey quality and purity. To deal with the complexity of the honey matrix, modelling needs more degrees of freedom, but this was limited in the current dataset available for some districts.

Section 2. NIR hyperspectral imaging system (547 - 1701 nm)

4.4. Materials and methods

4.4.1. Materials

The same sample set, but a total of 1656 honey samples, stored in 50 mL-polypropylene (contact clear) plastic containers were scanned under NIR hyperspectral imaging camera (547-1701 nm).

A line-scan hyperspectral imaging system was employed for collecting reflectance spectra of honey samples. As shown in Figure 4.8 (b), the system was centered on an HSI camera covering wavelengths in the Vis-NIR range of 547 - 1701 nm (Model 1003B - 10151, Headwall Photonics, Fitchburg, MA, USA). A mobile conveyor belt moved the honey samples being scanned by the camera. A halogen lamp (JCR 21 V 150 W/AL Japan 2DB) was employed as a light source. A computer running acquisition software (Headwall Hyperspec III, model E41211 vs 64, Headwall Photonics, Fitchburg, MA, USA) was used to monitor all settings. In all experiments conducted, the following settings were optimised and then used for ensuring that the quality of collected images is suitable for further analysis: the working distance between camera and sample surface was 600 mm; the speed of the conveyor belt was 38.3 mm/s; the camera aperture was 2.8 and acquisition time 19.8 ms.

For scanning, a set of carton trays were used to hold honey samples (as shown in Figure 4.8 (a)), each tray bearing up to 24 honey samples. The imaging system was then used to scan the trays, obtaining hypercubes of size 350 x 320 x 235 for each. A total of 74 hyperspectral images were captured from 74 trays covering the 1656 samples. The spatial resolution of the collected HSI images is dependent on the camara settings and the conveyor belt speed which created a square unit of 0.8 x 0.8 mm/pixel under a field of view (FOV) of 256 mm.

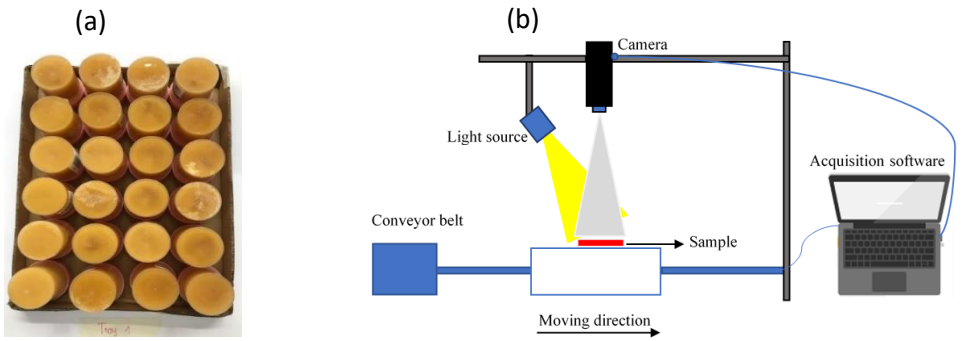

Figure 4.8. *A 24-honey-sample tray (a) and a line-scanning reflectance hyperspectral acquisition (b)*

4.4.2. Hyperspectral imaging segmentation

Segmentation is an important step in extracting regions of interest (ROIs) from an HSI image. Each image collected consists of spectral information from different honey samples. Figure 4.9 demonstrates the segmentation process in which ROIs for individual samples were segregated. The segmentation process was implemented on Python 3.8 with main packages: skimage, scipy, matplotlib, and spectral python (the python code script is attached in Appendix B). This process helps remove carton background, container shadow and saturation light or noise, keeping only ROIs. The approach used consists of three stages: multi-level thresholding (1), a set of morphological operations (opening, closing, region filling) (2), and connected components labelling (3). Then each ROI (i.e., segment) was extracted and linked to laboratory reference data of that sample. The centroids of the segments obtained were calculated and used to localise the segments and match them with the reference data.

For each segment, the spectral information was extracted as the mean spectrum of all pixels inside the segment. Then, the extracted average spectra of the 1656 honey samples were stacked into a matrix of size 1656 x 235, where 235 is the number of wavelengths (or variables) in the spectra collected. The reference data, including the UMF^{TM} score and the class of honey (mono-mānuka, multi-mānuka and non-mānuka), were also stacked in another matrix where each row represents the reference data of the same row in the spectral matrix. These two matrices were then used for modelling, data analysis and visualisation.

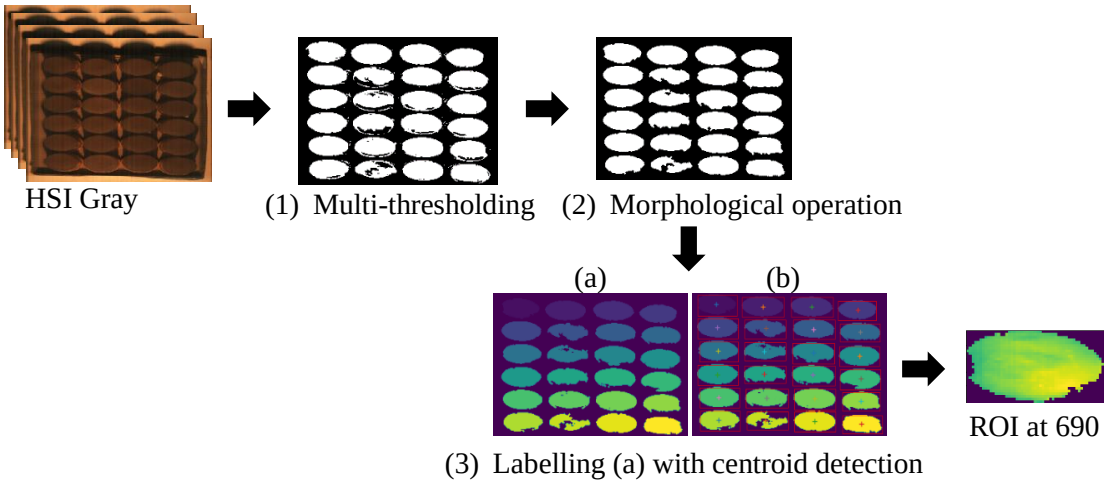

Figure 4.9. *The segmentation approach of a 24-sample hyperspectral image to select regions of interest (ROIs). Each ROI is a single honey sample*

4.4.3. Modelling method

PLS regression was employed for prediction of key chemical markers from hyperspectral signals. Similarly to the previous section (4.2.4), the global and region-based models obtained from hyperspectral imaging data were investigated to compare with the results of non-imaging data. Before modelling, calibration and test sets were generated by the Kennard-Stone algorithm from the raw data with ratio split 70:30. The same pre-processing and cross-validation techniques used for non-imaging data were investigated during modelling hyperspectral data. Outliers were detected before modelling using the Hotelling T^2 versus Q-residual plot. For selection of important variables, only the iPLS technique with 4 band intervals were employed.

4.5. Results

4.5.1. HSI reflectance and absorbance spectra

The reflectance spectra extracted from ROIs of hyperspectral images were converted into absorbance before modelling. Figure 4.10 displays the mean reflectance and absorbance spectra of 1656 samples plotted across eight geographic districts (Figure 4.10 a & c) and across three MPI honey classes (Figure 4.10 b & d). The absorption intensity is low in the 650 - 1150 nm range and then significantly increases from 1200 nm and finally drops after 1600 nm. Absorbance spectra of eight districts are visibly separated over 547 - 1600 nm. This suggests that the optical properties of honey samples among geographic districts are different. By contrast, the absorbance spectra between mono-mānuka, multi-mānuka and non-mānuka are slightly different beyond 700 nm and after 1200 nm. The absorption peaks around 1000 and 1450 nm could be relevant to 2^{nd} overtone and 1^{st} overtone of O-H of water molecules in the honey matrix (Golic, 2003; Jiang et al., 2016). Meanwhile, the absorption peaks around 1200 and 1400 nm could correspond to 2^{nd} overtone C-H and 1^{st} overtone C-H combination of carbohydrate groups (-CH_3,-CH_2 & -CH) (Xiaobo et al., 2010). This is similar to the case of the absorbance spectra of non-imaging data observed in the range 547 - 1701 nm.

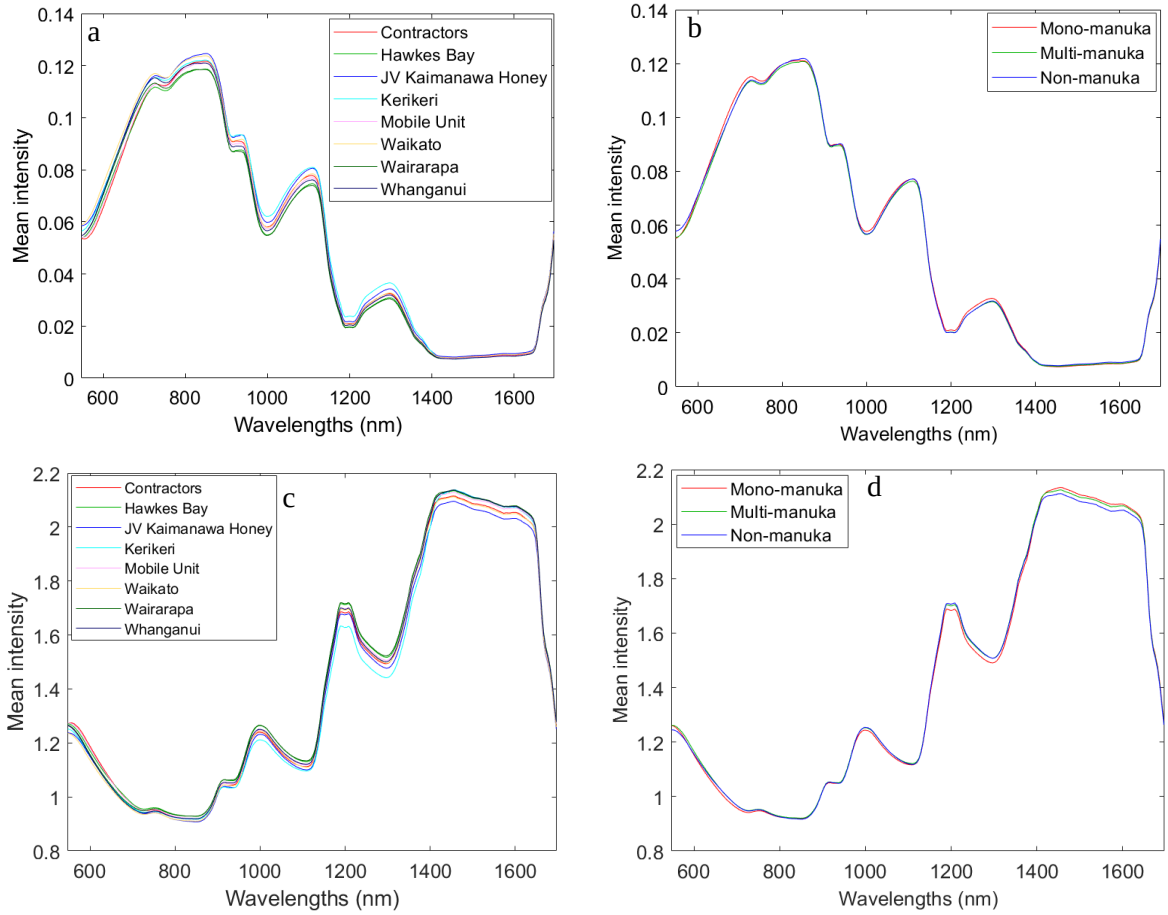

Figure 4.10. *The mean reflectance and absorbance spectra of 1656-honey samples for eight geographical districts (a & c) and the mean reflectance and absorbance spectra of mono-mānuka, multi-mānuka and non-mānuka honeys (b & d) extracted from hyperspectral images (547 - 1701 nm)*

4.5.2. Developments of HSI global models

Similar to non-imaging data, hyperspectral data with eight districts together were also run as global models. Table 4.4 illustrates the best iPLS-PLS calibration models for prediction of eight chemical makers and colour from HSI data. In general, PLS calibration models did not perform well on NIR hyperspectral data (547 - 1701 nm) when eight geographic districts were combined. This was also found in global models of NIR non-imaging data. The PLS cross-validated prediction models of most chemical markers resulted in accuracy values of R^2 (CV) $\approx$ 0.60, except for 3-PLA (R^2 (CV) = 0.68). Lepteridine™ was predicted least accurately (R^2 pred = 0.04). However, calibration models of DHA, MGO, 3-PLA, 4-HPLA and Leptosperin gave a RPD score $\geq$ 1.5 signalling ability to discriminate high from low values.

HSI global models (547 - 1701 nm) covering all eight districts were also clearly impacted by regional variation. This was evident when observing district by district for each global model (Figures 4.11 - 14). For most markers, Wairarapa, Kerikeri and Whanganui data showed linearity in the prediction. By contrast, Hawkes Bay, Waikato, Mobile Unit, JV Kaimanawa and Contractors data showed predicted values highly scattered around the linear line. These districts had small sample sizes which could also impact modelling due to constrained variation of key markers' levels. Wairarapa and Kerikeri had broad variation of each chemical marker followed by Whanganui. Overall, the presence of regional variability influenced the overall performance of global models (Table 4.4).

These results were in line with the findings from the NIR non-imaging data (350 - 2500 nm) (section 4.3.). In conclusion, NIR hyperspectral imaging global models predicted chemical markers similarly to those of NIR non-imaging despite different acquisition settings. For NIR hyperspectral data, Kerikeri district may be better served by region-specific models, while others may suit the global model better, drawn from all the data available.

Table 4.4. The best iPLS-PLS regression models of NIR HSI 1656-sample data (calibration = 1160 & test = 496)

PLS models	Pre-processing	LVs	R^2 (CV)	RMSE CV	Bias (CV)	R^2 (Pred.)	RMSEP	Bias (Pred)	RPD
DHA	MC	11	0.58	640.57	-3.07	0.55	611.16	-35.78	**1.52**
MGO	MSC	11	0.58	71.76	0.27	0.54	73.37	-7.71	**1.55**
3-PLA	SNV	10	0.68	283.38	-0.01	0.60	242.20	-30.09	**1.66**
4-HPLA	SNV	6	0.61	2.20	0.00	0.43	2.20	-0.08	**1.55**
2'-MAP	Normalised	11	0.54	9.21	-0.02	0.58	8.48	-0.14	1.47
2-MBA	SNV	11	0.47	2.75	-0.01	0.42	2.72	-0.41	1.37
Leptosperin	MC	11	0.58	183.11	-0.04	0.57	173.24	-25.14	**1.53**
Lepteridine™	MC	12	0.49	4.37	0.00	0.04	4.46	-0.22	1.41
Colour	SNV	7	0.74	6.61	-0.01	0.43	5.62	0.29	**1.78**

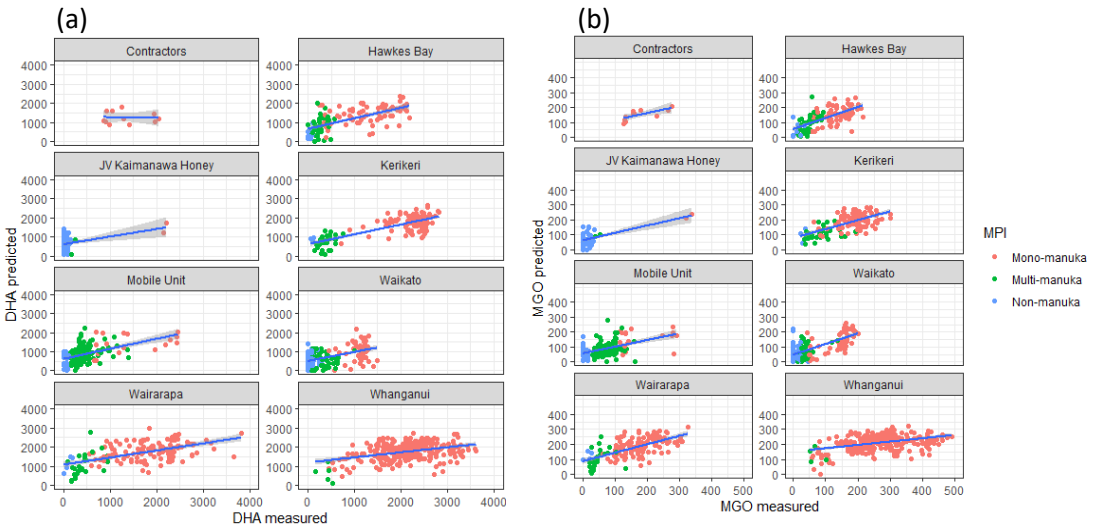

Figure 4.11. *Prediction of DHA (a), MGO (b) plotted across eight geographic districts coloured by mono-mānuka (red), multi-mānuka (green) and non-mānuka (blue) honeys*

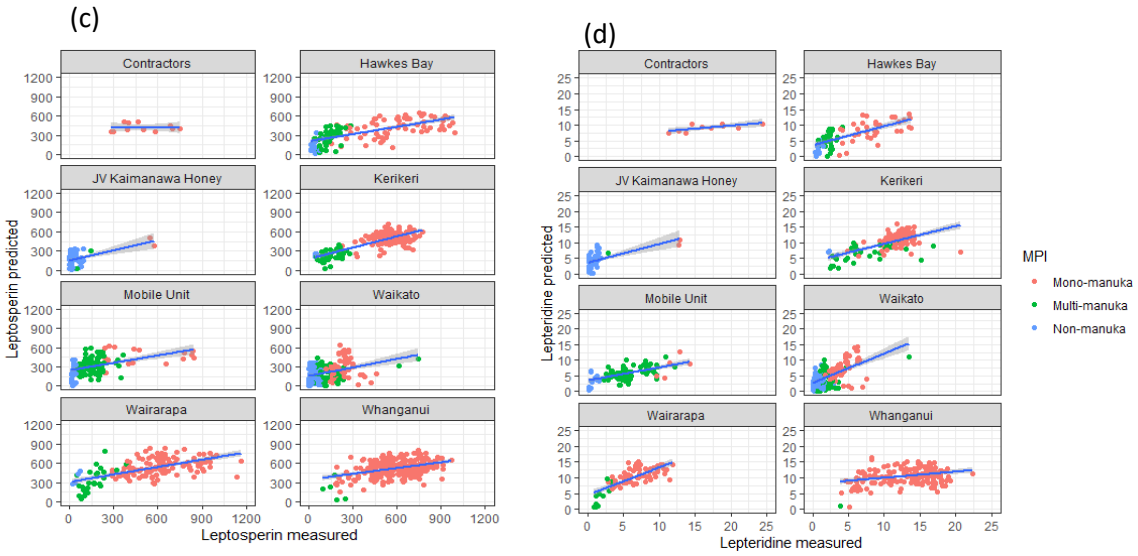

Figure 4.12. *Prediction of Leptosperin (c), Lepteridine™ (d) plotted across eight geographic districts coloured by mono-mānuka (red), multi-mānuka (green) and non-mānuka (blue) honeys*

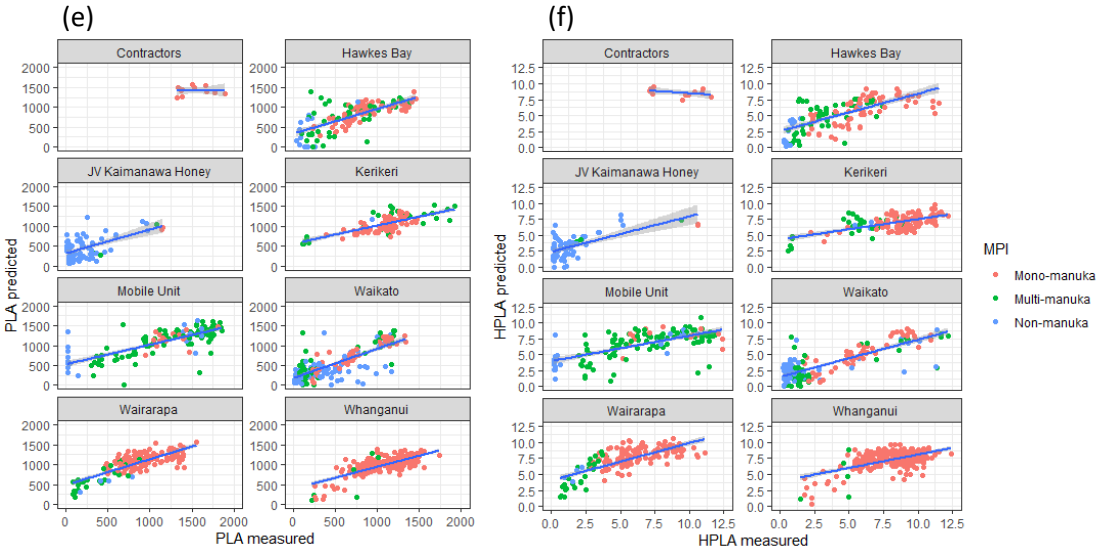

Figure 4.13. *Prediction of 3-PLA (e), 4-HPLA (f) plotted across eight geographic districts coloured by mono-mānuka (red), multi-mānuka (green) and non-mānuka (blue) honeys*

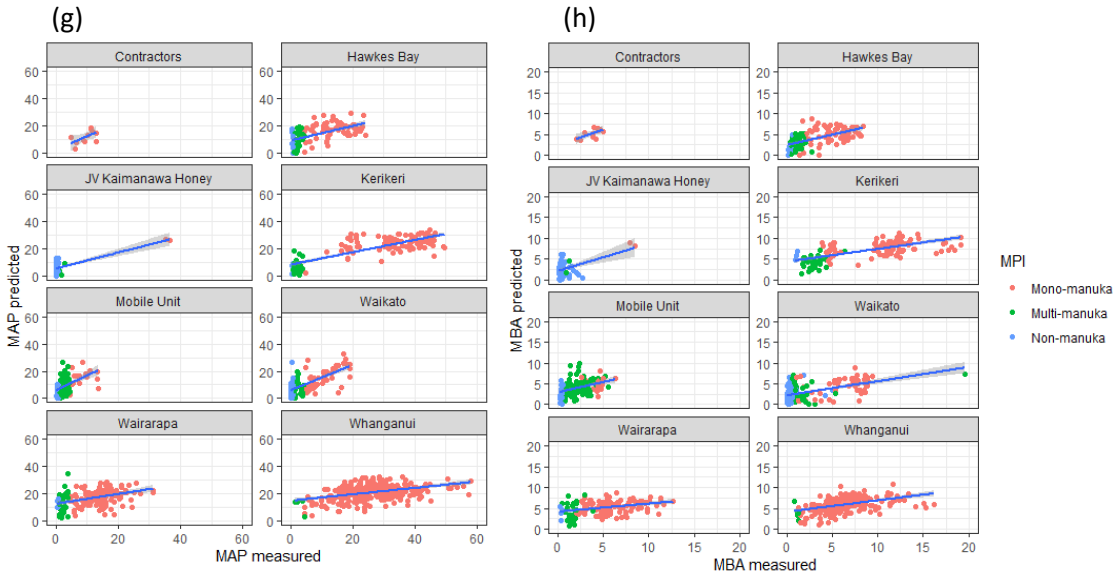

Figure 4.14. *Prediction of 2'-MAP (g), 2-MBA (h) plotted across eight geographic districts coloured by mono-mānuka (red), multi-mānuka (green) and non-mānuka (blue) honeys*

4.5.3. Understanding HSI region-based models

The NIR hyperspectral data in the 547 - 1700 nm range were modelled with SNV pre-processing for each district, using only data from that district. The best iPLS-PLS models selected with the lowest LVs and RMSECV performed as shown in Table 4.5. No districts had a good predictive result for all chemicals. The models from Kerikeri district predicted DHA, MGO, 2'-MAP and Leptosperin with an R^2 (CV) of 62 % and RPD 1.5 - 2.5. The remaining models estimated poorly (R^2 (CV) < 50 %, RPD < 1.5). Wairarapa and Whanganui were expected to obtain good prediction models of eight chemical markers, but most models from these districts were poor, except for models of 3-PLA and 4-HPLA from Wairarapa district which performed with R^2 (CV) > 60 % accuracy and RPD >1.5.

Compared to region-based models of NIR non-imaging data, HSI data (547 - 1701 nm) did not perform well for specific districts (Kerikeri, Wairarapa and Whanganui). Similarly, the Hawkes Bay and Waikato HSI models did not result in as good calibration models as did the region-based non-imaging models. The JV Kaimanawa and Mobile Unit seemed to provide the worst datasets from which to develop a specific model probably due to lack of sample variation (small sample size) (Figures 4.11 - 14).

Table 4.5. Summary of calibration models for each chemical prediction at each district

Regions	Kerikeri (n = 204)		Wairarapa (n = 240)		Whanganui (n = 442)		Hawkes Bay (n = 202)		Waikato (n = 273)		JV Kaimanawa (n = 109)		Mobiles Unit (n = 186)	
PLS models	R^2 CV	RPD	R^2 CV	RPD	R^2 CV	RPD	R^2 CV	RPD	R^2 CV	RPD	R^2 CV	RPD	R^2 CV	RPD
DHA	0.86	**2.49**	0.32	1.22	0.19	1.08	0.35	1.26	0.23	1.19	0.05	1.00	0.2	1.01
MGO	0.62	**1.54**	0.53	1.44	0.24	1.13	0.49	1.43	0.43	1.43	0.04	1.01	0.47	1.25
3-PLA	0.49	1.20	0.75	**1.88**	0.52	1.35	0.60	**1.62**	0.68	**1.75**	0.17	1.17	0.5	1.35
4-HPLA	0.51	1.33	0.63	**1.63**	0.4	1.21	0.52	**1.52**	0.74	**1.92**	0.12	1.14	0.42	1.28
2'-MAP	0.77	**1.94**	0.31	1.26	0.18	1.09	0.30	1.22	0.53	1.47	0.07	0.99	0.33	1.13
2-MBA	0.46	1.30	0.4	1.27	0.3	1.15	0.32	1.22	0.37	1.27	0.16	1.05	0.28	1.15
Leptosperin	0.76	**1.86**	0.4	1.31	0.2	1.08	0.41	1.34	0.1	1.03	0.03	1.04	0.13	0.96
Lepteridine™	0.49	1.23	0.38	1.26	0.24	1.11	0.36	1.29	0.31	1.14	0.10	1.03	0.4	1.15
Colour	0.84	**2.23**	0.61	**1.52**	0.68	**1.63**	0.38	1.20	0.85	**2.46**	0.44	1.29	0.45	1.28

Note: CV means cross-validation

4.5.4. Discussion

The NIR hyperspectral system (547 - 1701 nm) can be used to predict eight chemical markers. Global models, using data from all districts, could predict high and low levels of DHA, MGO, 3-PLA, 4-HPLA and Leptosperin, but predicted poorly for 2'-MAP, 2-MBA and Lepteridine™. The predictive performance for these eight chemical markers was poor by region-based models. Kerikeri, Wairarapa and Whanganui with large diverse sample sets were

expected to perform well, but the predictive models were poor when using NIR hyperspectral data.

Compared to region-based models built from Vis-NIR non-imaging data (350 - 2500 nm), regional models of hyperspectral imaging data (547 - 1701 nm) may have performed poorly, but global models from both data sets shared similar trends. Varying floral sources across different geographic districts may have imposed common limitations through both sets of spectral data. In addition, different acquisition settings between hyperspectral imaging and non-imaging data could also impact honey spectral signals captured. NIR hyperspectral acquisition was operated in the spectral range of 547 - 1701 nm. The interval band between two adjacent wavelengths was 5 nm, and the distance between the detector to the surface of honey sample was 660 mm. By contrast, the NIR non-imaging acquisition covered a broad spectral range of 350 - 2500 nm with much higher spectral resolution between two adjacent bands of 1 nm. The light source and the detector almost directly contacted samples being within 5 mm of the thin polypropylene plastic layer of the inverted sample container. The light penetration, the spectral range, spectral resolution and the sensor sensitivity between the two acquisition systems could generate differences in capturing honey spectral signals carrying chemical information.

Section 3. Capture of honey samples in the black 96-well plate

The potential of hyperspectral imaging was good enough for estimating chemical markers. In sections 4.4 & 4.5, honey samples were presented in 50 mL polypropylene plastic containers. The diameter of a container bottom was 40 mm. However, in industrial reality the diameter of a honey cell in the comb form is small. Modern beekeepers commonly use honey frame made from a black plastic substrate on which to lay wax comb for bees to fill with honey. Therefore, to mimic honey in combs, a subset of honey samples was filled in black 96-well plates with a diameter 6.96 mm per well and then scanned with a hyperspectral imaging system. This section discusses the NIR HSI system capability at capturing reflectance spectral signals of honey in black plates for prediction of chemical markers.

4.6. Materials and methods

4.6.1. Materials

Selected from the 1656 honey samples, a sub-dataset of 570 honey samples harvested in Dec 2019 - Jan 2020 were subsampled into black 96-well plates (NUN137103, ThermoFisher Scientific, MA, USA) before scanning. The same hyperspectral camera (547 - 1701 nm) was used to capture hyperspectral images of honey in the well plates. The hyperspectral settings for this scanning experiment were as follows: the working distance between the camera and the sample surface was 250 mm; the translational speed of the plate was 7.5 mm/s, camera aperture was 2.8 and the acquisition time 34 ms. A hyperspectral image with hypercube size (500 x 320 x 235) having spectral resolution of 5 nm and spatial resolution of 0.3 x 0.3 mm/pixel contained 10-honey samples with three replicates on each microplate was captured under FOV 96 mm (Figure 4.15).

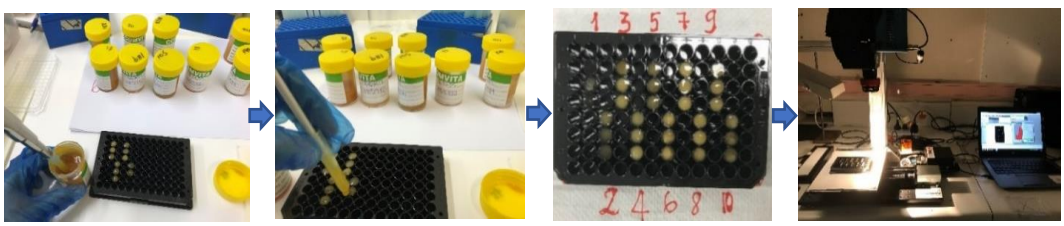

Figure 4.15. *The scheme of filling honey samples into the 96-well plate and capture of hyperspectral images by line-scanning hyperspectral camera*

4.6.2. Hyperspectral segmentation and analysis

Hyperspectral images having regions of interest (ROIs) were collected by Headwall Hyperspec III (E41211 vs64) software from the line-scanning acquisition. Similar to the previous section (4.4.2) three main stages of the segmentation process (multi-thresholding, morphological operation and labeling with centroid detection) was applied to remove all background and noise, even including the microplate background. Honey-only ROIs were collected from which were drawn the final spectral data. The diagram of hyperspectral segmentation and extraction of spectral information for modelling is illustrated in Figure 4.16.

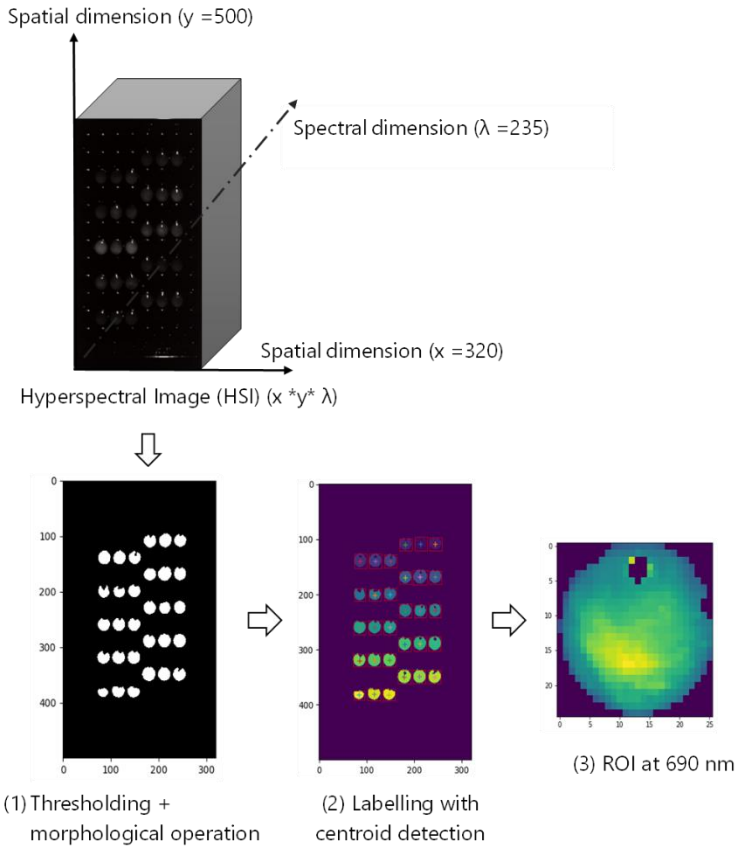

Figure 4.16. *A diagram of the segmentation process used to extract regions of interest (ROIs) in a hyperspectral image having honey samples captured from the 96-well plate*

Once spectral data were acquired, statistical analysis was performed using the PLS toolbox 8.8 and MIA toolbox 3.7 (Eigenvector Research, Inc., WA 98831, USA) in MATLAB R2109a (The MathWorks, Inc., Massachusetts 01760, USA).

Prior to multivariate analysis, the reflectance spectral data of 570 samples were converted to pseudo-absorbance data by Log (1/R) transformation. The transformed data were divided 70:30 for a calibration set and a test set using the Kennard-Stone method in PLS toolbox. Classification and regression models were undertaken by using different statistical methods coupled with several pre-processing techniques (Normalised (area), SNV, MSC, Smoothing, 1st & 2nd derivatives and their combination). The multivariate regression PLS method was applied to estimate concentrations of eight chemical markers.

4.7. Results

4.7.1. HSI honey spectra on the 96-well plate

A total of 570 honey samples in 96-well plates were scanned under a HSI camera on different days. Two honey batches were filled into the well-plates. The first batch was filled full of convex meniscus, but the second batch was filled just full of concave meniscus. Honey spectra of the first batch showed higher signals than the second batch. Pre-processing Standard Normal Variates (SNV) was applied to spectra of the two honey batches to remove additive, multiplicative and baseline effects due to scattering and imbalanced filling in the well. Figure 4.17 shows the mean reflectance and absorbance spectra of 570 samples after employing SNV pre-processing. Spectra across geographic districts are clearly different.

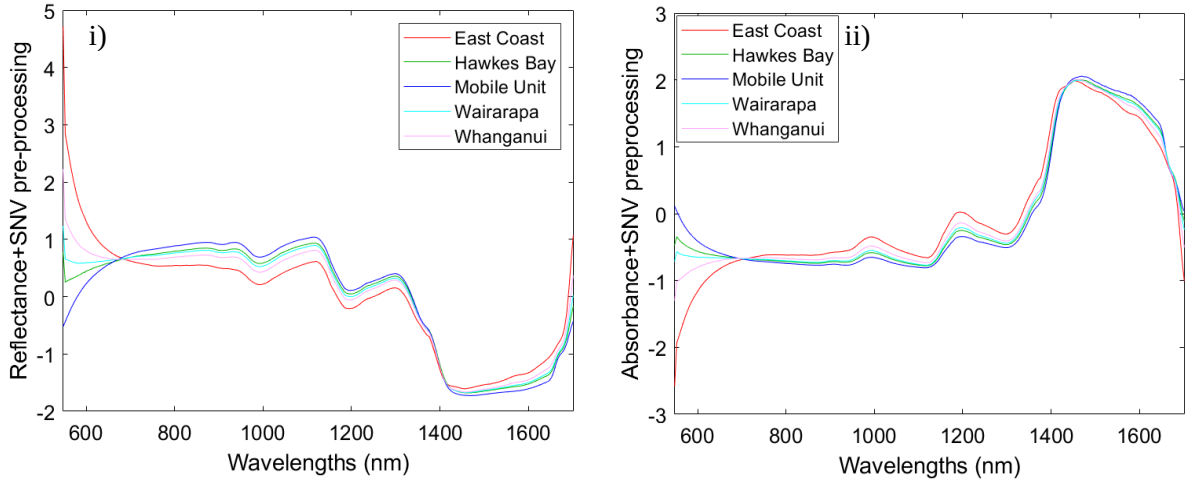

Figure 4.17. *Reflectance spectra after applying SNV pre-processing i) and absorbance spectra after applying SNV pre-processing ii) of 570 honey samples extracted from scans of black 96-well plates*

Absorption peaks are apparent at 1000, 1200 and 1450 nm. There are two other small peaks at wavelengths 980 nm and 1200 nm. These absorption peaks were also observed from non-imaging and hyperspectral imaging spectra extracted from transparent plastic containers in the range 700 - 1700 nm.

4.7.2. Prediction of chemical markers

PLS regression was applied on 570 samples spanning five districts (East Coast, Hawkes Bay, Mobile Unit, Wairarapa and Whanganui) for predicting chemical markers. Global models of 570-sample spectra extracted from 96-well plates were very poor (Table 4.6), even worse than those of 1656-sample HSI data. Overall, none of predictive models built from well-plates could be useful for further application. The signal-to-noise of HSI data captured from the 96-well plate (0.3 x 0.3 mm/pixel) was lower than that obtained from 50 mL plastic containers (0.8 x 0.8 mm/pixel) due to small FOV.

Table 4.6. The best iPLS-PLS regression results of combined two datasets of 570 honey samples for global models (calibration = 399 & test = 171)

PLS models	Pre-processing	LVs	R^2 (CV)	RMSE CV	Bias (CV)	R^2 (Pred.)	RMSEP	Bias (Pred)	RPD
DHA	SNV	8	0.37	714.41	-6.36	0.17	946.23	-169.23	1.3
MGO	SNV	7	0.31	95.51	-0.37	0.24	105.54	-32.37	1.1
3-PLA	SNV	6	0.35	380.07	0.83	0.17	431.05	-205.72	1.2
4-HPLA	SNV	6	0.43	2.15	0.03	0.08	2.99	-1.36	1.3
2'-MAP	SNV	7	0.35	9.71	-0.02	0.19	12.60	-2.12	1.3
2-MBA	SNV	6	0.24	0.26	0.08	0.24	2.80	-1.11	1.2
Leptosperin	SNV	6	0.25	244.71	-1.28	0.03	360.77	-184.30	1.1
Lepteridine™	SNV	5	0.23	5.89	0.01	0.07	6.86	-1.32	1.2

4.8. General discussion and conclusion

The current chapter addresses the capability of NIR non-imaging (350 - 2500 nm) and NIR hyperspectral imaging (547 - 1701 nm) for prediction of the eight key chemical markers. The findings indicate that variation in floral sources across geographic districts strongly impact modelling, in particular global models when all districts are combined. Varying floral sources is the nature of wild honeys at harvest, but this induces complexity in the honey matrix. Chemicals that are not from *L. scoparium* nectar can interfere with the signals of chemical markers in the honey matrix and can obscure prediction of chemicals of interest. The current chemometric modelling method, PLS regression, seems poor at modelling interferent signals of chemicals not derived from *L. scoparium* nectar.

NIR non-imaging data permitted better prediction of chemical markers than NIR hyperspectral imaging data, in particular with region-based data. This indicates that detection capability of NIR non-imaging is stronger than that of NIR hyperspectral imaging. The two systems have different acquisition settings as follows: sensor design, illumination, the spectral range of interest and spectral resolution. The non-imaging system directly captures diffuse reflectance signals from the sample while the hyperspectral system captures a signal that is split among a number of pixels. Thus, the amount of signal detected in the HSI system is smaller, which could lead to lower signal-to-noise ratio than the non-imaging system. In addition, the light source was set close to the surface of sample (< 5 mm) in the non-imaging design that gave a high energy flux irradiating the sample. By contrast, hyperspectral imaging employed a non-collimated light source placed 600 mm from the sample. The resulting light intensity per unity of area of subject in the imaging system was lower than in the non-imaging. The spectral range and spectral resolution also influence capture of good signal-to-noise. The non-imaging sensor covers a broad Vis-NIR range of 350 - 2500 nm while the hyperspectral imaging sensor used captures signals in the 547 - 1701 nm range. Signals below 547 nm and beyond 1701 nm are not detected with this NIR imaging system. The spectral resolution of the non-imaging system was 1 nm while that of the imaging system was 5 nm. This difference in spectral resolution could affect the ability to detect subtle signals from markers such as shoulders in the bands. All these factors influence ability to separate the signals of chemical markers from the signals of the honey matrix. The current study employs two systems different in sensor design and illumination which cannot change once scan data have been collected, but it is possible to investigate the effect of spectral range and resolution. In the next chapter, the study will investigate this effect.

In conclusion, NIRS provides the capability to capture signals of the eight chemical markers, which can be used to assess the quality and identity of mānuka honeys. This chapter shows that prediction of most chemical markers gave about 60 % accuracy when using standard chemometrics PLS method and that the complexity of the honey matrix affects modelling performance.

Chapter 5
Comparison between NIR non-imaging and hyperspectral imaging systems

5.1. Introduction

NIR non-imaging and hyperspectral imaging (HSI) systems have been employed to capture spectral signals of honey. Both systems show capacity to capture honey signals good enough to predict the eight chemical markers (Chapter 4). The NIR non-imaging system performed better than the NIR HSI system mainly due to several different settings (sensor design, illumination, the spectral range and spectral resolution). Since sensor design and illumination were fixed when scanning honeys, the current chapter can only investigate the effect of difference in the spectral range and resolution between these two systems in capturing honey signals for prediction of eight chemical markers of mānuka honey.

5.2. Research question

This chapter considers whether the poorer performance of HSI relative to non-imaging was due to primarily due to the narrow spectral range of sensor or was due to reduced spectral resolution inside that narrower band. The third influence, that of different sensor design and illumination setting is assumed relatively minor. To test this question, existing non-imaging data were narrowed in spectral range by selecting similar wavelengths as the hyperspectral data and then non-imaging data were compressed five-fold by averaging five adjacent bands to generate a spectral resolution of 5 nm, thus simulating HSI data.

5.3. Materials and method

5.3.1. Materials

Two different datasets were generated from the previously collected raw non-imaging data to compare performance in prediction of chemical markers with the current hyperspectral imaging data of the same samples.

1) A selected and compressed dataset: a set of 235 bands of wavelengths were generated from the non-imaging dataset to match the more limited range and 5 nm spectral resolution of a hyperspectral imaging dataset: by first selecting data between 547 and

1701 nm then by averaging five adjacent 1 nm bands of the raw non-imaging data to reduce spectral resolution to 5 nm, equivalent to hyperspectral data.

2) A compressed dataset contained 430 wavelengths of 5 nm width averaged as above, across the range 352 - 2497 nm.

5.3.2. Method

PLS regression with SNV pre-processing was employed to analyse the two datasets for prediction of eight chemical markers. The iPLS technique with 4-band interval was used during modelling of the selected and compressed data while the iPLS with 30-band interval was employed for the compressed data. The final PLS model was selected based on the lowest RMSEC & RMSECV with a small number of LVs. Outliers were detected and removed in the final model using the plot of Q residuals vs Hotelling T^2.

Before modelling, these datasets were split to calibration and validation sets with the ratio 70:30 using the Kennard-Stone technique. Venetian blind cross-validation was employed for all models. Each dataset was investigated as a global model (covering eight geographic districts) and as region-based models, where each district was modeled using data from only that district. Modelling and pre-processing techniques were operated with PLS toolbox 8.8 (Eigenvector Research, Inc., WA 98831, USA)

5.4. Results

5.4.1. Prediction of chemical markers by non-imaging data selected and compressed to simulate HSI data

5.4.1.1. Selected and compressed non-imaging versus raw non-imaging data

Table 5.1 displays prediction results of eight chemical markers from selected & compressed non-imaging in comparison with raw non-imaging data. At the global level, prediction was better with selected and compressed data than raw non-imaging data. Most chemical markers could be predicted as low or high concentration with accuracy > 60 % as indicated by RPD numbers > 1.5. Lepteridine^{TM} could be predicted with only 56 % accuracy.

When modelling district by district using selected & compressed non-imaging data the situation reversed. Prediction accuracy was poorer for almost all chemical markers compared to raw non-imaging data, in particular, for three districts: Kerikeri, Wairarapa and Whanganui (Table 5.2). Differences are less marked for other districts.

Overall, the global models of selected & compressed non-imaging data showed better performance than those of raw non-imaging data. The high frequency noise due to the imperfect sensor may have been minimised by selection and compression that may have helped generating better prediction of chemical markers. However, this benefit did not show up when modelling at regional level. This suggests that spectral ranges below 547 nm and beyond 1701 nm were essential to generate good predictive performance of chemical makers from region-based models.

Table 5.1. Comparison of prediction results of eight chemical markers between raw non-imaging and selected & compressed non-imaging data at global level

	Raw data (350 - 2500 nm @ 1 nm, 2151 bands)					Selected & compressed data (547 - 1701 nm @ 5 nm, 235 bands)				
PLS models	R^2 (CV)	R^2 (Pred.)	RMSECV	RPD	Bias (CV)	R^2 (CV)	R^2 (Pred.)	RMSECV	RPD	Bias (CV)
DHA	0.59	0.53	646.38	**1.50**	0.00	0.7	0.72	556.68	**1.83**	0.00
MGO	0.47	0.42	83.93	1.47	0.02	0.59	0.56	73.54	**1.59**	0.06
3-PLA	0.59	0.44	325.92	1.40	1.5	0.61	0.61	313.36	**1.56**	0.00
4-HPLA	0.56	0.40	2.41	1.42	0.00	0.63	0.55	2.21	**1.6**	0.00
2'-MAP	0.53	0.42	9.99	1.47	-0.04	0.62	0.56	8.85	**1.58**	-0.01
2-MBA	0.52	0.53	2.69	1.34	0.01	0.58	0.59	2.61	1.46	0.01
Leptosperin	0.54	0.44	200.10	**1.58**	-0.09	0.64	0.67	173.87	**1.69**	0.00
Lepteridine™	0.42	0.37	4.78	1.39	0.02	0.56	0.44	4.18	**1.53**	0.00

Table 5.2. Comparison of prediction results of chemical markers between raw non-imaging and selected & compressed non-imaging data at Kerikeri, Wairarapa and Whanganui districts

Regions	Kerikeri (n = 198)				Wairarapa (n = 240)				Whanganui (n = 442)			
	Raw data		S & C data		Raw data		S & C data		Raw data		S & C data	
PLS models	R^2 (CV)	RPD	R^2 (CV)	RPD	R^2 (CV)	RPD	R^2 (CV)	RPD	R^2 (CV)	RPD	R^2 (CV)	RPD
DHA	0.88	**2.86**	0.86	**2.59**	0.71	**1.81**	0.48	1.29	0.71	**1.76**	0.32	1.16
MGO	0.74	**1.92**	0.52	1.37	0.63	**1.91**	0.46	1.28	0.62	**1.59**	0.37	1.20
3-PLA	0.81	**2.48**	0.71	**1.74**	0.76	**1.97**	0.78	**1.96**	0.65	**1.65**	0.5	1.32
4-HPLA	0.67	**3.77**	0.69	**1.73**	0.61	**1.71**	0.57	1.44	0.64	**1.63**	0.39	1.21
2'-MAP	0.86	**2.60**	0.79	**2.06**	0.71	**1.78**	0.49	1.33	0.61	**1.56**	0.28	1.18
2-MBA	0.79	**2.19**	0.39	1.24	0.77	**2.09**	0.31	1.14	0.68	**1.63**	0.44	1.28
Leptosperin	0.86	**2.68**	0.68	**1.67**	0.66	**1.57**	0.55	1.39	0.49	1.38	0.39	1.22
Lepteridine™	0.72	**1.87**	0.55	1.40	0.63	**1.65**	0.65	**1.59**	0.47	1.39	0.29	1.15

Note: S & C refers to selection of 547-1701 nm and compressed to 5 nm wavebands

5.4.1.2. Selected & compressed non-imaging versus hyperspectral imaging data

Prediction results for all chemical markers from models built from the selected & compressed non-imaging data were compared with those built from HSI data with the same wavelengths 547 - 1701 nm and the same spectral resolution 5 nm. Most global models from selected & compressed non-imaging data showed a similar trend of prediction results to HSI data. DHA, MGO, 3-PLA, 4-HPLA, and Leptosperin could be successfully predicted at high or low level for both datasets. Predictions of 2-MBA and Lepteridine™ were poor for both datasets, but predictions of 2'-MAP obtained from selected & compressed non-imaging data performed better than that from HSI data. This suggests that the difference in sensor design and illumination setting between non-imaging and HSI systems had minor impacts on capture of signals of key chemical markers.

Table 5.3. Comparison of global models of chemical markers obtained from HSI data and from selected & compressed non-imaging data

	HSI data (547 - 1701 nm @ 5 nm, 235 bands)					Selected & compressed non-imaging data (547 - 1701 nm @ 5 nm, 235 bands)				
PLS models	R^2 (CV)	R^2 (Pred.)	RMSECV	RPD	Bias (CV)	R^2 (CV)	R^2 (Pred.)	RMSECV	RPD	Bias (CV)
DHA	0.57	0.55	640.6	**1.52**	-3.07	0.7	0.72	556.7	**1.83**	0.00
MGO	0.57	0.54	71.76	**1.55**	0.27	0.59	0.56	73.54	**1.59**	0.06
3-PLA	0.67	0.6	283.4	**1.66**	-0.01	0.61	0.61	313.4	**1.56**	0.00
4-HPLA	0.61	0.43	2.20	**1.55**	0.00	0.63	0.55	2.21	**1.60**	0.00
2'-MAP	0.54	0.58	9.21	1.47	-0.02	0.62	0.56	8.85	**1.58**	-0.01
2-MBA	0.47	0.42	2.75	1.37	-0.01	0.58	0.59	2.61	1.46	0.01
Leptosperin	0.57	0.57	183.1	**1.53**	-0.04	0.64	0.67	173.9	**1.69**	0.00
Lepteridine™	0.49	0.04	4.37	1.41	0.00	0.56	0.44	4.18	**1.53**	0.00

Predictions of chemical markers were poor for almost all districts using region-based models obtained from either HSI or selected & compressed non-imaging data in the 547 - 1701 nm range (Tables 5.4 a & b). Perhaps there was a lack of key important wavelengths below 547 or beyond 1701 nm range which helped capture good signals of chemical markers for Kerikeri, Wairarapa and Whanganui districts. For other districts, perhaps the presence of spectrally active chemicals from non-*Leptosperin scoparium* floral sources interfered with signals of key chemical compounds, and this effect showed through the limited datasets at these districts.

Table 5.4a. Comparison of prediction of chemical markers between HSI data and selected & compressed non-imaging data at Kerikeri, Wairarapa and Whanganui districts

Districts	Kerikeri (n = 198)				Wairarapa (n = 240)				Whanganui (n = 442)			
	HSI data		S & C data		HSI data		S & C data		HSI data		S & C data	
PLS models	R^2 (CV)	RPD	R^2 (CV)	RPD	R^2 (CV)	RPD	R^2 (CV)	RPD	R^2 (CV)	RPD	R^2 (CV)	RPD
DHA	0.86	**2.49**	0.86	**2.59**	0.32	1.22	0.48	1.29	0.19	1.08	0.32	1.16
MGO	0.62	**1.54**	0.52	1.37	0.53	1.44	0.46	1.28	0.24	1.13	0.37	1.20
3-PLA	0.49	1.20	0.71	**1.74**	0.75	**1.88**	0.78	**1.96**	0.52	1.35	0.5	1.32
4-HPLA	0.51	1.33	0.69	**1.73**	0.63	**1.63**	0.57	1.44	0.4	1.21	0.39	1.21
2'-MAP	0.77	**1.94**	0.79	**2.06**	0.31	1.26	0.49	1.33	0.18	1.09	0.28	1.18
2-MBA	0.46	1.30	0.39	1.24	0.4	1.27	0.31	1.14	0.3	1.15	0.44	1.28
Leptosperin	0.76	**1.86**	0.68	**1.67**	0.4	1.31	0.55	1.39	0.2	1.08	0.39	1.22
Lepteridine ™	0.49	1.23	0.55	1.40	0.38	1.26	0.65	**1.59**	0.24	1.11	0.29	1.15

Note: S & C refers to selection of 547 - 1701 nm and compressed to 5 nm wavebands

Table 5.4b. Comparison of prediction of chemical markers between HSI data and selected & compressed non-imaging data at Hawkes Bay, Waikato and Mobile Unit districts

Districts	Hawkes Bay (n = 202)				Waikato (n = 273)				Mobiles Unit (n = 186)			
	HSI data		S & C data		HSI data		S & C data		HSI data		S & C data	
PLS models	R^2 (CV)	RPD	R^2 (CV)	RPD	R^2 (CV)	RPD	R^2 (CV)	RPD	R^2 (CV)	RPD	R^2 (CV)	RPD
DHA	0.35	1.3	0.56	**1.53**	0.23	1.19	0.17	1.12	0.2	1.01	0.22	0.99
MGO	0.49	1.4	0.49	1.43	0.43	1.43	0.38	1.33	0.47	1.25	0.43	1.17
3-PLA	0.60	**1.6**	0.62	**1.68**	0.68	**1.75**	0.49	1.40	0.5	1.35	0.47	1.30
4-HPLA	0.52	**1.5**	0.59	**1.58**	0.74	**1.92**	0.44	1.35	0.42	1.28	0.16	1.02
2'-MAP	0.30	1.2	0.45	1.36	0.53	1.47	0.36	1.28	0.33	1.13	0.28	1.02
2-MBA	0.32	1.2	0.43	1.35	0.37	1.27	0.25	1.16	0.28	1.15	0.39	1.20
Leptosperin	0.41	1.3	0.53	1.45	0.1	1.03	0.13	0.99	0.13	0.96	0.17	0.97
Lepteridine ™	0.36	1.3	0.36	1.27	0.31	1.14	0.12	0.99	0.4	1.15	0.38	1.10

Note: S & C refers to selection of 547 - 1701 nm and compressed to 5 nm wavebands

5.4.2. Non-imaging data compressed but not selected

Section 5.4.1 reported the effect of simulating HSI data by compressing and selecting spectral data collected by non-imaging instrument. Predictive capacity of models from modified data was similar to that of models built for HSI indicating that spectral range and/or spectral resolution were important, probably more so than other system settings. This next section examines whether spectral range or resolution is the more important by compressing data across the full range available 350 - 2500 nm.

5.4.2.1. Models from raw and compressed non-imaging data

Table 5.5 describes global models of eight chemical markers comparing raw and compressed non-imaging data. In general, global models of compressed non-imaging data gave better prediction than those of the raw data. Most chemical markers were predicted with accuracy above 62 %, except for Lepteridine™. Calibration models of DHA, MGO, 3-PLA, 4-HPLA, 2'-MAP, 2-MBA and Leptosperin gave RPD values above 1.6. It seems that by averaging of five adjacent bands, high frequency noise was also removed at little cost in valuable information. This is encouraging for HSI which compression was seeking to emulate.

Table 5.5. Comparison of prediction of chemical markers obtained from raw non-imaging with from compressed non-imaging data at global level

	Raw data (350 - 2500 nm, 2151 bands)					Compressed data (352 - 2497 nm, 430 bands)				
PLS models	R^2 (CV)	R^2 (Pred.)	RMSECV	RPD	Bias (CV)	R^2 (CV)	R^2 (Pred.)	RMSECV	RPD	Bias (CV)
DHA	0.59	0.53	646.4	**1.50**	0	0.73	0.74	534.2	**1.91**	0.98
MGO	0.47	0.42	83.93	1.47	0.02	0.64	0.63	69.96	**1.67**	0.05
3-PLA	0.59	0.44	325.92	1.40	1.5	0.65	0.61	305.6	**1.6**	0.18
4-HPLA	0.56	0.40	2.40	1.42	0	0.63	0.56	2.19	**1.61**	0.01
2'-MAP	0.53	0.42	9.99	1.47	-0.04	0.65	0.63	8.31	**1.68**	0.09
2-MBA	0.52	0.53	2.68	1.34	0.01	0.66	0.73	2.31	**1.65**	0.01
Leptosperin	0.54	0.44	200.1	**1.58**	-0.09	0.66	0.69	170.8	**1.72**	0.44
Lepteridine™	0.42	0.37	4.78	1.39	0.02	0.54	0.48	4.30	1.48	0.01

The pattern was less clear with region-based models: those from compressed non-imaging data performed no better than those from raw non-imaging data (Table 5.6). For both data types, Kerikeri models performed best. Overall, the results indicate that filtering noise by taking the average of five adjacent bands did not help when modelling at the regional level. The effect of filtering noise becomes less important than the honey matrix effect due to variation of botanical sources when modelling each district separately.

Table 5.6. Comparison of prediction of chemical markers between raw non-imaging and compressed non-imaging data at Kerikeri, Wairarapa and Whanganui districts

Regions	Kerikeri (n = 198)				Wairarapa (n = 240)				Whanganui (n = 442)			
	Raw data		Compressed data		Raw data		Compressed data		Raw data		Compressed data	
PLS models	R^2 (CV)	RPD	R^2 (CV)	RPD	R^2 (CV)	RPD	R^2 (CV)	RPD	R^2 (CV)	RPD	R^2 (CV)	RPD
DHA	0.88	**2.86**	0.87	**2.85**	0.71	**1.81**	0.77	**2.03**	0.71	**1.76**	0.67	**1.61**
MGO	0.74	**1.92**	0.75	**2.06**	0.63	**1.91**	0.53	1.40	0.62	**1.59**	0.63	**1.56**
3-PLA	0.81	**2.48**	0.64	**1.95**	0.76	**1.97**	0.75	**1.93**	0.65	**1.65**	0.59	1.43
4-HPLA	0.67	**3.77**	0.50	1.42	0.61	**1.71**	0.64	**1.65**	0.64	**1.63**	0.49	1.31
2'-MAP	0.86	**2.60**	0.85	**2.60**	0.71	**1.78**	0.65	**1.62**	0.61	**1.56**	0.44	1.25
2-MBA	0.79	**2.19**	0.68	**1.79**	0.77	**2.09**	0.63	**1.61**	0.68	**1.63**	0.56	1.37
Leptosperin	0.86	**2.68**	0.83	**2.48**	0.66	**1.57**	0.55	1.46	0.49	1.38	0.49	1.33
Lepteridine™	0.72	**1.87**	0.60	**1.60**	0.63	**1.65**	0.5	1.40	0.47	1.39	0.41	1.29

5.4.2.2. Compressed non-imaging versus hyperspectral imaging data

Prediction of key chemical markers obtained from compressed non-imaging data (352-2497 nm) were compared with that of HSI data (547 - 1701 nm) (Table 5.7). Both datasets had a similar spectral resolution of 5 nm between two adjacent bands, but different spectral range. Overall, global models obtained from compressed non-imaging data performed better predictions than those built from HSI data, in particular for prediction of 2'-MAP, 2-MBA and Leptosperin. Both datasets predicted well for DHA, MGO, 3-PLA and 4-HPLA with RPD > 1.5 but worse for Lepteridine™ (RPD < 1.5). The results indicate that the difference in spectral range between two datasets is indeed important to prediction of chemical markers at the global level.

Region-based models of compressed non-imaging data also showed better prediction of chemical markers than HSI data for some districts, in particularly Kerikeri and Wairarapa districts (Tables 5.8a & 5.8b). This reconfirmed that wavelengths below 547 nm and beyond 1701 nm were important to prediction of chemical markers at regional level.

Table 5.7. Comparison of global models of chemical markers obtained from HSI data with from compressed non-imaging data

	HSI data (547 - 1701 nm @ 5 nm, 235 bands)					Compressed non-imaging data (352-2497 nm @ 5 nm, 430 bands)				
PLS models	R^2 (CV)	R^2 (Pred.)	RMSECV	RPD	Bias (CV)	R^2 (CV)	R^2 (Pred.)	RMSECV	RPD	Bias (CV)
DHA	0.57	0.55	640.6	**1.52**	-3.07	0.73	0.74	534.2	**1.91**	0.98
MGO	0.57	0.54	71.76	**1.55**	0.27	0.64	0.63	69.96	**1.67**	0.05
3-PLA	0.67	0.6	283.4	**1.66**	-0.01	0.65	0.61	305.6	**1.60**	0.18
4-HPLA	0.61	0.43	2.20	**1.55**	0	0.63	0.56	2.19	**1.61**	0.01
2'-MAP	0.54	0.58	9.21	1.47	-0.02	0.65	0.63	8.31	**1.68**	0.09
2-MBA	0.47	0.42	2.75	1.37	-0.01	0.66	0.73	2.31	**1.65**	0.01
Leptosperin	0.57	0.57	183.1	**1.53**	-0.04	0.66	0.69	170.8	**1.72**	0.42
Lepteridine™	0.49	0.04	4.37	1.41	0.00	0.54	0.48	4.30	1.48	0.01

Table 5.8a. Comparison of prediction of chemical markers between HSI and compressed non-imaging data at Kerikeri, Wairarapa and Whanganui districts

Regions	Kerikeri (n = 198)				Wairarapa (n = 240)				Whanganui (n = 442)			
	HSI data		Compressed data		HSI data		Compressed data		HSI data		Compressed data	
PLS models	R^2 (CV)	RPD	R^2 (CV)	RPD	R^2 (CV)	RPD	R^2 (CV)	RPD	R^2 (CV)	RPD	R^2 (CV)	RPD
DHA	0.86	**2.49**	0.87	**2.85**	0.32	1.22	0.77	**2.03**	0.19	1.08	0.67	**1.61**
MGO	0.62	**1.54**	0.75	**2.06**	0.53	1.44	0.53	1.40	0.24	1.13	0.63	**1.56**
3-PLA	0.49	1.20	0.64	**1.95**	0.75	**1.88**	0.75	**1.93**	0.52	1.35	0.59	1.43
4-HPLA	0.51	1.33	0.50	1.42	0.63	**1.63**	0.64	**1.65**	0.4	1.21	0.49	1.31
2'-MAP	0.77	**1.94**	0.85	**2.60**	0.31	1.26	0.65	**1.62**	0.18	1.09	0.44	1.25
2-MBA	0.46	1.30	0.68	**1.79**	0.4	1.27	0.63	**1.61**	0.3	1.15	0.56	1.37
Leptosperin	0.76	**1.86**	0.83	**2.48**	0.4	1.31	0.55	1.46	0.2	1.08	0.49	1.33
Lepteridine™	0.49	1.23	0.60	**1.60**	0.38	1.26	0.5	1.40	0.24	1.11	0.41	1.29

Table 5.8b. Comparison of prediction of chemical markers between HSI and compressed non-imaging data at Hawkes Bay, Waikato and Mobile Unit districts

Regions	Hawkes Bay (n = 202)				Waikato (n = 273)				Mobiles Unit (n = 186)			
	HSI data		Compressed data		HSI data		Compressed data		HSI data		Compressed data	
PLS models	R^2 (CV)	RPD	R^2 (CV)	RPD	R^2 (CV)	RPD	R^2 (CV)	RPD	R^2 (CV)	RPD	R^2 (CV)	RPD
DHA	0.35	1.3	0.61	**1.64**	0.23	1.19	0.5	1.43	0.2	1.01	0.36	1.23
MGO	0.49	1.4	0.69	**1.77**	0.43	1.43	0.63	**1.71**	0.47	1.25	0.38	1.25
3-PLA	0.60	**1.6**	0.79	**2.31**	0.68	**1.75**	0.7	**1.87**	0.5	1.35	0.38	1.20
4-HPLA	0.52	**1.5**	0.66	**1.76**	0.74	**1.92**	0.55	**1.53**	0.42	1.28	0.29	1.14
2'-MAP	0.30	1.2	0.48	1.38	0.53	1.47	0.6	**1.69**	0.33	1.13	0.33	1.16
2-MBA	0.32	1.2	0.40	1.32	0.37	1.27	0.35	1.21	0.28	1.15	0.33	1.19
Leptosperin	0.41	1.3	0.34	1.22	0.1	1.03	0.15	1.02	0.13	0.96	0.27	1.14
Lepteridine™	0.36	1.3	0.51	1.42	0.31	1.14	0.29	1.12	0.4	1.15	0.37	1.22

5.5. Discussion and conclusion

This chapter reports modifying non-imaging data to match characteristics of hyperspectral imaging to ascertain whether spectral range and/or spectral resolution and/or other system settings have greatest impact. Global models with all eight geographic districts, built from selected & compressed data and from compressed data, gave better prediction results of most chemical markers than did models built from raw non-imaging data and hyperspectral data. This was due to the effect of compression and selection removing noise from the system and enhancing prediction accuracy across the global models generated. Region-based models of modified data (selected & compressed) performed less well than those of raw non-imaging data, but similarly to those of hyperspectral data. These results imply that the spectral range and spectral resolution are important for modelling at regional level.

Differences in sensor design and illumination setting between non-imaging and HSI systems seem to have minor impact. This became apparent when comparing selected & compressed non-imaging and HSI data with the same spectral range and spectral resolution. The finding revealed that the spectral range below 547 and/or beyond 1701 nm is important for prediction of chemical markers. In addition, this study also indicates (through differences between global and region-based models) that prediction of eight chemical markers can be affected by the presence of other chemical compounds from non-*Leptosperin scoparium* nectar that could absorb in the same wavelengths in the spectral range of interest. This obscures signals of chemical markers, in particular for districts containing high variation in botanical sources.

In conclusion, the current chapter shows that the spectral range greatly influences prediction of key chemical markers and spectral resolution may also be important. Future work is suggested examining non-imaging data in the narrow 547 - 1701 nm range having resolution 1 nm in comparison with HSI data with the same spectral range but resolution 5 nm. This would measure the impact of spectral resolution independently from spectral range. In the next chapters, the study investigates alternative techniques to enhance assessment of mānuka honey quality and identity. One way is to use an advanced modelling technique (e.g., deep learning) to minimise the impact of the complex honey matrix (Chapter 9). Another way is to apply different optical methods (e.g., fluorescence) to capture better signals of chemical markers, in particular in the visible range (Chapter 10).

Chapter 6
Prediction of potency and purity mānukaness

6.1. Introduction

Previous chapters showed the capability of NIR methods to capture signals of eight chemical markers in mānuka honey (Chapters 4 & 5). Standard chemometric methods such as PLS regression can model NIR spectral signals to predict concentration of chemical markers, but the findings indicate the regional variation impacts modelling performance. The complexity of the honey matrix due to regional variation of floral sources diminished prediction of chemical markers when all geographic districts were combined (global models). When PLS modelling NIR data at each geographic district (regional models), model performance of each chemical marker was different from district to district. The results suggested that the presence of other chemical compounds from non-*Leptospermum scoparium* nectar could interfere with prediction of chemical markers. This matrix interference, or the complex honey matrix, is difficult to minimise since in nature honey is often mixed from different nectar sources. Quality assessment of mānuka honey based on chemical markers can be applicable but challenging if the honey matrix changes every year.

To search for an alternative approach to assess honey quality and purity of mānuka honey, the current study has introduced two new quality measurement terms, so-called potency mānukaness based on measurement of UMF^{TM} score, and purity mānukaness based on verification of botanical origin from MPI criteria (MPI, 2017b; UMFHA, 2022). The research question was: could NIR methods can measure UMF^{TM} score and verify the botanical origin of mānuka honeys? Two honey quality attributes were assessed as: 1) a continuous variable (so-called potency) based on UMF^{TM} score that reflects the concentration of key chemical markers; and 2) a discrete scale (so-called purity) that defines boundaries among concentration of chemical markers defining the floral sources. The potency allows quality assessment of honey even if it comes mostly from the same floral source while the purity allows the segmentation of honey among floral sources. Honey samples from eight different geographic districts were utilized to provide variability in botanical sources. Vis-NIR spectra in the 350-2500 nm range (non-imaging system) and the 547 - 1701 nm range (hyperspectral imaging system) were collected non-invasively from the samples. Models for predicting the continuous

variable and a discrete category from the spectra were investigated including methods capable of handling non-linearities inherent in the interaction between light and honey.

6.2. Mānukaness terminology

The UMF^{TM} rating system and MPI criteria are currently used to evaluate mānuka honey quality and identity (purity), respectively (MPI, 2017b; UMFHA, 2021). The UMF^{TM} rating system measures the quality of mānuka honeys based mainly on two key bio-actives methylglyoxal (MGO) and Leptosperin. MGO mainly represents the antibacterial properties while Leptosperin broadly corresponds to the anti-inflammatory characteristic. According to the UMF^{TM} rating system, MGO and Leptosperin concentrations must exceed 83 mg/kg and 100 mg/kg respectively to signify genuine mānuka honey originated from New Zealand with UMF^{TM} 5+ (UMFHA, 2021). Purity of mānuka honey is indicated by concentrations of 2'-MAP, 2-MBA, 4-HPLA, 3-PLA and the pollen DNA test for *L. scoparium* (MPI, 2017b).

"Mānukaness" is introduced in this study as a spectral quality mark for estimating mānuka honey quality and purity based on spectral analysis. Assessment of mānukaness reflects both the quality and purity of mānuka honey measured from the current UMF^{TM} rating system and MPI criteria. The quality and purity of mānuka honey are spectrally predicted as so-called potency and purity mānukaness, respectively. Chemometric methods (regression and classification) were applied to spectral data to generate predictive tools. The regression approach was applied to spectral data to predict UMF^{TM} scores as a proxy for potency mānukaness. Meanwhile, the classification approach was employed to classify between mono-, multi-, and non-mānuka honeys as a proxy measure of purity mānukaness. Potency and purity mānukaness predictions given together could allow honey companies degrees of freedom in decision-making. Prediction of potency and purity mānukaness from spectral data are both indirect measurements since spectral signals contain footprints of chemical markers (MGO & Leptosperin) for UMF^{TM} values and (2'-MAP, 2-MBA, 3-PLA & 4-HPLA) for mānuka honey identity. Thus, the mānukaness prediction could contain two systematic errors from imperfect chemical laboratory data and imperfect spectral modelling.

6.3. Materials and methods

6.3.1. Materials

The NIR non-imaging data (350 - 2500 nm) of 1451 honey samples and the NIR hyperspectral imaging (547 - 1701 nm) of 1656 honey samples (Chapter 4), both collected from eight districts of the North Island of New Zealand were investigated to predict potency and purity mānukaness.

To evaluate how well potency and purity mānukaness could be predicted from two datasets (non-imaging and hyperspectral imaging), the laboratory data of the same 1656-sample dataset was also computed for potency and purity mānukaness based on chemical profile that was provided by Comvita® (laboratory data are shown in the Appendix, Section 1).

6.3.2. Statistical measurements of mānukaness

Regression techniques were used to analyse the spectral data of honey samples, including partial least squares (PLS) regression and support vector machine regression (SVR); and classification tools employed included partial least squares discriminant analysis (PLSDA) & support vector machine discriminant analysis (SVMDA). All chemometric methods were run with PLS toolbox 8.8 (Eigenvector Research, Inc., WA 98831, USA), except the SVR model which was run with Statistics and Machine Learning toolbox. Both toolboxes were run in MATLAB R2021a (The MathWorks, Inc., Massachusetts 01760, USA).

6.3.2.1. Estimation of UMF™ scores

Linear PLS and SVR regression methods were employed to predict UMF™ scores from spectral data. For modelling, the spectral data of eight districts were divided into calibration and validation sets using the Kennard-Stone technique. This technique was applied to split the sample set 70:30 calibration to validation samples. The PLS and SVR models were optimised using the 10-fold leave-one-out venetian blind cross-validation procedure. Ten sub-models were formed during one-fold of calibration dataset leave-out. The output of a calibration model was obtained by the average of all sub-models' prediction results. The calibration model performance was tested on validation data and goodness-of-fit was evaluated.

PLS uses latent variables to maximise the covariance between the spectral data and the response (described more fully in chapter 4). Analogous to PLS, support vector machine regression (SVR) operates on a classification problem by employing a support vector machine algorithm to return continuous-valued results. With SVR, an ϵ-tube insensitive region is

formulated around a regression line, and support vectors of the training dataset lie outside the boundary of the ϵ-tube. SVR with linear kernel worked better than radial basic function (rbf) kernel for prediction of UMF^{TM} scores. A linear kernel was selected which used a loss function $min_w \frac{1}{2}\|w\|^2$ to minimise the prediction error. The box constraint or regularization C value in the linear SVR model was searched in the 10 - 150 value range with an automatic selection default of Epsilon (ϵ) and standardized data. A larger C significantly minimises prediction error, but the chance of over-estimation rises. Therefore, an optimised C value was chosen in the model in which the prediction correlation R^2 was high with the lowest prediction error (Awad & Khanna, 2015; Saeys, 2018). RPD value was calculated for evaluation of model performance of both PLS and SVR models.

6.3.2.2. Classification of MPI honey classes

Classification into three MPI classes (mono-mānuka, multi-mānuka and non-mānuka honeys) was performed by PLSDA and SVM (rbf) models. The linear PLSDA method transforms spectral data into a simple matrix with few latent variables. This way, the covariance between the spectral data and dummy matrix with zeros for non-mānuka and ones for mānuka was maximised (Yang et al., 2020). Ten-fold leave-one-out venetian blind cross-validation was applied. Pre-processing techniques (SNV, MSC, normalised, first and second derivatives) and their combinations were examined which rescale the raw spectra into dimensionless data prior to modelling. The 30-interval iPLS and VIP (automatic) techniques were applied to the spectral data to select dominant spectral bands. The best classification model was selected based on RMSECV and the classification overall accuracy (Lu et al., 2020; Saeys et al., 2019; Xiaobo et al., 2010).

As with PLSDA, SVMDA (rbf) was applied for classifying mono-, multi- and non-mānuka honeys. SVMDA often works with a binary classification for two classes which separate them by support vectors. For multi-classes, the pairwise "one versus one" classification approach is driven. SVMDA (rbf) with the Gaussian function $G(x_i, x_j) = e^{(-\|x_i - x_j\|^2)}$ transforms the input data into the high dimensional kernel space for modelling the honey classes. The rbf kernel was defined by Cost (C) and gamma (γ) hyperparameters which determine the number of support vectors needed. The support vectors create the kernel margin or hyperplane which separate the target class from another by minimizing the misclassification error. A larger kernel margin or more support vectors mean a target class would be discriminated more easily, but it also drives over-estimation and low classification accuracy

(Truong et al., 2021). Optimising kernel hyperparameters (C, γ) is necessary to enhance classification accuracy with a small numbers of support vectors. In PLS toolbox 8.8, a set of default values of the 11-C parameter ranging 10^{-3} - 10^{2} and $15-\gamma$ values ranging 10^{-6} - 10^{1} were run to optimize the kernel function. In this SVM (rbf) modelling, PCA-based mode was kept off since it did not help to improve the classification performance. The best SVM model was automatically selected from PLS toolbox that gave the highest average classification overall accuracy and the lowest classification error (Lu et al., 2020; Saeys et al., 2019; Xiaobo et al., 2010).

6.3.2.3. Mānukaness prediction

Potency and purity mānukaness were generated from the linear PLS prediction of UMF^{TM} score and classification of three MPI classes respectively following the equation,

$$\mathbf{y} = \mathbf{X\beta}+\mathbf{e}$$ (Nilsson et al., 1997; Pullanagari et al., 2021)

Where **β** is the vector of PLS regression coefficients of each spectral variable, **X** is the input spectral data, **y** is the vector of predicted values and **e** is the vector of error values (Pullanagari et al., 2021).

Potency mānukaness was calculated from prediction of UMF^{TM} which represents the relationship between the predictive UMF^{TM} value and the true UMF^{TM} reference for the whole population. Meanwhile, purity mānukaness was generated from PLS classification of mono-, multi- and non-mānuka honeys that reflects the correlation between the classification ratio of the predictive and the true classes over the whole population. The predictive values are expected to equal the true reference values for which the coefficient of determination r^2 is close to 1 (Aleixandre-Tudo et al., 2018).

6.4. Results and discussion

Section 1. NIR non-imaging data

6.4.1. Prediction of non-imaging potency mānukaness

6.4.1.1. Regression results

Spectral data (350 - 2500 nm) were modelled by PLS regression to estimate UMF^{TM} scores. A 30-interval iPLS technique first applied on a full range to discard unnecessary bands. Later, only the 370 - 1700 nm spectral range was selected for modelling since below 370 and beyond 1700 nm contained noise and irrelevant information. The latter PLS model (370 - 1700 nm) used 4 interval-iPLS and automatic VIP to optimise dominant spectral bands for UMF^{TM}

prediction. A raw 1451-honey dataset with UMF™ score profile between 0 and 20 quantified at harvest time (UMF™ 0-month) and after 10-month storage (UMF™ 10-month) were observed. A linear PLS model against UMF™ 10-month gave a correlation coefficient R^2 (0.74) similar to a model against UMF™ 0-month (R^2 = 0.72). Usage of UMF™ 10-month for honeys scanned a year after harvest for PLS modelling was more compatible with the experiment time. Thus, a PLS model of UMF™ 10-month was chosen.

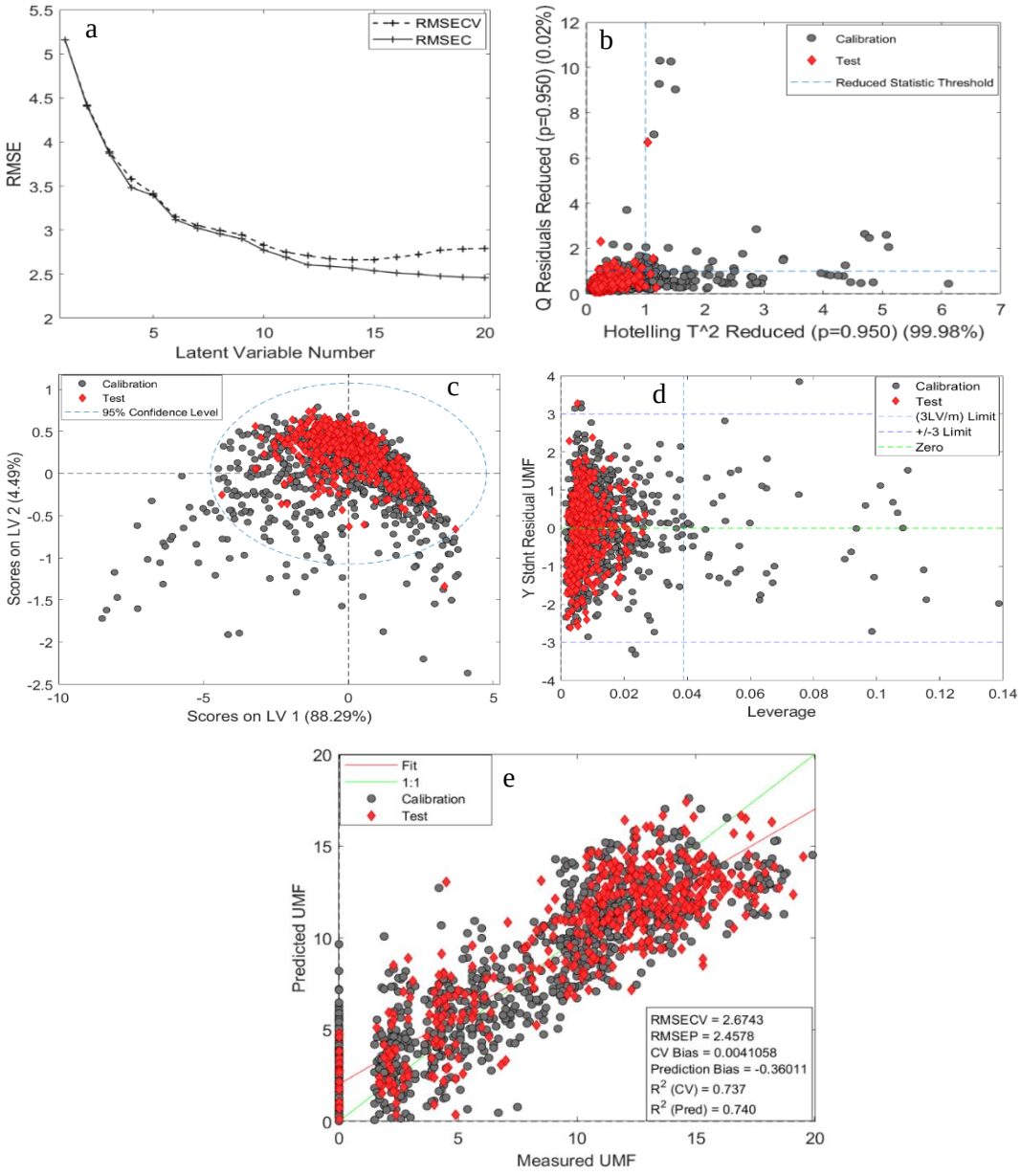

Figure 6.1. *Output of non-imaging PLS model with SNV pre-processing for UMF™ score estimation with calibration set (black circle) and test set (red diamond): a) Latent variable plot versus RMSE (calibration: solid line, cross-validation: dash line & test: solid line with stars) b) Q residuals & Hotelling T^2 plot, c) PLS score plot, d) Leverage plot and e) regression plot between measured and estimated UMF™ scores*

Figure 6.1 shows the regression output of a final PLS model for prediction of UMF^{TM} scores. SNV pre-processing was applied to the spectral data and thirteen latent variables were selected which gave the first lowest root mean squared error of cross-validation (RMSECV) & calibration (RMSEC) values. The PLS model achieved an R^2 (CV) of 0.71 and R^2 (Pred.) of 0.72 with RMSECV and RMSEP values of 2.83 and 2.55, respectively. The residual predictive deviation (RPD) for this PLS calibration model was 1.84. In this model, the UMF^{TM} estimation (Figure 6.1e) contained some negative values and some over-predictive points at UMF^{TM} reference 0. This hinted at some bias or constraints that could not be explained by the model.

As with the results of the PLS regression model, SVR was trained to predict the UMF^{TM} values over a full spectral range (350 - 2500 nm). A trained SVR model obtained an R^2 of 0.66 and RMSE 2.87 revealing a poorer prediction accuracy than that of PLR, but SVR predictive capability was slightly higher with RPD 1.86. The SVR model when tested on the validation set gave R^2 0.74, and RMSE (validation) 2.82 that was higher than in the PLS model (RMSEP 2.55).

6.4.1.2. Variable selection from the regression model

A total of 204 spectral variables were used in the final PLS model after applying iPLS and VIP (auto) techniques. The PLS loading plot shows 21 important features giving high loading weight values (Figure 6.2). Two influential spectral regions can be discerned. The first region covers spectral features below 700 nm that could be relevant to the absorptions of DHA, MGO and some flavonoids. Another important region between 991 and 1373 nm could correspond to footprints of local water molecules and carbohydrate groups. Table 6.1 indicates dominant spectral bands which could link to some specific compounds. Wavelengths around 1000 nm correspond to the 2nd overtone O-H stretching band while bands in 1342 - 1374 nm range indicate the 1st overtone combination of C-H stretching of -CH_3 groups. By contrast, bands near 1155 - 1245 nm reflect the presence of the 2nd overtone C-H stretching of -CH_3, -CH_2 & -CH groups (Xiaobo et al., 2010).

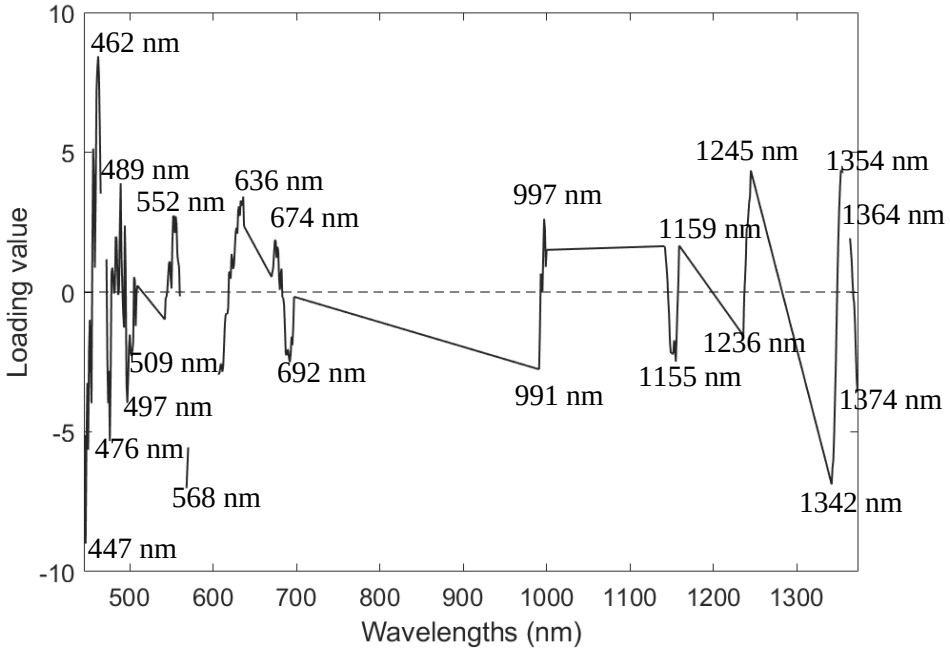

Figure 6.2. *Important spectral features extracted from non-imaging PLS regression loading plot for UMF™ prediction*

Table 6.1. The important spectral features and correspondent chemical footprints defined from the non-imaging PLS-UMF™ prediction

Spectral regions (nm)	Identified wavelengths (nm)	Relevant chemical footprints	Relevant compounds discussed
Below 700	447, 462	MGO	MGO
	476, 489, 497, 509	DHA	DHA
	552	flavonoids	quercetin
	607, 636, 674, 692 & 697	colour pigments	chlorophyl
991-1373	991, 997, 1000	2nd overtone O-H	H_2O
	1342, 1354, 1364 & 1374	1st overtone C-H combination of $-CH_3$	MGO, DHA & other carbohydrate groups
	1155, 1159, 1236 & 1245	2nd overtone C-H of $-CH_3$, $-CH_2$ & -CH	MGO, DHA & other carbohydrate groups

Note: MGO: methylglyoxal; DHA: dihydroxyacetone

6.4.1.3. Generalisation of potency mānukaness

Potency mānukaness was generalised from the linear PLS regression of UMF^{TM} prediction. Figure 6.3 describes potency mānukaness of eight different geographic districts with a correlation r^2 of 0.74. Whanganui district possessed the highest UMF^{TM} values with a high prediction value of potency mānukaness compared to that obtained from the remaining districts. There were some samples from districts Waikato, Mobile Units and JV Kaimanawa with UMF^{TM} 0 scores for which the model overestimated potency mānukaness, implying either a weakness in the predictive ability of the model, or noise in the parent data.

Compared to the lab-based model of potency mānukaness, the predictability of the NIR non-imaging model gave 22 percentage points lower accuracy. A large variation of potency predictive values was observed in the output of non-imaging potency mānukaness, which was not seen from that of the lab-based data. However, NIR non-imaging could still pick up information of chemical markers associated to potency mānukaness.

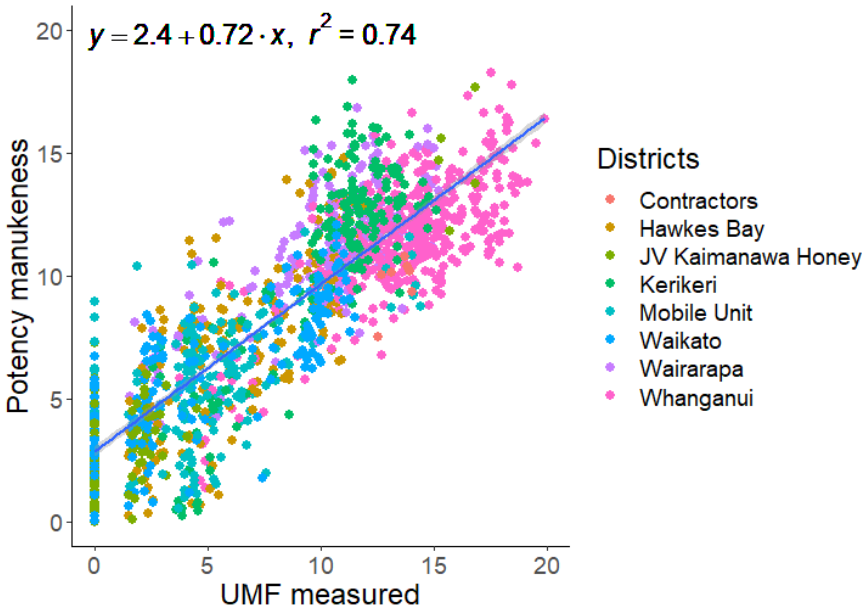

Figure 6.3. *Linear regression between non-imaging potency mānukaness and UMF^{TM} measured of the 1451-honey samples of eight geographic districts combined*

6.4.2. Prediction of non-imaging purity mānukaness

6.4.2.1. Classification results

Two multivariate linear PLSDA and non-linear SVMDA (rbf) classifiers were employed to analyse the full Vis-NIR spectral data range of 1451 honey samples. The three MPI honey classes were chosen as classification categories. The cross-validated classification models of PLSDA and SVMDA produced an accuracy of ≈ 82 %. Table 6.2 shows the prediction results of both classifiers on the 450-sample validation set which gave 88 - 89 % overall accuracy. SVMDA classification of multi-mānuka and non-mānuka obtained 73.7 % and 65.8 %, respectively which were higher by 3 - 5 % than those of PLSDA (69.4 %, 62.8 %). However, PLSDA classification of the highly valuable mono-mānuka honeys resulted in above 97 % accuracy which was better than that of SVMDA at 94.9 % accuracy. Figure 6.4 illustrates the receiver operating characteristic (ROC) curves from the output of the PLSDA model on the validation set. The sensitivity and specificity of classifying mono-mānuka, multi-mānuka and non-mānuka honeys ranged 0.8 - 0.95. Classification of the three honey classes was highly effective with the area under the curve of ROC above 90 %. Additionally, an extra PLSDA model was built on a 397-sample calibration set containing only multi- and non-mānuka honeys. This PLSDA model was tested on a 169 sample-validation set which performed with 82.5 % (multi-mānuka) and 62.1 % (non-mānuka) accuracies. Relative to a PLS model with three classes, the PLS sub-model increased classification accuracy by 17 percentage points for multi-mānuka honeys but did not improve accuracy for non-mānuka honeys. By contrast, the additional SVMDA model built showed an improvement in accuracy for both multi-mānuka (81.1 %) and non-mānuka (65.5 %).

Table 6.2. Classification performance on the test dataset for linear PLSDA and non-linear SVMDA models

Test data (n = 450)	PLSDA (CV: 82.2 %)	SVMDA (rbf) (CV: 82.2 %)
Mono-mānuka	97.44 %	94.89 %
Multi-mānuka	65.82 %	72.73 %
Non-mānuka	62.79 %	69.44 %
Kapa	0.73	0.74
Prediction accuracy	88.3 %	89.43 %

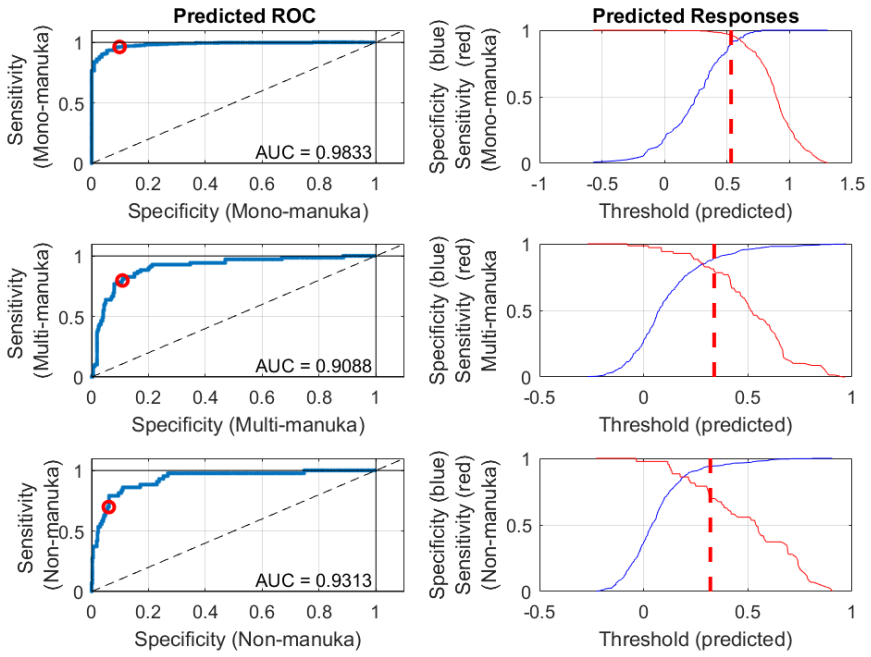

Figure 6.4. *Receiver operating characteristic (ROC) curves from non-imaging PLSDA model on the test set*

6.4.2.2. Variable selection from the classification model

The PLSDA model was used to select important wavelengths for classification of mono-, multi-, and non-mānuka honeys. A total of 360 dominant bands were contained in a final model after employing 30-interval iPLS and VIP (auto). The PLS loading plot specified the important spectral features which possessed high loading values (Table 6.3). Four important spectral regions were identified such as below 600 nm and around 830 - 860 nm, 1000 - 1400 nm and 1850 - 1873 nm. Table 6.3 indicates specific features which could link to specific compounds. The assignment of spectral features to chemical groups is similar to that discussed above for regression models. Based on these important spectral bands, it seems apparent that phytochemicals, water, and carbohydrates in the honey matrix contribute strongly when classifying mono-, multi-, and non-mānuka honeys.

Table 6.3. The important spectral features and corresponding chemical footprints were identified from the non-imaging PLSDA classification of mono-mānuka, multi-mānuka and non-mānuka honeys

Spectral regions (nm)	Identified wavelengths (nm)			Relevant chemical footprints	Discussed compounds
	Mono-mānuka	Multi-mānuka	Non-mānuka		
Below 600	413, 417, 438, 441	412, 417, 437, 444	412, 417, 433, 455	MGO	MGO
	470, 499	471, 499	475, 494	DHA	DHA
	589	564	589	flavonoids	Unknown
830-860	859	859	859	3rd overtone C-H	carbohydrate groups
	1000	1006	1007	2nd overtone O-H	H_2O
	1160	1166	1160	2nd overtone C-H	carbohydrate groups
1000-1400	1309	1295	1309	1st overtone C-H combination	MGO, DHA, carbohydrate groups
	1340, 1367, 1398	1349, 1364, 1382	1340, 1370, 1394	1st overtone C-H combination	MGO, DHA, carbohydrate groups
1873-1879	1879	1872	1873	2nd overtone C=O stretching + 1st overtone OH combination	C=O (DHA, MGO) + water molecule

6.4.2.3. Generalisation of purity mānukaness

Purity mānukaness was generalised from classification of non-mānuka, multi-mānuka and non-mānuka honeys. The PLSDA and SVMDA (rbf) models both classified three MPI classes with high accuracy (Kappa 0.73 - 0.74). Linear PLSDA modelling was chosen to calculate purity mānukaness. Three classes of MPI were valued 1 for non-mānuka, 2 for multi-mānuka and 3 for mono-mānuka as the measured weight value. Purity mānukaness was estimated by multiplying the regression weight with the whole spectral dataset. Figure 6.5 illustrates violin distribution plots of estimated purity mānukaness of mono-mānuka, multi-mānuka and non-mānuka honeys. The ‘box’ inside of each ‘violin’ shape represents 75 % of the population which confirms that there is no overlap between these boxes. However, the ‘violin’ distribution tail between high purity mānuka with the other two types are a little overlain. This was also found between low purity mānuka with the other classes. Overall, the most of overlapping takes place at the boundaries of the classes.

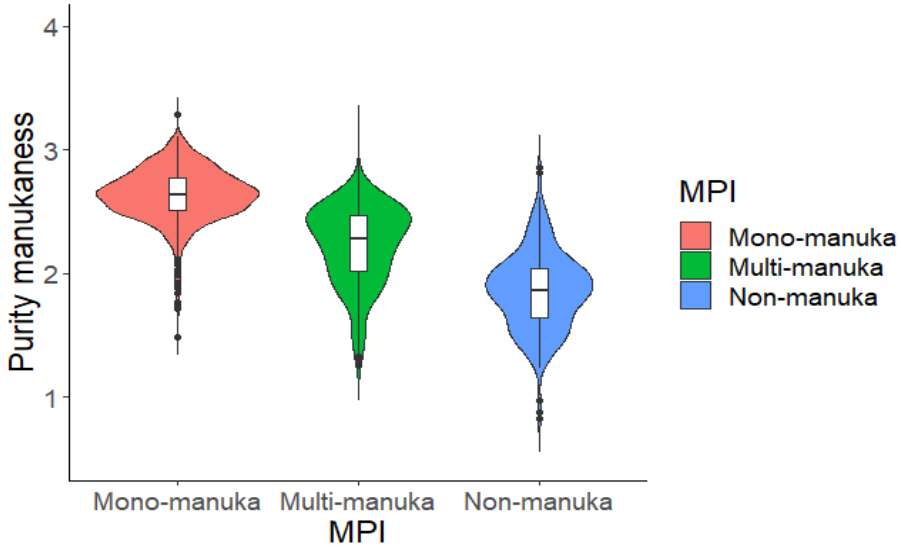

Figure 6.5. *Violin distribution plot of purity mānukaness estimated from a non-imaging PLSDA model against reference mono-mānuka, multi-mānuka and non-mānuka honeys*

6.4.3. Non-imaging potency and purity mānukaness plot

The relationship of potency and purity mānukaness obtained from the NIR non-imaging spectral data is shown in Figure 6.6 with r^2 = 0.77, while potency and purity plot from lab-based data gave r^2 0.85 (the results was put in the Appendices). This implies that NIR non-imaging could estimate the quality and identity of mono-mānuka honeys based on the spectral signals of chemical markers. Figure 6.6a displays all samples of eight districts scattered around the regression line between NIR-based potency and purity, with little or no regional effect apparent. However, honey samples of each region were more scattered around the regression line (Figure 6.6b).

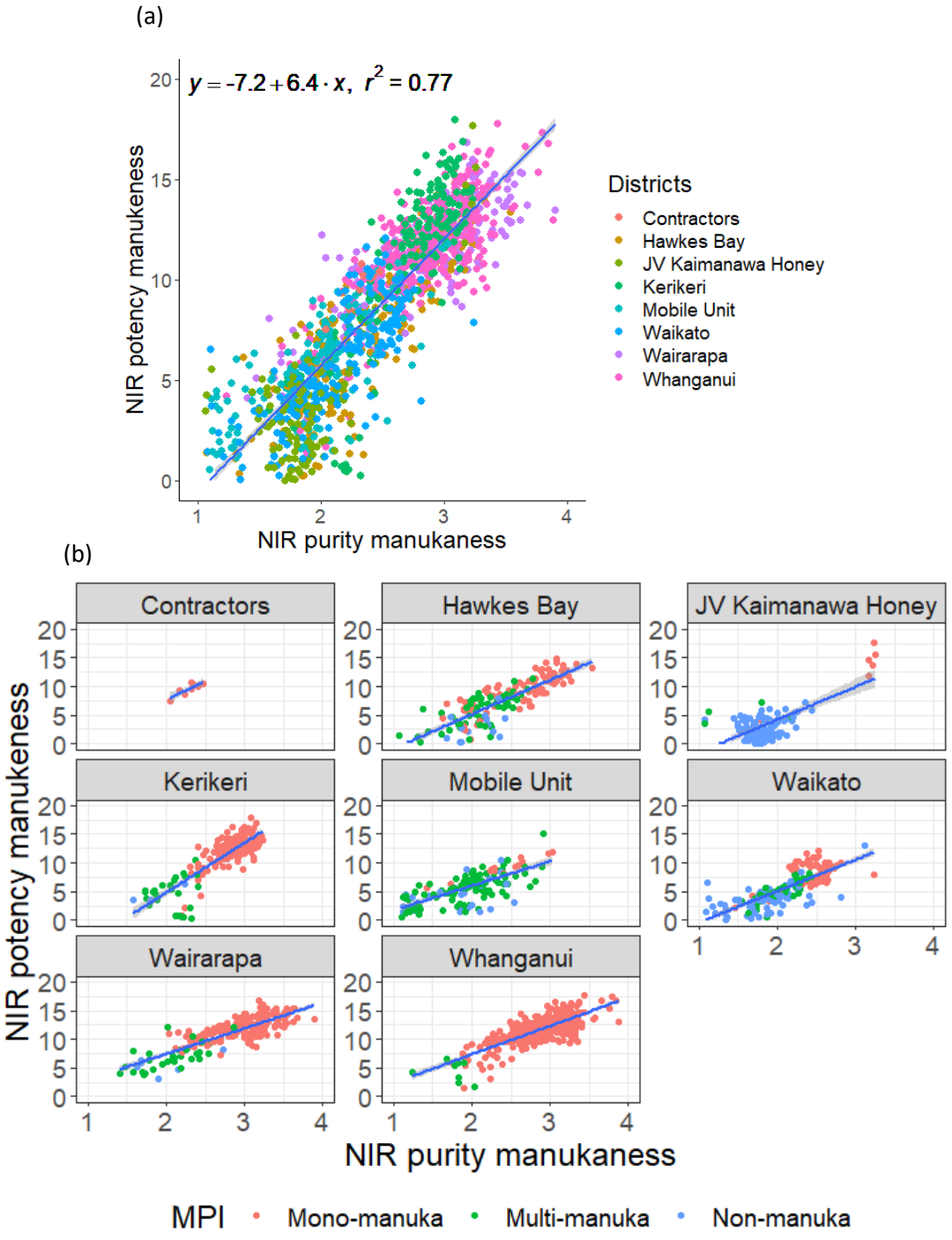

Figure 6.6. *NIR non-imaging potency and purity mānukaness plot for all districts (a) and for each district (b) grouping by three MPI honey classes. Note the blue line plotted is identical for each despite the changing axes and is the model line*

6.4.4. Discussion

Spectral signals in the 350 - 2500 nm Vis-NIR range were captured using a non-imaging sensor from 1451 honey samples spanning mono-mānuka, multi-mānuka and non-mānuka honeys from eight districts of the North Island. The mean absorbance spectra of honeys at each district were quite different in the 500 - 1500 nm range (Figure 4.2 C). Meanwhile, spectra of mono-mānuka, multi-mānuka and non-mānuka honeys were slightly different in 500 - 1500 nm, but more separable in the middle infrared 1500 - 2500 nm (Figure 4.2 D).

Several studies have sought to determine botanical origin of honeys using NIR methods. Molecular vibration of O-H, C-H and C-O bonds are commonly identified for differentiating a specific honey in the NIR range. For example, authentication of mono-floral and multi-floral honeys in the 4200 and 5200 cm^{-1} (1923 – 2381 nm) range was reported mostly due to C-O and C-C stretching regions of saccharides (Ruoff, Luginbühl, Bogdanov, Bosset, Estermann, et al., 2006). Corsican and non-Corsican honeys were separated in the 1100 - 2498 nm range based on six important chemical bonds, which were relevant to hydroxyl groups (1^{st} overtone O-H stretching, the combinations O-H stretching and O-H deformation (1935 nm)), carbohydrate groups (1^{st} overtone -CH_2 & combination of -CH_2 stretching and deformation (1460 nm), combination of C-H stretching (2095 & 2280 nm), C-O stretching) and the absorptions of fructose and glucose (Woodcock et al., 2009). Similarly, Yang et al. (2020) also classified raw mānuka honeys from syrup-blended mānuka honeys and corn syrup using 1300 - 1600 nm (first overtone of O-H stretching) and 1600-1800 nm (carbohydrate vibration). The absorption of water molecules (1300 - 1600 nm) played an important role in differentiation of mānuka honeys and adulterated mānuka honeys (Yang et al., 2020). This was also found in the study of Bazar et al. (2016) for characterising raw honey and syrup-adulterated honeys (Bazar et al., 2016). However, the network of water molecules in honey matrices of mono-mānuka, multi-mānuka and non-mānuka honeys in the current study might differ from that of mono-mānuka, syrup-blended mānuka honeys and corn syrup in the study of Yang et al. (2020).

According to Stephens et al. (2006), UMF^{TM} activity dropped when mono-mānuka honeys were blended with other honeys collected from different nectar source (e.g., to become multi-mānuka honeys). Non-mānuka honeys generally had very low UMF^{TM} score < 2.5. Differences in chemical marker profiles, polyphenolic contents and free water molecules in honey matrix could also impact on the estimation of UMF^{TM} scores. Therefore, the absorption of chemical markers of mānuka honeys that presents in spectral ranges (440 - 700 nm) & (990-1400 nm) could potentially contribute to the UMF^{TM} prediction. Firstly, DHA, MGO and

Leptosperin are discussed since they are present in high amounts in mono-mānuka honeys, and they are primary compounds contributing to UMF^{TM} activity. DHA is a 3C carbonyl compound, which gradually converts to MGO by dehydration in the honey matrix (Grainger et al., 2016a). DHA potentially reacts with amino acids in the presence of water to form brown pigments during Maillard reactions (Grainger et al., 2016b). According to Nguyen et al. (2003), DHA-induced brown pigments absorb in both UV at 340 nm and Vis in 460 - 520 nm (Nguyen & Kochevar, 2003). Thus, it is hypothesised that the important wavelengths (462, 476, 489, 497, 509 nm) characterised from the PLS loading plot near 460 - 520 nm could indirectly reflect the presence of DHA. The absorption of free MGO was strongly discerned in 350 - 480 nm range with a broad peak in 410 - 450 nm. This work also assumed that wavelength 447 nm could be relevant to footprints of MGO compound in mānuka honeys. When honeys are exposed to exciting radiant energy at below 420 nm, MGO could experience photolysis to form CH_3CO + HCO radicals (Staffelbach et al., 1995). The presence of these free radical compounds containing -CH_3, and CO groups could contribute the stretching of 1st & 2nd overtone combination C-H stretching of -CH_3 (Table 6.1). Besides, several side reactions of MGO during photolysis might happen in the honey matrix (Staffelbach et al., 1995). Leptosperin is another chemical marker to identify mānuka honeys which also contributes UMF^{TM} score (Bong et al., 2016; Bong et al., 2017; Johnston et al., 2018; Stephens et al., 2017). According to Bong et al. (2017), Leptosperin strongly absorbs in UV range (maximum at 270 nm) which was out of range of this work in 350 - 2500 range (Bong et al., 2017), but sub-chemical bonds of Leptosperin (-CH_3, O-H and CO) might be captured in the NIR range.

Mānuka honeys generally contain significant amounts of phenolic compound (e.g., 250.18 ± 14.39 µg/g (Yiuchung et al., 2019)) characteristic of botanical origin (Oelschlaegel et al., 2012; Stephens et al., 2010). Phenolic acids and flavonoids are secondary plant metabolites present in honeys which may also play key roles in UMF^{TM} activity (Alqarni et al., 2016; Johnston et al., 2018; Stephens et al., 2010; Wang, 2011). According to Bogdanov et al. (2004), phenolic compounds derived from propolis also occur in mono-floral honeys. This might have some impact on differences among mono-floral honeys (Bogdanov et al., 2004). Phenolic acids typically absorb light in the UV range rather than Vis-NIR region (Aleixandre-Tudo et al., 2018; Ang et al., 2013; Danila et al., 2018; Wang, 2011). Flavonoids are also essential compounds contributing a variety of UMF^{TM} activity among honeys. Mānuka honeys are known to contain several flavonoids such as hesperitin, naringin, hesperidin, quercitrin, myricetin, morin, luteolin + quercetin, naringenin, apigenin, kaempferol, chrysin, galangin, and tangeretin (Yiuchung et al., 2019). Almost all these flavonoids absorb in two specific ranges

(300 - 400 nm) and (240 - 300 nm) corresponding to cinnamoyl system and benzoyl ring, respectively (Wang et al., 2020). Quercetin is exceptional, absorbing maximally at 515 - 550 nm with a shoulder around 440 - 450 nm in water at pH 2.5/5.5 (Amorati et al., 2017). Thus, it is hypothesised that the waveband near 552 nm (515 - 550 nm) relates to quercetin.

Honeys are different in colour that could reflect their quality (Negueruela & Perez-Arquillue, 2000; Stephens, 2006). Chlorophyl, carotenoids, xanthophylls and anthocyanins are colour pigments found in honeys which might differ between honeys. In mono-mānuka honeys, these pigments are derived entirely from *Leptospermum scoparium* nectar (Alqarni et al., 2016; Danila et al., 2018; Negueruela & Perez-Arquillue, 2000). Carotenoids and xanthophylls absorb in the range 400 - 500 nm while anthocyanins absorb in the 520 - 540 nm range (Aleixandre-Tudo et al., 2018; Nagao et al., 2015). Wavelengths near 400 - 540 nm might also be relevant to carotenoids, xanthophylls and anthocyanins. Chlorophyl a & b absorb light energy in the blue (428 - 453nm) and red regions (661 - 672 nm) (Pedrós et al., 2008). It is suggested that important features (636 & 674 nm) characterised in this study could link to the second peak of chlorophyl a & b. Other remaining bands in Vis range might be relevant to some unknown chromophores in honeys. However, further research is suggested to test hypotheses.

The 991 - 1374 nm region reflects absorption of water molecules and carbohydrate characteristics (Xiaobo et al., 2010; Yang et al., 2020). Absorption by water molecules at local peaks at 991 and 997 nm may also indicate differences of UMF^{TM} activity in honeys. The vibration of 1st overtone C-H combination (1342, 1354, 1364 and 1374 nm) and 2nd overtone C-H stretching (1155, 1159, 1236 & 1245 nm) of carbon groups -CH , -CH_2 and – CH_3 correspond to differences in quality and identity among honey samples (Xiaobo et al., 2010). Overall, the contribution of free water molecules and carbon characteristics in the honey matrix likely plays an important role in the estimation of UMF^{TM} scores.

The prediction of potency mānukaness mainly relates to the UMF^{TM} activity. The quality of honeys in terms of UMF^{TM} activity differs between geographic districts (Figure 6.3). This was in line with the study of Stephens (2006) who stated that the UMF^{TM} activity depends on geographical factors within and between regions. Varieties of *Leptospermum scoparium* and the abundance of other florals both differ between districts (Stephens, 2006). The estimation of potency mānukaness in Vis-NIR range obtained 74 % accuracy, good enough to distinguish between high and low UMF^{TM} scores among honey frames before lumped extraction. Validation of the potency model performance by independent datasets (unpublished results) showed that the prediction of potency mānukaness (Figure 6.3) could overestimate true UMF^{TM}

values by 2.4 units for samples with UMF^{TM} below 7.5, and underestimate true UMF^{TM} values by 2.4 for samples with UMF^{TM} above 15. Between 2.5 and 15 UMF^{TM}, the model performed well. The poorer prediction performance on validation data could be due to a paucity of samples with UMF^{TM} above 15 in the raw dataset, and not necessarily fundamental to the method. Further research would suggest adding more samples in this range could improve model performance. In addition, a complex model is also suggested to confront the regional variation which further improves the UMF^{TM} prediction.

PLSDA and SVMDA (rbf) classifiers gave overall accuracies of 82 % (cross-validation) and 88 - 89 % (prediction) (Table 6.2). These results were compatible with the study of Noviyanto & Abdulla (2020), who used SVMDA to classify clover, mānuka blend and mono-mānuka honeys with 75 - 99 % accuracy. However, these authors used commercial mānuka honey products, which were quite different from the single composite honey samples in this current study which were recently extracted from honey frames and pooled from known apiaries.

Classification results showed mono-mānuka honeys significantly discriminated with 94-97 % accuracy which was 20 % higher than those of multi-mānuka and non-mānuka honeys (62 - 72 %) (Table 6.2). This could be partly due to a large dataset of this group. The investigation of discrimination between multi-mānuka and non-mānuka honeys showed that multi-mānuka was classified with 78 - 89 % accuracy from non-mānuka with 65 - 75 % accuracy. Ruoff et al. (2006) found that discrimination of a small group of mono-floral honeys from poly-floral honeys might be challenging due to the unequal dataset. However, mono-mānuka honeys were a majority group (70 % dataset) in this study while multi-mānuka and non-mānuka honeys represented around 15 % per each. In general, PLSDA performed classification of three MPI classes (mono-, multi- and non-mānuka) and two classes (multi-and non-mānuka) as well as did SVMDA. Moreover, the area under curve (AUC) of PLSDA-ROC shows the probability of separation of each honey group exceeded 90 %. The sensitivity and specificity of classification of mono-mānuka honeys approached 1 and those of multi-mānuka and non-mānuka honeys were around 0.8. This means that models might not be badly affected by the imbalanced dataset in this study.

Important spectral ranges selected were (400 - 600 nm), (859 & 1000 - 1400 nm) and (1850 - 1880 nm). This was in line with the study of Noviyanto & Abdulla (2020) but was different from Yang et al. (2020). Noviyanto & Abdulla (2020) discriminated mono-floral mānuka honeys from mānuka-blend, clover and between mono-mānuka honeys with different UMF^{TM} levels in 400 - 1000 nm (Noviyanto & Abdulla, 2020). The selected range in the study

of Noviyanto & Abdulla (2020) contained the Vis range similarly to the current study. However, the authors did not indicate any chemical footprints linked to spectral features. In the current work, important bands in (400 - 600) could be relevant to footprints of DHA, MGO and colour pigments while (859 & 1000 - 1400 nm) and (1850 - 1880 nm) could reflect carbohydrate characteristics and water molecules in the honey matrix (Table 6.3). By contrast, Yang et al. (2020) selected the region of 1300 - 1800 nm to differentiate mono-mānuka honeys from syrup-blended mānuka honeys and corn syrup. In their research, the bands of interest mostly corresponded to the absorption of water in the honey matrix (Yang et al., 2020). In this study, the absorption peaks of local water molecules were also identified at 1000 nm, 1398/1399 nm and 1850/1852 nm. The matrix of fresh mono-, multi-, and non-mānuka honeys is different from adulterated honeys studied by Yang et al. (2020). In this study, the presence of key chemical markers, polyphenolic compounds and water molecules was profoundly important for the classification of mono-, multi- and non-mānuka honeys.

In conclusion, Vis-NIR spectroscopy (Vis-NIRS) showed the capability to estimate the honey quality in terms of potency and purity mānukaness. The analysis of spectral information (based on important spectral bands) showed the ability of Vis-NIRS to capture unique chemical information related to potency and purity. These important spectral features were identified in both Vis and NIR ranges which could mostly correspond to DHA, MGO, flavonoids, colour pigments, and water molecules in the honey matrix. Classification models for purity of mono-mānuka honey achieved above 90 % accuracy in being discriminated from the other sources (multi-mānuka and non-mānuka honeys). However, the model for potency prediction showed a moderate prediction performance due to the regional impact. Overall, the proposed approach would allow the assessment of honey quality by spectral estimation of the biological activity as well as the botanical origin.

Section 2. NIR hyperspectral imaging data

6.4.5. Prediction of HSI potency mānukaness

6.4.5.1. Regression models

Similarly to NIR non-imaging data, a 1656-honey HSI dataset in the 547 - 1701 nm range was modelled by PLS & SVR to estimate 10-month UMF^{TM} scores. The 4-interval iPLS and VIP (auto) techniques were applied on the PLS output to enhance the predictive performance. Figure 6.7 displays the PLS output of UMF^{TM} prediction from HSI data. Fourteen latent variables were employed to minimise the prediction error. The model obtained the R^2 (CV) 0.7

and R^2 (Pred.) around 0.66. The root mean squared error of cross-validation (RMSECV) and prediction (RMSEP) were 2.75 and 2.61, respectively. The residual predictive deviation (RPD) was 1.82. Relative to PLS regression, the SVR model did not improve the prediction of UMF^{TM} score (results not shown in this chapter) since RPD < 2.

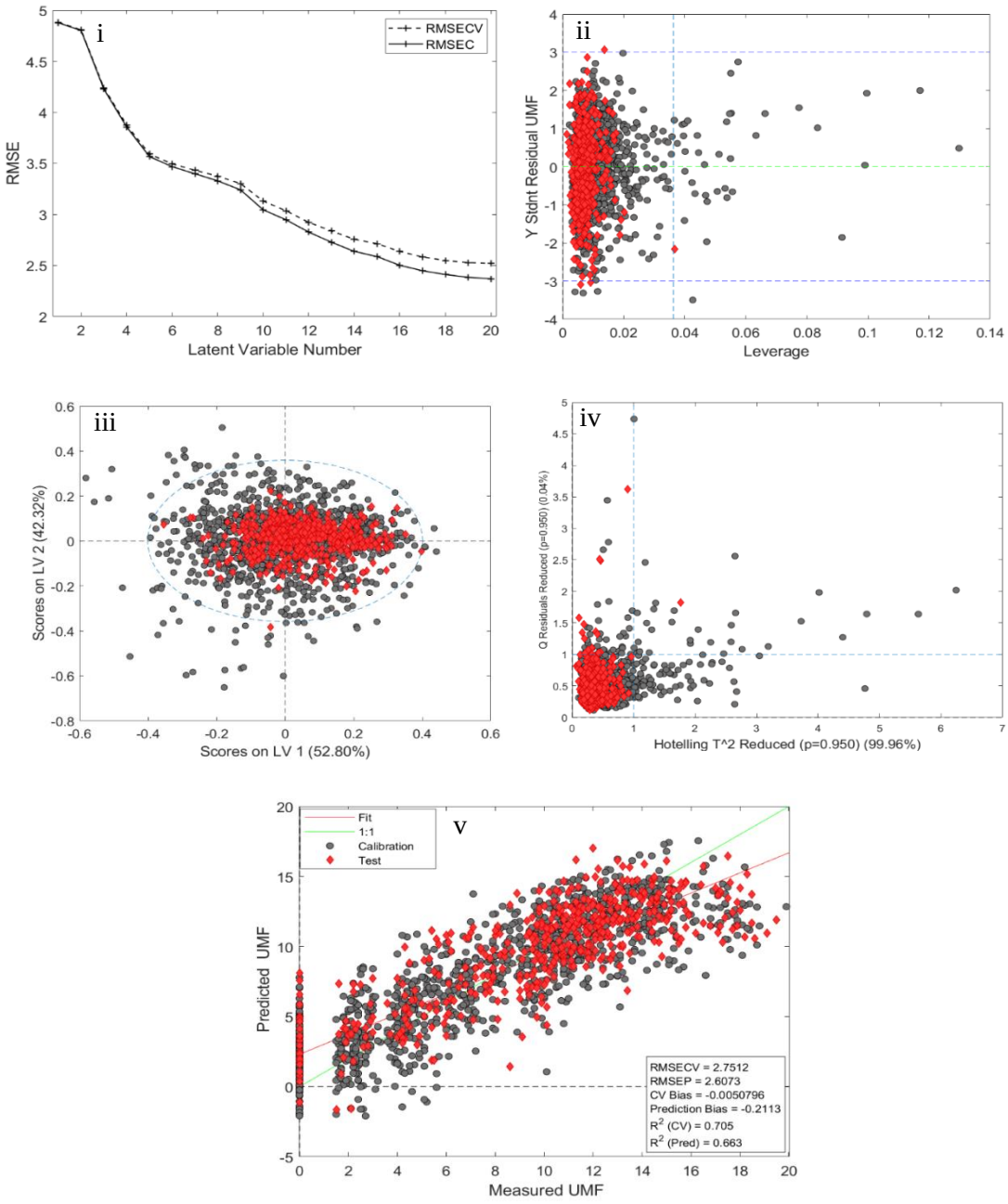

Figure 6.7. *The output of HSI PLS regression on UMF^{TM} prediction with calibration set (black circle) and test set (red diamond): i) Latent variable plot versus RMSE (cross-validation: dash line with cross & test: solid line with cross), ii) Leverage plot, iii) PLS score plot, iv) Q residuals & Hotelling T^2 plot, v) regression plot between measured and predicted UMF^{TM} scores*

In the PLS model, the UMF^{TM} estimation (Figure 6.7-v) contained some negative values and some over-predictive points at UMF^{TM} reference 0. This could imply some bias or constraints that could not be explained by the model. The results of the HSI PLS model were quite similar to those of the non-imaging PLS model, but the HSI predictability was lower by 6 percentage point accuracy than that of non-imaging.

6.4.5.2. Variable selection from the regression model

Since PLS and SVR obtained similar RPD values, a PLS model was chosen to select important wavelengths for understanding chemical signature impacts on prediction of UMF^{TM} score. A total of 108 variables were contained in a final PLS model. The PLS loading plot shows 27 important spectral features having the highest loading weight (Figure 6.8 & Table 6.4). Four spectral regions were discerned: below 700 nm, between 730 - 922, 972 - 1011 nm and beyond 1090 nm. The first region with bands 607, 626, 651, 671, 696 could relate to color pigments. The second region (730, 765, 794, 828, 873, 888 and 922 nm) reflects stretching of 3rd and 4th overtone C-H of carbohydrate groups (-CH, -CH_2 & -CH_3). The third region indicates the local absorption of water molecules at 972, 991, 1011 & 1425 nm due to 2nd and 1st overtone of O-H. The fourth region relates to 2nd overtone C-H (1090, 1134, 1114, 1164, 1174, 1277 & 1292 nm) and 1st overtone C-H combination of -CH_3, -CH_2 & -CH (1327, 1341, 1327 & 1351 nm) (Xiaobo et al., 2010).

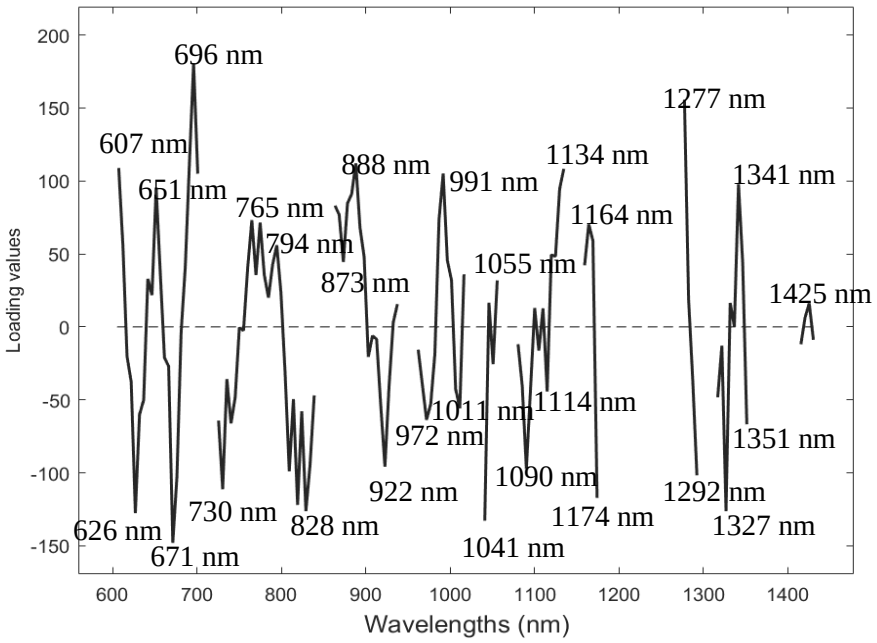

Figure 6.8. *Important spectral features extracted from HSI PLS regression loading plot for UMF^{TM} prediction*

Table 6.4. The important spectral features and corresponding chemical footprints characterised from the HSI PLS-UMF^{TM} prediction

Spectral regions (nm)	Identified wavelengths (nm)	Relevant chemical footprints	Relevant compounds discussed
Below 700	607, 626, 651, 671 & 696	color pigments	chlorophyl
730-922	730	4th overtone C-H of -CH_3	MGO, DHA & other carbohydrate groups
	765,794 & 828	4th overtone C-H of CH_2, -CH and/ or 3rd overtone O-H	carbohydrate groups and/or H_2O
	873, 888 & 922	3rd overtone C-H of -CH_3, -CH_2 & -CH	MGO, DHA & other carbohydrate groups
972-1011	972, 991, 997, 1011	2nd overtone O-H	H_2O
Beyond 1090	1090, 1134, 1114, 1164, 1174, 1277 & 1292	2nd overtone C-H of -CH_3, -CH_2 & -CH	MGO, DHA & other carbohydrate groups
	1327, 1341, 1327 & 1351	1st overtone C-H combination of -CH_3	MGO, DHA & other carbohydrate groups
	1425	1st overtone O-H	H_2O

6.4.5.3. Generalisation of HSI potency mānukaness

Potency mānukaness value was generalised from linear PLS regression. Figure 6.9 displays global prediction of HSI potency mānukaness across eight different districts with a coefficient of determination r^2 0.62. This shows that potency mānukaness can be a reasonable proxy for UMF^{TM} values identified in the UMF^{TM} rating system, although its 62 % accuracy compares poorly with the 74 % (r^2 0.74) achieved for non-imaging data against the same lab-derived chemical data with 96 % (r^2 0.96). The potential for using non-destructive spectral methods to estimate potency mānukaness is discerned, and even this level of accuracy could be useful at the point of honey extraction.

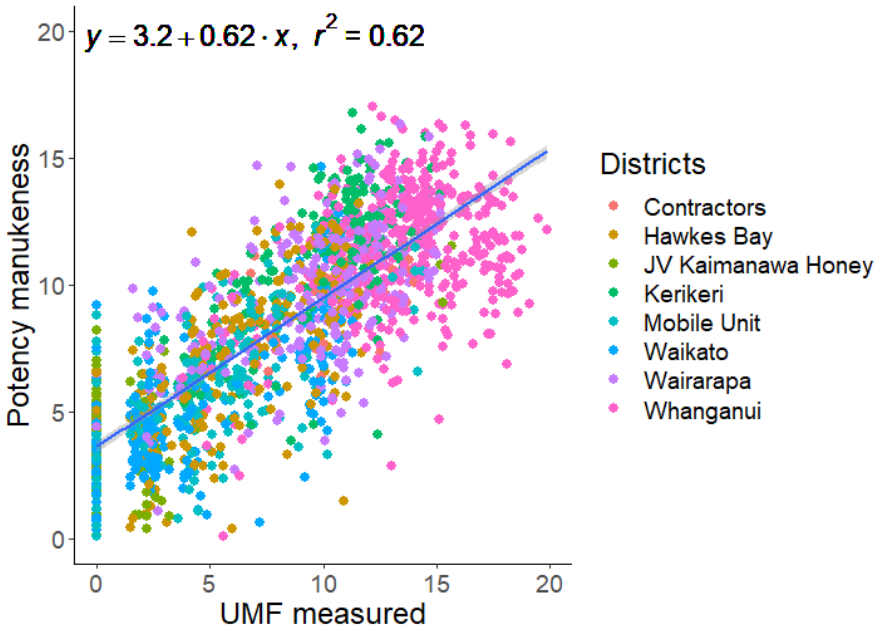

Figure 6.9. *Prediction of potency mānukaness from the HSI NIR data over eight districts*

6.4.6. Prediction of HSI purity mānukaness

6.4.6.1. HSI classification models

PLSDA and SVMDA (rbf) classifiers were employed to analyse HSI data for classifying mono-mānuka, multi-mānuka and non-mānuka honeys. Table 6.5 displays the classification results obtained with the test set. The PLSDA model gave overall classification (OA) accuracy of 84.5 % and class accuracies (CA) for mono-mānuka, multi-mānuka and non-mānuka were 95.1 %, 52.6 % and 55.2 %, respectively. Meanwhile, SVMDA classifier obtained OA 86.3 % and CA were 90.4 %, 73.2 % and 66.7 %, respectively. Overall, the non-linear SVM classifier gave better discrimination accuracy than the linear PLSDA (Table 6.5). Sub-classification models of only two classes of multi-mānuka and non-mānuka were also built since the three-classed data were unbalanced with the majority of samples being mono-mānuka honeys. A sub-SVMDA model performed with OA ~74 % on the test set, higher than the sub-PLSDA model (69.6 %) (Table 6.6). However, both models could classify multi-mānuka with 70 – 77 % accuracy which was higher by ~ 15 percentage points than the model achieved with three classes. For classification of non-mānuka, a PLSDA model of two classes obtained seven percentage points better accuracy.

Compared to non-imaging classification results, the classification output of HSI data gave about 10 % lower cross-validation accuracy, but the predictability of new samples was similarly above 80 %. This indicates that HSI classification models was also good enough to classify mono-, multi and non-mānuka honeys with the predictive accuracy 84 - 86 %.

Table 6.5. Comparison between HSI PLSDA and SVMDA (rbf) for classification of mono-mānuka, multi-mānuka and non-mānuka honeys

Model	Recall			Precision			F1			OA
	Mono	Multi	Non	Mono	Multi	Non	Mono	Multi	Non	(%)
PLSDA	0.90	0.69	0.48	0.83	0.89	0.97	0.93	0.59	0.52	84.5
SVMDA	0.97	0.43	0.55	0.63	0.95	0.98	0.94	0.51	0.60	86.3

Table 6.6. Comparison between HSI PLSDA and SVMDA (rbf) for classification of multi-mānuka and non-mānuka honeys

Model	Recall		Precision		F1		OA (%)
	Multi	Non	Multi	Non	Multi	Non	
PLSDA	0.75	0.61	0.61	0.75	0.75	0.61	69.6
SVMDA	0.81	0.62	0.62	0.81	0.79	0.65	73.91

6.4.6.2. Selection of important variables

A PLSDA model was selected to interpret important wavelengths for classifying three honey classes. A total of 44 spectral variables were selected after applying 4- iPLS and VIP techniques. Again, important regions of these spectral bands (Table 6.7) were similar to those mentioned in previous section for predicting UMF^{TM} score. Exceptions were the 587 and 602 nm bands which could not be detected as important in the PLS regression model but were identified in the PLS classification model. These bands could be relevant to flavonoids giving colour of honey.

Table 6.7. The important spectral features and corresponding chemical footprints were identified from the HSI PLSDA classification of mono-mānuka, multi-mānuka and non-mānuka honeys

Spectral regions (nm)	Identified wavelengths (nm)			Relevant chemical footprints	Relevant compounds discussed
	Mono-mānuka	Multi-mānuka	Non-mānuka		
Below 600	587 & 602	587 & 602	587 & 602	flavonoids	quercetin
	631 &651	632 & 651	626 & 651	color pigments	chlorophyl
	730, 740 & 750	730, 735, 740 & 750	730, 735 & 750	4th overtone C-H of CH_3, and/ or 3rd overtone O-H	MGO, DHA, carbohydrate groups and/or H_2O
830 - 860	844, 888 & 900	843, 888 & 898	843, 883 & 897	3rd overtone C-H of -CH_3, -CH_2 & -CH	MGO, DHA & other carbohydrate groups
1000 - 1350	1110 &1114	1110 & 1115	1099 & 1110	2nd overtone O-H	H_2O
	1144 & 1159	1144 & 1154	1149 & 1144	2nd overtone C-H of -CH_3 & -CH_2	MGO, DHA, carbohydrate groups
	1297 & 1320	1297,1302,1322 & 1331	1297 & 1331	1st overtone C-H combination of -CH_3,	MGO, DHA, carbohydrate groups

6.4.6.3. Generalisation of HSI purity mānukaness

A linear regression PLSDA model of three classes were chosen to estimate purity mānukaness since a non-linear SVMDA model was not easy to interpret. Three classes of MPI were coded 1 for non-mānuka, 2 for multi-mānuka and 3 for mono-mānuka as the measured weight value. Purity mānukaness was generalised from the linear regression weight for the whole dataset. Figure 6.10 illustrates HSI purity mānukaness as generated from a PLSDA model. Similar to non-imaging and lab-based data, HSI purity mānukaness showed three classes quite overlapped although the boxes showing 75 % variance of distribution were separated. Most of mono-mānuka, multi-mānuka and non-mānuka honeys had overlapped each other in 1 - 3 purity range. Some samples from three classes had negative values (bias) which could not be explained in the model.

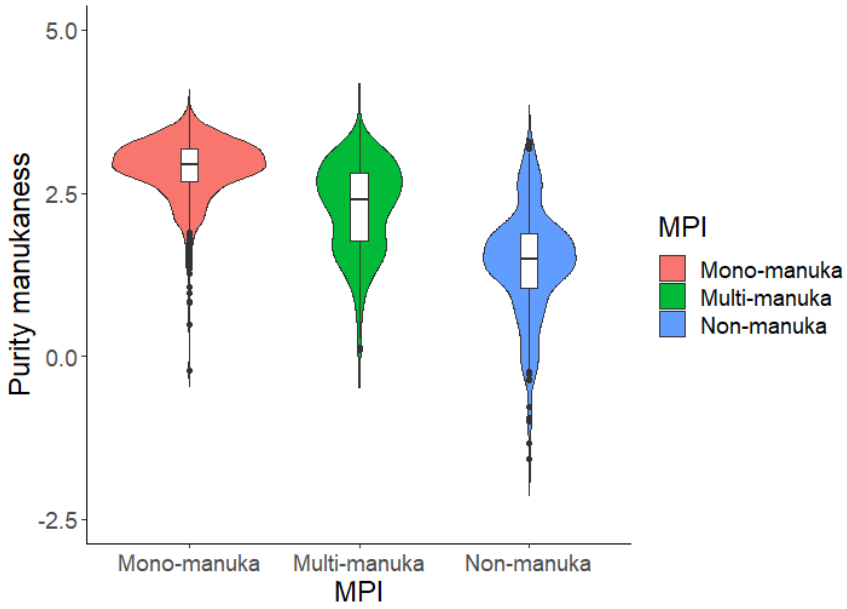

Figure 6.10. *Violin distribution plot of prediction of HSI purity mānukaness for classification of mono-mānuka, multi-mānuka and non-mānuka honeys*

6.4.7. HSI potency and purity mānukaness plot

The linear relationship between potency and purity mānukaness obtained from HSI data was strong but the correlation of determination r^2 was only 0.56 (Figure 6.11). Compared to non-imaging data and lab-based data, the HSI linear accuracy between potency and purity mānukaness reduced by 21 and 39 percentage points, respectively. This indicates that there were non-linearities between potency and purity mānukaness obtained from HSI data due to the complexity of honey matrix that cannot be explained by modelling.

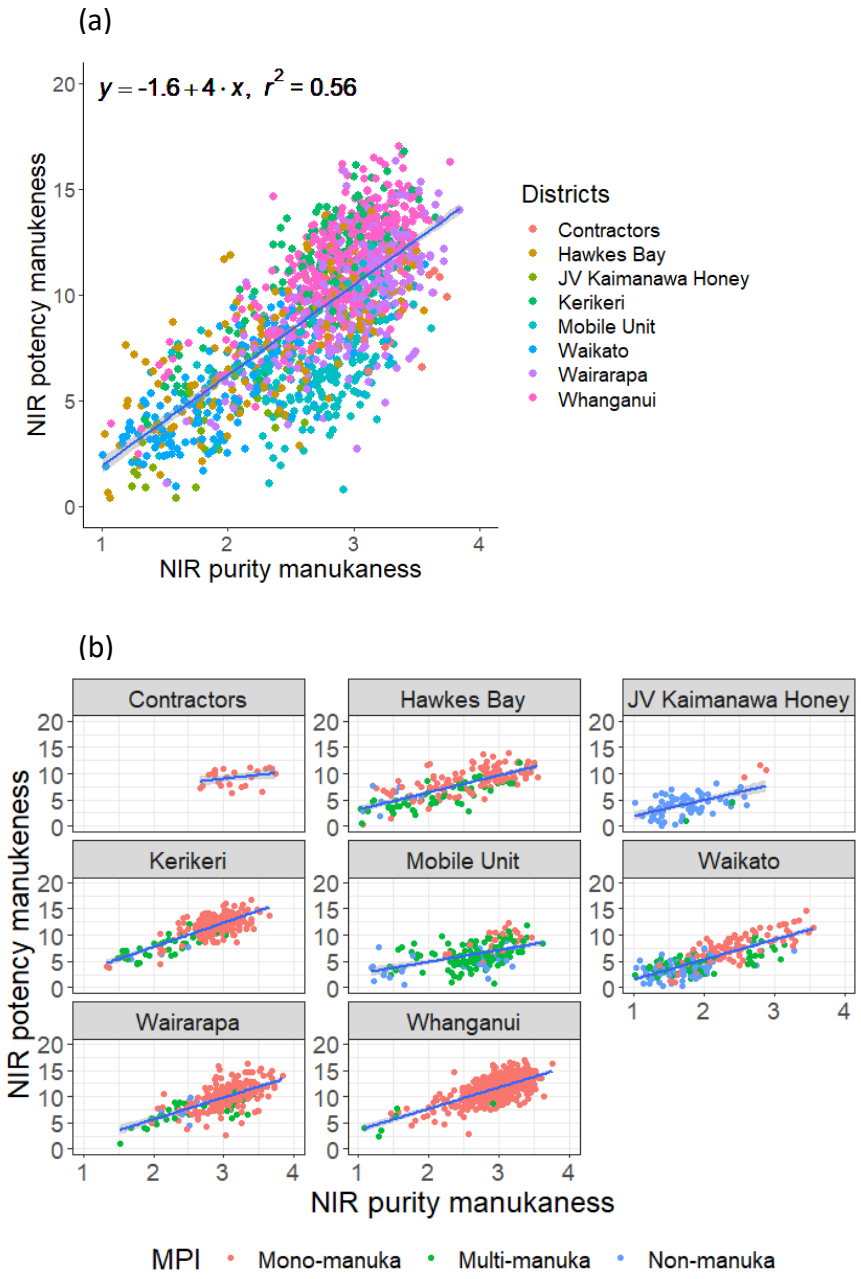

Figure 6.11. *NIR HSI potency and purity mānukaness plot for all districts (a) and for each district (b) grouping by three classes of MPI criteria. Note the blue line plotted is identical for each despite the changing axes and is the model line*

6.4.8. Discussion

The NIR hyperspectral imaging system (547 – 1701 nm) showed ability to predict potency and purity mānukaness, but less well than did the NIR non-imaging system (350 - 2500 nm). The predictive results of HSI data showed a decrease in prediction accuracy 10 - 15

percentage points for the estimation of both potency and purity mānukaness in comparison to the results from non-imaging data. Factors differentiating non-imaging from HSI data were discussed in Chapter 5. In addition, the complex honey matrix also influences the HSI prediction results which cannot be explained by PLS modelling. However, the HSI system still showed potential for prediction of potency and purity mānukaness.

The spectral wavelengths identified as important for prediction of UMF^{TM} score and classification of MPI honey classes are displayed in Tables 6.4 & 6.7. These wavelengths were close to bands obtained from non-imaging models. Overall, the absorption of chemical markers (DHA, MGO), flavonoids and water molecules in Vis-NIR range was important to characterising mono-mānuka honeys from other honeys.

6.5. General discussion and conclusions

The current chapter investigated NIR non-imaging and hyperspectral imaging methods for prediction of potency and purity mānukaness in comparison with lab-based analyses. Prediction of potency mānukaness obtained 74 % accuracy for non-imaging data (r^2 = 0.74) but only gave 62 % accuracy for hyperspectral imaging data. Prediction of purity mānukaness from non-imaging data (OA = 89 %) was also higher by 3 percentage points than that from hyperspectral imaging data (OA = 86 %). In general, hyperspectral imaging data resulted in poorer prediction of potency and purity mānukaness than non-imaging consistent with the discussion in Chapter 5. This suggests that the signal-to-noise ratio between two systems and the complex honey matrix may have affected prediction of potency and purity. The signal-to-noise can be changed to enhance the prediction accuracy, but the complex honey matrix is still present due to different botanical sources originated from different geographic districts. The complexity of honey matrix affects NIR data that was also observed in the lab-based data for the prediction of mānukaness (Appendix, Section 1).

In conclusion, potency and purity mānukaness can be used as spectral quality marks to measure the quality and purity of mānuka honey. Vis-NIR non-imaging and imaging both show the ability to predict potency and purity mānukaness. However, the prediction performance was likely limited by the nature of wild harvest honey data which carries botanical variation from different districts. This chapter generally supports the potential described in Chapters 4 and 5.

Chapter 7

Investigating the impact of NIR methods for grading mānuka honeys into different UMF™ buckets

7.1. Introduction

Quality assessment of mānuka honey using NIR methods is being studied. Previous chapters have shown the possibility of NIR methods for evaluation of mānuka honey quality based on potency and purity. Overall, the prediction of potency and purity achieved 60 - 80 % accuracy. There are limitations on prediction accuracy due to modelling error and the complex honey matrix reflecting regional variation. Regression and classification approaches were used to score potency and purity mānukaness, respectively. The classification process seemed to give better performance than regression. Potency mānukaness was estimated based on UMF™ score which is a continuous value. Conventionally, mānuka honey is sold at retail as > UMF™ 5, > UMF™ 10, > UMF™ 15 or > UMF™ 20. Therefore, it could be useful to assess potency mānukaness with a category of '*n*' UMF™ buckets. Honeys with different levels of UMF™ could be divided into several UMF™ buckets (for example, very high, high, medium and low) for quality assessment of honey frames. This process could improve modelling accuracy and still could get the benefits for grading of mānuka honey quality as it prevents honey frames with high UMF™ scores being mixed with low UMF™ scores.

In the current chapter, the UMF™ bucket approach was employed to investigate the impact of NIR methods on modeling performance predicting UMF™ scores and classifying three MPI classes. This helps to assess the NIR methods in categorising quality UMF™ buckets with minimum impact of the honey matrix effect. In practice, beekeepers and honey producers can decide the number and size of UMF™ buckets which could optimise their production.

7.2. Materials and methods

We have used two datasets, one of 1451 samples from the non-imaging sensor and one of 1656 samples from the imaging sensor. The results of prediction of UMF™ scores using PLS regression and of classification of three MPI classes using PLSDA and SVM (rbf) were examined in Chapter 6 for sorting into different UMF™ buckets.

Five UMF™ buckets were selected based on UMF™ scores of honey samples: UMF™ bucket 0 (UMF™ $\leq$ 2.5), UMF™ bucket 5 (2.5 < UMF™ $\leq$ 7.5), UMF™ bucket 10 (7.5 <

UMF^{TM} ≤ 12.5), UMF^{TM} bucket 15 (12.5 < UMF^{TM} ≤ 17.5), UMF^{TM} bucket 20 (UMF^{TM} > 17.5).

Classification of UMF^{TM} buckets was evaluated by confusion matrix, misclassification, overall accuracy (OA) and class accuracy (CA). From the regression and classification results, honey samples were counted for each UMF^{TM} bucket and displayed in the confusion matrix and misclassification tables. Then, overall accuracy and class accuracy were calculated on MATLAB (version 2020) based on the confusion matrix results.

7.3. Results

Section 1: NIR non-imaging data

7.3.1. Assessment of the SVM (rbf) classification model

Linear PLSDA and SVM (rbf) were employed on NIR (non-imaging) data to classify mono-mānuka, multi-mānuka and non-mānuka honeys. PLSDA and SVM (rbf) models obtained overall classification accuracy of 82 % and Kappa 0.73 ~ 0.74 (Chapter 6). However, SMV (rbf) gave higher class accuracy than PLSDA. Therefore, a SVM model was chosen for sorting UMF^{TM} buckets.

Table 7.1 shows the cross-validated results of a SVM model. Mono-mānuka, multi-mānuka and non-mānuka honeys were separated with class accuracy 95.4 %, 84.2 % and 83.1 %, respectively. Prediction of the test set showed a similar trend with cross-validated results with overall accuracy of 89 % (the results were showed in Chapter 6).

Table 7.1. Confusion matrix of non-imaging CV-SVM classification results for mono-mānuka, multi-mānuka and non-mānuka honeys

CV-SVM (rbf) model Overall accuracy = 82 %; (n = 1015 samples)			
Class	Mono-mānuka	Multi-mānuka	Non-mānuka
Predicted mono-mānuka	554	21	6
Predicted multi-mānuka	8	181	26
Predicted non-mānuka	6	31	182
Class accuracy	95.4 %	84.2 %	83.1 %

Note: CV means cross-validated

The predicted classes of the SVM model were plotted against the measured UMF^{TM} scores (UMF^{TM} 10 month) (Figure 7.1). There was a distribution gap between UMF^{TM} 0 and UMF^{TM} 2.5 due to some error in the lab dataset. In general, there was an overlap between

mono-mānuka, multi-mānuka and non-mānuka honey samples that had UMF^{TM} scores < 7.5. The SVM model indicated mono-mānuka honeys with UMF^{TM} >10 were well classified. Some of mono-mānuka samples were misclassified as multi-mānuka and non-mānuka honeys that were mostly from UMF^{TM} bucket 0 (UMF^{TM} ≤ 2.5) and bucket 5 (2.5 < UMF^{TM} < 7.5). Some multi-mānuka honeys were misclassed as non-mānuka and some non-mānuka honeys were mislabelled as multi-mānuka honeys. These samples were almost all from UMF^{TM} bucket 0 and bucket 5.

Tables 7.2 a & b describe the confusion matrix and misclassification of the CV-SVM model. The precision values of UMF^{TM} buckets 10, 15 and 20 were above 90 %. Following were UMF^{TM} buckets 0 and 5 with 78 - 85 % precision score (Table 7.2 a). Some samples in UMF^{TM} bucket of 5 were misclassed with samples from bucket 10, but almost no samples from bucket 0 (B_UMF_0) were misclassed with samples in Buckets 10, 15 & 20, except for 1 sample of bucket 10 (B_UMF_10) was predicted as non-mānuka (Table 7.2 b). The highest misclassification rate was at buckets 0 and 5. Some honeys in the UMF^{TM} bucket of 15 were misclassified with samples in bucket 10. No honeys in UMF^{TM} buckets 20 (B_UMF_20) were misclassified. Overall, honeys in high-ranking buckets (10, 15, 20) were nicely separated from honeys in buckets 0 & 5.

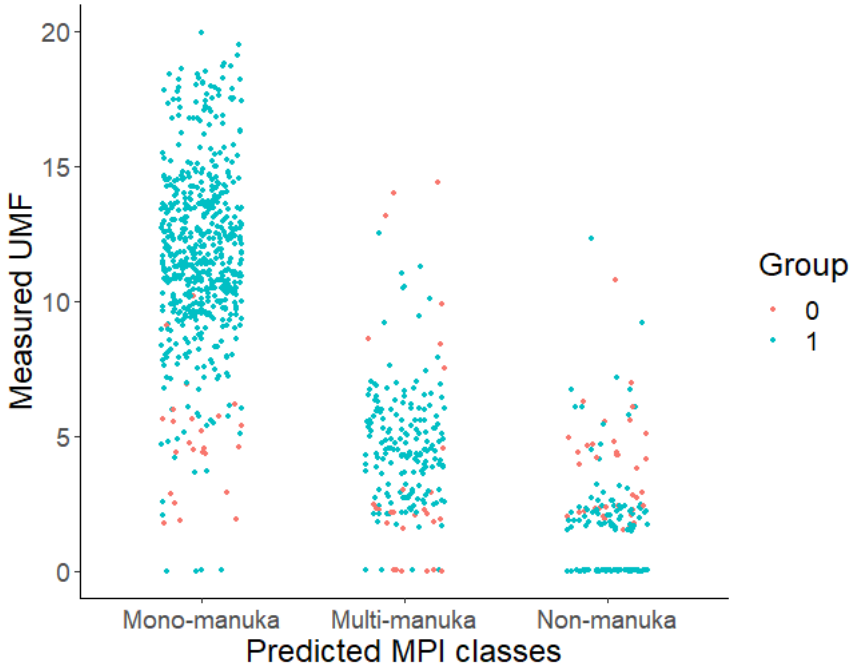

Figure 7.1. *Plotting non-imaging CV-SVM classification results with the measured UMF^{TM} (10 months). Group: 0-misclassed and 1-correct honeys*

Table 7.2a Confusion matrix of honey samples correctly classified from a non-imaging CV-SVM model and then sorted in different UMF™ buckets

	Correct classification			
Prediction	Mono-mānuka	Multi-mānuka	Non-mānuka	Precision
B_UMF_0_ref	7	21	158	0.78
B_UMF_5_ref	36	155	20	0.85
B_UMF_10_ref	315	5	4	0.98
B_UMF_15_ref	172	0	0	0.98
B_UMF_20_ref	24	0	0	1.00
Sum	554	181	182	

Note: ref means reference data & precision was calculated by dividing the number of correctly predicted samples of a bucket by the total number of samples in that bucket.

Table 7.2b Misclassification of honey samples predicted from a non-imaging CV-SVM model and counted in different UMF™ buckets

	Misclassification			
Prediction	Mono-mānuka	Multi-mānuka	Non-mānuka	Misclassed ratio
B_UMF_0_ref	5	31	15	0.22
B_UMF_5_ref	8	14	16	0.15
B_UMF_10_ref	1	4	1	0.02
B_UMF_15_ref	0	3	0	0.02
B_UMF_20_ref	0	0	0	0
Sum	14	52	32	

Note: ref means reference data & misclassed ratio was calculated by dividing the number of misclassed samples of a bucket by the total number of samples in that bucket.

Honeys from each district were plotted to understand which districts had highest misclassification. Figure 7.2 illustrates the cross-validated SVM results grouped by eight districts. Honeys with red colour were misclassed. Mono-mānuka honeys from Hawkes Bay and Mobile Units seemed quite often misclassed as multi-mānuka honeys. Meanwhile, most of the multi-mānuka honeys are misclassified as non-mānuka honeys mainly came from Hawkes Bay and Waikato. Some non-mānuka misclassed as multi-mānuka honeys were found in Mobile Units, Waikato and Wairarapa. This suggested that honey composition may vary district by district. The impact of regional variation on the results of global model performance (e.g., SVM) was well-noted.

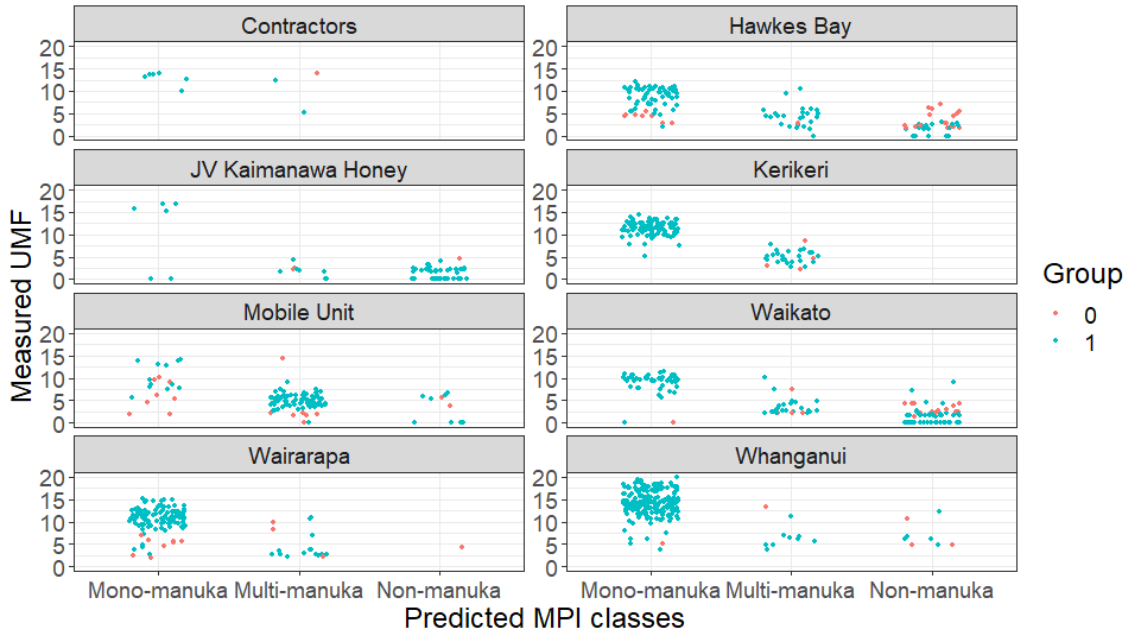

Figure 7.2. *Plotting non-imaging CV-SVM classification results grouped by eight districts against the measured UMF™ score. Group: 0-misclassed and 1-correct*

7.3.2. Assessment of the PLS regression model

A CV-PLS regression model for predicting UMF™ scores from non-imaging data spanning eight districts combined was investigated. The prediction result gave 72 % accuracy (Chapter 6). To understand the prediction performance, honey samples with PLS predicted UMF™ values were sorted into five UMF™ buckets. Table 7.3 displays the confusion matrix of honey samples between PLS predicted values and the measured values from the laboratory. Samples from UMF™ buckets 0 and 5 (B_UMF_0 and B_UMF_5) were mostly misclassed together, but only 4 % of these buckets were misclassed with samples from UMF™ buckets 10 & 15 (B_UMF_10 and B_UMF_15). None of them were predicted as belonging to bucket 20 (B_UMF_20). About 11 % and 20 % samples from UMF™ bucket 10 were misclassed with lower zones (B_UMF_0 and B_UMF_5) and higher zones (B_UMF_15 & B_UMF_20), respectively. About 50 % and 13 % samples from UMF™ bucket 15 were misclassed with samples from UMF™ buckets 10 and 20, respectively.

The PLS regression model showed that it could predict well for samples in UMF™ buckets 5 and 10 with above 65 % accuracy. Overall, the model was able to separate honey samples above UMF™ 7.5 (samples in B_UMF_10, B_UMF_15 & B_UMF_20) from samples with UMF™ below 7.5 (samples in B_UMF_0 & B_UMF_5). As expected, the

misclassification took place on the boundaries of each class. Figure 7.3 illustrates the percentage of each UMF^{TM} bucket predicted from the non-imaging CV-PLS model. The misclassification at each UMF^{TM} bucket showed the overestimation or underestimation happening at boundaries of each UMF^{TM} bucket. Intuitively, when the boundary of each UMF^{TM} bucket changes, the sample distribution could also change.

Table 7.3. Confusion matrix of samples predicted from a non-imaging CV-PLS regression model were sorted into five UMF^{TM} buckets

Prediction	B_UMF_0	B_UMF_5	B_UMF_10	B_UMF_15	B_UMF_20
B_UMF_0_ref	98	129	10	0	0
B_UMF_5_ref	32	181	35	1	0
B_UMF_10_ref	1	38	226	65	0
B_UMF_15_ref	0	1	102	72	27
B_UMF_20_ref	0	0	5	19	0
Class accuracy	41.4 %	72.7 %	68.5 %	41.1 %	0

Note: ref means reference data

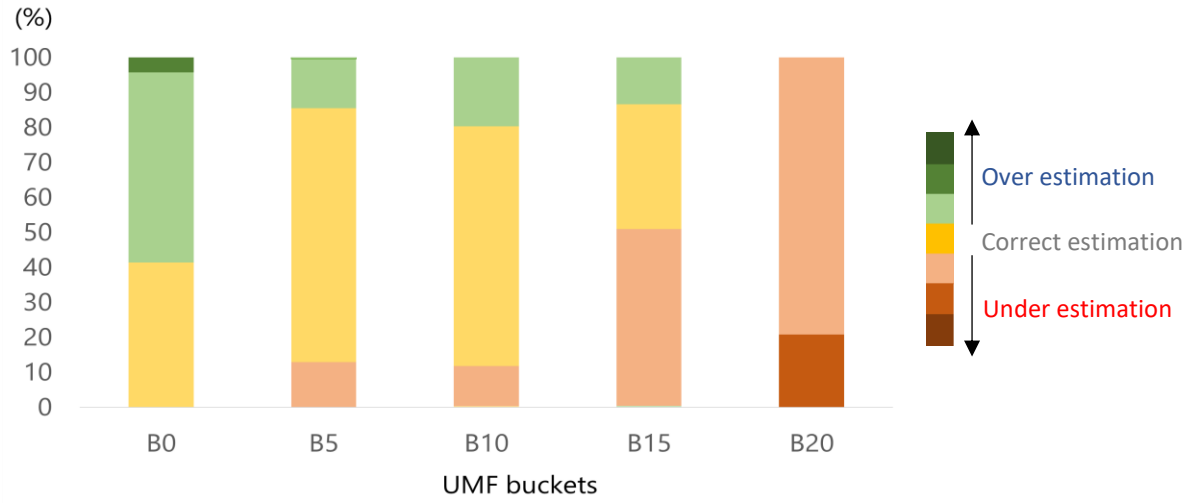

Figure 7.3. *The stacked bar chart indicating the percentage of each UMF^{TM} bucket correctly estimated (yellow), over-estimated (green) and under-estimated (red) from the non-imaging CV-PLS model. Note: the percentage error increases with dark color.*

Section 2: NIR hyperspectral imaging data

7.3.3. Assessment of the HSI SVM (rbf) classification model

The SVM (rbf) model achieved higher classification accuracy than did the PLSDA model (Chapter 6). Therefore, the CV-SVM model was chosen to investigate the model performance when sorting into different UMF™ buckets. The CV-SVM classification results of mono-mānuka, multi-mānuka and non-mānuka honeys are shown in Table 7.4. As with the non-imaging SVM model, the HSI SVM model only obtained 78.5 % overall accuracy, which is ~ 6 percentage point lower accuracy than that of the non-imaging SVM model. Class accuracy of each honey class was also about 10 % under the accuracy of the non-imaging SVM model (Table 7.1).

Table 7.4. Cross-validated SVM classification results of hyperspectral data for classifying mono-mānuka, multi-mānuka and non-mānuka honeys

	CV-SVM (rbf) (OA = 78.5 %; n = 1160 samples)		
Class	Mono-mānuka	Multi-mānuka	Non-mānuka
Predicted Mono-mānuka	600	80	22
Predicted Multi-mānuka	37	151	48
Predicted Non-mānuka	14	48	160
Class accuracy	85.5 %	63.9 %	72.1 %

Note: CV means cross-validated

CV-SVM was used to classify into five different UMF™ buckets. Firstly, the correct and misclassed were plotted against UMF™ scores (Figure 7.4). Honeys with green colour were correctly classified while honeys with red colour were misclassified. Almost all mono-mānuka honeys were well-classified as mono-mānuka with UMF™ above 7.5. About 1 % mono-mānuka honeys with UMF™ scores > 7.5 were misclassed as multi-mānuka honeys. Approximately 7 % mono-mānuka honey samples with UMF™ < 7.5 were misclassified as multi-mānuka or non-mānuka honeys. In addition, about 39 % multi-mānuka and non-mānuka honeys were misclassed together and as mono-mānuka honeys.

Tables 7.5 a & b show that honey samples were correctly classified and misclassified after separating into five different UMF™ buckets. Overall, almost all misclassed samples fell into UMF™ buckets of 0 and 5 (B_UMF_0 and B_UMF_5). Only one misclassed sample was predicted as mono-mānuka from UMF™ bucket of 15. The CV-SVM model could predict with a precision of 90 % accuracy for all mono-mānuka honey samples in UMF™ buckets of 10, 15 & 20.

When grouping the SVM cross-validation results by geographic districts, mono-mānuka honeys from Whanganui district were well-classified (Figure 7.5), followed by Kerikeri and Wairarapa. Mono-mānuka honeys from Mobiles Unit, Hawkes Bay and Waikato districts were mostly misclassed as multi-mānuka honeys. These districts also showed misclassification between multi-mānuka and non-mānuka honeys. These results were similar to those found in non-imaging classification results. The misclassification ratio of the imaging SVM model was 10 % higher than that of the non-imaging SVM model.

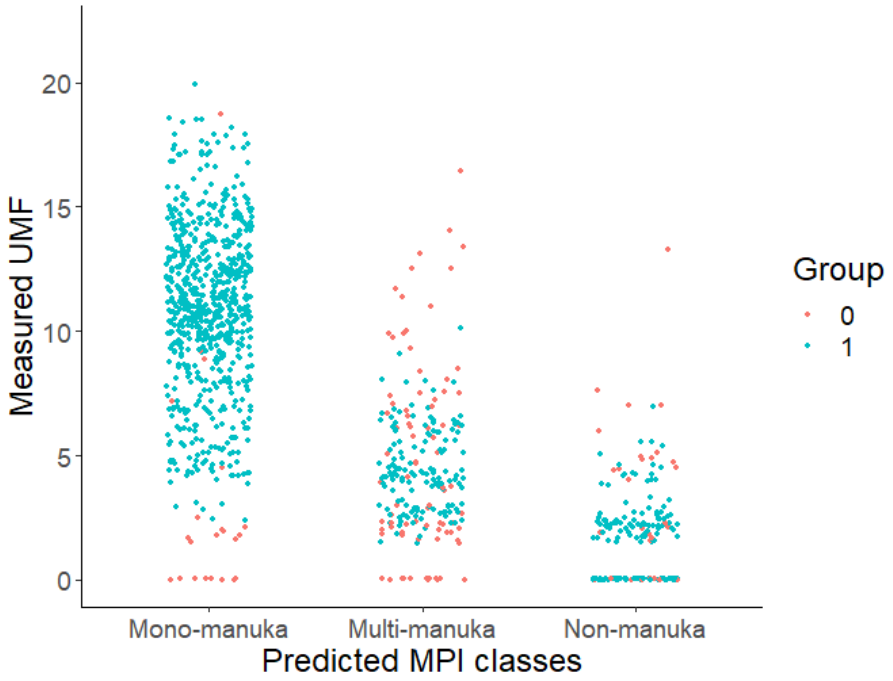

Figure 7.4. *Plotting HSI CV-SVM classification results with the measured UMF™ scores. Group: 0-misclassed and 1-correct honeys*

Table 7.5a. Confusion matrix of honey samples correctly classified from a HSI CV-SVM model and then sorted in different UMF™ buckets

	Correct classification			
Prediction	Mono-mānuka	Multi-mānuka	Non-mānuka	Precision
B_UMF_0_ref	1	11	131	0.57
B_UMF_5_ref	40	132	29	0.65
B_UMF_10_ref	340	8	0	0.92
B_UMF_15_ref	196	0	0	0.98
B_UMF_20_ref	23	0	0	0.96
Sum	600	151	160	

Note: ref means reference data & precision was calculated by dividing the number of correctly predicted samples of a bucket by the total number of samples in that bucket.

Table 7.5b. Misclassification of honey samples predicted from a HSI CV-SVM model and counted in different UMF^{TM} buckets

Prediction	Misclassification			
	Mono-mānuka	Multi-mānuka	Non-mānuka	Misclassed ratio
B_UMF_0_ref	22	48	37	0.43
B_UMF_5_ref	23	52	31	0.35
B_UMF_10_ref	5	24	1	0.08
B_UMF_15_ref	0	4	1	0.02
B_UMF_20_ref	1	0	0	0.06
Sum	51	128	70	

Note: ref means reference data & Misclassed ratio was calculated by dividing the number of misclassed samples of a bucket by the total number of samples in that bucket.

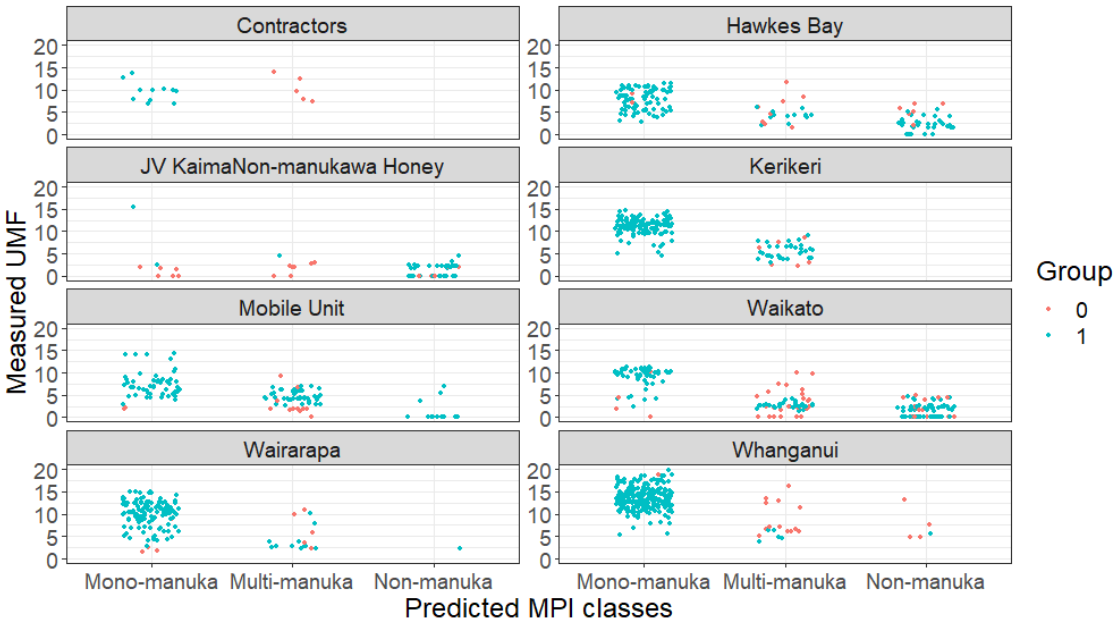

Figure 7.5. *Plotting HSI CV-SVM classification results grouped by eight districts against the measured UMF^{TM} scores. Group: 0-misclassed and 1-correct honeys*

7.3.4. Assessment of the HSI PLS regression

The CV-PLS model based on imaging data (n = 1160) covering eight geographic districts predicted UMF^{TM} scores with an accuracy 67 % (Chapter 6). The predicted UMF^{TM} values were sorted into five UMF^{TM} buckets to understand the prediction model performance. Samples from UMF^{TM} buckets 0 and 5 (B_UMF_0 & B_UMF_5) were separated well from samples in UMF^{TM} buckets 15 and 20 (B_UMF_15 & B_UMF_20). Some samples from bucket 10 (B_UMF_10) were misclassified with samples from bucket 5 (B_UMF_5) and only one sample of bucket 10 were misclassified in bucket 0. However, many samples from buckets 15 and 20

were predicted as samples from buckets 10. Unfortunately, no samples from UMF^{TM} bucket 20 (B_UMF_20) could be identified as B_UMF_20, but instead of misclassifying in buckets 5, 10 and 15. This was due to a paucity of samples in this zone for building the model, but it is probably not a fundamental issue. Although the imaging regression model was not better than the non-imaging regression model, after separating samples from UMF^{TM} buckets, samples from B_UMF_5 could be predicted with 65 % accuracy and samples from B_UMF_10 above 67 % accuracy. Figure 7.6 displays the percentage of UMF^{TM} buckets predicted from the HSI CV-PLS model. Overall, high-quality honeys (e.g, B_UMF_20) were predicted into low-quality honeys and similarly low-quality honeys were rated as high-quality honeys. This issue was worse in imaging PLS model than did non-imaging PLS model.

Table 7.6. Confusion matrix of samples predicted from a HSI CV-PLS model were sorted into different UMF^{TM} buckets

Prediction	B_UMF_0	B_UMF_5	B_UMF_10	B_UMF_15	B_UMF_20
B_UMF_0_ref	89	146	15	0	0
B_UMF_5_ref	38	202	66	1	0
B_UMF_10_ref	1	46	256	75	0
B_UMF_15_ref	0	2	103	95	1
B_UMF_20_ref	0	2	16	6	0
Class accuracy	35.6 %	65.8 %	67.7 %	47.3 %	0 %

Note: ref means reference data

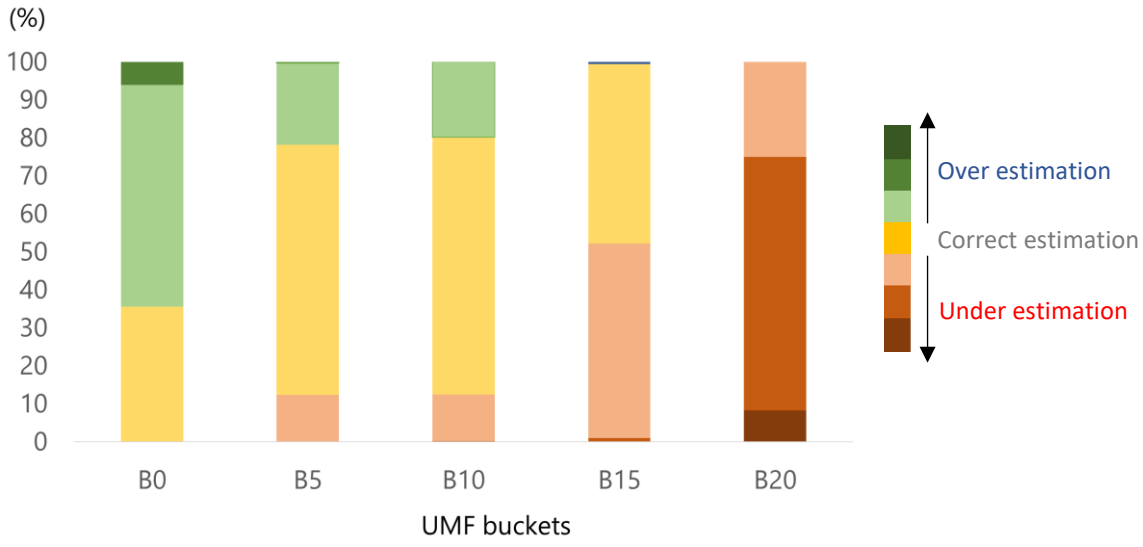

Figure 7.6. *The stacked bar chart indicating the percentage of each UMF^{TM} bucket correctly estimated (yellow), over-estimated (green) and under-estimated (red) from the HSI CV-PLS model. Note: the percentage error increases with dark color.*

7.4. Discussion and conclusion

Chapter 6 showed NIR non-imaging models gave better prediction and classification results than those of imaging data probably due to different acquisition settings. The complexity of the honey matrix resulting from variation in botanical sources impacts prediction of potency (UMF^{TM} scores) and purity (verification of mono-mānuka, multi-mānuka and non-mānuka honeys) when using NIR methods. The current chapter employed UMF^{TM} buckets as quality categories to grading honeys. Using UMF^{TM} buckets seems to minimise the complex honey matrix effect and enhance the predictability of NIR methods. This provides a benefit to grading honey by avoiding mono-floral mānuka honeys being diluted with other floral sources. Overall, the regression and classification models of NIR non-imaging and imaging data showed that samples in UMF^{TM} buckets of 15 and 20 were well separated from low UMF^{TM} buckets of 0 and 5. There was some overlapping classification mostly happening at UMF^{TM} bucket boundaries, in particular, between boundaries of buckets 5 and 10 and of buckets 10 and 15.

NIR models seemed to predict low for high UMF^{TM} samples in buckets 15 and 20 and predict high for low UMF^{TM} samples in buckets 0 and 5 into the bucket 10. This could impose a risk of missing high UMF^{TM} honeys by loss into lower buckets (e.g., buckets 15 & 20), and the risk of diluting low with higher UMF^{TM} honeys (e.g., bucket 5). However, this only takes place at the boundaries of these buckets. NIR methods can still provide benefit by dividing honey quality into different UMF^{TM} buckets compared with lumping all honeys together. The matrix effect seemed mild when applying UMF^{TM} buckets. For example, Whanganui district possessed many high UMF^{TM} honey samples compared to other districts. The complexity of the matrix honey due to variation among geographic districts may impact less on prediction of category UMF^{TM} buckets than on the continuous values of UMF^{TM} scores.

In conclusion, using UMF^{TM} buckets helps reduce the influence of the complex honey matrix when applying modelling to NIR spectral data, and this can benefit grading of honey quality. This chapter reveals the ability of NIR methods to sort honeys into different UMF^{TM} buckets. There was some overlapping at boundaries between buckets. The choice of UMF^{TM} boundary for buckets could impact the distribution of honey samples between buckets. At the extraction plant, honey companies can decide suitable UMF^{TM} buckets to optimise production and value.

Chapter 8

Economic benefits of NIR methods when assessing mānuka honey quality before bulk extraction

8.1. Introduction

The current chapter considers how NIR technology can contribute value in the New Zealand honey industry. This project is premised on the belief that predicting the quality and identity of mānuka honey at frame level before extraction, and thus avoiding mixing of higher and lower value honeys in the extraction process will lead to higher returns. Intuitively, this is expected because the UMF^{TM}/$$ curve (i.e., pricing curve) is concave upwards. The proposition is also based on the belief that real apiaries are likely to contain considerable frame-to-frame variation. To date the project is premised on these assertions. Not until an NIR non-imaging (spectroscopy) or hyperspectral imaging (HSI) unit is placed in an extraction plant and data collected from thousands of frames from dozens of apiaries will the real situation clarify. This chapter seeks to examine the impact on revenue of applying NIR spectroscopy or hyperspectral imaging to assess mānuka honey quality before extraction under a range of different levels of variability within apiaries and for a range of different shapes of pricing curve.

Several models were developed to predict UMF^{TM} score and classify mono-floral-, multi-floral- and non-mānuka honeys, and were discussed in the previous chapters. In this chapter 8, we investigate the potential of NIR applied to imaginary apiaries. An imaginary apiary is a set of 300 imaginary frames, each having a spectrum and a single suite of laboratory data. Imaginary apiaries were tested by PLS regression and classification models. After estimating UMF^{TM} values by a regression model, imaginary honey frames were sorted into multiple UMF^{TM} buckets and the value was calculated in two ways: (1) summed across each bucket (simulating possible future prediction), and (2) summed across all frames mixed together as a single lot (simulating current practice). Additionally, imaginary frames were classified into MPI identity groups. Four pricing curves were applied in this study to represent a range of likely price/quality scenarios over years. And four different scenarios were used for different types of variability that might arise in an apiary. Then how much revenue increase NIR technology could bring was calculated for both NIR non-imaging and hyperspectral imaging systems by grouping honey frames into different UMF^{TM} buckets relative to grouping as a single averaged lot.

8.2. Materials, methodology, hypotheses and NIR model performance

8.2.1. UMF™ buckets

Five different UMF™ buckets were elected to sort honey frames at apiaries into categories of honey quality. Each UMF™ bucket has 5-unit interval of UMF™:

- Bucket 0 (B_UMF_0) possessed UMF™ level less than or equal 2.5.
- Bucket 5 (B_UMF_5) covered in the 2.5 - 7.5 UMF™ range ($2.5 < UMF \leq 7.5$).
- Bucket 10 (B_UMF_10) run from 7.5 to 12.5 ($7.5 < UMF \leq 12.5$).
- Bucket 15 (B_UMF_15) had UMF™ score between 12.5 and 17.5 ($12.5 < UMF \leq 17.5$)
- Bucket 20 (B_UMF_20) contained UMF™ more than 17.5.

Samples with high UMF™ level were segregated into buckets 15 and 20, while samples in buckets 0 and 5 were considered low UMF™ levels. Samples in bucket 10 were in the middle.

Table 8.1 shows the 1451-sample dataset separated into five different UMF™ buckets by laboratory UMF™ value before modelling. Bucket 0, bucket 5 and bucket 15 contained 281 - 334 samples while bucket 10 consisted of 478 samples. In contrast, bucket 20 only contained 33 samples. Adding more samples in bucket 20 was not possible since the honey season 2019-2020 had passed. This base dataset before modelling was quite unbalanced although some chemometric methods (e.g., PLS and PLSDA) could deal with an unbalanced dataset.

Table 8.1. Number of 1451 honey samples separated in five different UMF™ buckets

UMF™ buckets	B_UMF_0	B_UMF_5	B_UMF_10	B_UMF_15	B_UMF_20
Samples	281	325	478	334	33

8.2.2. Methodology

We built imaginary frames from real samples (provided by Comvita and scanned by non-imaging NIR and by HSI instruments) by randomly selecting 25 real samples and then combining them in pairs to generate (calculate) new ones. This way, we used the same background variability as is embedded in the real data we have at hand but could generate very large data sets. We could manipulate an imaginary apiary to be essentially high value with some poorer frames hidden within, or perhaps mainly low UMF™ (and less likely to grade as

mānuka) with some high value frames hidden within. For each imaginary frame, we applied several models to predict UMF^{TM} and classification of MPI honey classes.

8.2.3. Hypotheses

We sought to test two hypotheses.

Hypothesis 1: sorting honey frames into different buckets could bring more benefit in return than the current averaging method of all honey frames together - this we could test using the laboratory data alone.

Hypothesis 2: NIR technology could predict honey quality sufficiently well to evaluate the quality of each frame (based on UMF^{TM} scores) before the extraction process, to be able to exploit hypothesis 1.

To test hypothesis 1, firstly four imaginary apiaries were generated from randomly selected data points of the 1451-sample dataset. Each apiary consisted of 300 imaginary frames and was considered as an independent new dataset having been created from combinations of 25 raw datapoints. The imaginary apiaries should each cover a large UMF^{TM} distribution (0 - 20). In addition, one should be constructed to have 80 % high UMF^{TM} frames and 20 % low frames. Another one should have 80 % low and 20 % high. Honey frames from each apiary were separated into different UMF^{TM} buckets based on their laboratory UMF^{TM} values (regarded as true UMF^{TM}). The revenue derived from each apiary was calculated to assess whether sorting frames into UMF^{TM} buckets was better than averaging all frames. Revenue was calculated according to four pricing scenarios (see 8.2.5 below).

For evaluation of hypothesis 2, NIR models were firstly built on spectral data of 1451 (non-imaging data) and 1656 (imaging data) honey samples harvested between December 2019 and April 2020. All samples were sorted into five different UMF^{TM} buckets (section 8.2.1) based on their true UMF^{TM} values from laboratory data. Two NIR systems: non-imaging (350-2500 nm) and hyperspectral imaging (547 - 1700 nm) were employed to collect spectral data. Multivariate regression and classification models were built from each honey dataset based on UMF^{TM} levels. The classification model classified samples directly into different buckets. In contrast, the regression model predicted continuous UMF^{TM} values and then samples were lumped into five UMF^{TM} buckets according to those values. The best NIR models were selected to use with the dataset of four imaginary apiaries.

Hypothesis 2 was assessed based on predicted or classified values from NIR models. Honey frames were again sorted into five buckets and the percentage change of NIR revenue was calculated relative to the averaging method. To know whether NIR offers more benefit by

separating frames in multiple buckets, the NIR revenue percentage was compared with that calculated from the lab data from hypothesis 1.

The bucket system employed in this study is only a device to test these hypotheses and not a suggestion for real life extraction. In reality, the extraction plant manager can decide on buckets and may choose to operate two only buckets on the basis of some appropriate heuristic.

8.2.4. Imaginary apiaries

To evaluate the predictive model performance, four imaginary apiaries were created to mimic true apiaries. An apiary often contains around 240 - 300 frames. So, this work created 300 frames in each apiary by 300 combinations of two data points built by 25 randomly drawn samples from the raw 1451-sample dataset. Averaging was applied for generating a new frame from two data points. All procedures were conducted by R command (version R 4.1.1).

Each imaginary frame had both spectral and chemical information generated from two original data points by averaging. Chemical marker concentrations of new frames could be calculated by simple arithmetic averaging. However, UMF^{TM} scores may not be a linear function of DHA, MGO and Leptosperin contents. Thus, arithmetic averaging of UMF^{TM} score from those of raw data point might not be appropriate. However, it found that there was a high correlation r^2 (0.95 - 0.99) between averaged UMF^{TM} scores and the predicted UMF values estimated using concentration of DHA, MGO and Leptosperin. Therefore, this work assumed that averaging UMF^{TM} scores from laboratory data would adequately generate UMF^{TM} values for new frames.

Four criteria were applied to generate four different imaginary apiaries (H1, H2, H2+ and H3) for selection of random data points from 1451-sample data (Table 8.2). The idea was to create different distributions of UMF^{TM} level. In reality, honey frames at apiaries could contain a large variation of UMF^{TM} scores (criterion 1). Moreover, some apiaries could have 80 % “good” frames (high UMF^{TM} scores) mixed with 20 % “bad” frames (low UMF^{TM} scores) (criteria 2 & 3), and reversely (criterion 4).

Table 8.2. Four criteria of randomly selected datapoints from the raw 1451-sample dataset

Criteria	Criterion 1 (H1)	Criterion 2 (H2)	Criterion 3 (H2+)	Criterion 4 (H3)
UMF™ characteristics	Cover a full variation of 0 - 20 UMF™ level range	- 80% high UMF range > 17.5 & - 20% low UMF range < 2.5	- 80% high UMF range > 7.5-17.5 & - 20% low UMF range < 2.5	- 80 % low UMF range 0- 7.5 & - 20 % high UMF range > 17.5
Sample selection	5 data points in each UMF™ buckets	- 10 data points in B_UMF_15 - 10 data points in B_UMF_20 - 5 data points in B_UMF_0	- 10 data points in B_UMF_10 - 10 data points in B_UMF_15 - 5 datapoints in B_UMF_0	- 10 data points in B_UMF_0 - 10 data points in B_UMF_5 -2 data points in B_UMF_15 -3 data points in B_UMF_20

8.2.5. Scenarios of mānuka honey's price values

Mānuka honey value has continuously been increasing since 1990. Higher quality or higher UMF™ scores will attract higher prices. Four honey pricing scenarios were based on the price experience over 20 years. A logistic function or logistic curve was fitted to generate a generic pricing curve ($/kg) as follows:

$$f(x) = \frac{L}{1 + e^{-k(x-xo)}}$$

where x_o is the x value of the sigmoid' s midpoint;

L is the curve's maximum value;

k is the logistic growth rate or steepness of the curve.

Table 8.3 shows the logistic curve's parameters used to generate the pricing curve scenarios. Figure 8.1 illustrates the four sigmoid pricing curves expressed by $/kg. Scenario 1 shows the steepest price curve when UMF™ score is at the point of inflection of 15. Following are scenario 2 and 3. Scenario 4 is almost linear. None of these will be a perfect representation but they should be useful for the purposes of this study.

For a sample of known UMF™ value (from laboratory or from predicted models) the pricing curve of each scenario was consulted to calculate the price $/kg. At each imaginary apiary, the prices from the four scenarios were calculated for each frame and averaged for all frames. Then, percentage gain in revenue was computed between the sum of each frame's value and the average of all frames' value.

Table 8.3. Parameters of the logistic curve generated for each pricing curve scenario

Parameters	Scenario 1	Scenario 2	Scenario 3	Scenario 4
x_o	15	15	15	10
L	90	95	99	140
k	0.8	0.6	0.5	0.3

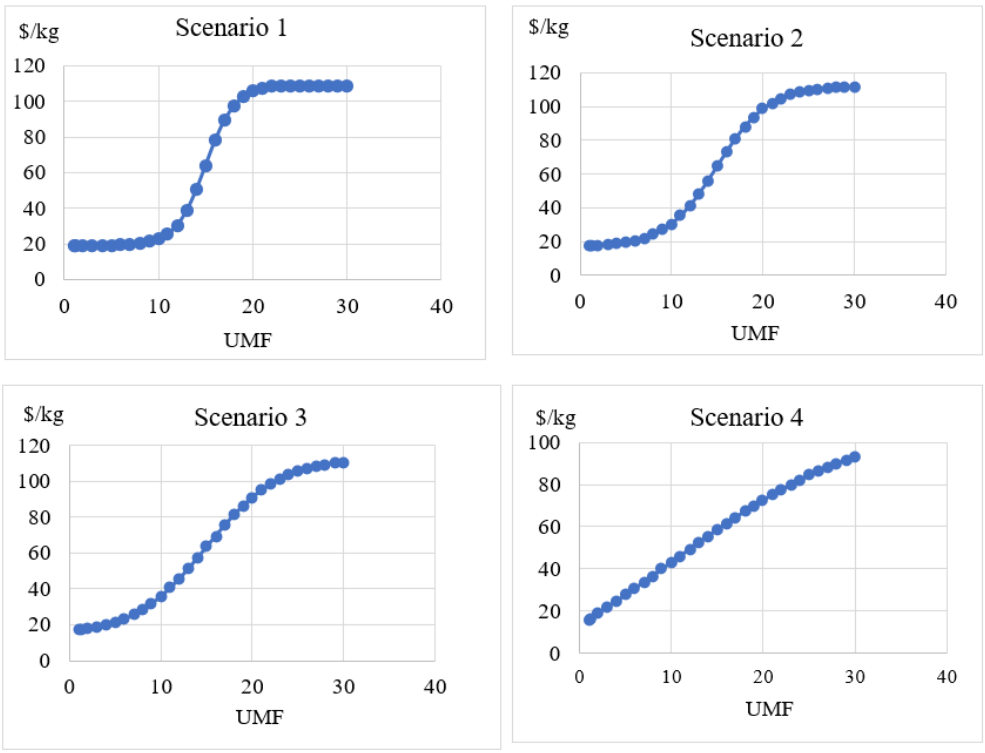

Figure 8.1. *Four scenarios of mānuka honey's pricing values over the past 20 years*

8.2.6. NIR regression and classification models

8.2.6.1. Non-imaging system

❖ Prediction of UMF™ score

Multivariate linear partial least squares (PLS) and linear support vector machine (SVR) regression were employed to predict UMF™ scores from NIR data of 1451 honey samples. A final PLS model gave 72 % accuracy on the test set while SVR model produced 75 % accuracy. The residual predictive deviation (RPD) values obtained were 1.84 & 1.85 for PLS and SVR models, respectively that indicate the potential capability of these models to discriminate between low and high UMF™ values. Since PLS and SVR showed similar RPD values, the PLS model was chosen, being the less complex model.

❖ Classification of UMF™ buckets

Linear partial least squares discriminant analysis (PLSDA) and non-linear support vector machine discriminant analysis (SVMDA) with Gaussian radial basis kernel (rbf) classifiers were used to discriminate five different UMF™ buckets (B_UMF_0, B_UMF_5, B_UMF_10, B_UMF_15 and B_UMF_20) of the 1451 honey dataset. PLSDA classification after optimising spectral regions of interest (Vis: 440 - 700 nm & NIR: 1000 - 1400 nm) by iPLS technique seemingly performed better than SVMDA operated over the full NIR range (350 - 2500 nm). PLSDA and SVMDA gave overall accuracies on the test set of 58.6 % and 55.4 %, respectively. SVMDA could not predict any samples in B_UMF_20 since the number of samples in this class was very small and was considered as a minority group compared to other groups. PLSDA could predict samples in B_UMF_20 although only with 25 % accuracy. Moreover, PLSDA classified samples in B_UMF_10 a full 10 % better than did SVMDA. Other class accuracies of both models were quite comparable (Table 8.4). Thus, the PLSDA model was selected as a final classification model for the NIR non-imaging system.

Table 8.4. Classification outputs of five different UMF™ buckets on the test set of non-imaging PLSDA and SVMDA models

Test data (n = 450 s)	PLSDA CV accuracy: 62 (%)	SVMDA (rbf) CV accuracy: 64.7 (%)
B_UMF_0	78.3	78.6
B_UMF_5	68.1	68.3
B_UMF_10	58.2	47.6
B_UMF_15	54.6	57.8
B_UMF_20	25.0	0
Kappa	0.51	0.36
Prediction accuracy	58.6	55.4

Note: CV means cross-validated

8.2.6.2. Hyperspectral imaging system

❖ Prediction of UMF™ scores

Linear PLS and SVR regression methods were used to estimate UMF™ scores. After discarding irrelevant wavelengths, an optimised PLS model resulted in R^2 (CV) 0.7 & RMSECV 2.756 and R^2 (pred) 0.66 & RMSEP 2.608 on cross-validation and test sets. Analogous to PLS, SVR gave R^2 (CV) 0.64 & RMSECV 3.022 and R^2 (pred) 0.57 and RMSEP 2.944. The RPD number of PLS and SVR were 1.84 and 1.68 which indicates both models could only predict between high and low UMF™ levels. The linear PLS model optimised in

(600 - 1000 & 1040 - 1400 nm) showed a higher predictive performance than the linear SVR model in the full 547 - 1700 nm range. So, the PLS model was chosen as a final model to estimate UMF^{TM} values in hyperspectral imaging system.

❖ Classification of UMF^{TM} buckets

PLSDA and SVMDA (rbf) classifiers were used to differentiate five UMF^{TM} buckets of 1451 samples each with spectrum collected by a hyperspectral imaging system (547 - 1700 nm). SVMDA gave 59 % overall classification accuracy, better than PLSDA (47 % accuracy). Again, SVMDA could not pick up information of samples in B_UMF_20 zone. PLSDA only classified this bucket with a low accuracy of 10 %. Overall, SVMDA did better than PLSDA. The SVMDA model were chosen as a final model. However, this study also calculated the model benefit from a PLSDA model to compare between non-imaging and hyperspectral imaging systems.

Table 8.5. Classification outputs of five different UMF^{TM} buckets on the test set of HSI PLSDA and SVMDA models

Test data (n=450 s)	PLSDA CV accuracy: 47.9 (%)	SVMDA (rbf) CV accuracy: 61.2 (%)
B_UMF_0	67.4	70.0
B_UMF_5	56.7	57.6
B_UMF_10	57.4	58.9
B_UMF_15	47.9	56.1
B_UMF_20	10.3	0
Kappa	0.30	0.36
Prediction accuracy	47.1	59.1

8.3. Results and discussion

8.3.1. Distribution of four imaginary apiaries

Four imaginary apiaries were generated to reflect different scenarios at beehives. H1 contained broad distribution of UMF^{TM}, while H2 and H2+ had at least 63 % frames with high UMF^{TM} (UMF > 17.5 and 12.5 ≤ UMF < 17.5, respectively) and at most 26 % frames of low UMF^{TM} (0 - 7.5). On contrast, H3 had at most 66 % frames of low UMF^{TM} (0 - 7.5) and 4 % frames of high UMF^{TM} > 17.5. These criteria were used for both non-imaging (Figure 8.2) and hyperspectral imaging data (Figure 8.3).

Figures 8.2 and 8.3 display the distribution of four apiaries plotted against UMF^{TM} generated from laboratory data and predicted from both non-imaging and hyperspectral

imaging by PLS regression method. Overall, PLS regression models in both systems predicted lower than laboratory-data derived UMF™ values for samples with UMF™ above 17.5. By contrast, PLS models estimated higher than laboratory-data derived UMF™ values for samples with UMF™ below 5. One reason to explain this might be the imbalanced dataset of 1451 honey samples on which the PLS models were built since the number of samples with UMF™ > 17.5 (B_UMF_20) was less than 50. Most samples were quite equally spread across B_UMF_0, B_UMF_5, B_UMF_10 and B_UMF_15. A balanced calibration dataset might improve the regression model performance.

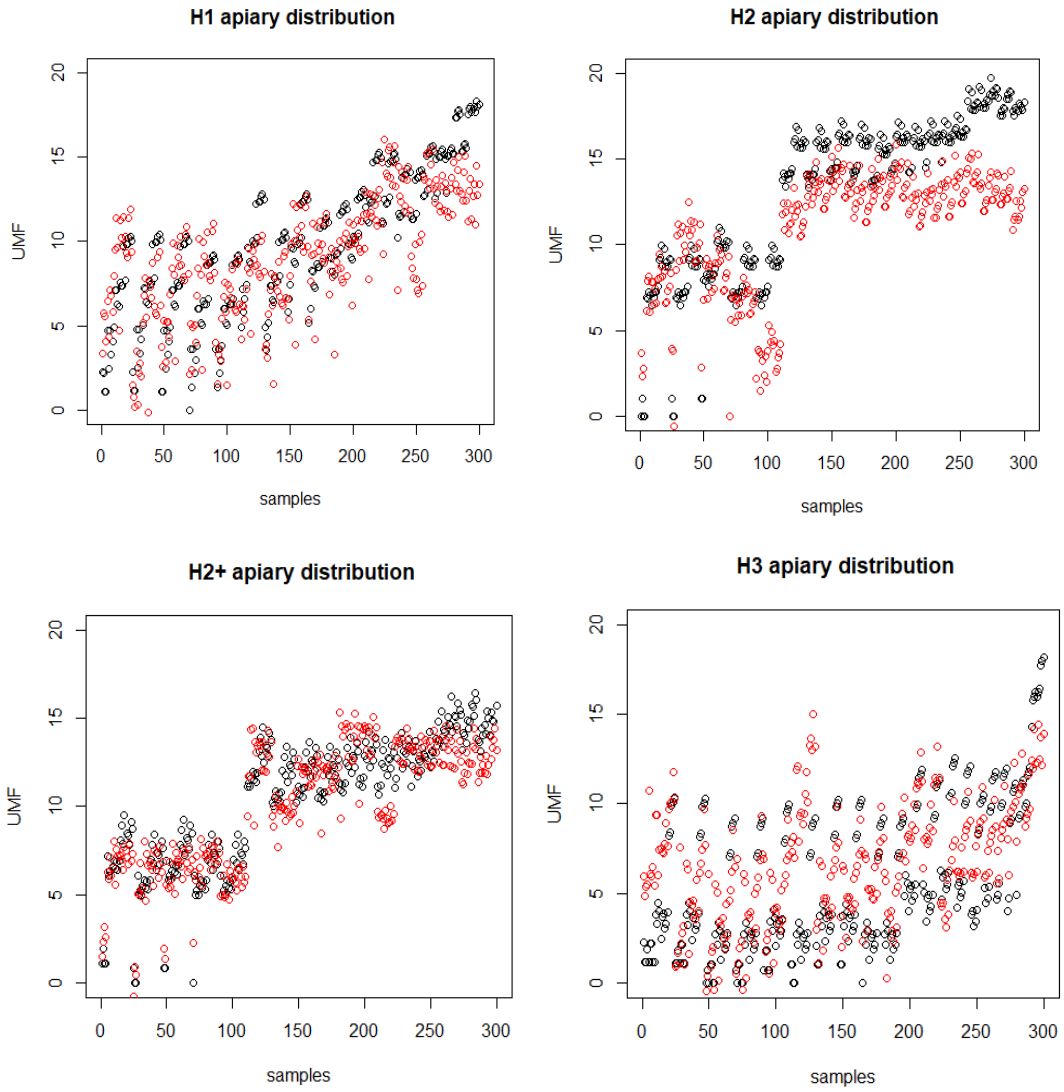

Figure 8.2. *Distribution of four apiaries from non-imaging data. Black circles were honey samples with generated UMF™ scores from the lab. Red circles were predicted UMF™ samples from the PLS regression model*

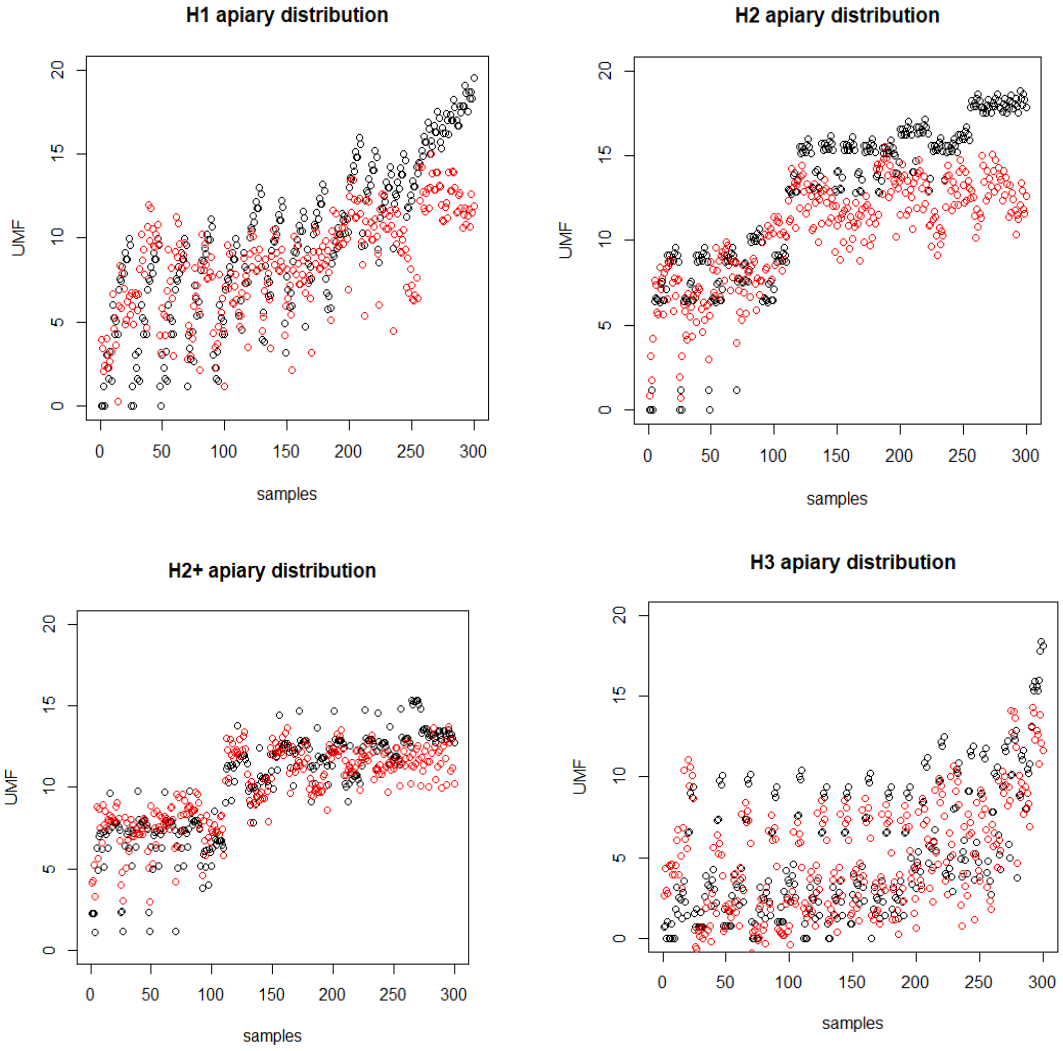

Figure 8.3. *Distribution of four apiaries from hyperspectral imaging data. Black circles were honey samples with generated UMF™ scores from the lab. Red circles were predicted UMF™ samples from PLS regression model*

8.3.2. What benefit arises if honey frames are sorted into different UMF™ buckets?

Currently, mono-floral honey quality is valued on the UMF™ score of a single composite sample taken from a drum with many frames extracted and mixed together. We have imagined that honey-frame UMF™ levels are checked prior to extraction and frames grouped into five different notional buckets (B_UMF_0, B_UMF_5, B_UMF_10, B_UMF_15 and B_UMF_20).

We wish to test whether sorting frames into notional buckets is a good strategy in terms of revenue benefit in comparison to averaging all frames via a real drum.

To test this hypothesis, four apiaries having their UMF^{TM} levels calculated from laboratory data were sorted into five different buckets. Each UMF^{TM} bucket has a pricing value at each pricing curve scenario. Figure 8.4 illustrates the revenue impact of division into buckets as the percentage increase (positive) or decrease (negative) over the bulk average of all frames for four apiaries (H1, H2, H2+ & H3) for both non-imaging and hyperspectral imaging data.

Overall, separation of honey frames into five different buckets brought more benefit for all apiaries (H1, H2, H2+ and H3). The greatest benefit came under the scenario 1 mānuka honey pricing curve with the steepest sigmoid curve. Least gain came from the nearly linear scenario 4 curve.

Figure 8.4 shows the revenue gain of four imaginary apiaries for four different pricing scenarios. Apiaries H1 and H2 gained greatest revenue for pricing scenario 1 for both non-imaging and hyperspectral imaging systems. A similar trend was followed by H2+, then apiary H3. Apiaries H2 & H2+ gained less than 1 % for the pricing scenario 4.

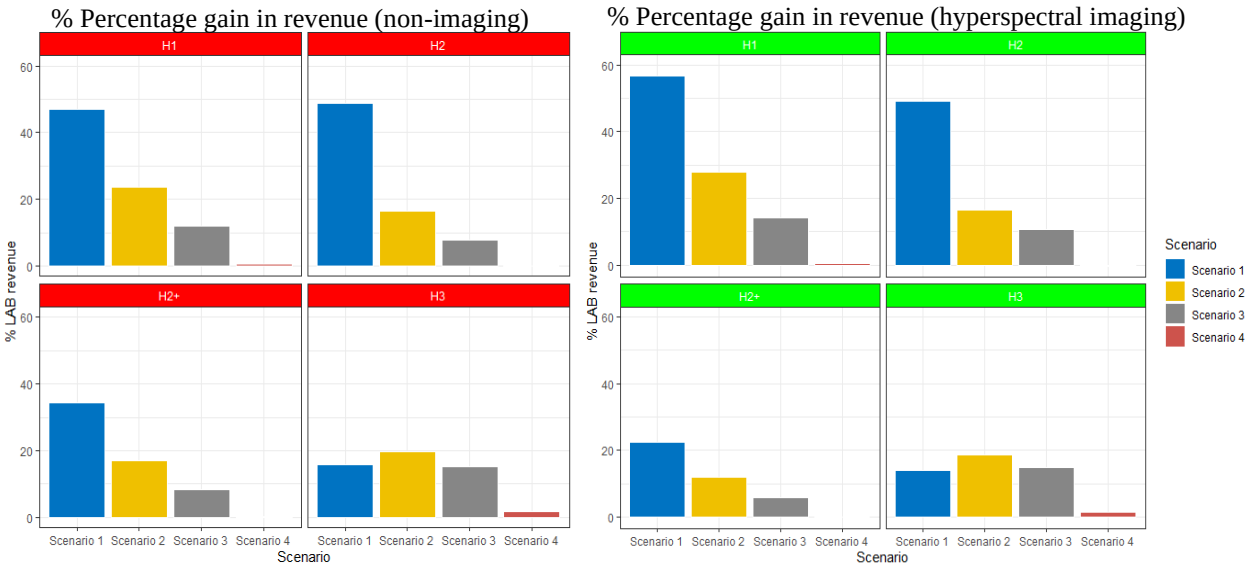

Figure 8.4. *Percentage gain in honey revenue was calculated for four pricing scenarios for four imaginary apiaries (H1, H2, H2+ and H3) with non-imaging laboratory data (left) and hyperspectral imaging laboratory data (right). Revenue percentage was the difference between values from sorting frames in* UMF^{TM} *buckets and averaging all frames*

This dichotomy was not expected with sorting frames into buckets. It was expected that the current bulk averaging system would be the best in apiaries with all frames with UMF^{TM} > 17.5 although this situation was not always true. Closer inspection shows three things: (1) under the linear pricing curve of scenario 4 there is little change in revenue performance gained by apportioning into buckets. And (2) those imaginary apiaries dominated by samples falling where the pricing curve is concave upwards gain the greatest benefit while (3) those dominated by samples in the concave downward portion of the curve gain most revenue where all samples are bulked together. It appears that if a honey is high on a strongly sigmoid pricing curve, there are diminishing returns to higher UMF^{TM} and more gain is had by mixing it to bring the bulk up into the steeper part of the curve. This implies that if the pricing curves is not sigmoid, but continues to steepen, then it is always better to segregate than to mix.

In conclusion, application of sorting honey frames into different buckets before extraction can bring considerable benefit relative to bulk extraction effectively into a single bucket. But this only applies for apiaries which are having a large variation of UMF^{TM} score or all frames with UMF^{TM} < 17.5. It will be better to keep frames together if apiaries have less variation or all frames have UMF^{TM} >17.5.

As yet, we do not know how much of the gain made possible by discriminating into buckets is lost by poor prediction. Next, we compare revenue gains by the bucket method operating on NIR technology results or directly on laboratory-estimated UMF^{TM} level. Sections (8.4 and 8.5) discuss incremental revenue gains brought by bucket classification of laboratory data then from NIR non-imaging and hyperspectral imaging data.

8.3.3. Benefit of NIR non-imaging (350 - 2500 nm)

8.3.3.1. Calculation of regression revenue

- **Evaluation of NIR regression performance based on the revenue benefit**

The selected PLS model was employed to estimate UMF^{TM} scores of apiary H1. Samples with predicted values were put into five different UMF^{TM} buckets. Table 8.6 shows the number of true samples sorted in five buckets against with predictive samples. 6 % Of samples in B_UMF_5 misclassified with B_UMF_10. 14 % Of samples in B_UMF_10 misclassified in B_UMF_15 and 30 % misclassified in B_UMF_5. No samples in B_UMF_0 misclassified with samples in B_UMF_15 and B_UMF_20. No samples in B_UMF_20 were predicted in B_UMF_20, but they were misclassified in B_UMF_15 and B_UMF_10. This meant that the PLS model predicted lower UMF^{TM} values than the true UMF^{TM} reference. The misclassification rate of prediction of UMF^{TM} score for H1 was 0.37. Underprediction at high UMF^{TM} was of particular concern.

The revenue impact of the bucket method over bulk average from a drum was calculated for apiary H1 (Figure 8.5). On the left-hand panel, applying bucket classification to the actual laboratory data gave over 40 % revenue gain for pricing curves 1 down to nil for the linear scenario 4. Non-imaging NIR data from apiary H1 gave gains around half this. The greatest revenue gain occurred under scenario 1 with the greatest curvature in the price-quality relationship. By contrast, negative benefit was gained under the linear pricing scenario 4 from separating honey frames into multiple buckets.

Table 8.6. Non-imaging PLS regression results were sorted in five different buckets for the apiary H1

H1	Reference					
Prediction	B_UMF_0	B_UMF_5	B_UMF_10	B_UMF_15	B_UMF_20	sum
B_UMF_0	6	7	0	0	0	13
B_UMF_5	10	47	18	3	0	78
B_UMF_10	0	24	97	29	3	153
B_UMF_15	0	0	8	38	10	56
B_UMF_20	0	0	0	0	0	0
sum	16	78	123	70	13	300

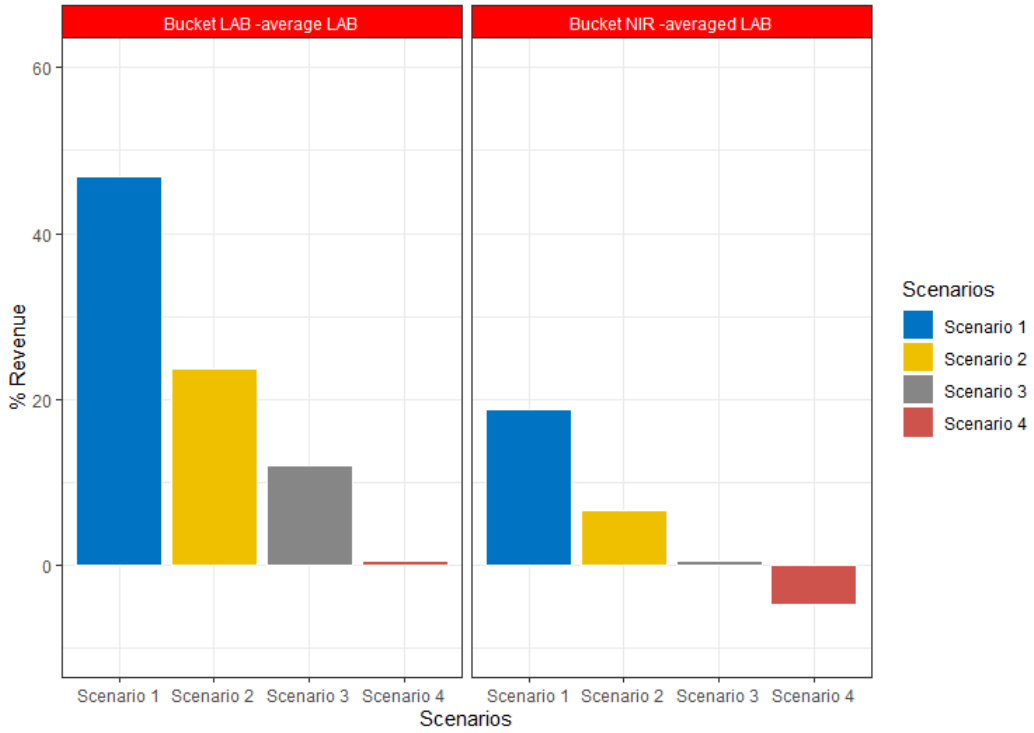

Figure 8.5. *Percentage gain in honey revenue by classifying into multiple quality buckets using a PLS regression model based on non-imaging NIR data revenue (right) compared to the gain achieved by classifying on laboratory data (left) for four different pricing curve scenarios, all for apiary H1 (i.e., 300 frames evenly spread 0 – 20 UMF^{TM})*

If the PLS model of non-imaging data could predict samples in B_UMF_10 (Table 8.7) with 100 % accuracy, limited further revenue gains are made under scenarios 3 and 4 (Figure 8.6). By contrast, if the PLS model correctly estimated 100 % samples in B_UMF_15 (Table 8.8), all scenarios would gain more, up to 12 % revenue increase compared to the original predicted buckets (Figure 8.7). And, if the PLS model could precisely sort 100 % samples in B_UMF_20 (Table 8.9), up to 10 % more revenue could be gained for all scenarios (Figure 8.8) compared to the original PLS model prediction.

Table 8.7. Non-imaging PLS regression results were sorted in different buckets if achieving 100 % prediction into bucket 10 at apiary H1

H1 Prediction	Reference B_UMF_0	B_UMF_5	B_UMF_10	B_UMF_15	B_UMF_20	sum
B_UMF_0	6	7	0	0	0	13
B_UMF_5	10	47	0	3	0	60
B_UMF_10	0	24	123	29	3	179
B_UMF_15	0	0	0	38	10	48
B_UMF_20	0	0	0	0	0	0
sum	16	78	123	70	13	300

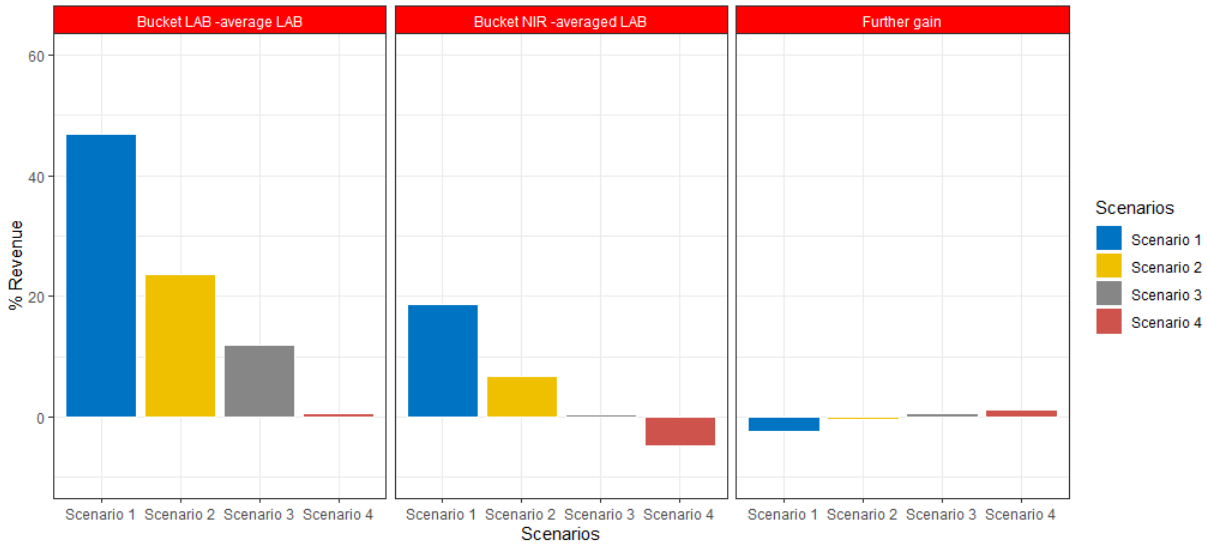

Figure 8.6. *Percentage gain in honey revenue by classifying into multiple quality buckets using a PLS regression model based on non-imaging NIR data revenue with absolute accuracy of prediction at Bucket 10 (middle); additional gain made by perfect accuracy at bucket 10 (right); compared to the gain achieved by classifying on laboratory data (left) for four different pricing curve scenarios, all for apiary H1*

Table 8.8. Non-imaging PLS regression results were sorted in different buckets if achieving 100 % prediction into bucket 15 at apiary H1

H1	Reference					
Prediction	B_UMF_0	B_UMF_5	B_UMF_10	B_UMF_15	B_UMF_20	sum
B_UMF_0	6	7	0	0	0	13
B_UMF_5	10	47	18	0	0	75
B_UMF_10	0	24	97	0	3	124
B_UMF_15	0	0	8	70	10	88
B_UMF_20	0	0	0	0	0	0
sum	16	78	123	70	13	300

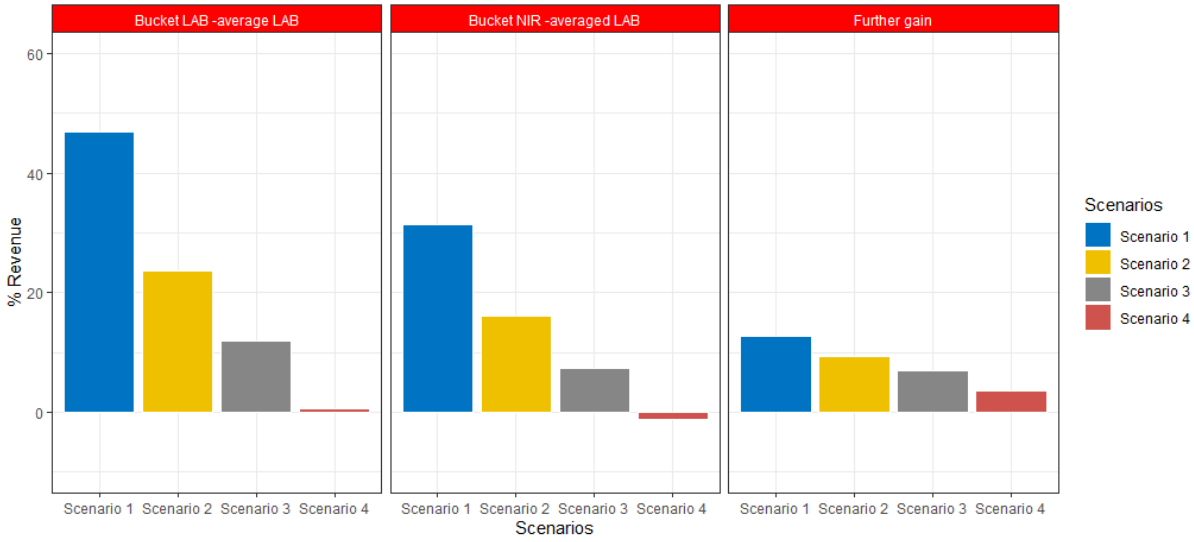

Figure 8.7. *Percentage gain in honey revenue by classifying into multiple quality buckets using a PLS regression model based on non-imaging NIR data revenue with absolute accuracy of prediction at Bucket 15 (middle); additional gain made by perfect accuracy at bucket 15 (right); compared to the gain achieved by classifying on laboratory data (left) for four different pricing curve scenarios, all for apiary H1*

Table 8.9. Non-imaging PLS regression results were sorted in different buckets if achieving 100 % prediction into bucket 20 at apiary H1

H1 Prediction	Reference B_UMF_0	B_UMF_5	B_UMF_10	B_UMF_15	B_UMF_20	sum
B_UMF_0	6	7	0	0	0	13
B_UMF_5	10	47	18	3	0	78
B_UMF_10	0	24	97	29	0	150
B_UMF_15	0	0	8	38	0	46
B_UMF_20	0	0	0	0	13	13
sum	16	78	123	70	13	300

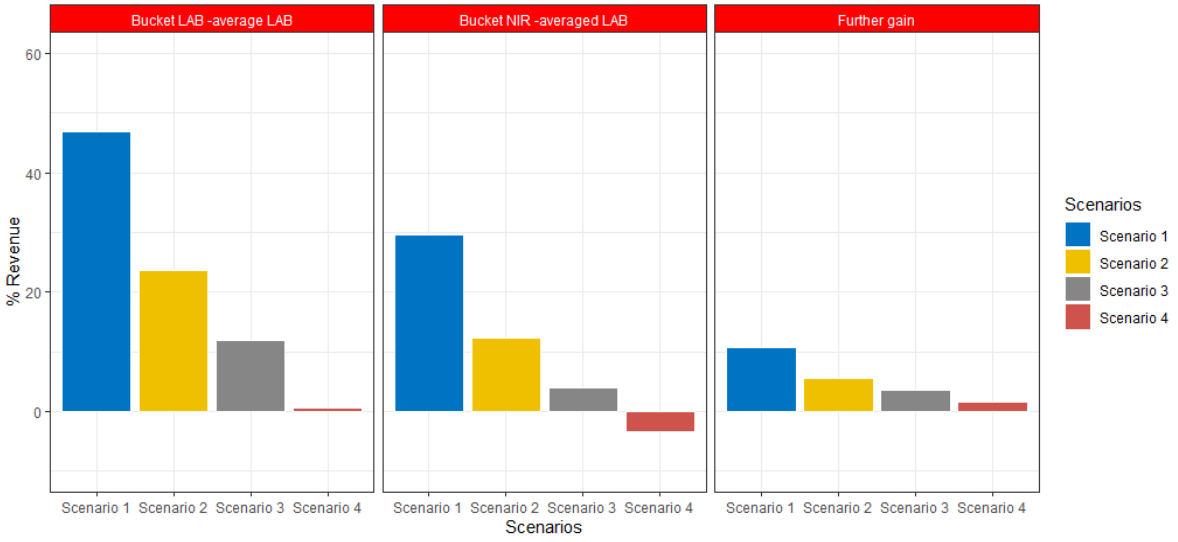

Figure 8.8. *Percentage gain in honey revenue by classifying into multiple quality buckets using a PLS regression model based on non-imaging NIR data with absolute accuracy of prediction at Bucket 20 (middle); additional gain made by perfect accuracy at bucket 20 (right); compared to the gain achieved by classifying on laboratory data (left) for four different pricing curve scenarios, all for apiary H1*

This analysis shows that revenue gains are possible if the predictions are accurate in the right zones. Therefore, future modelling aims to improve the accuracy of the PLS regression model performance for samples in B_UMF_15 and B_UMF_20 zones. Improving the accuracy of predicting samples in B_UMF_20 might not be easy for the current dataset due to the relatively small number of samples (< 50) in that zone. Enhancing the precision of estimating samples in B_UMF_15 could be possible. It is suggested that using a classification method for each UMF^{TM} bucket might be better than a regression method (next section 8.4.2).

❖ Impact of apiary variability on revenue gains using NIR-based UMF™ predictions

Figure 8.9 illustrates the total percentage revenue gain (or loss) for four imaginary apiaries (H1, H2, H2+ and H3) using non-imaging NIR data and laboratory data for sorting into five different buckets relative to the current method of bulk extraction. The right-hand panel shows laboratory data grouped into buckets relative to laboratory data lumped into a single bucket; the left panel shows non-imaging NIR data relative to laboratory data in a single bucket. As mentioned in section 8.3.1, apiary H2 with a large proportion of its UMF™ distribution above 17.5 UMF™ did not earn any additional value through assigning frames into different buckets using an NIR data-derived model. This looks to be a modelling deficiency deriving from a paucity of top-quality samples in the calibration set and is not fundamental.

Laboratory data show greater revenue in all cases, with greater increase for greater price-quality curvature. The model built from non-imaging NIR data shows revenue increase for three imaginary apiaries H1, H2+ and H3. Greatest benefit was obtained under scenario 1 for apiaries H1 & H2+. Apiary H3 was anomalous having most benefit under scenario 2 and 3 - H3 contained mainly samples with UMF™ level (7.5 -12.5) (Figure 8.9). For scenario 4, the near straight-line price-quality curve, H1 and H2+ did not increase in value using multiple buckets but apiary H3 gained over 10 % (Figure 8.9).

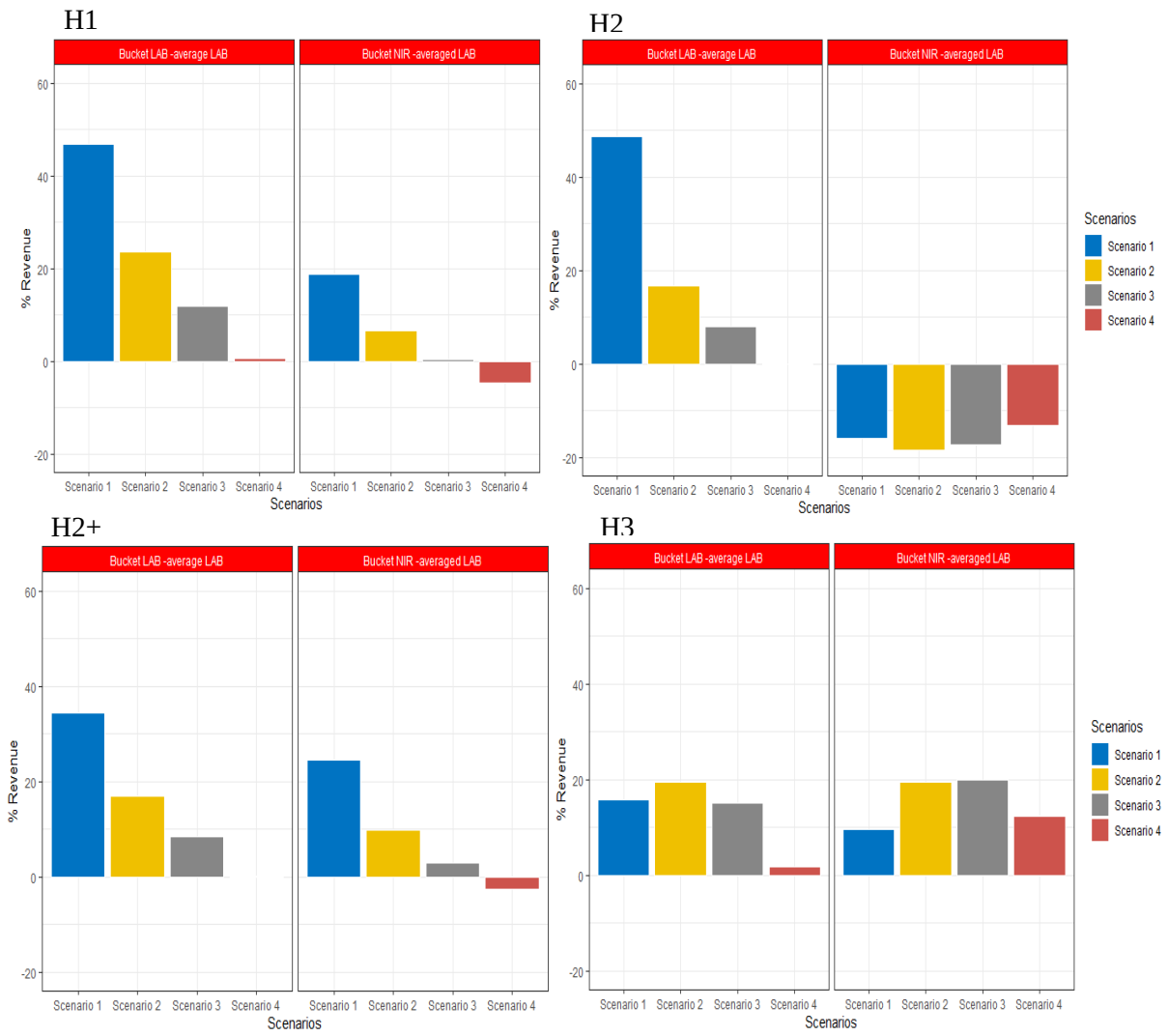

Figure 8.9. *Percentage gain in honey revenue by separating into different UMF™ buckets by PLS model of non-imaging NIR (right) and laboratory-derived data (left) for four different pricing curve scenarios (Scenario 1, Scenario 2, Scenario 3 and Scenario 4) at apiaries H1, H2, H2+ and H3*

Figure 8.10 displays contour plots of UMF™ against pricing scenarios. Contours reflect percentage revenue change of grouping frames at each non-imaging NIR model-predicted UMF™ bucket relative to the averaged laboratory revenue for four different pricing scenarios. Any zone coloured black represents reduced revenue. Red zones represent over 50 % gain in revenue from grouping into five buckets on NIR predication rather than into one bucket by laboratory data. To generate smooth contour plots adjacent pricing curves were interpolated by Origin software (Origin, version 2020). As expected, greatest benefit was from pricing curve 1 for all apiaries containing frames in UMF™ bucket 15 (H2, H2+). No benefit was obtained from UMF™ bucket 20 for any apiary, especially apiary H2 since the NIR non-imaging model

underpredicted UMF^{TM} > 17.5. H2+ showed the largest NIR revenue gain from UMF^{TM} bucket 15 for pricing scenario 1. Meanwhile, apiaries H1 and H3 had greatest revenue in UMF^{TM} buckets 5 and 10, respectively relative to their majority frames in these bucket zones.

In summary, apiaries having a large variation of UMF^{TM} benefited most from classifying into multiple buckets. Only apiaries with a predominance of very high-quality honey failed to benefit, but that appears to be a weakness in the current predictive models rather than a problem fundamental to the approach. Ultimately models may need to be selected for their ability to perform well at the most sensitive parts of the quality range.

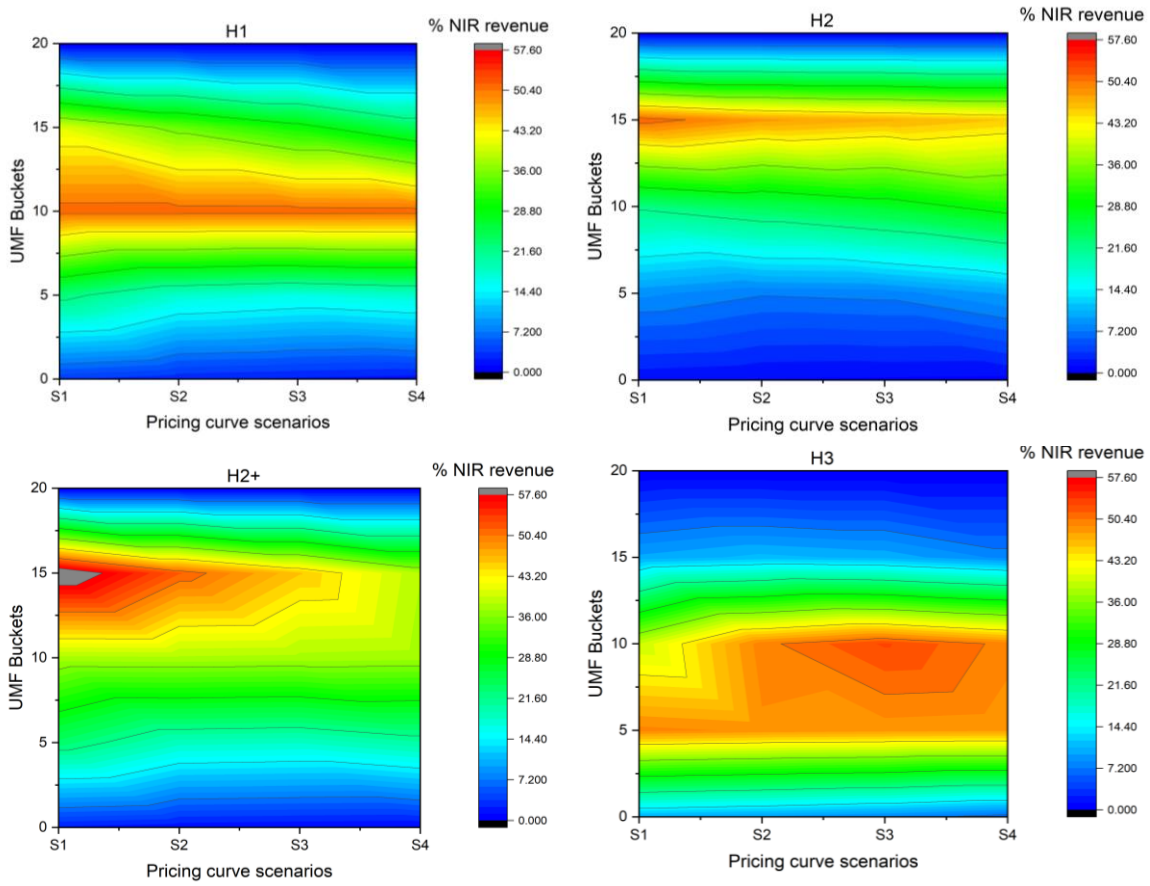

Figure 8.10. *Contour plots of percentage change in revenue from grouping frames into UMF^{TM} buckets by model based on non-imaging NIR relative to revenue from averaging across all frames UMF^{TM} calculated from laboratory data, for four different pricing curve scenarios (Scenario 1, Scenario 2, Scenario 3 and Scenario 4) for apiaries H1, H2, H2+ and H3*

8.3.3.2. Calculation benefit from the PLSDA classification model

In contrast to PLS regression, the PLSDA classification model discriminated samples between B_UMF_0, B_UMF_5 and B_UMF_10, but misclassification arose between samples in B_UMF_10 and B_UMF_15 and B_UMF_20. Figure 8.11 illustrates the percentage of samples classified in different buckets from the final PLSDA classification model compared with the true laboratory values for all four imaginary apiaries. The misclassification rate of this PLSDA model was 0.41 which was higher than that of the PLS regression model.

In general, the PLSDA model over-rated samples which originally came from B_UMF_10 into B_UMF_15 & B_UMF_20. No sample from B_UMF_0 was misclassified into B_UMF_15 & B_UMF_20, and no samples in B_UMF_5 were misclassified into B_UMF_20; few samples were misclassified in B_UMF_15.

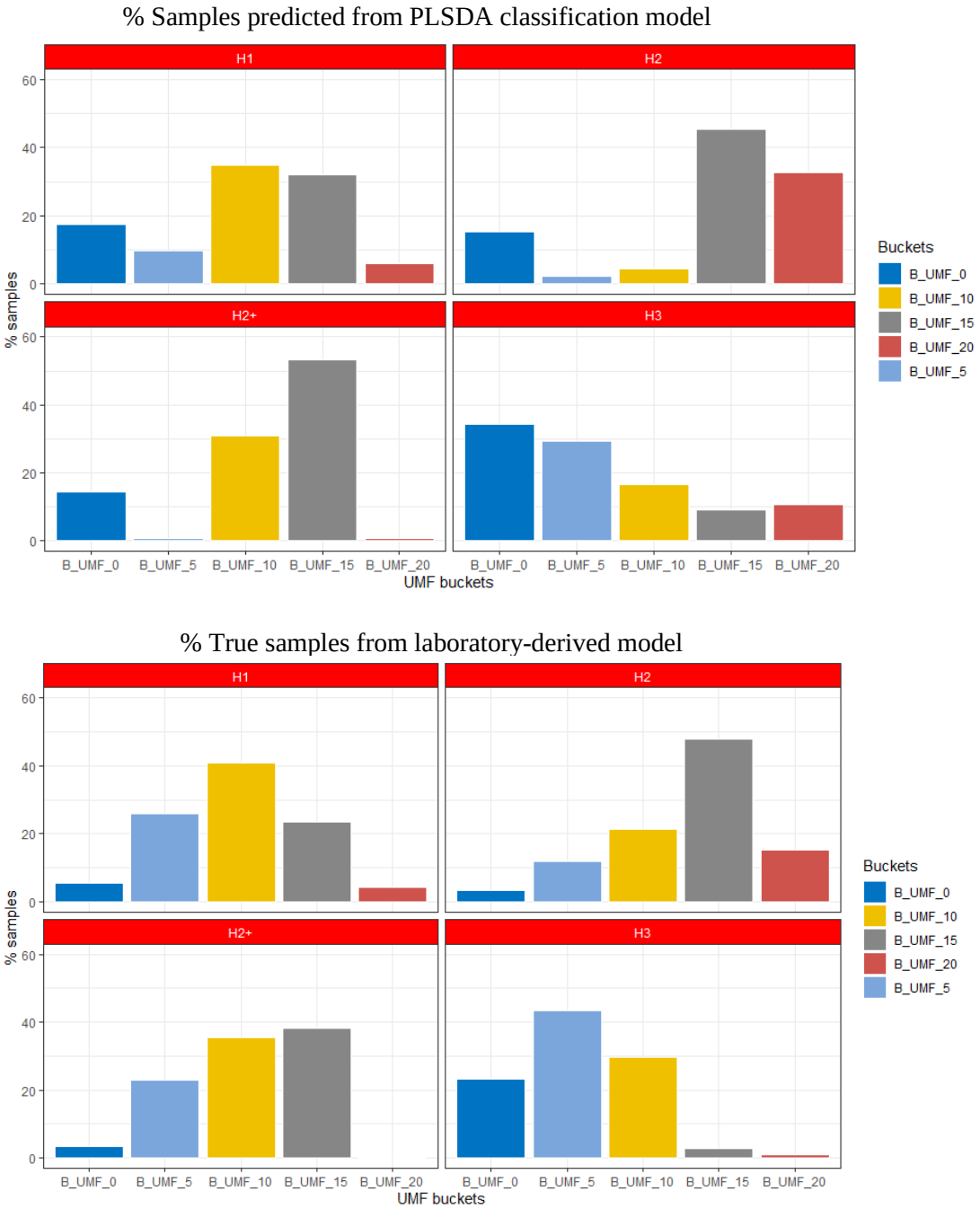

Figure 8.11. *Percentage of samples classified from a non-imaging NIR PLSDA classification model (top) and from laboratory-derived model of true samples (bottom) sorted in five different buckets (B_UMF_0, B_UMF_5, B_UMF_10, B_UMF_15 and B_UMF_20) at apiaries H1, H2, H2+ and H3*

The percentage revenue gain from the NIR PLSDA classification was calculated for four imaginary apiaries with four different mānuka honey pricing scenarios (Figure 8.12). As with the PLS regression models, additional revenue from NIR PLSDA was earned with apiaries H1,

H2+ and H3 for four pricing scenarios. Apiary H2 also obtained further gain in revenue at most 5 %, but only for scenarios 2 and 3, an effect not seen with the PLS regression models. All apiaries (H1, H2+ & H3) were predicted to increase revenue more by the NIR PLSDA than by the laboratory data-derived model using the scenario 1 pricing curve. This linked to a high number of samples estimated into B_UMF_15 & B_UMF_20.

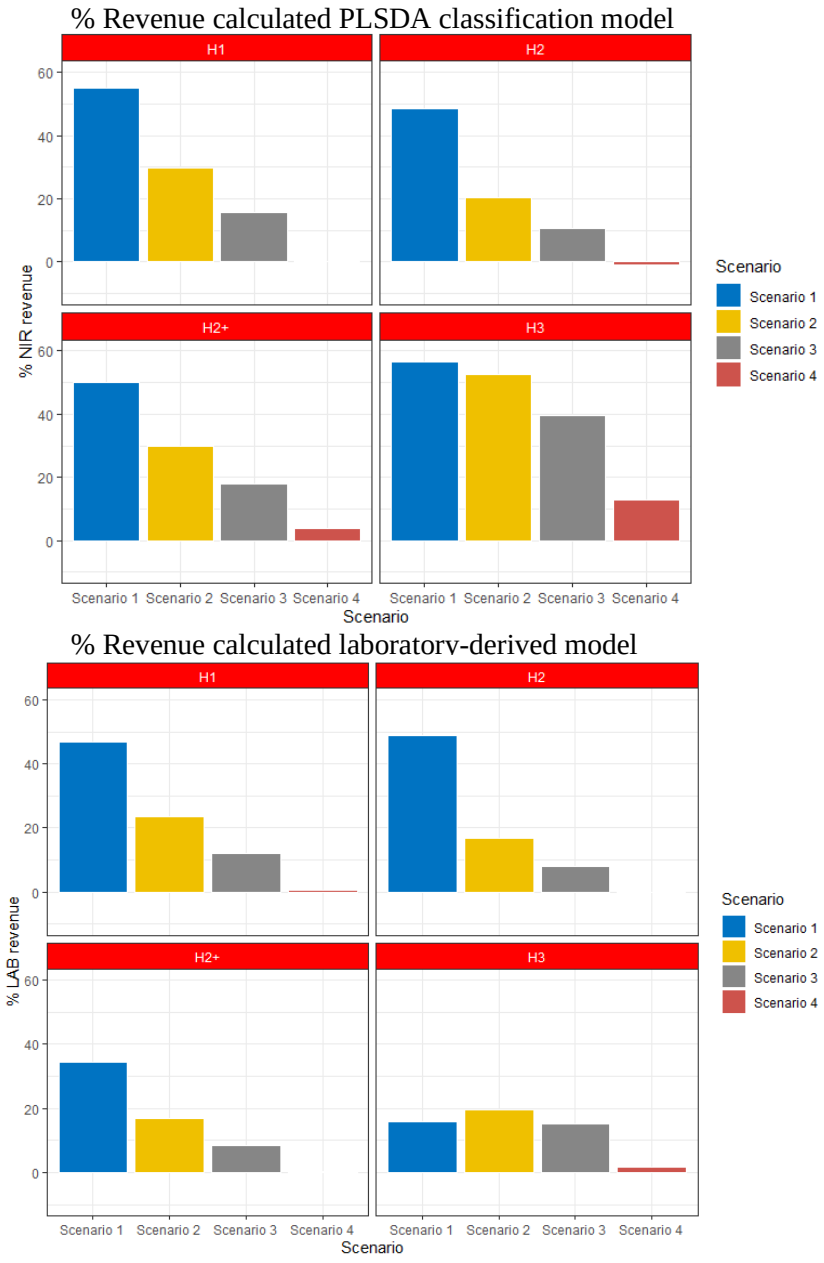

Figure 8.12. *Percentage gain in honey revenue was quantified from a non-imaging NIR classification PLS model (top) compared with that of laboratory-derived model (bottom) for four different scenarios (Scenario 1, Scenario 2, Scenario 3, and Scenario 4) at apiaries H1, H2, H2+ and H3*

8.3.3.3. Comparison between regression and classification models

The additional revenue calculated from the classification method exceeded that of regression, but it may have over-rated samples into higher classifications (Figure 8.13). The regression model predicted lower UMF^{TM} scores for samples in B_UMF_20 (UMF^{TM} > 17.5) but may have under-estimated UMF^{TM} at the high-quality end. Thus, the classification method returned more benefit than regression at this stage of model development.

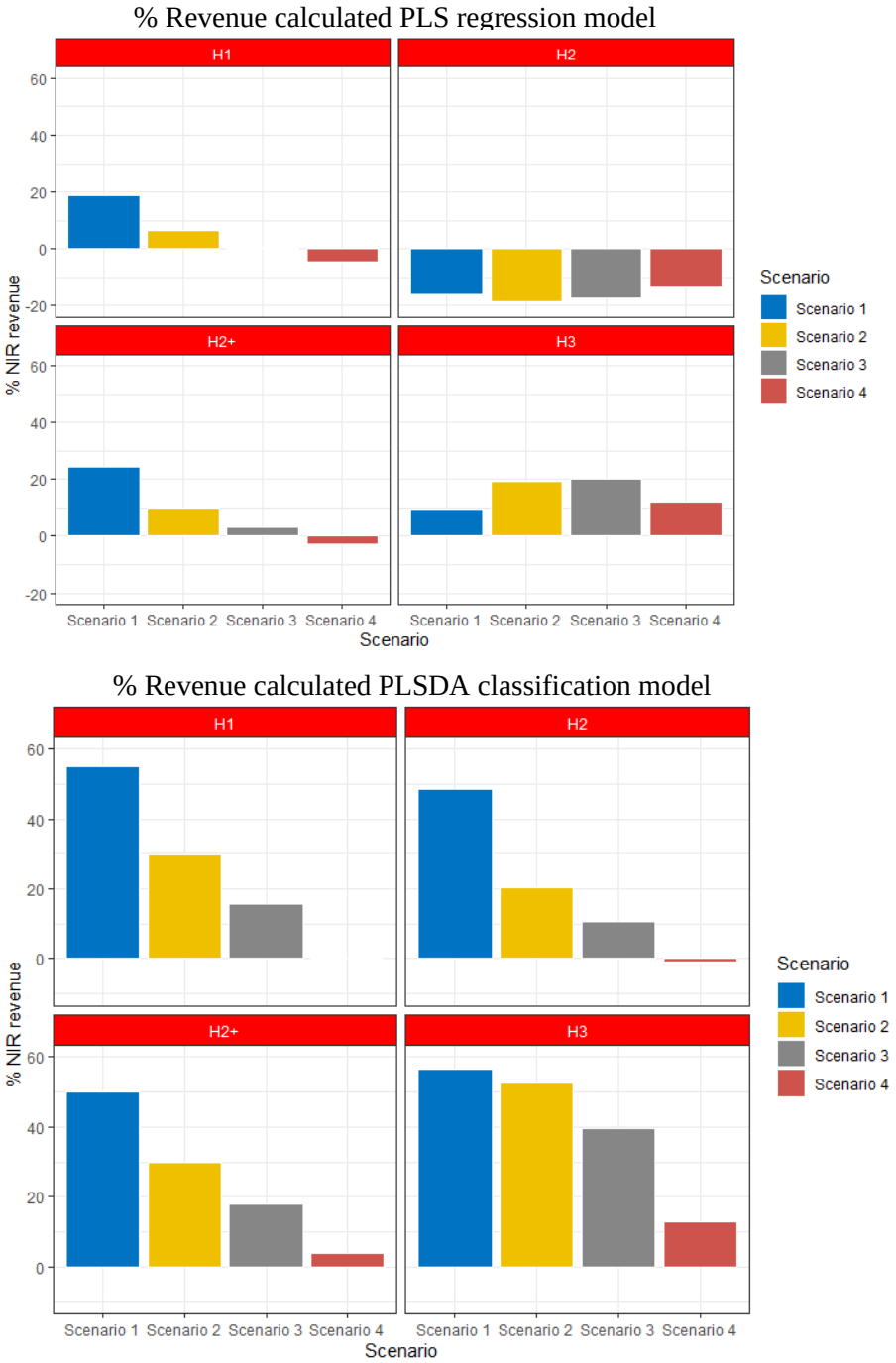

Figure 8.13. *Percentage gain in honey revenue was quantified from a non-imaging NIR regression PLS model (top) compared with that of classification PLSDA model (bottom) for four different scenarios (Scenario 1, Scenario 2, Scenario 3, and Scenario 4) at apiaries H1, H2, H2+ and H3*

8.3.4. Benefit of NIR hyperspectral imaging (547 – 1700 nm)

8.3.4.1. Calculation of regression revenue

- **Evaluation of HSI NIR regression performance based on the revenue benefit**

The final PLS regression model built from hyperspectral imaging data was used to estimate UMF^{TM} scores for all imaginary honey frames from four apiaries H1, H2, H2+ and H3. Table 8.10 displays the regression prediction at apiary H1 after putting frames into five different UMF^{TM} buckets. The results showed there was misclassification between samples in B_UMF_5 and B_UMF_10 or between B_UMF_10 and B_UMF_15. No sample in B_UMF_0 was misclassified with samples in B_UMF_15 and B_UMF_20. However, there were a few samples in B_UMF_5 misclassified with samples in B_UMF_15. No samples were predicted in B_UMF_20, but true samples in B_UMF_20 were misclassed as B_UMF_10 or B_UMF_15. The misclassification rate was 0.45, which was 0.1 higher than that of a PLS regression model from non-imaging data. A familiar pattern is visible however: higher quality samples were underrated, and lower ones overrated.

Figure 8.14 shows the percentage change in revenue from apiary H1 from sorting frames into different buckets. Apiary H1 contained a large variation of UMF^{TM} distribution from 0 to 20. Only under mānuka honey pricing scenario 1 did earnings increase. No benefit was found in cases of scenario 2, 3 and 4. This is a long way short of the increased returns available using laboratory data (left side of Figure 8.14) and was lower than results for four scenarios of non-imaging NIR data modelled by PLS regression (section 8.3.3.1). The predictive models need further tuning.

Table 8.10. HSI PLS regression results were sorted in different buckets for the apiary H1

H1		Reference				
Prediction	B_UMF_0	B_UMF_5	B_UMF_10	B_UMF_15	B_UMF_20	sum
B_UMF_0	4	4	0	0	0	8
B_UMF_5	17	48	26	4	0	95
B_UMF_10	1	17	93	50	9	170
B_UMF_15	0	0	1	21	5	27
B_UMF_20	0	0	0	0	0	0
sum	22	69	120	75	14	300

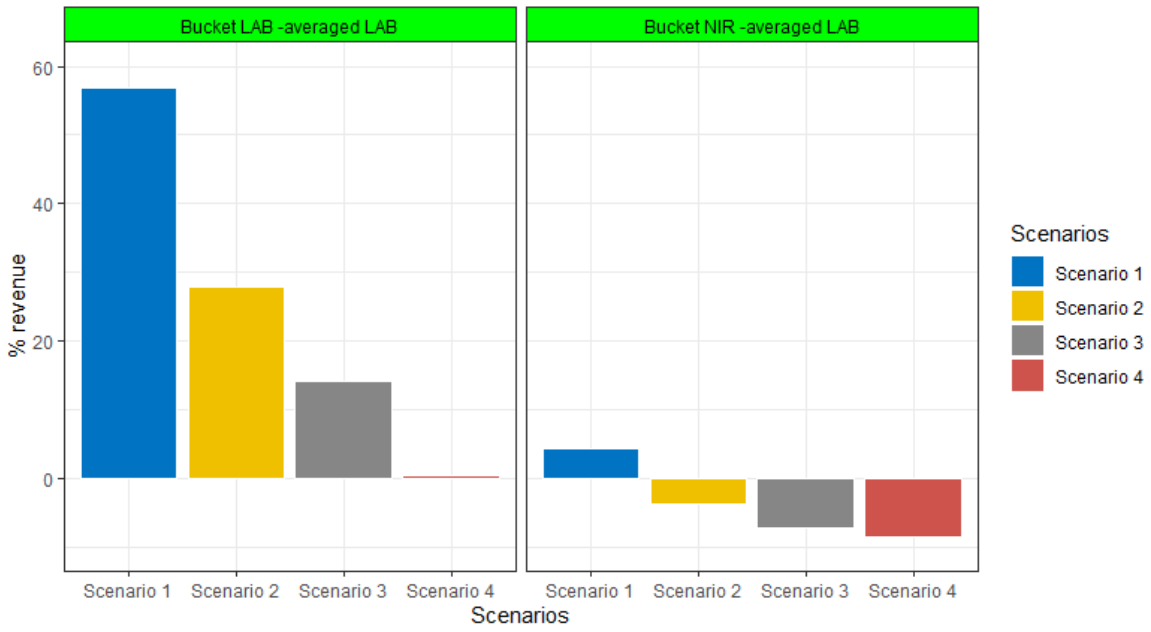

Figure 8.14. *Percentage gain in honey revenue by classifying into multiple quality buckets using a PLS regression model based on HSI NIR data (right) compared to the gain achieved by classifying on laboratory data (left) for four different pricing curve scenarios, all for apiary H1 (i.e., 300 frames evenly spread 0 – 20 UMF™)*

If a HSI NIR PLS regression model could improve to 100 % accuracy in predicting all samples at B_UMF_10 (Table 8.11 & Figure 8.15), the revenue could increase more, but under 5 % more. If samples in B_UMF_15 were estimated at 100 % accuracy (Table 8.12 & Figure 8.16), all scenarios of mānuka pricing value gain further revenue increase, up to 16 % beyond the base model. And if 100 % of all samples in B_UMF_20 were correctly estimated, up to 15 % more revenue could be earned (Table 8.13 & Figure 8.17). Thus, the model predictive accuracy needs to be improved in the B_UMF_15 & B_UMF_20 zones.

Table 8.11. HSI PLS regression results were sorted in different buckets if achieving 100 % prediction into bucket 10 at apiary H1

H1		Reference				
Prediction	B_UMF_0	B_UMF_5	B_UMF_10	B_UMF_15	B_UMF_20	sum
B_UMF_0	4	4	0	0	0	8
B_UMF_5	17	48	0	4	0	91
B_UMF_10	1	17	120	50	9	120
B_UMF_15	0	0	1	26	5	81
B_UMF_20	0	0	0	0	0	0
sum	22	69	120	75	14	300

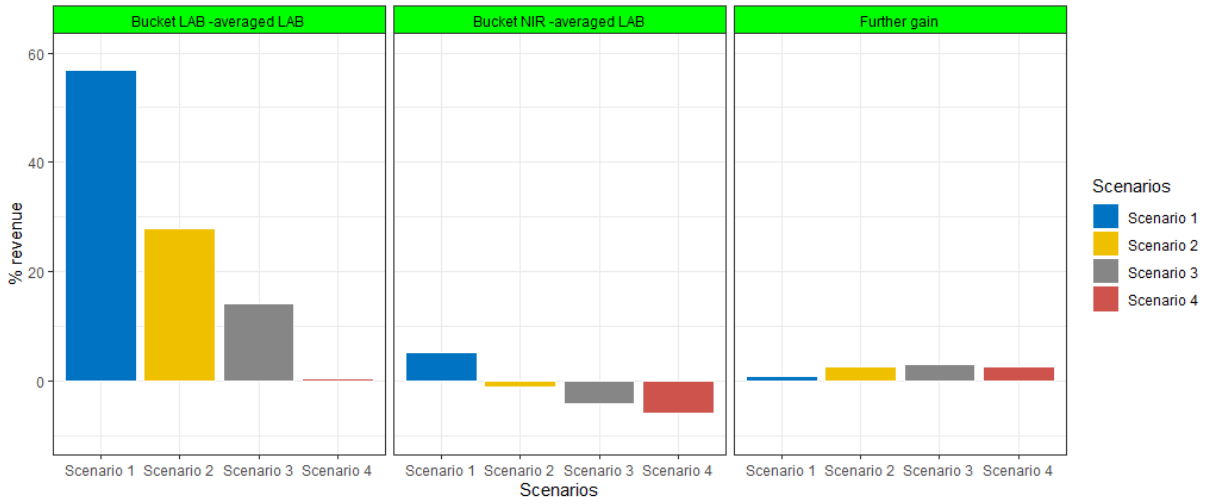

Figure 8.15. *Percentage gain in honey revenue by classifying into multiple quality buckets using a PLS regression model based on HSI NIR data with absolute accuracy of prediction at Bucket 10 (middle); additional gain made by perfect accuracy at bucket 10 (right); compared to the gain achieved by classifying on laboratory data (left) for four different pricing curve scenarios, all for apiary H1*

Table 8.12. HSI PLS regression results were sorted in different buckets if achieving 100 % prediction into bucket 15 at apiary H1

H1		Reference				
Prediction	B_UMF_0	B_UMF_5	B_UMF_10	B_UMF_15	B_UMF_20	sum
B_UMF_0	4	4	0	0	0	8
B_UMF_5	17	48	26	0	0	91
B_UMF_10	1	17	93	0	9	120
B_UMF_15	0	0	1	75	5	81
B_UMF_20	0	0	0	0	0	0
sum	22	69	120	75	14	300

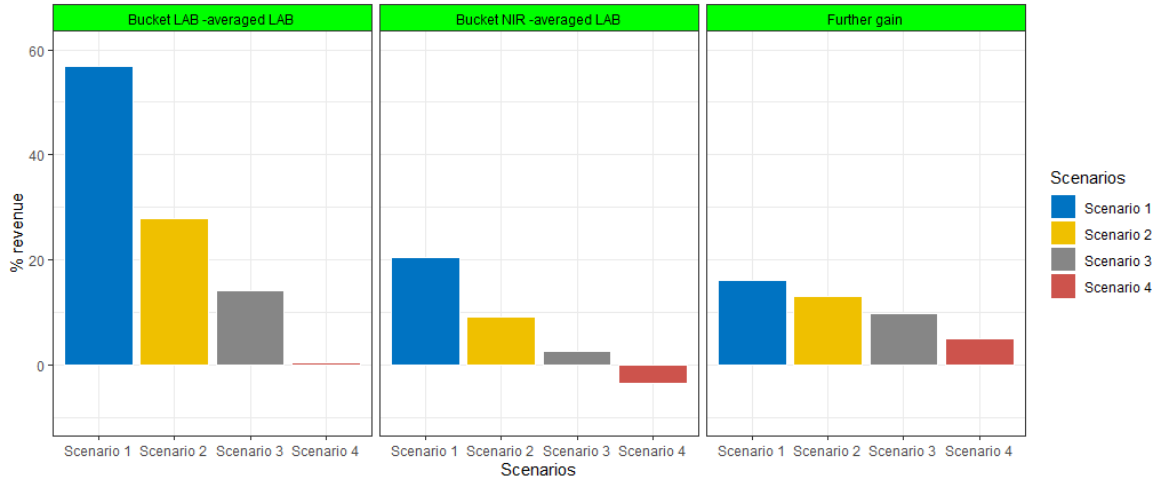

Figure 8.16. *Percentage gain in honey revenue by classifying into multiple quality buckets using a PLS regression model based on HSI NIR data with absolute accuracy of prediction at Bucket 15 (middle); additional gain made by perfect accuracy at bucket 15 (gain); compared to the gain achieved by classifying on laboratory data (left) for four different pricing curve scenarios, all for apiary H1*

Table 8.13. HSI PLS regression results were sorted in different buckets if achieving 100 % prediction into bucket 20 at apiary H1

H1 Prediction	Reference B_UMF_0	B_UMF_5	B_UMF_10	B_UMF_15	B_UMF_20	sum
B_UMF_0	4	4	0	0	0	8
B_UMF_5	17	48	26	4	0	95
B_UMF_10	1	17	93	50	0	161
B_UMF_15	0	0	1	21	0	22
B_UMF_20	0	0	0	0	14	14
sum	22	69	120	75	14	300

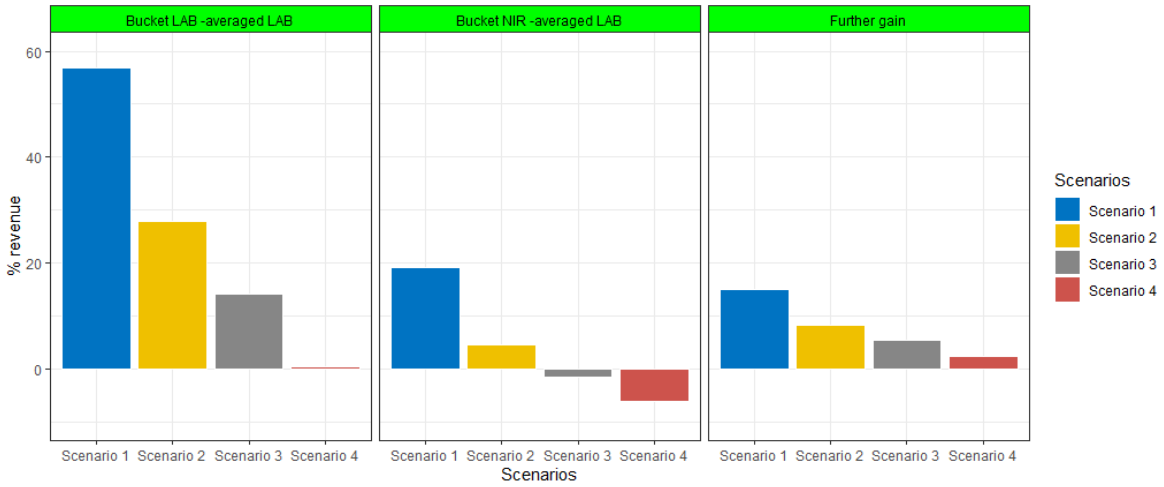

Figure 8.17. *Percentage gain in honey revenue by classifying into multiple quality buckets using a PLS regression model based on HSI NIR data with absolute accuracy of prediction at Bucket 20 (middle); additional gain made by perfect accuracy at bucket 20 (right); compared to the gain achieved by classifying on laboratory data (left) for four different pricing curve scenarios, all for apiary H1*

❖ Comparison of the revenue among four different apiaries

Figure 8.18 shows the total percentage gain in honey revenue from a NIR-derived model (right) and a laboratory-derived model (left) for four imaginary apiaries. Overall, only apiaries H1, H2+ and H3 benefited from the current HSI NIR regression model when separating frames into five UMF^{TM} buckets. Apiary H2 with a high level of UMF^{TM} >17.5 lost revenue by separating frames into different UMF^{TM} buckets due to the underestimation of UMF^{TM} values in buckets 15 and 20. Further investigation indicates that it is better to keep frames together if all frames obtained UMF^{TM} > 17.5. If there is a large variation of UMF^{TM} levels or UMF^{TM} < 17.5, it is suggested to divide frames into different buckets.

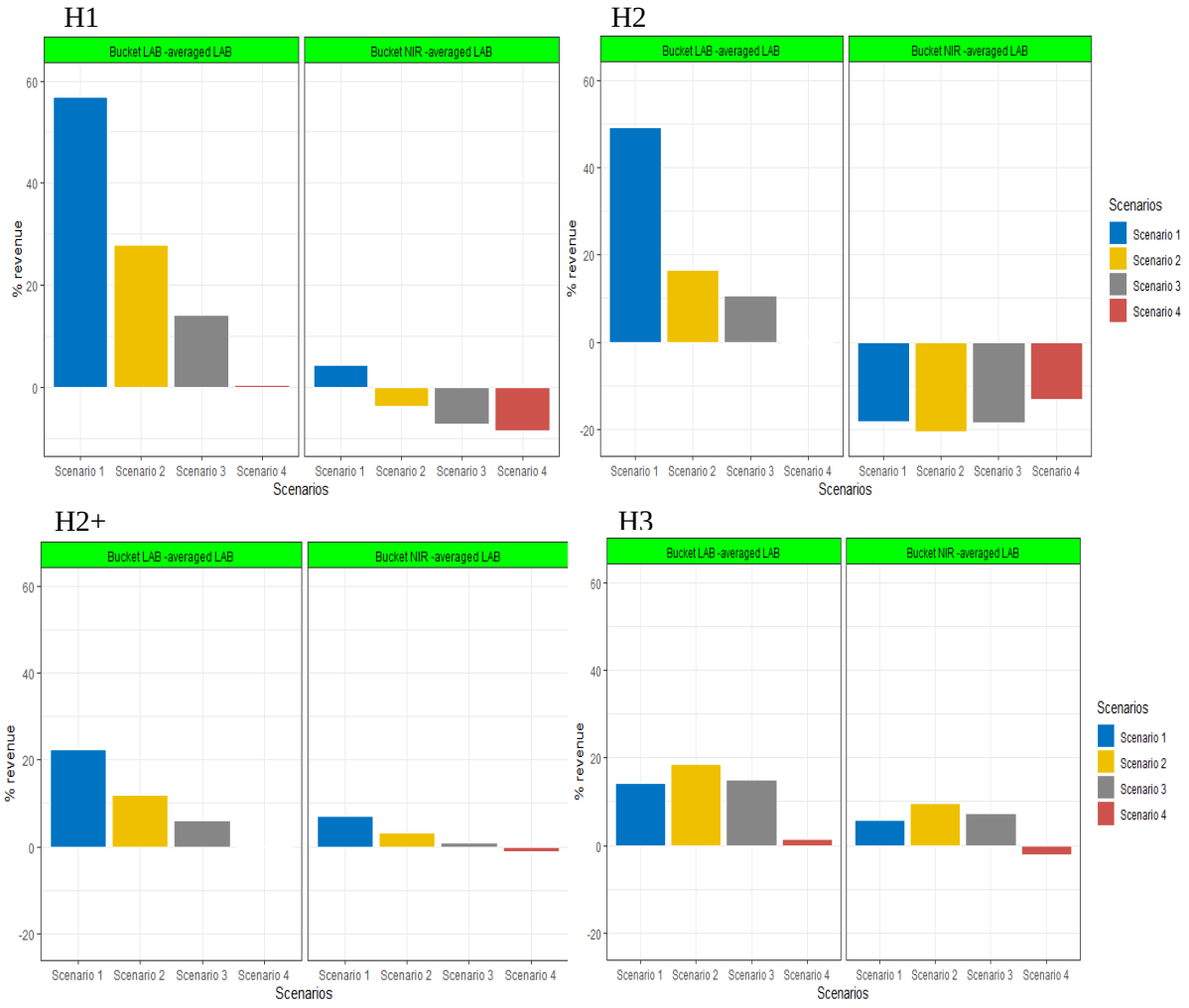

Figure 8.18. *Percentage gain in honey revenue of HSI NIR model (right) and laboratory-derived model (left) for four different scenarios (Scenario 1, Scenario 2, Scenario 3, and Scenario 4) at apiary H1, H2, H2+ and H3*

Figure 8.19 displays contour plots of percentage change in revenue generated by grouping frames at each HSI NIR model-predicted UMF^{TM} bucket relative to the averaged laboratory revenue for four different pricing scenarios. It was unexpected that greatest benefit did not come from the pricing curve 1 due to the underprediction of the HSI regression model for frames with UMF^{TM} > 15. No benefit was returned from UMF^{TM} bucket 20 for any apiary. H2 did not get the highest NIR revenue gain in bucket 20 and 15 for pricing scenario 1 but had the greatest revenue in UMF^{TM} bucket 10 under the pricing scenario 4. Also, H1 & H2 did not gain revenue in UMF^{TM} bucket 20 and 15. Their greatest revenue gain was obtained from frames in bucket 10 (7.5 ≤ UMF^{TM} <12.5) for all pricing scenarios. H3 obtained the highest revenue gain in bucket 5 for the pricing curve 4. Overall, the HSI NIR regression model underestimated even more than did the non-imaging NIR regression model, which did not bring much revenue gain of frames in UMF^{TM} buckets 20 and 15. This seemed to correspond to both a deficiency of samples in bucket 20 and the inefficiency of regression modelling for estimating frames in bucket 15.

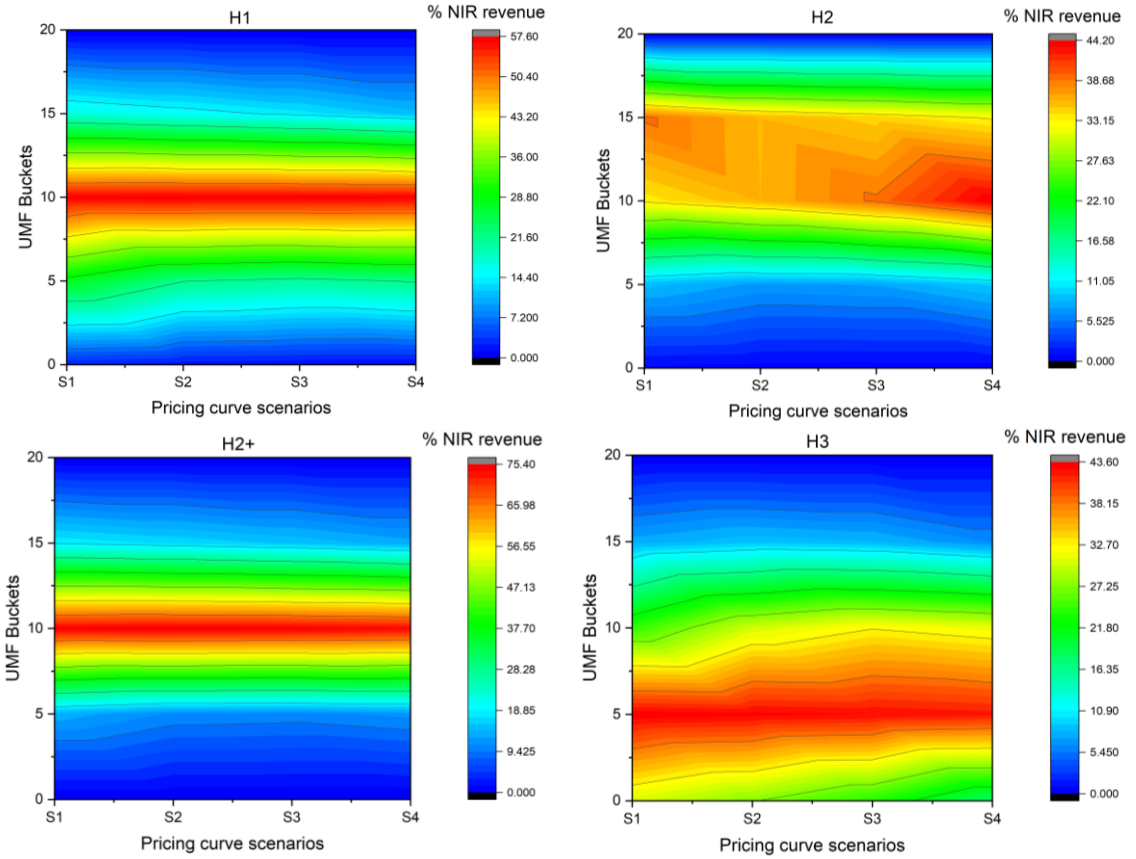

Figure 8.19. *Contour plots of percentage change in revenue from grouping frames into UMF^{TM} buckets by model based on HSI NIR relative to revenue from averaging across all frames UMF^{TM} calculated from laboratory data, for four different pricing curve scenarios (Scenario 1, Scenario 2, Scenario 3 and Scenario 4) for apiaries H1, H2, H2+ and H3*

8.3.4.2. Calculation of HSI classification revenue

To improve the accuracy of sorting frames into B_UMF_15 and B_UMF_20, HSI classification technique was applied to sort frames into five different buckets. The SVMDA model obtained 66 % overall accuracy which was better than the PLSDA model (54 % accuracy). SVMDA may have improved the accuracy of prediction of samples in B_UMF_15, but no true samples were correctly placed in B_UMF_20; instead they were misclassified into B_UMF_10 & UMF_15 (Figure 8.20).

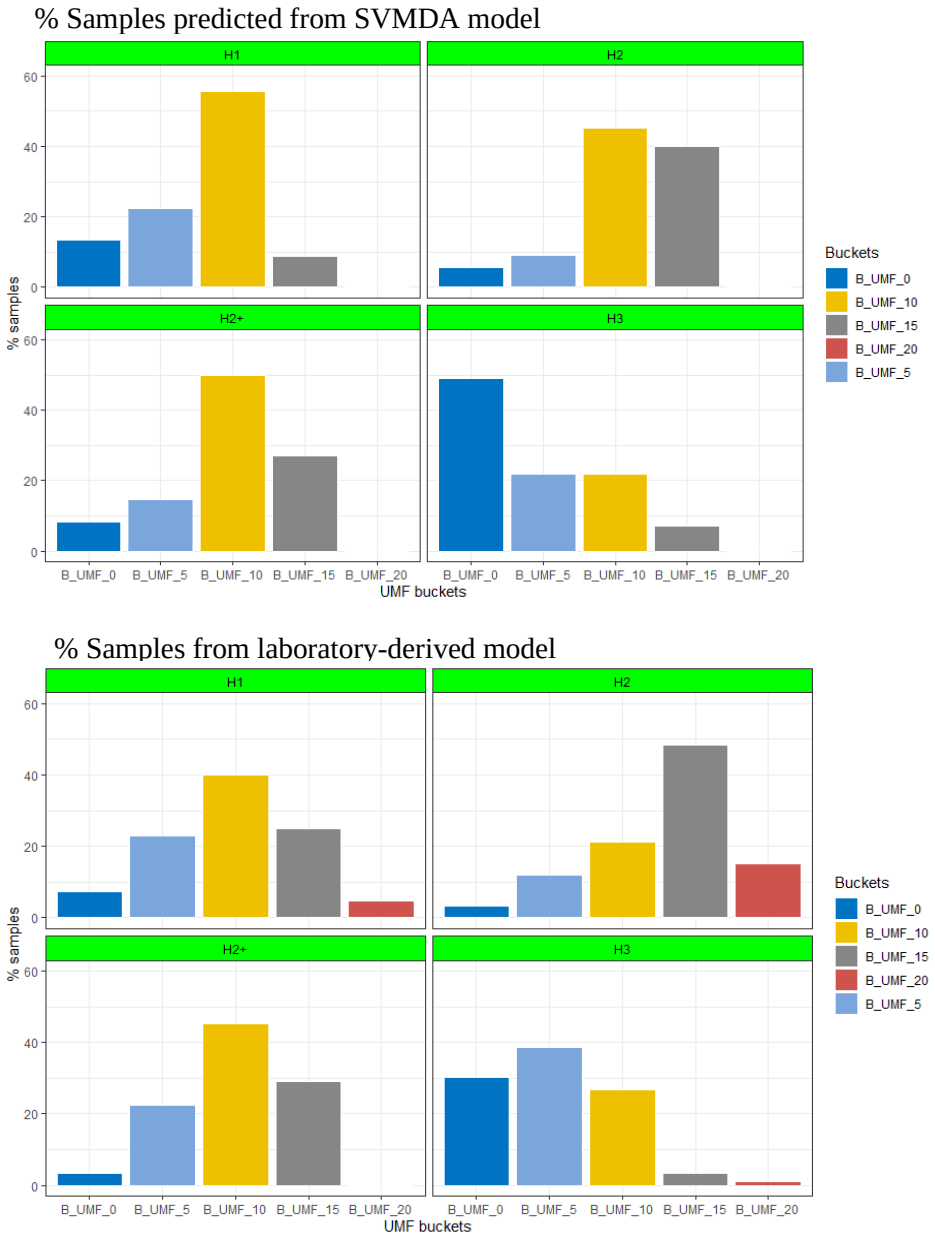

Figure 8.20. *Percentage of samples were classified by HSI SVMDA (top) and laboratory-derived model (bottom) into five different buckets (B_UMF_0, B_UMF_5, B_UMF_10, B_UMF_15 and B_UMF_20) for four apiaries H1, H2, H2+ and H3*

Figure 8.21 shows the percentage gain in revenue built from the SVMDA model for four apiaries. Only apiaries H2+ and H3 gained revenue and did so for three pricing scenarios 1, 2 and 3, but not for scenario 4. Apiary H1 only gained 4 % under the pricing scenario 1 but did not gain for other scenarios. Negative gain was found from apiary H2 for the HSI NIR model. The SVMDA model showed a familiar pattern in the predictive revenue gain similar to the PLS regression model (Figure 8.24-top).

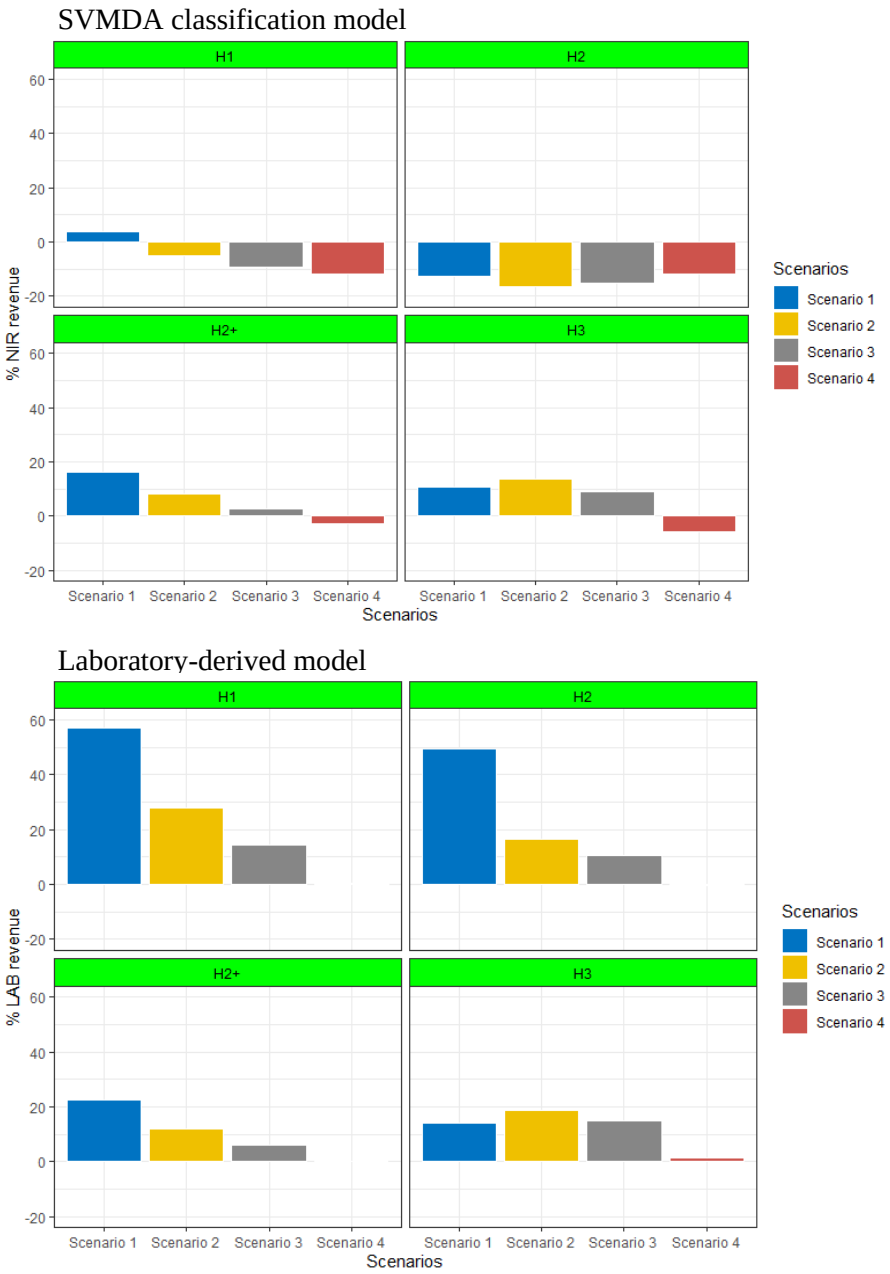

Figure 8.21. *Percentage gain in honey revenue were quantified from the HSI NIR classification SVMDA model (top) compared with that of laboratory-derived model (bottom) for four different scenarios (Scenario 1 (S1), Scenario 2 (S2), Scenario 3 (S3), and Scenario 4 (S4)) at apiaries H1, H2, H2+ and H3*

To compare non-imaging and hyperspectral imaging classification's revenue benefit, a PLSDA model was also used to calculate the percentage gain in revenue. Figure 8.22 displays the percentage gain of the multiple bucket system estimated by HSI PLSDA compared with the true sample reference from laboratory data. In general, PLSDA predicted fewer samples in B_UMF_10 and more samples in B_UMF_20 for all apiaries. HSI PLSDA gave a misclassification rate 0.53, which was 0.18 higher than that of HSI SVMDA at 0.35. Compared to non-imaging PLSDA, the misclassification rate of HSI PLSDA was also 0.12 higher than that of non-imaging PLSDA.

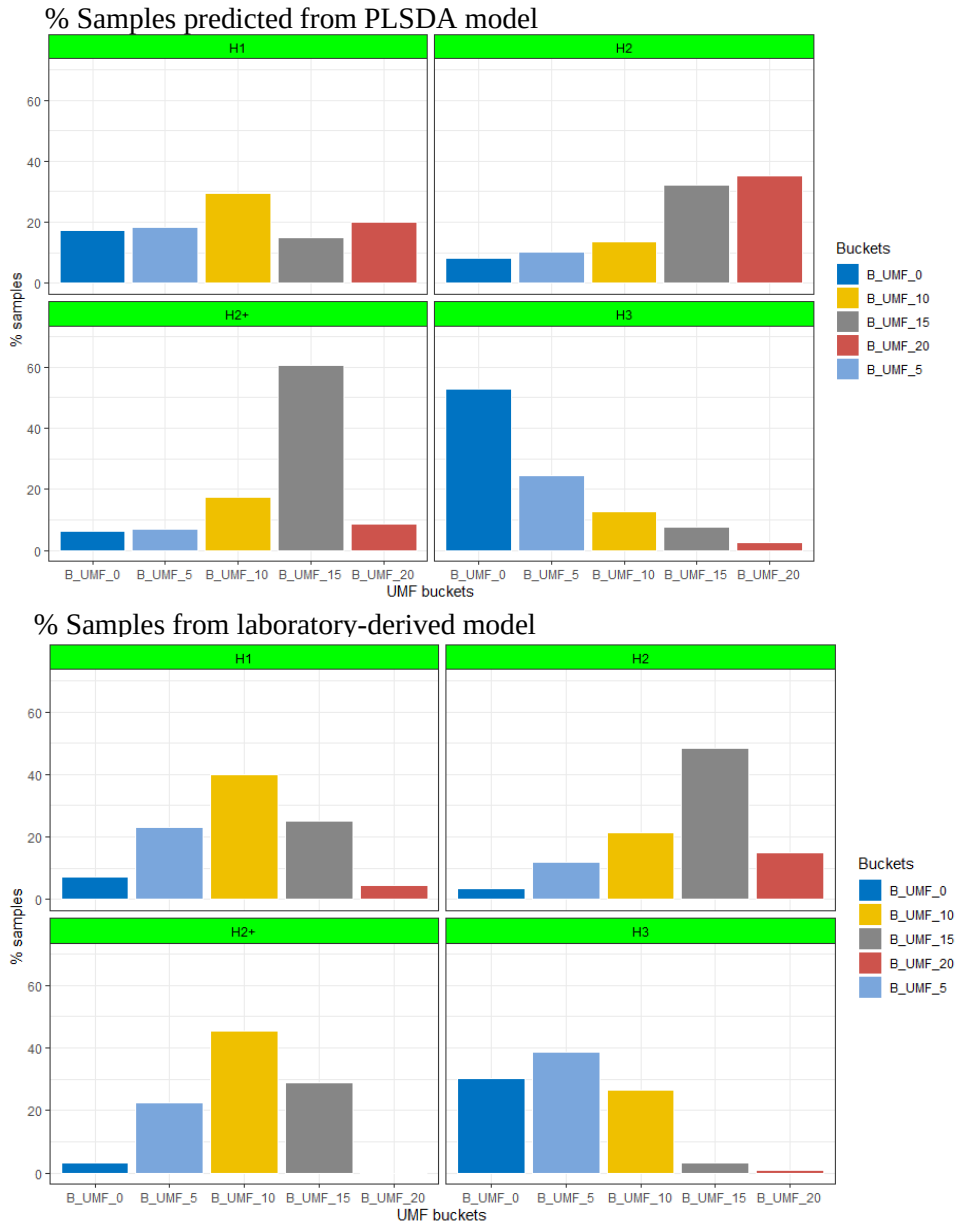

Figure 8.22. *Percentage of samples were classified by HSI PLSDA (top) and from laboratory-derived model (bottom) into five different buckets (B_UMF_0, B_UMF_5, B_UMF_10, B_UMF_15 and B_UMF_20) for four apiaries H1, H2, H2+ and H3*

Figure 8.23 illustrates the revenue percentage gain of the HSI PLSDA model. It was obvious that HSI PLSDA estimated additional revenue as did the laboratory-derived model, but it may have over-rated samples into B_UMF_20 zone.

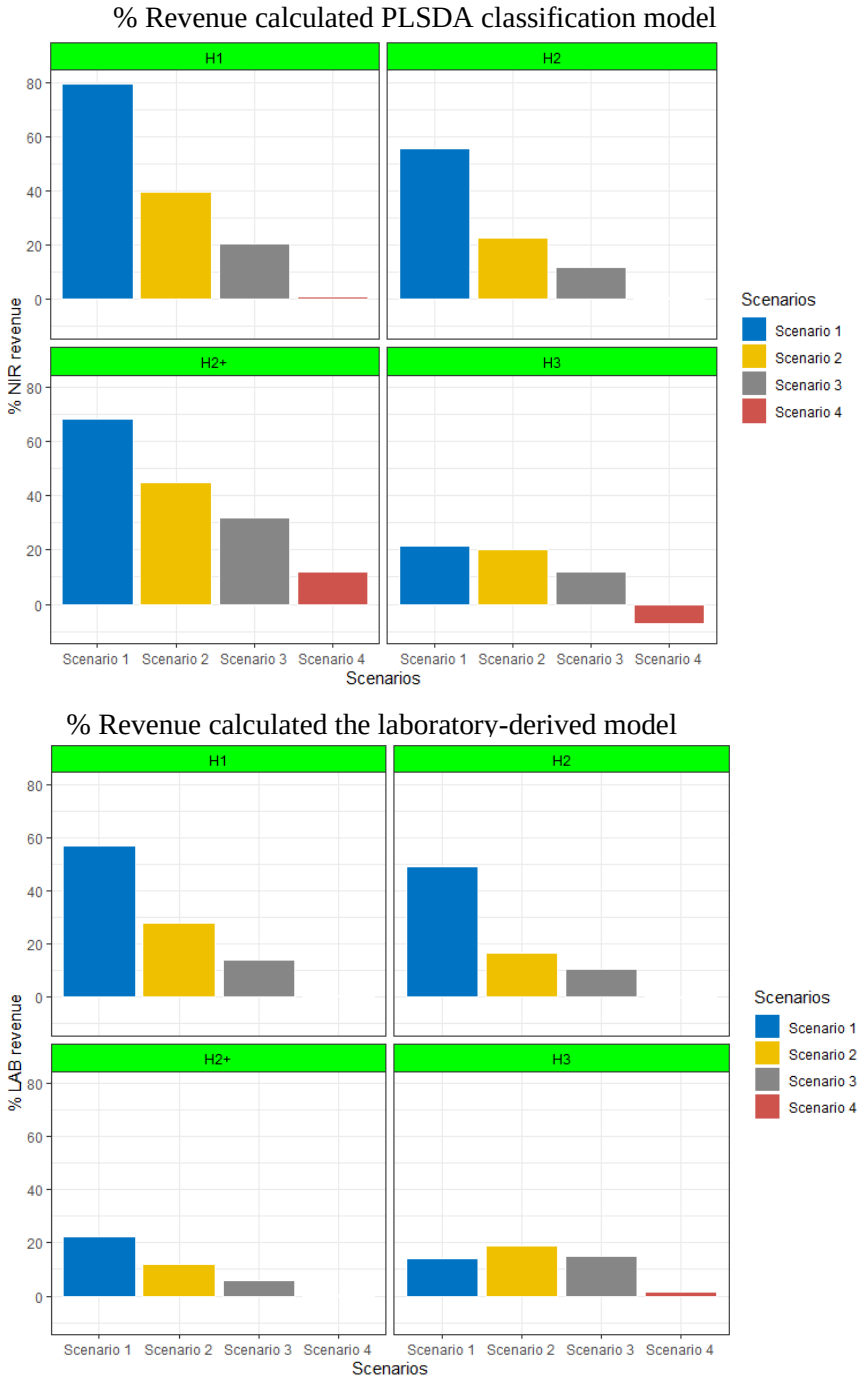

Figure 8.23. *Percentage gain in honey revenue was quantified from HSI NIR PLSDA model (top) compared with that of laboratory-derived model (bottom) for four different scenarios (Scenario 1 (S1), Scenario 2 (S2), Scenario 3 (S3), and Scenario 4 (S4)) at apiaries H1, H2, H2+ and H3*

8.3.4.3. Comparison of benefits between regression and classification

Comparing HSI PLS regression and HSI PLSDA classification models, the percentage revenue obtained from classification was higher than from the regression model (Figure 8.24). Regression showed benefit loss in apiary H2 while classification indicated no loss by separating frames into UMF^{TM} buckets. This was also found in non-imaging PLSDA.

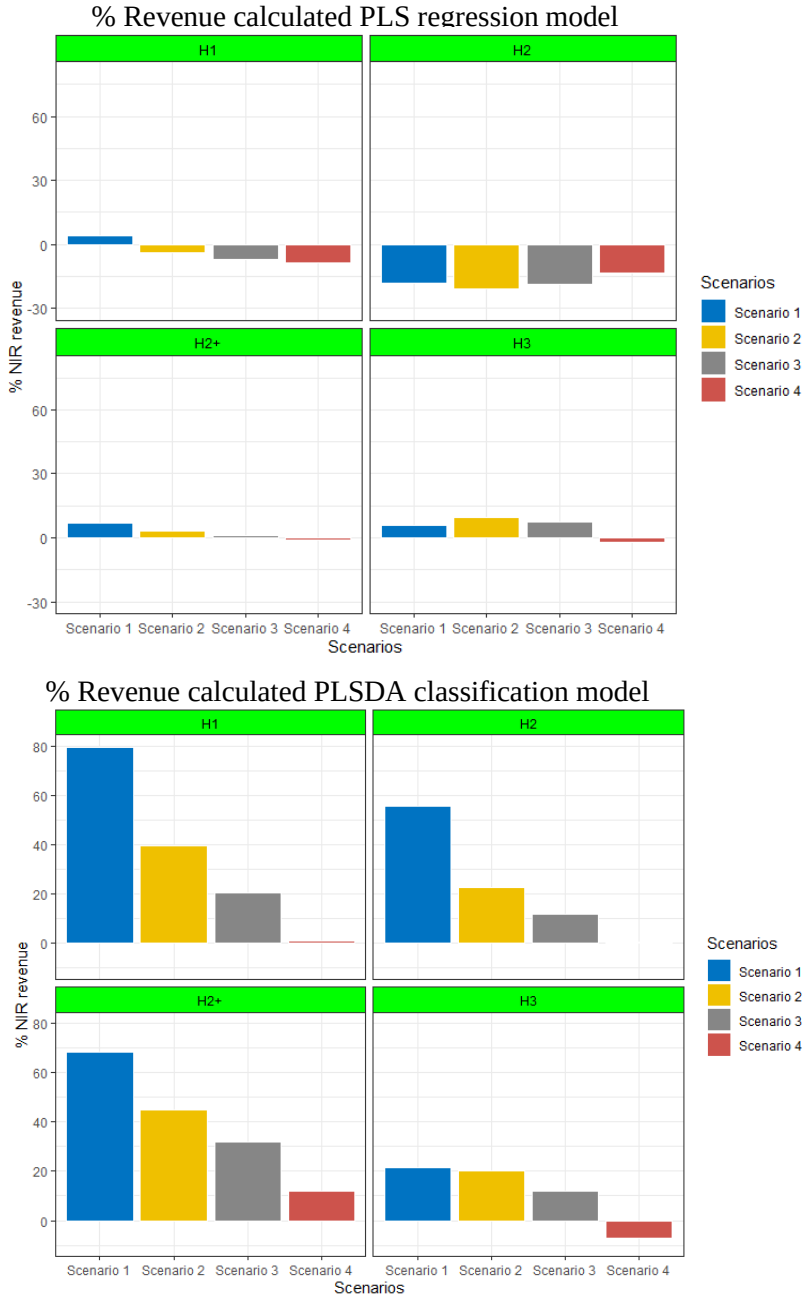

Figure 8.24. *Percentage gain in honey revenue was quantified from a HSI NIR regression PLS model (top) compared with a HSI NIR classification PLSDA model (bottom) for four different scenarios (Scenario 1 (S1), Scenario 2 (S2), Scenario 3 (S3), and Scenario 4 (S4)) at apiaries H1, H2, H2+ and H3)*

8.4. Discussion

The current chapter calculated the economic benefit of the approach of sorting frames into UMF^{TM} buckets before bulk extraction over the current method of averaging all frames. The results indicate that grouping honey frames into five UMF^{TM} buckets (B_UMF_0, B_UMF_5, B_UMF_10, B_UMF_15 and B_UMF_20) could enhance revenue compared to the current practice of lumping of all honey frames from one apiary together. This is in line with the study of Stephens (2006) where the author suggested grouping different levels of UMF^{TM} level for optimising the quality value of mono-floral mānuka honeys. However, the level of benefit derived depends on the level of variability amongst frames in an apiary and on the shape of the price-quality curve. The benefit is clear when the proposition is tested using laboratory data for measuring UMF^{TM}, but also applies using NIR models. The study assessed the impact of the accuracy from NIR non-imaging and hyperspectral models on the benefits of sorting into five UMF^{TM} buckets. The highest economic benefit came from an NIR non-imaging model for prediction of UMF^{TM} scores with 74 % accuracy. This allowed additional revenue of up to 25 % in some apiaries when sorting into different UMF^{TM} buckets.

In this exercise a sigmoid pricing curve was used – concave upward below UMF^{TM} 15 and concave downward above that point. Revenue gains (of a five-bucket over one-bucket approach) were greater at UMF^{TM} < 17.5 since the value curve was concave upward in that zone. If all frames have UMF^{TM} > 17.5, little benefit was gained, and lumping frames together may be the best option. Here, MGO-rich material is being added into honey at a steeper part of the pricing curve. Clearly the benefit to be gained from classification before extraction depends on the shape of the price-quality curve. Where the curve is always concave upward, there is probably always value to gain. Where the sigmoid curve is nearly straight there may never be value to gain. Where the sigmoid is pronounced, the greatest value is at the steepest point with least value gain where it is concave downward.

The gains are demonstrably available where the honey quality is known with the precision of laboratory data – as showed by using models based directly on laboratory data. It is also possible to apply both NIR non-imaging regression and classification models to separate honey frames into five UMF^{TM} buckets. At the current stage of development, the regression models tend to underpredict honey quality in the top bucket (UMF > 17.5 (B_UMF_20)) while classification may overrate higher-quality samples and inflate that bucket. The parent data set on which the models were trained were leanest in this high-value zone. There is room for improvement in the models. There are still new modelling techniques available, and it may

make sense to tune a model for most accurate performance at the upper quality end where consequences are greatest.

Hyperspectral imaging (HSI) has the advantage of providing spatial and spectral information simultaneously. This would allow the operator to understand variability across frames and also offer the option removing pixels not associated with clean honey. From the above research findings, HSI based models showed similar strengths and weaknesses to non-imaging NIR despite narrower spectral range and lower spectral resolution, but with slightly less good predictive performance and consequently slightly reduced revenue enhancement. The current work has only tested extracted samples so far, without the interference of wax or any other contaminant on the surface of a newly uncapped frame. The imaging approach offers the advantage of removing contaminated pixels before spectral analysis. The jury is still out on the choice of non-imaging or HSI approaches.

The model can be of a regression type giving continuous values of a dependent variable (in the case tested this was UMF^{TM}), or it can be a classification model assigning frames to buckets – effectively a discontinuous variable. Both work and it may depend on the model performance which is better for a particular application. It may yet prove best to use a two-tier system where SVMDA is first used to assigned frames to buckets then a regression model chosen for that UMF^{TM} range is used to predict final UMF^{TM} value.

The current study used five buckets. There is no magic in the number five, but it was convenient for testing the classification technique against regression.

This work did not look closely at classification into the three MPI purity classes which also impacts heavily on value. This is probably best not studied by direct classification. Rather the accuracy of prediction of the chemical markers used in the MPI classification is likely to be more useful since that may allow a specific chemical to be targeted almost regardless of accompanying MGO level under some circumstances.

8.5. Conclusions and future suggestions

Both non-imaging and hyperspectral imaging NIR systems potentially bring benefit for sorting honey frames into different UMF^{TM} buckets. NIR methods applied to frames showed the gain in revenue depends on pricing curvature, honey variability and model accuracy. Greatest benefit came when applying to frames which had a broad spread of UMF^{TM} values and pricing curves which are concave downward. If the curve is concave upward and all frames had high UMF^{TM} values >17.5, it would be the best for all frames to be lumped and extracted

together. In addition, apiaries having a broad variation in botanical sources would benefit the most when sorting into different UMF^{TM} buckets.

Further research is suggested to improve the performance of both classification and regression models. It is noted that the complexity of honey matrix could not be totally removed since it is the nature of wild honey when harvesting. In addition, the reference laboratory data also contain errors when calculating the UMF^{TM} value from MGO concentration. So, modelling accuracy could not reach 100 %. However, it can be improved. Two approaches are suggested to enhance prediction accuracy. On the one hand, use of advanced modelling techniques (e.g., convolutional neural networks (CNN)) could tune a complex model which can eliminate the complexity of honey matrix to enable improving the predictive accuracies. On the other hand, using other optical technique that is different from NIR method could minimise the impact of the complex honey matrix. Fluorescence is noteworthy and fusion of fluorescence and NIR methods combined is promising to enhance the model predictability despite the matrix effect. In the next chapters (Chapter 9 and 10), these two approaches are investigated.

Chapter 9

At-line assessment of mānuka honey quality and monoflorality using hyperspectral imaging combined with deep learning

9.1. Introduction

Rapid assessment of honey quality during processing is of great interest to the industry and non-invasive techniques are envisaged to ensure the final product meets consumer expectations. The previous chapter (Chapter 8) shows the economic benefit of NIR methods for assessment of mānuka honey quality and monoflorality (purity) before bulk extraction. NIR hyperspectral imaging is promising for at-line assessment of honey quality while still in the frame. However, the complexity of the honey matrix due to variation in botanical sources is a source of noise which heavily affects modelling. Traditional chemometric methods, linear partial least squares (PLS), and support vector machine (SVM), showed limitations when applied to chemical footprints of mānuka honey due to the impact of regional variation (Truong et al., 2022). The regional impact was severe when modelling hyperspectral data (547-1701 nm) by linear techniques resulting in poor predictions of potency and monoflorality. Therefore, this study investigates deep learning as a non-linear advanced modelling method which uses multiple training layers to extract chemical information carried in hyperspectral signals (Al-Sarayreh et al., 2020).

Convolutional neural network (CNN), known as a deep learning technique, extracts complex self-learned features from among the input variables enabling relationship identification between the input variables to accomplish tasks such as supervised classification or regression (Al-Sarayreh et al., 2020; Pullanagari et al., 2021). Previous studies indicate that CNN models are robust and flexible for simultaneously analysing spatial and spectral information of HSI image data (Huang et al., 2019; Motta et al., 2020; Shen & Viscarra Rossel, 2021; Soni et al., 2021). Al-Sarayreh et al. (2020) employed three-dimensional-CNN networks (3D-CNN) for classification of different types of meat. Soni et al. (2021) also used one-dimensional CNN (1D-CNN) for detection and quantification of *Clostridium sporogenes* in food products. Both studies found sufficient robustness and efficiency of CNN to analyse hyperspectral image data with > 90 % accuracy (Al-Sarayreh et al., 2020; Soni et al., 2021).

Therefore, in the current study, CNN was applied to hyperspectral data of a real-world honey dataset collected from different geographic regions across New Zealand.

9.2. Research hypothesis

The current study hypothesised that hyperspectral imaging captured complex interactions between light and the honey sample, and this complexity can be modeled with deeper CNN models. To test this hypothesis, the main objectives and contributions of this study are as follows:

1) Development and evaluation of a 1D-CNN regression model for prediction of honey potency based on a prediction of UMF^{TM} score and comparison with traditional machine learning models such as PLS and SVM.

2) Development and evaluation of a 1D-CNN classification model for classification of mono-floral mānuka honeys (prediction of monoflorality) at both sample-based and pixel-based levels and comparison of results with traditional machine learning classification models such as PLSDA and SVMDA (rbf).

3) Evaluation and extraction of important variables (wavelengths) used by the 1D-CNN models developed, for understanding chemical footprints of honey spectra.

4) Testing the robustness of 1D-CNN modelling on an unseen set of HSI images that simulates the practical use of the proposed methods and models.

9.3. Materials and methods

9.3.1. Sample dataset and hyperspectral imaging system

The hyperspectral dataset of 1656 honey samples spanning eight geographic districts, scanned under a line-scan hyperspectral camera (covering wavelengths in the range of 547-1701 nm) (Model 1003B-10151, Headwall Photonics, Fitchburg, MA, USA), was used for modelling with 1D-CNN. The hyperspectral dataset and its segmentation are described in Chapter 4.

9.3.2. Spectral pre-processing

Spectral pre-processing is a common step prior to modeling HSI spectral data, aiming at improving the quality of the collected data by reducing the impact of noise and baseline correction. The reflectance spectra were inverted to obtain the absorbance spectra by using a logarithm function (Log(1/R)) (Saeys, 2018; Truong et al., 2021). Then, several spectral pre-processing methods were investigated to reduce the impact of additive and multiplicative noise.

These methods are standard normal variate (SNV), first derivative, second derivative, and combinations of them.

9.3.3. Standard chemometrics and machine learning

Linear Partial Least Squares (PLS) and Support Vector Machine regression (SVR) were used to analyse HSI spectral data for estimating UMF^{TM} score. Partial Least Squares Discriminant Analysis (PLSDA) and Support Vector Machine Discriminant Analysis (SVMDA) with rbf kernel were used to classify the three MPI honey classes (mono-mānuka, multi-mānuka and non-mānuka) (Chapter 6).

All chemometric methods were run with PLS toolbox 8.8 (Eigenvector Research, Inc., WA 98831, USA), except the SVR model which was run with Statistics and Machine Learning toolbox. Both toolboxes were run in MATLAB R2021a (The MathWorks, Inc., Massachusetts 01760, USA).

9.3.4. One-dimensional convolutional neural network

The basic architecture of the proposed one-dimensional convolutional neural network (1D-CNN) contains of an input layer, three convolutional blocks, two fully connected layers and an output layer as shown in Figure 9.1.

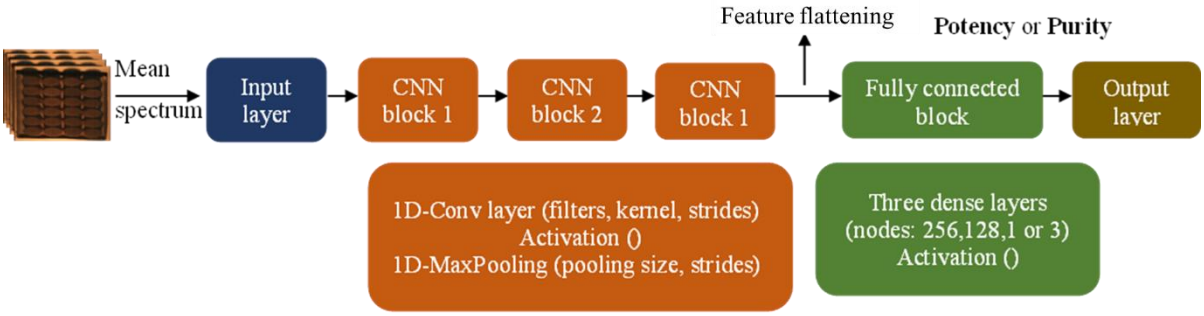

Figure 9.1. *The proposed architecture of one-dimensional convolutional neural network regression/classification framework to predict potency or monoflorality of honey in hyperspectral images*

The input layer presents spectral data as a vector. The three convolutional blocks (hidden layers) are considered as detector layers (or feature extraction layers) for filtering specific features in an hierarchical way during the training process of the 1D-CNN (Dertat, 2017). Each block sequentially performs three different operations: convolutional layer (feature extraction), activation layer (non-linear transformation of features) and pooling layer for down-sampling

the resulting features. Each convolutional layer has a number of features (feature maps), convolutional kernel size and hyperparameters (stride, padding & kernel regularizer). The number of feature maps defines the number of features to be extracted by the convolutional block. Kernel size sets the filter size which allows specific features to be detected. Stride & padding functions help to maintain the same dimension of the input and detected features. The stride specifies the convolutional kernel step which moves along the input array, while the padding adds zeros on the array edge (Shen & Viscarra Rossel, 2021). Kernel regularizer is used as a penalty at each layer to optimise the network and to avoid overfitting. The activation layer is used to transform the resulting features from the convolutional layer into another space allowing capture of non-linear relationships between these features. Moreover, an activation function such as *ReLu* can accelerate the optimisation process during training of deep learning models.

The 1D-CNN architecture is operated with the support of the pooling layer and learning-operative function that smoothly cooperates with convolutional layers in convolution blocks. Pooling is the process of merging to reduce the size of features. The pooling layer also has hyperparameters (pooling size, stride, and padding). These hyperparameters allow the input dimensionality of features to be reduced by maximising/averaging methods to shorten the training time and avoid overfitting (Al-Sarayreh et al., 2020; De Ketelaere et al., 2022; Pullanagari et al., 2021; Shen & Viscarra Rossel, 2021).

In the final CNN layer, all extracted features were flattened into a vector (i.e., one-dimension structure). These flattened features were projected into fully connected (FC) layers to optimise the relationship between the predicted and measured features. *ReLu* activation was used to activate the resulting features from each fully connected layer. The output layer in the proposed architecture depends on the purpose of the model. For regression models, the output layer is a fully connected layer with a size of 1 and linear activation. This layer is used to generate regression values. Meanwhile for classification, the size of the fully connected output layer depends on the number of target classes, and the activation function used is S*oftmax* (Al-Sarayreh et al., 2020; Jeong, 2019; Shen & Viscarra Rossel, 2021; Soni et al., 2021).

Training of the proposed 1D-CNN model consists of two main processes: feed-forward and back-propagation. In the feed-forward process, a batch of samples (batch size) is fed to the model to compute an error function between the model prediction and the measured outputs of that batch. Then, depending on the measured error, the model parameters (called weights) are adjusted in a systematic way to minimise the defined error function. This process is known as back-propagation. The optimisation method used to adjust the weights is a stochastic gradient

descent (SGD) algorithm. These processes are repeated several times (epoch number) to make sure that the training and optimisation process can reach a point with best values of the model weights. Batch size and epoch numbers are optimised to enhance the learning process in convolutional neural networks (Shen & Viscarra Rossel, 2021). Batch size indicates the number of samples inserted for each training iteration while epoch is the number of training times that specify the weight optimisation (Wikieigenvector, 2021). Batch normalisation is applied for each convolutional block. Higher batch size and epoch numbers could lead to overestimation. Optimising these parameters first is suggested. Later, optimising of number of convolutional blocks, kernel size and kernel regularizer can reduce computational effort (Shen & Viscarra Rossel, 2021).

9.3.5. Modelling preparation and evaluation

The collected dataset (1656 honey samples) was split for training and test sets using Kennard-Stone technique with a ratio of 70:30. The training set of samples was used for training all regression and classification models, including the base-line machine learning models (i.e., PLS and SVM) and the proposed 1D-CNN model. In the training phase, 10-fold cross-validation was used for hyperparameter tuning and the best model selected. Then, the test set of samples was used to evaluate models for reporting an unbiased comparison between all models investigated.

To evaluate the performance of regression models, the following standard measures were used: coefficient of determination (R^2), root mean square error (RMSE), residual predictive deviation (RPD), and the bias. Recall, precision, F1-score and overall accuracy metrics were used for evaluating classification models. (Zhang & Abdulla, 2022). The base-line machine learning models (i.e., PLS and SVM) and the 1D-CNN model were developed in Python environment (version 3.8, used packages: Keras, TensorFlow, Sklearn and OpenCV).

During 1D-CNN training, 10-fold cross validation is utilised to optimise the tunable parameters of the proposed architecture to avoid overfitting and underfitting. For example, the optimal values of batch size and epochs were obtained using the 10-fold cross validation strategy. After obtaining the optimal values of all parameters, the final performance of the model was examined using the independent test set that had been set aside during the training process (Al-Sarayreh et al., 2020). A sample-based 1D-CNN model was built for prediction of UMF^{TM} scores (regression model) using the average spectra of the extracted ROIs from the images. For classification, both sample-based and pixel-based 1D-CNN models were

constructed to observe the classification output. The average spectra of all pixels which represent a honey sample were projected into a sample-based model. By contrast, selected pixels from each ROI, including the averaged pixel, were inserted into a pixel-based model. The idea was to investigate the prediction result at the image level (for frames) and at the pixel level (for honeycomb). The output of the pixel-based model was evaluated by the voting system in which the class assigned is that with the majority of pixels.

9.4. Results

9.4.1. 1D-CNN regression model

Table 9.1 shows the details of the proposed 1D-CNN regression model, including the tunable parameters, the search space, and the optimised values of each parameter. The linear PLS & SVR models showed limitations when predicting UMF^{TM} scores from hyperspectral data spanning eight geographic districts. Meanwhile, deep 1D-CNN improved prediction of UMF^{TM} score by 8 percentage points compared to PLS and SVR (Table 9.2). The RPD value obtained from the proposed 1D-CNN regression model exceeded 2.5 indicating that it was useful for predicting UMF^{TM} values from new datasets. 1D-CNN seemed to be minimising the impact of regional variation (Figure 9.2b). However, a model bias was obvious for some samples with UMF^{TM} 0 which were predicted larger than 0. This apparent bias could be partly due to a real lift in UMF^{TM} during storage of samples.

Table 9.1. The architecture of the proposed 1D-CNN regression model for prediction of UMF^{TM} scores

1D-CNN hyperparameters	Search space	Optimized values
Convolutional layer	2, 3, 4	3
Number of nodes	8 - 64	8, 16, 32
Kernel size	2 - 4	3
Stride	1 - 3	1
Non-linear activation	*ReLu*	*ReLu*
Pooling	Maximum, average	Maximum
Regularizer	1e-03 - 1e-08	1e-05
Learning rate	0 - 0.5	0.001
Fully connected layers	64 - 512	256, 128, 1
Optimizer	Adam	Adam

Table 9.2. Comparison of prediction results of UMF™ scores between 1D-CNN, PLS and SVR

Models	Pre-processing	R^2 (CV)	RMSE CV	Bias CV	R^2 (test)	RMSE (test)	Bias (test)	RPD
PLS	Abs+SNV	0.71	2.75	0	0.66	2.61	-0.21	1.91
SVR	Abs	0.73	2.66	0	0.67	2.56	-0.14	1.98
1D-CNN	Abs+1st der.	0.87	2.05	-0.59	0.73	2.35	-0.89	2.56

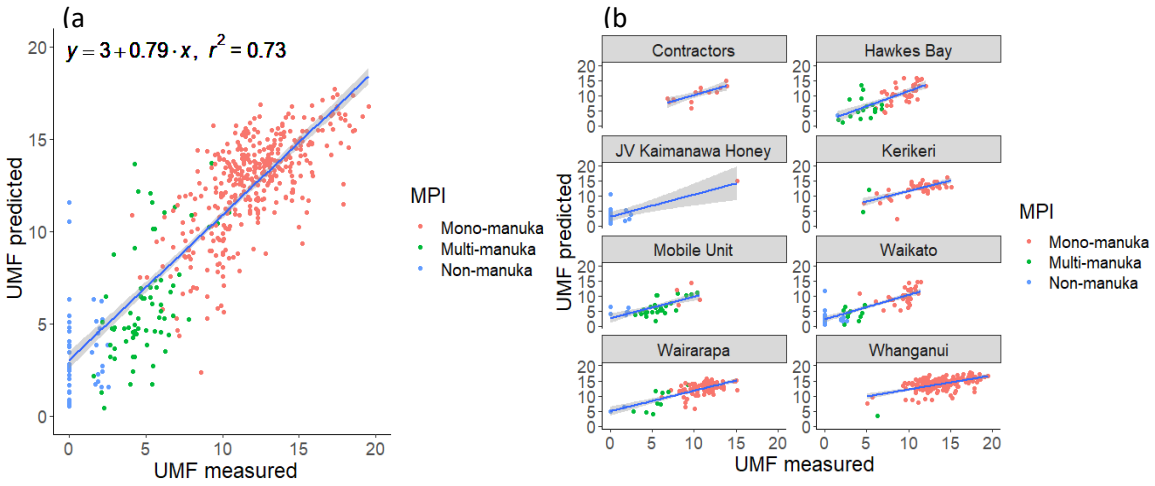

Figure 9.2. *The 1D-CNN regression plot of an independent 450 sample test set (a) and regression plot observed by eight geographic districts (b)*

Assessment of the importance of variables from the output of 1D-CNN model was also investigated. The deep learning explanation method "SHAP" (Shapley additive explanations) was employed to calculate the impact of input wavelengths on the prediction of UMF™ score (López, 2022; Zhang, 2021). A total of 50 honey samples was randomly selected from 100 samples giving the highest prediction (lower RMSE values). For each sample, SHAP first calculates a "target value" for all spectral features. Then, the contribution score of each wavelength is computed to yield a SHAP value.

Figure 9.3 illustrates SHAP values scaled from -1 to 1. The values that are close to 1 (positive correlation) or -1 (shared negative correlation) mean that the relevant wavelengths are significantly important. Wavelengths that give SHAP values near 0 suggest non-importance. Overall, spectral features in 637 - 696 nm revealed it to be the most significant region for prediction of UMF™ score. Features below 637 nm also contributed to UMF™

prediction. By contrast, features in the range 932 - 962, 1169 - 1128, 1287 - 1406 and beyond 1642 nm were not important.

Interestingly, samples with UMF^{TM} ≥ 10 showed positive correlation in the 637 - 696 nm range for prediction of UMF^{TM} score. By contrast, samples with UMF^{TM} < 10 showed negative correlation (Figure 9.3). Some samples having the same UMF^{TM} value (i.e., UMF^{TM} 11.4 or 12) showed both positive and negative correlation. This indicates that these honeys could have different biochemical profiles, mostly relating to original botanical sources (different varieties of *L. scoparium* or different contaminating nectars) but yield the same UMF^{TM} score.

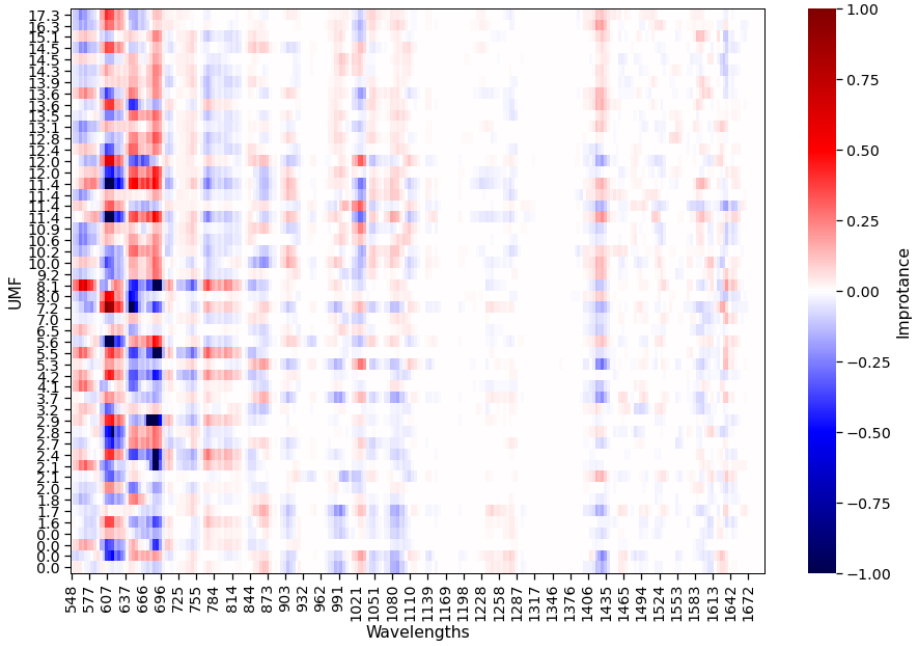

Figure 9.3. *Selection of important wavelengths by 1D-CNN using SHAP method for 50 samples giving superior UMF^{TM} prediction*

9.4.2. 1D-CNN classification models

Two advanced 1D-CNN models at sample-based and pixel-based levels were constructed to observe the classification output. Table 9.3 shows the details of the proposed 1D-CNN classification model, including the tunable parameters, the search space and the optimised values of each parameter. With the proposed 1D-CNN architecture, the sample-based model achieved slightly better prediction than the pixel-based model. Overall, classification of mono-mānuka gave ~ 90 % accuracy while only 51 - 54 % and 60 - 64 % for multi-mānuka and non-mānuka, respectively (Table 9.4).

In comparison with standard models, the cross-validated 1D-CNN model gave 83 % accuracy that was 4 - 7 percentage points higher than with SVMDA and PLSDA. Table 9.5 shows the classification results of mono-, multi- and non-mānuka honeys on the test set. The overall accuracy between three models is not significantly different (84 – 86 % accuracy). Mono-mānuka honeys can be classified with above 90 % accuracy while multi-and non-mānuka honey only gave 50 - 60 % accuracy for all models. This was possibly due to the unbalanced dataset favouring mono-mānuka honeys. However, 1D-CNN (Precision = 0.93) gave significantly higher precision values for classification of mono-mānuka honeys than did PLSDA (Precision = 0.63) and SVMDA (Precision = 0.83) (Table 9.6). This indicates that 1D-CNN performance was better than PLSDA and SVMDA.

Table 9.3. The architecture of the proposed 1D-CNN classification model

1D-CNN hyperparameters	Search space	Optimized values
Convolutional layer	2,3,4	3
Number of nodes	8-64	8, 16, 32
Kernel size	2-4	3
Stride	1-3	1
Non-linear activation	*ReLu* & *softmax*	*ReLu* & *softmax*
Pooling	Maximum & average	Maximum
Regularizer	1e-03 - 1e-08	1e-04
Learning rate	0-0.5	0.001
Fully connected layers	64-512	256,128,3
Optimizer	Adam	Adam

Table 9.4. The output of the sample-based (pre-processing: 1st Derivative) and pixel-based (pre-processing: SNV) 1D-CNN models on the test set for classification of mono-mānuka, multi-mānuka and non-mānuka honeys

		Sample-based (OA= 84.27 %)				Pixel-based (OA= 82.26 %)			
	N	Recall	Precision	F1	CA (%)	Recall	Precision	F1	CA (%)
Mono-mānuka	384	0.91	0.93	0.92	91.41	0.89	0.93	0.91	89.06
Multi-mānuka	71	0.55	0.53	0.54	54.93	0.55	0.48	0.51	54.93
Non-mānuka	41	0.68	0.60	0.64	68.29	0.66	0.55	0.60	65.85

Table 9.5. Comparison between 1D-CNN and PLSDA and SVMDA (rbf) for classification of mono-, multi- and non-mānuka honeys

Model	Recall			Precision			F1			OA (%)
	Mono	Multi	Non	Mono	Multi	Non	Mono	Multi	Non	
PLSDA	0.90	0.69	0.48	0.83	0.89	0.97	0.93	0.59	0.52	84.48
SVMDA	0.97	0.43	0.55	0.63	0.95	0.98	0.94	0.51	0.60	86.29
1D-CNN	0.91	0.55	0.68	0.93	0.53	0.60	0.92	0.54	0.64	84.27

Sub-models of the balanced dataset of multi-mānuka and non-mānuka honeys were built as illustrated in Table 9.6. Overall accuracy of three models were also not significantly different (69 - 73 %). Multi-mānuka can be discriminated from non-mānuka honeys with 75 -79 % accuracy. Again, 1D-CNN obtained a precision value for classifying multi-mānuka honeys higher than traditional models. Classification of multi-mānuka honeys from all two-classed honey models increased ~20 percentage points over the three-classed models. However, all models performed poorly when classifying non-mānuka honeys. This could be because non-mānuka honeys originated from multiple nectar sources that were not *L. scoparium* (the chemical profile of interest is different). These indicate that the classification results from three modelling methods were likely more heavily impacted by the complexity of the honey matrix rather than by the imbalanced dataset.

Table 9.6. Comparison 1D-CNN model versus PLSDA and SVMDA (rbf) for classification of multi- and non-mānuka honeys

Model	Recall		Precision		F1		OA (%)
	Multi	Non	Multi	Non	Multi	Non	
PLSDA	0.75	0.61	0.61	0.75	0.75	0.61	69.57
SVMDA	0.81	0.62	0.62	0.81	0.79	0.65	73.91
1D-CNN	0.80	0.59	0.76	0.65	0.78	0.62	71.74

9.4.3. Prediction of hyperspectral images

The pixel-based 1D-CNN model was applied on 74 hyperspectral images of honey trays for prediction of mono-, multi- and non-mānuka honeys. By using the majority vote mechanism, the model identified a sample as belonging to a honey class. Figure 9.4 illustrates the resulting classification maps of hyperspectral images with green pixels for mono-mānuka, red pixels for multi-mānuka and blue pixels for non-mānuka.

Overall, the majority of the pixels are correctly classified. In Figure 9.4 A, all mono-mānuka honeys were classified as mono-mānuka honeys. However, some samples had misclassed pixels. Figure 9.4 B & C shows some multi-mānuka honeys misclassed as mono-mānuka honeys, and non-mānuka honeys but labeled as multi-mānuka honeys. In general, most misclassed samples had UMF^{TM} < 10. Mono-mānuka honey samples with UMF^{TM} > 10 were well-classified. Figure 9.4 D indicated the weakness of the pixel-based 1D-CNN model since some samples were misclassed across all three types of pixel.

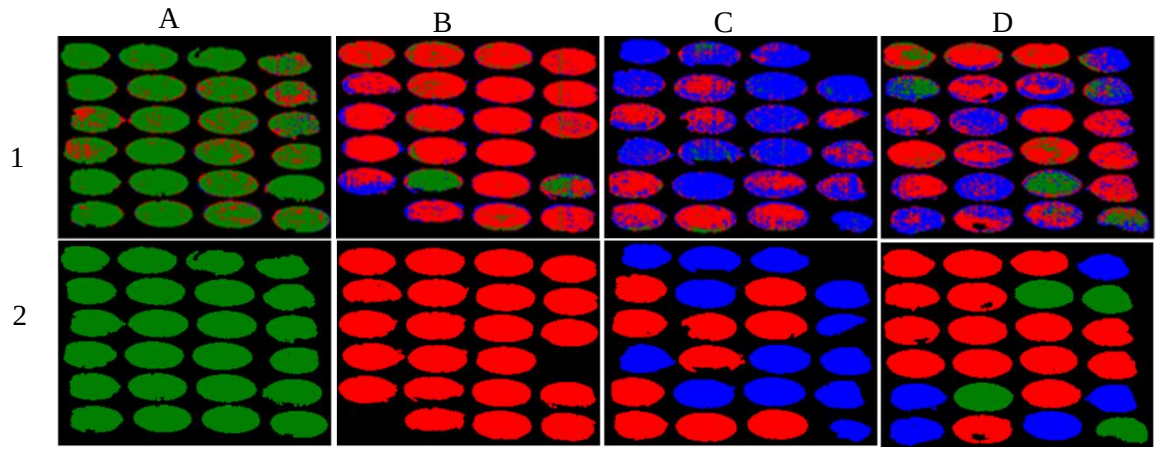

Figure 9.4. *Prediction maps for honey trays from a pixel-based 1D-CNN classification model of mono-mānuka honeys (green), multi-mānuka honeys (red) and non-mānuka honeys (blue) using majority voting mechanism: predicted images (1) and ground truth (2) where A, B, C, D are honey trays [image elongation is artifact of high conveyor belt speed under HSI camera]*

9.4.4. 1D-CNN interpretation of important variables

A total of 50 samples were randomly selected from 100 samples which gave superior classification scores in 1D-CNN models for assessment of the importance of variables using SHAP method. Figures 9.5 illustrates the important features selected from the pixel-based and sample-based 1D-CNN models for classification of mono-, multi- and non-mānuka honeys. The "SHAP values" were scaled in the range from -1 to 1 for comparing relative importance among variables (wavelengths).

Overall, selection of important variables was more consistent for the sample-based 1D-CNN model than for the pixel-based 1D-CNN model (Figure 9.5) across 547 - 1600 nm. This was because the pixel-based model showed more noise compared to the sample-based model. In the sample-based model, the mean spectra were used to reduce random variation among spectra compared to the bulked spectra used in the pixel-based model. However, both models indicated that important wavelengths having positive correlation for prediction of mono-mānuka honey were in the regions of 666 - 740 nm and 991 nm. The spectral region below 637 nm in the sample-based model contributed to prediction of mono-mānuka honey, but negatively correlated. This region (< 637 nm) did not show importance in the pixel-based model.

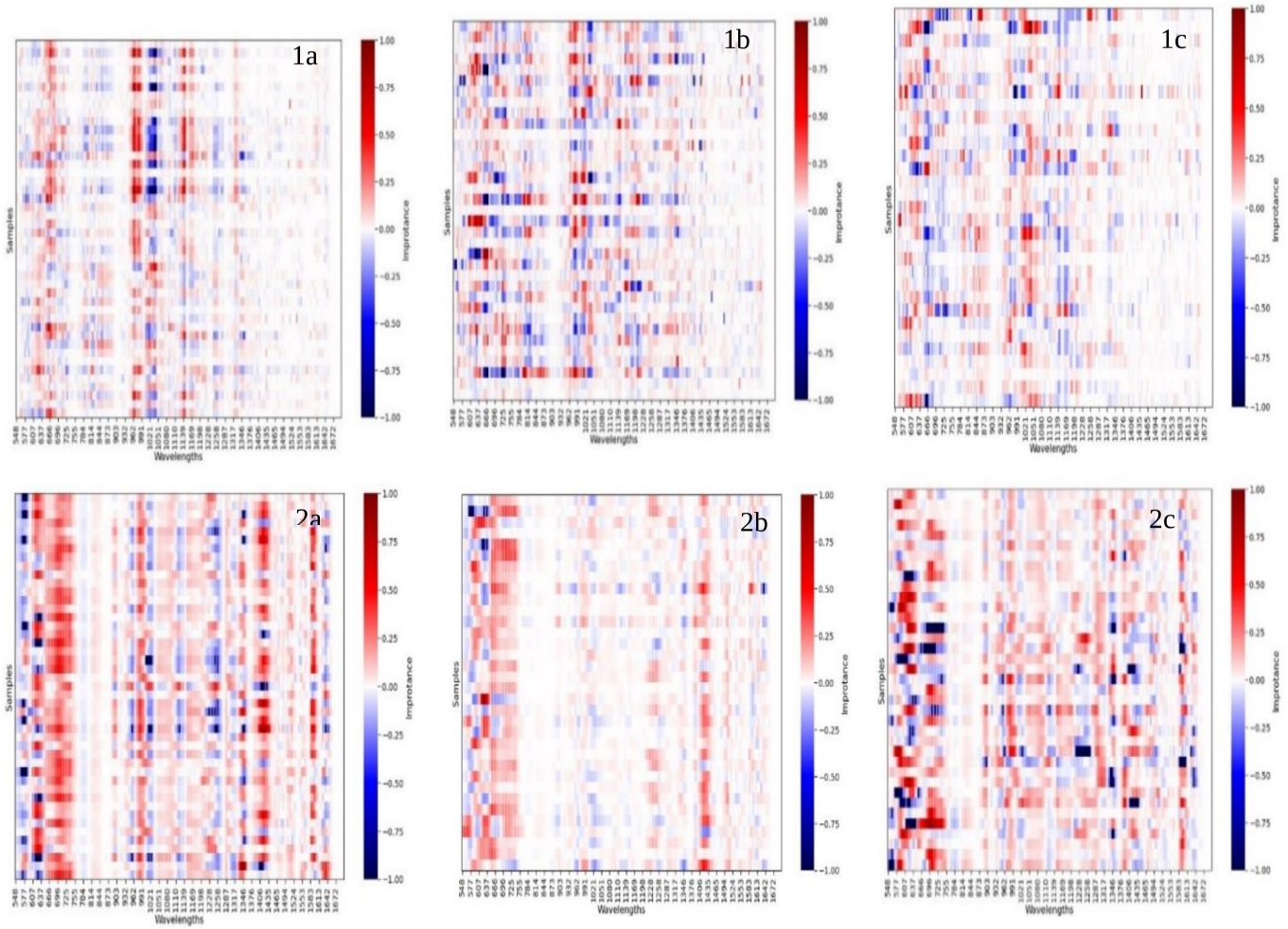

Figure 9.5. *Assessment of important wavelengths from a pixel-based 1D-CNN (1) and a sample-based 1D-CNN model (2) for classification of three MPI classes: mono-mānuka (a), multi-mānuka (b) and non-mānuka (c)*

The sample-based model additionally identified spectral regions 1406 - 1435 and 1583 nm as important, positively supporting classification of mono-mānuka honeys. These regions were not highlighted in the pixel-based model. The pixel-based model did not provide clear spectral ranges for prediction of multi-mānuka and non-mānuka honeys. By contrast, the sample-based model suggested 666 - 740 nm and 991 nm gave positive contributions for prediction of multi-mānuka honeys and also clearly indicated mono-mānuka honeys. Regions below 755 nm and 1583 nm positively and negatively contributed to prediction of non-mānuka honey. Regions around 844 - 873 nm and beyond 1642 nm did not indicate importance for classification of any of the three types of honey in either model.

The wavelength 991 nm was highly associated with prediction of mono-mānuka honeys but was not dominant for prediction of non-mānuka honeys. Figure 9.6 illustrates the "SHAP value" plot between 991 and 1435 nm obtained from the sample-based 1D-CNN model. It is obvious that almost all mono-mānuka honeys were well classified from the other two honeys, but multi-and non-mānuka honeys overlapped. This suggested that 991 and 1435 nm were key wavelengths contributing to classification of mono-mānuka honey from multi- and non-mānuka honeys.

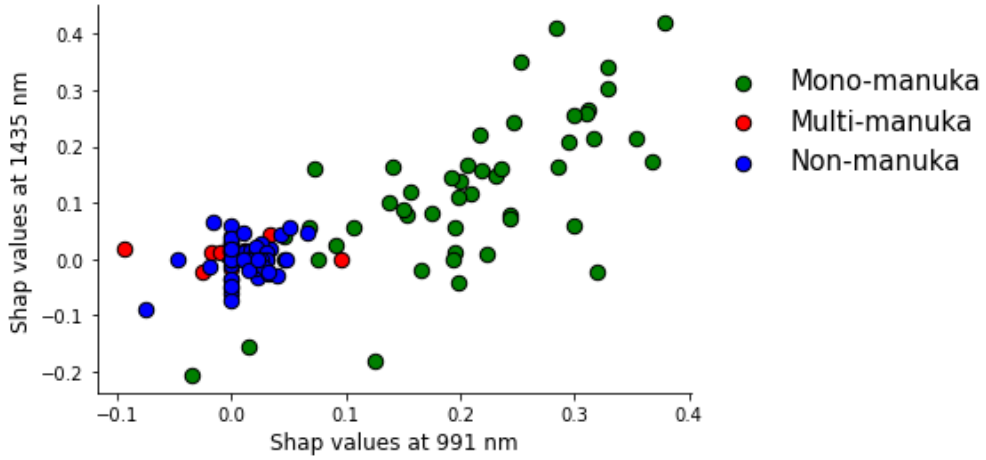

Figure 9.6. *The SHAP value plot of 50 superior prediction samples extracted from the three-classed 1D-CNN model at 991 and 1435 nm*

As with the three-class 1D-CNN model, the two-class 1D-CNN model revealed clearly important regions for prediction of multi-and non-mānuka honeys. A total of 30 samples drawn from 60 samples giving superior prediction were randomly selected for variable detection using the SHAP method. Figure 9.7 shows that the wavelength 1435 nm was a positive indicator in classifying non-mānuka honeys. Spectral regions 814 - 903, 1110 - 1198, 1317 - 1406 nm

showed no contribution for classification performance. By contrast, regions below 637 nm were important for either class. Figure 9.8 illustrates the SHAP value plot at 1435 nm against the absorption values. Multi-mānuka and non-mānuka honeys appeared to be adequately separated. This reconfirmed that the 1435 nm band was significant when classifying multi-and non-mānuka honeys.

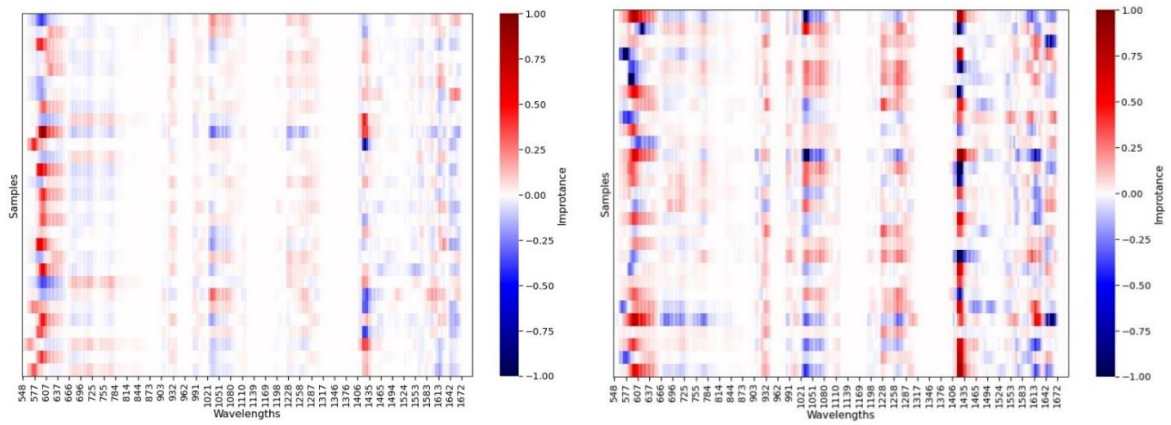

Figure 9.7. *Assessment of important wavelengths from the two-classed sample-based 1D-CNN model for classification of two MPI classes: multi-mānuka (left) and non-mānuka (right)*

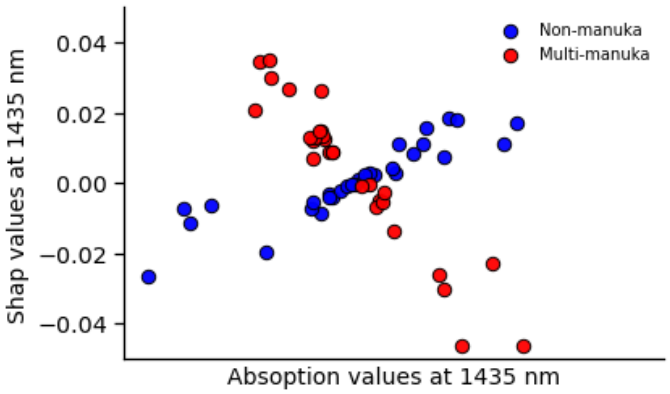

Figure 9.8. *The SHAP value plot of 30 superior prediction samples extracted from the two-classed 1D-CNN model at 1435 nm*

In general, CNN combined with SHAP method showed the capacity to identify important wavelengths associated with model performance. For instance, on the one hand the sample-based CNN models of three and two honey classes suggested that 991 and 1435 nm were important for classification of mānuka and non-mānuka honeys. These wavelengths are relevant to the 2nd overtone and 1st overtone O-H vibrations, respectively (Beganović et al., 2019; Golic, 2003; Xiaobo et al., 2010). According to Jiang et al. (2016), O-H vibration at 991 nm likely corresponds to absorption by free water molecules associating with various moieties in a food matrix (Jiang et al., 2016). In addition, Beganović et al. (2019) declared that O-H vibration at 1435 nm is mostly relevant to water spectra in interaction with sugar (glucose, fructose). These may indicate that the network of water in the honey matrix in which water interacts with phytochemical compounds was different between mānuka and non-mānuka honeys. On the other hand, sample-based CNN models indicated that regions of 755 - 784 and 844 - 873 nm were not important possibly since these spectral regions were mostly relevant to third overtone of sugar OH stretching (Golic, 2003) common to all honeys.

9.5. Discussion

Measurement of UMF™ score is used to evaluate the quality of mānuka honey while verification of botanical origin is separately required following MPI criteria to identify mono-floral, multi-floral and non-mānuka honeys (MPI, 2017b; Stephens et al., 2005). Quality and monoflorality of mānuka honey varies between and within geographic districts due to the presence of different varieties of *L. scoparium* and other floral nectar sources (Stephens, 2006). This was apparent in the honey spectra (547 - 1600 nm) collected from eight geographic districts (Chapter 4, Figure 4.9)

The current study employed hyperspectral imaging and deep learning to assess both the quality and monoflorality of mānuka honey. The proposed 1D-CNN model showed utility in interpreting hyperspectral data for prediction of UMF™ scores compared to traditional chemometric methods (PLS and SVR). Deep learning significantly improved the UMF™ prediction accuracy by up to 8 percentage points and the impact of regional variation seemed to be minimised (Figure 9.2). Classification of mono-mānuka honeys from multi- and non-mānuka honeys achieved ~ 90 % accuracy for all models, but less than 60 % and 70 % accuracies for classifying between multi-mānuka and non-mānuka honeys. Additionally, the 1D-CNN sub-model increased the identification of multi-mānuka up to 80 % accuracy, but it did not improve identification of non-mānuka honeys. This could be because non-mānuka

honeys originate from multiple different types of floral source, while mānuka honeys predominantly come from *L. scoparium* nectar alone.

The current study applied 1D-CNN models to analysing spectral information extracted from hyperspectral images. Beyond initial segmentation, the spatial information has not been employed. According to Al-Sarayreh et al. 2020, the use of the spatial information (2D-CNN) and combined spatial and spectral information (3D-CNN) could improve the prediction accuracy (Al-Sarayreh et al., 2020). The 3D-CNN approach seems to give better prediction than 2D-CNN and 1D-CNN (Al-Sarayreh et al., 2020). Therefore, potentially applying 2D-CNN and 3D-CNN for the HSI honey dataset could enhance both prediction of UMF^{TM} scores and classification of honey classes.

Selection of important spectral variables from 1D-CNN models using the SHAP method for prediction of UMF^{TM} scores and classification of three honey classes was closely aligned with the PLS-based approach. Overall, the spectral features identified in Vis range (637 - 696 nm) are important for prediction of UMF^{TM} score. This spectral region could correspond to footprints of DHA/MGO-brown pigments and chlorophyl (Nguyen & Kochevar, 2003; Truong et al., 2022). Similarly, classification of mono-mānuka honey also identified important spectral ranges in Vis extending to near infrared (666 - 770 nm). The Vis range could link to DHA/MGO and chlorophyl meanwhile the near infrared (750 - 770 nm) may indicate molecular vibration 4th overtone of CH_3 group that could relate to the presence of DHA/MGO (Truong et al., 2022; Xiaobo et al., 2010). Two additional wavelengths, 991 and 1435 nm, identified for classifying mānuka honeys from non-mānuka honeys are relevant to water-OH bond. The 991 nm band was unique to mānuka honeys largely originating from the absorption of C=O bonds near 1000 nm (Iwamoto, 2010) that indicates footprints of DHA and MGO since these carbonyl compounds are uniquely abundant in mānuka honeys. By contrast, the 1435 nm band mostly corresponds to water-OH associated with glucose and fructose observed in almost all honeys (Beganović et al., 2019). This suggests that the interaction of water molecules with DHA and MGO via hydrogen bonds between OH and C=O at 991 nm plays an important role in classifying mono-mānuka honey from others (Iwamoto, 2010). In addition, the presence of unique protein molecules (e.g., arabinogalactan protein) in mānuka honey may also contribute to mono-mānuka honey's signal at 991 nm since protein carbonyls likely interact with water molecules via hydrogen bonds (Gannabathula et al., 2012). Leptosperin is unique and abundant in mānuka honey, but this compound mostly absorbs in the UV range (Bong et al., 2017). However, molecular vibration of -CH_3,-OH and CO groups in Leptosperin can also contribute to classifying mono-mānuka honeys (Truong et al., 2022).

Behaviour of the network of water in the honey matrix may be key to classifying mānuka honey. Water is relatively scarce in the honey matrix and is competed for by various moieties. This may render water a useful contrast. Yang et al. (2020) identified the spectral region in 1324 - 1586 nm, relevant to water OH vibration, as being important to differentiating mānuka honeys from corn syrup and syrup-blended mānuka honeys. Pure mānuka honeys showed strong hydrogen bonds of water in 1486 - 1586 nm while adulterated honeys indicated weaker hydrogen bonding of water, or less highly structured water-OH bonding in the honey matrix in the 1324 - 1460 nm range (Yang et al., 2020). The current study also found that the vibration of water-OH at 1435 nm was important for classifying non-mānuka honeys while the water-OH vibration at 991 nm was significant for classifying mānuka honeys. This implies that the network of water with other phytochemicals in non-mānuka is different from that in mānuka honeys. This study did not identify the 1486-1586 nm range was important for classifying mānuka honeys as reported by Yang et al. (2020).

Prediction from hyperspectral images showed the potential benefit of generating seamless spatial maps. At the pixel level, mono-mānuka honeys were well-classified on hyperspectral images. In particular, mono-mānuka honeys are commonly UMF^{TM} ≥ 10 and are derived mainly from *L. scoparium* nectar. These were separated well from multi-mānuka and non-mānuka honeys. Honey samples with UMF^{TM} < 10 were more frequently misclassed due presumably to the presence of nectar from multiple sources. Some multi-mānuka and non-mānuka were also misclassed as mono-mānuka honeys. This misclassification accounted for ~ 20 % of samples. At the industrial level, the benefit of 90 % accuracy for classification of mono-mānuka and 20 % misclassed honeys may be acceptable and provide an economic benefit over common current practice of extracting all of one apiary in a single pool. The combination of HSI with deep learning algorithms is promising. Future research is required to improve the prediction accuracy by exploring 2D-CNN and 3D-CNN algorithms.

9.6. Conclusion

Assessment of the quality and monoflorality of mānuka honey in the frame before bulk extraction could bring benefit to honey companies, beekeepers, and landowners. The current chapter showed the potential of hyperspectral imaging and deep learning (CNN) for at-line evaluation of mānuka honey's quality and monoflorality. Key chemical markers (e.g., DHA, MGO), and their impact on water molecules in the honey matrix significantly contribute to the identification of mānuka honey from other floral honeys. Potentially, hyperspectral imaging combined with deep learning could be used for automating assessment of honey while still in

the frame before bulk extraction. As such it points to the next major improvement in engineering the honey extraction process line.

Chapter 10

Quality assessment of mānuka honey by combined reflectance fluorimetry, NIR and chemometrics

10.1. Introduction

NIR non-imaging and hyperspectral imaging have been studied to assess the quality and purity of mānuka honey (Chapter 4 - 9). NIR methods combined with chemometrics, machine learning and deep learning showed the capability to evaluate mānuka honey quality based on concentration of chemical markers and potency (UMF^{TM} score). Purity classification into UMT^{TM} buckets or MPI honey classes also achieved 90 % (for mono-mānuka honey) accuracy. The current study still searches for a better non-invasive method to enhance quality assessment of mānuka honey while still in the frame.

Fluorescence is noteworthy since mānuka honey contains two unique fluorescence markers: Leptosperin and Lepteridine^{TM} that are chemically stable during storage (Bong et al., 2017; Ishisaka et al., 2017; MPI, 2017b). Leptosperin and Lepteridine^{TM} were found maximally absorbing and exhibited fluorescence signals at $\lambda_{ex/em}$ 270/365 nm & 330/ 470 nm, respectively when measuring honeys diluted with water to 2 % (Bong et al., 2018; Bong et al., 2017; Lin et al., 2017). The two fluorescent markers are easily detectable in diluted mode (absorbance < 0.1) and measured fluorescence intensity is linear with concentration (Lakowicz, 2006; Wang et al., 2017). By contrast, when measuring undiluted honey (absorbance > 1), the relationship between fluorescence intensity and fluorophore concentration is relatively non-linear due to inner filter effects (Chen et al., 2018; Kumar Panigrahi & Kumar Mishra, 2019). These effects are also known to be fluorescence quenching phenomena where the absorption and fluorescence spectra overlap (Chen et al., 2018). Fluorescence signals could not be well-detected since the fluorescence emission was reabsorbed by the high absorbance solution. As a result, fluorescence signals are distorted and non-linear with concentration (Chen et al., 2018).

There are two types of inner filter effect. The primary inner effect, when the light beam excites concentrated solutions (e.g. undiluted honey), the incoming light can just penetrate the surface and is then attenuated (Chen et al., 2018). Lower layers receive reduced light flux to induce fluorescence emission to be detected. Subsequently, the excitation spectrum could be

twisted (Bevilacqua et al., 2020). Following this event, fluorescence emission could be reabsorbed by the solution, the so-called second inner filter effect, causing a misshapen emission spectrum (Bevilacqua et al., 2020). Self-quenching is found in the 2nd inner effect since the fluorescence signal of a certain fluorophore is quenched by other compounds or moieties (fluorescent or non-fluorescent compounds). Consequently, fluorescence intensity of high absorbance solutions may not faithfully reflect the concentrations of fluorescent compounds. This causes difficulties in using fluorescence methods on untreated samples (Wang et al., 2017). Recently, several methods have been developed for correcting fluorescence signals heavily impacted by inner filter effects (Ceresa et al., 2021; Chen et al., 2018; Fonin et al., 2014; Luciani et al., 2013). According to Wang et al. (2017), using mathematical models, instrumental and parameter approaches could correct signals from the influence of inner effects. However, almost all these corrections have advantages and disadvantages (Wang et al., 2017).

Intuitively, inner filter effects impact fluorescence measurements of high absorbance solutions, but geometry configurations could eliminate these effects. Fonin et al. (2014) measured fluorescence signals of dye solutions with different levels of absorbance (0 - 2.5) by right-angle geometry fluorescence spectroscopy. The results showed the inner filter effects greatly impacted fluorescence measurements of high absorbance samples and the fluorescence intensity showed non-linearity with concentration (Fonin et al., 2014). By contrast, frontal geometry fluorescence spectroscopy eliminated inner filter effects when applied to unpretreated samples (Bevilacqua et al., 2020; Kao et al., 1998; Ruoff, Luginbühl, Bogdanov, Bosset, Künzli, et al., 2006). Ruoff et. al. (2006) employed front-face fluorescence spectroscopy to authenticate the botanical and geographical origin of honey without dilution. By using fluorescence spectra from the front-face configuration, mono-floral and multi-floral honeys from different botanical and geographical origins were well-classified with an accuracy above 90 %. However, their study did not discuss inner filter effects since their goal was only to determine floral sources of honey rather than measure concentrations of target fluorescence compounds. By contrast, Mashadi et al. (2022) used laser induced fluorescence spectroscopy to measure furosine and riboflavin in undiluted honeys. By measuring from different angles on the surface of cuvette, this study showed inner filter effects are minimised (Mashhadi et al., 2022). Bevilacqua et al. (2020) investigated front-face fluorescence spectroscopy for measurements of tryptophan, riboflavin, and nicotinamide adenine dinucleotide (NADH) with different absorbance levels (3.81×10^{-4} - 0.1). The results showed that the 2nd inner filter effects distorted the fluorescence signals due to the presence of interferents (Bevilacqua et al., 2020).

Overall, these studies indicated that the geometry of fluorescence configuration plays a role in generation of inner filter effects. According to Kao et al. (1998), in-line geometry fluorescence spectroscopy reduced inner effects better than did front-face geometry. Moreover, total internal reflection fluorescence spectroscopy shows most promise in eliminating inner filter effects (Kao et al., 1998). Therefore, in-line geometry fluorescence spectroscopy (Figure 2.7 - Chapter 2) was investigated for measurements of undiluted honeys (absorbance > 2 at λ_{ex} 270 nm) filled in a 96-well plate. The large angle LUX detector used in this work can detect the signals reflected from much of the upper surface of a well. This study considered the large internal reflectance fluorescence signals captured from the well to be similar to total internal reflection cell fluorescence measurements. Two unique fluorescence markers were mainly measured in the complex honey matrix containing diverse interferents for quality assessment of mānuka honeys.

Traditional chemometrics models (partial least squares (PLS)) are usually applied on an unfolded emission matrix (samples x emission bands). High absorbance solutions resulted in poor predictions due to non-linearity between fluorescence and concentration of target compounds (Wang et al., 2017). In contrast to standard two-way PLS, multi-way analyses (PARAFAC, n-PLS, Tucker-1, Tucker-2 & Tucker-3) have been investigated on three-way matrices of EEM data. According to Bevilacqua et al. (2020), the multi-way models provide a better approach for analysing fluorescence signals from high absorbance solutions. Therefore, multi-way analyses PARAFAC and n-PLS were employed in this study to examine three-way fluorescence EEM data of undiluted honeys captured by the internal reflectance cell configuration.

The study also investigated the fusion of fluorescence with NIR to assess mānuka honey quality and purity in the undiluted state. Fluorescence captures the characteristic signal of fluorophores resulting from specific electronic transitions. Meanwhile NIR captures the change in molecular vibration of a wide range of chemical species as well as the interaction among compounds and the effect of the matrix due to scattering properties. The two methods offer complementary information when combined. Multi-block approach was employed to analyse the combined data with different series of spectral variables. Multi-block allows these datasets to join in a conjugated block for modelling (Kohonen et al., 2008; Mishra et al., 2021). The fusion of fluorescence and NIR was investigated as a way to overcome the challenge imposed by the complex honey matrix and to enhance the interpretation of fluorescence signatures.

Overall, the current study aimed to investigate methods to overcome the effect of inner filter effects due to the complex honey matrix when predicting two fluorescence markers based

on reflectance measurements. Mānuka honeys from multiple botanical sources were assessed by measuring honey quality (UMF™ score) and purity (verification of botanical sources of mono-floral, multi-floral, and non-mānuka honeys). Fusion of fluorescence and NIR data was explored to evaluate honey quality and purity. This work helps assessment of quality and purity of mānuka honey at source as well as its authenticity in the market.

This chapter aims to answer the research hypothesis 2 that it is possible to develop chemometric methods to eliminate the effect of undiluted honey matrix on fluorescence emission and to detect fluorescence signatures associated with mānuka honey in frames.

10.2. Materials and methods

10.2.1. Materials

A suite of 100 honey samples harvested from the 2019 - 2020 season, kept at room temperature and provided by Comvita® Ltd. were selected to give a broad spread of Leptosperin and Lepteridine™ levels (Table 10.1). The dataset consisted of four different geographic districts from North Island of New Zealand (Whanganui, Wairarapa, Mobile Unit and Hawkes Bay). The chemical profile of Leptosperin, Lepteridine™ and UMF™ in this dataset were measured by Comvita two years before collecting fluorescence data. Leptosperin, Lepteridine™ are stable chemicals over time in storage (Bong et al., 2018; Bong et al., 2017), but UMF™ could change due to the changes in MGO concentration. All samples were stored at 4^{o} C after receiving from Comvita® until scanning.

Table 10.1. Statistical summary of Leptosperin and Lepteridine™ contents in 100-honey sample dataset

n=100	DHA (mg/kg)	MGO (mg/kg)	Lepteridine™ (mg/kg)	Leptosperin (mg/kg)	UMF™ score
Average	1080	135	7.40	369	7.86
Min	0	0	0.2	14	0
Max	3651	511	25.9	1022	18.7

Figure 10.1 shows the relationship of the two unique fluorophores with UMF™ score for the set of selected honey samples and plotted by three honey classes (mono-mānuka, multi-mānuka and non-mānuka). Table 10.1 gives a statistical review of DHA, MGO, Leptosperin and Lepteridine™ concentrations (mg/kg) including UMF™ scores in the same dataset.

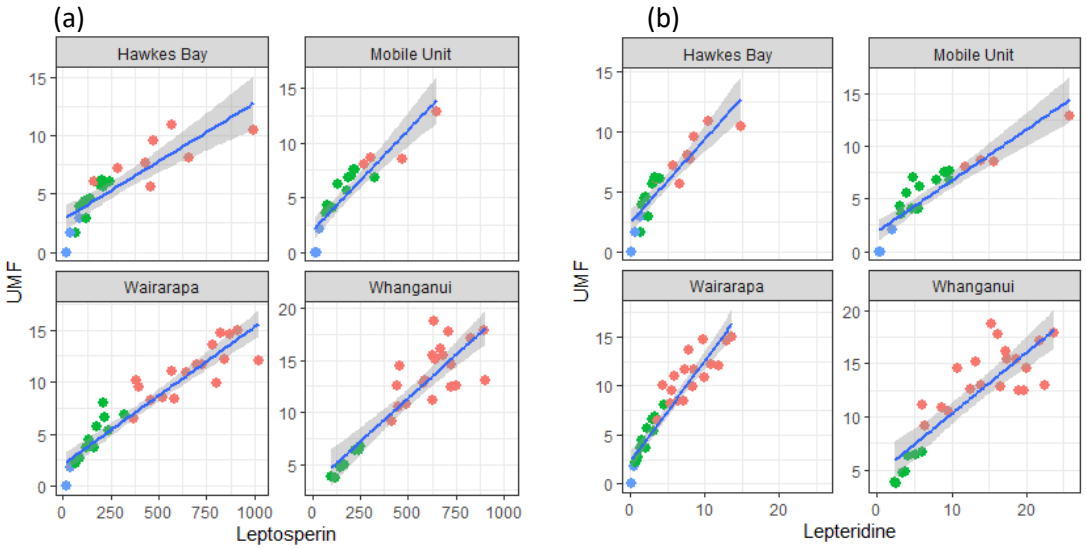

Figure 10.1. *The relationship plot of Leptosperin (a) and Lepteridine™ (b) with UMF™ scores obtained from 100-honey sample dataset: mono-mānuka honey (red), multi-mānuka honey (green) and non-mānuka honey (blue)*

10.2.2. Pure standards preparation

Pure analytical grade Leptosperin and Lepteridine™ used as chemical standards for this study were provided by Comvita® Ltd and were diluted in Milli-Q water and in "dummy honey". Dummy honey was made following the MPI protocol (No. 2017/30), and mainly consists of fructose, glucose, maltose and sucrose (MPI, 2017a). These sugar compounds were diluted in Milli-Q water to give a density of approximately 1.4 g/mL. The idea of using dummy honey was to generate a concentrated sugar solution as a blank highly analogous to the honey matrix.

Three levels of Leptosperin (1000 ppm, 500 ppm and 300 ppm) and Lepteridine™ (30 ppm, 20 ppm and 10 ppm) dissolved in Milli-Q water and in dummy honey were used as standards to compare fluorescence signals with those of diluted and undiluted honeys. Fluorescence intensity quoted was determined by subtracting the spectrum of the Milli-Q water or the dummy honey blank as appropriate.

10.2.3. Fluorescence measurements on optical 96-well plates

The set of 100 samples was kept at room temperature for 2 hours prior to the experiment. Then, these samples were diluted to 2 % (w/v) with milli-Q water following the dilution procedure of Bong et al. (2018). Both the 100 diluted samples (200 µL per sample) and the

matching suite of 100 undiluted samples (~ 0.5 g per sample) were subsampled into optical 96-well plates (product 3603, Corning®, NY, USA). Three replicates of ten samples were filled into each well-plate. The optical 96-well plate used is made of polystyrene (black sides and clear flat bottom) that can contain maximum 360 µL. A VARIOSKAN LUX spectrofluorometer (SN 3020-1333, ThermoFisher Scientific, MA, USA) was used to capture fluorescence signals from the well-plate without lid at room temperature (22 - 25^{o} C). The fluorescence measurement protocols and collected data were controlled by a Skanlt software (version 6.0.1, ThermoFisher Scientific, MA, US) via an external computer connected to the VARIOSKAN device.

In-line reflectance geometry fluorescence scanning was applied such that the vertical light beam illuminated the cell, and the fluorescence emission was captured from the majority of the upper sample surface of the well being interrogated, with little interference from the styrene well perimeter. The light source and the detector were put at the same side for top reading. This configuration of fluorescence measurement is independent of the position captured and can be considered as similar to the total of internal reflectance cell configuration as mentioned by Kao et al., (1998).

All samples were scanned in the excitation emission matrix (EEM) of the 250 - 400 nm excitation range with an increment of 5 nm, and of the 300 - 600 nm emission range with spectral resolution 5 nm. During scanning, the cut-off function was used to trim off the uppermost 50 nm of the default excitation band which generated noisy information from Raman and Rayleigh scatters. The Xenon lamp light source was flashed for 100 ms per well during which time the detector recorded and averaged a series of ten 10 ms readings. This top reading optical system was chosen to capture fluorescence emission only from the sample in the well, with no interference from the well-side (i.e., avoid crosstalk fluorescence interference). The auto range sensitivity was set from 0.001 to 1500 relative fluorescence units (RFU) to allow detection of 0.4 fmol fluorescein/well (top reading).

10.2.4. Hyperspectral data in NIR range (547 - 1701 nm)

Hyperspectral data of the same subset of 100 honey samples, presented in black polystyrene 96-well plates (NUN137103, ThermoFisher Scientific, MA, USA), were generated by scanning under a hyperspectral camera (Model 1003B-10151, Headwall Photonics, Fitchburg, MA, USA) in the NIR range 547 - 1701 nm. First, regions of interest (ROIs) representing honey samples were segmented from the hyperspectral images. Then the spectral

signals of each sample were extracted by averaging all pixels for each ROI. The information of hyperspectral acquisition settings and the segmentation process were described in Chapter 4.

10.2.5. Fluorescence analysis

Kennard-Stone technique was applied to split fluorescence datasets into calibration and validation sets with a ratio of 70:30 before modelling. All chemometric methods were run with PLS Toolbox 9.0 (Eigenvector Research, Inc., Manson, WA 98831, USA) in MATLAB environment.

10.2.5.1. Partial least squares multivariate analysis

Two matrices of fluorescence data at λ_{ex} 270 and 330 nm were organised by sample in rows and by emission wavelength in columns with cells containing fluorescence intensity. Concentrations of the two key fluorescence markers were modeled by PLS regression. Classification between mono-mānuka, multi-mānuka and non-mānuka honeys was conducted by PLSDA. Mean-center pre-processing and venetian blind cross-validation techniques were employed for each model. During modelling, the one-interval partial least squares (iPLS) variable selection technique was turned on to select domain emission variables for improving model performance. In general, the PLS algorithm uses a few latent variables to maximise the covariance between fluorescence intensity and the measured concentration values. The number of latent variables was chosen based on the trade-off between the lowest root mean square error (RMSE) of cross-validation and of calibration. The coefficient correlation R^2, RMSE and bias were used to evaluate PLS prediction results. For classification by PLSDA, the recall, precision, F1 and class accuracy (CA) were employed.

10.2.5.2. Multi-way analysis

Trilinear parallel factor analysis (PARAFAC) and tri-partial least squares (tri-PLS) methods were employed for analysing three-way dimensional fluorescence data. The excitation emission matrix (EEM) containing fluorescence measurements of 100-honey samples were reshaped into a cube of sample x excitation x emission (Bro, 1997; Bro & Gallagher, 2022).

The PARAFAC principle is to search for the uniqueness of chemical components contained in EEM data. A likely match of component to a certain fluorescence signal based on a binary of excitation-emission channels was estimated using alternating least squares. This algorithm works in a decreasing order match that allows identification of an unknown chemical

component (Bro & Gallagher, 2022). The number of components chosen for a PARAFAC model was based on the knowledge of fluorescent compounds contained in the sample and the core consistency value. The core consistency plot shows how the likely components identified are separated from unknown components. A good PARAFAC model usually provides consistency close to 1 and small average residuals. The excitation and emission band plots are also useful to identify fluorescence peaks relevant to the target compounds.

Three-way PLS (tri-PLS) is an extension of two-way PLS which is employed for analyzing a full matrix of EEM data. The independent three-way fluorescence EEM data of 100 samples (either diluted or undiluted data) contained excitation-emission spectral variables and fluorescence intensity of samples. Tri-PLS also searches for a few latent variables (LVs) maximising the covariance between fluorescence data and responses**.** In this tri-PLS model, pre-processing multiway center technique with venetian blind cross-validation was used.

10.2.4.1. Multi-block PLS regression

Multi-block was recently introduced for the analysis of combined datasets which contain variables captured in different processes or different optical instruments (Kohonen et al., 2008). The data are combined as blocks or divided into meaningful blocks. Multi-block PLS regression is similar in principle to standard PLS where the scores and loading weights are calculated by maximising the covariance between predictors and responses. Instead of working in a block as for standard PLS, multi-block PLS regression works with several blocks of different sets of variables. The scores and loading weights are computed for each block and assure the maximisation of predictors and responses for the whole conjugated block (Kohonen et al., 2008; Mishra et al., 2021).

In this work, each fluorescence dataset at λ_{ex} 270 nm and at λ_{ex} 330 nm was separately combined with NIR hyperspectral data (547 - 1701 nm) for modelling with multi-block PLS regression. For each multi-block model, the standard PLS model was run first and inserted into the multi-block approach prior to modelling. A total of 4 blocks (fluorescence data, standard PLS model of fluorescence data, NIR data, standard PLS model of NIR data) were combined for running in a multi-block model. Data-preprocessing was implemented by two steps. First, the block variance scaling was used to eliminate the block effects in both raw NIR and fluorescence data (Mishra et al., 2021) while auto-scale pre-processing was applied to blocks of standard PLS models. Then, different pre-processing techniques (MC, SNV, MSC, 1st and 2nd derivatives) were investigated in the joined data of a multi-block model to remove noise and multiplicative effects. Venetian blind cross-validation with 10 folds was used. During

modelling, the iPLS variable selection technique of four intervals was applied to select important features.

10.3. Results

10.3.1. The influence of the black polystyrene 96-well plate

The polystyrene 96-well plate (clear flat bottom, black sides) was used for fluorescence measurement. The use of the black microplate aims to avoid fluorescence crosstalk meanwhile the clear bottom (20 % polystyrene) eliminates the autofluorescence background. However, fluorescence emission from polystyrene was still found in the UV range when measuring non-fluorescent water and dummy honey as blanks (Figure 10.2). Polystyrene seems to be releasing strong signals in the 320 - 340 nm range at excitation bands of 280 - 290 nm when measuring Milli-Q water. By contrast, when measuring dummy honey (non-fluorescence solution) the maximal emission of polystyrene shifts to $\lambda_{ex/em}$ 310 - 330/350 - 380 nm probably due to the reflection and re-absorption of light for a saturated liquid (dummy honey).

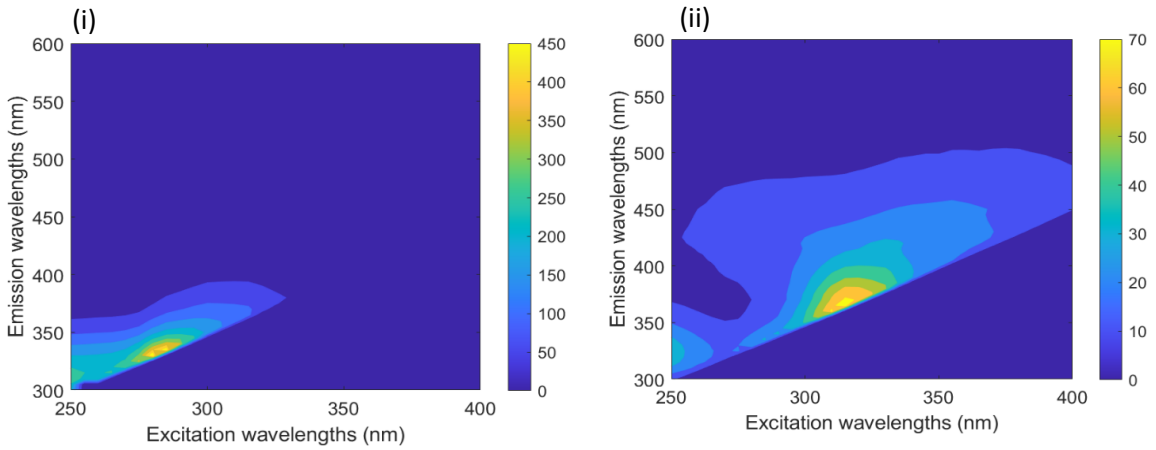

Figure 10.2. *Excitation emission matrices of Milli-Q water (i) and of dummy honey (ii) captured on a 96-well plate (clear polystyrene bottom, black polystyrene sides)*

10.3.2. Fluorescence emission of Leptosperin and Lepteridine™ standards

Leptosperin (1000 ppm, 500 ppm and 300 ppm) and Lepteridine™ (30 ppm, 20 ppm and 10 ppm) standards diluted in Milli-Q water and in dummy honey were scanned in the EEM range of 250 - 400/300 - 600 nm. Strong fluorescence emission of Leptosperin was found in the range 350 - 400 nm for excitation below 280 nm that differs from fluorescence emission of polystyrene. Polystyrene autofluorescence background did not strongly affect the signal of

Leptosperin and it could be minimised by subtracting the blank. Figures 10.3 a & b show the fluorescence signal of 300 ppm Leptosperin in the default EEM. At 300 ppm, a clearer maximal fluorescence region of Leptosperin emission was observed than for 1000 ppm or 500 ppm. The higher absorbance solutions may generate a stronger primary inner filter effect (Kimball et al., 2020). As a result, the signal of Leptosperin was merged with that of polystyrene.

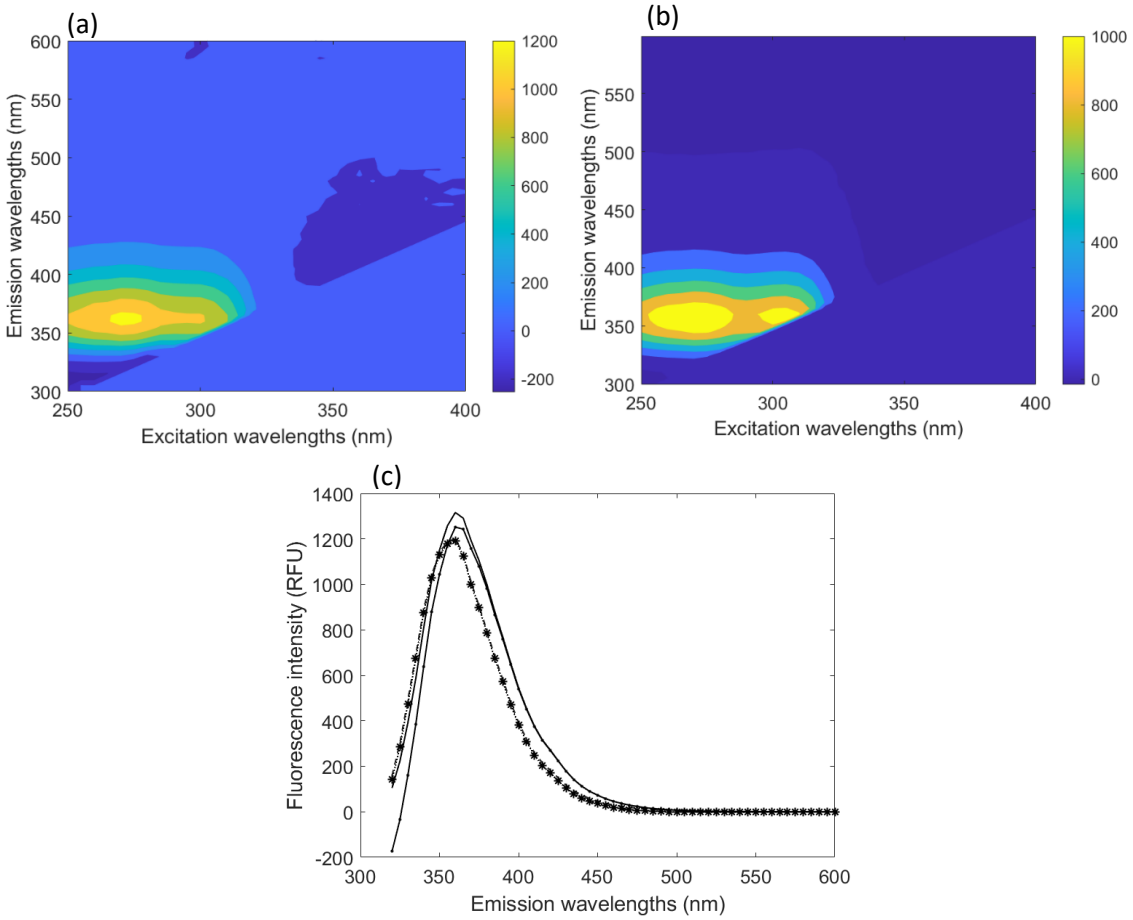

Figure 10.3. *Fluorescence excitation emission matrices after blank subtraction for 300 ppm Leptosperin diluted in Milli-Q water (a) & in dummy honey (b),* and *fluorescence emission spectra at excitation 270 nm: raw spectra in water (solid line) & after subtracting water spectrum (solid-dot line); raw spectra in dummy honey (dotted line) & after subtracting dummy honey spectrum (star-line)*

In water, the signal of pure 300 ppm Leptosperin induced a strong emission at 355 - 365 nm in the excitation range of 265 - 275 nm (Figure 10.3 a). In dummy honey, Leptosperin fluorescence emission at 300 ppm showed a strong signal at 345 - 370 nm for the excitation range 255 - 285 nm (Figure 10.3 b). The signal of polystyrene ($\lambda_{ex/em}$: 295-310/350-360 nm) was also found in the EEM (Figure 10.3 a & b), but it was separated from that of Leptosperin. Figure 10.3 c illustrates the fluorescence emission spectra of Leptosperin standard captured in both water and in dummy honey at excitation band 270 nm before and after blank subtraction. In general, pure Leptosperin produced a fluorescence emission peak at 365 nm in both solutions at excitation wavelength 270 nm. This implies that inner filter effects were eliminated and not detrimental to the emission spectra of undiluted honeys.

Similarly, fluorescence signals of a pure Lepteridine™ standard in water and in dummy honey are illustrated in Figure 10.4. With concentrations of 30 ppm, 20 ppm and 10 ppm, Lepteridine™ induced clear signals in both environments. In the excitation range 250 - 370 nm, Lepteridine™ strongly released two fluorescence zones in 450 - 500 nm and in the 350-400 nm range. In water, the strongest fluorescence peak of pure Lepteridine™ was found in the excitation-emission range of 320 - 340/450 - 500 nm with a small fluorescence tail in $\lambda_{ex/em}$ 320 - 340/360 - 400 nm (Figure 10.4 a). Lepteridine™ also absorbs below 270 nm and released a strong emission signal at 450 - 500 nm. It is likely that there was also a little fluorescence tail in 360 - 400 nm, but it did not show in EEM due to the fluorescence intensity scale. In dummy honey, Lepteridine™ gave the strongest fluorescence signal in excitation-emission range of 320 - 340/350 - 400 nm and a small signal in 320 - 340/450 - 500 nm range (Figure 10.4 b). This phenomenon was opposite with the Lepteridine™ signal in water. The reason could be due to the 2nd inner filter effect for highly concentrated solutions. The emission bands of the first fluorescence signal (350 - 400 nm) could be reabsorbed again as excitation for the second fluorescence peak (450 - 500 nm). This was also found for the absorption of Lepteridine™ below excitation 270 nm (Figure 10.4 b).

Figures 10.4 c & d display fluorescence emission spectra of Lepteridine™ standard captured in water and in dummy honey at excitation 250 and 330 nm. It is apparent that Lepteridine™ in water induced the strongest fluorescence signal at 470 nm for λ_{ex} 330 nm while in dummy honey Lepteridine™ induced the strongest signal at 380 nm with λ_{ex} 330 nm.

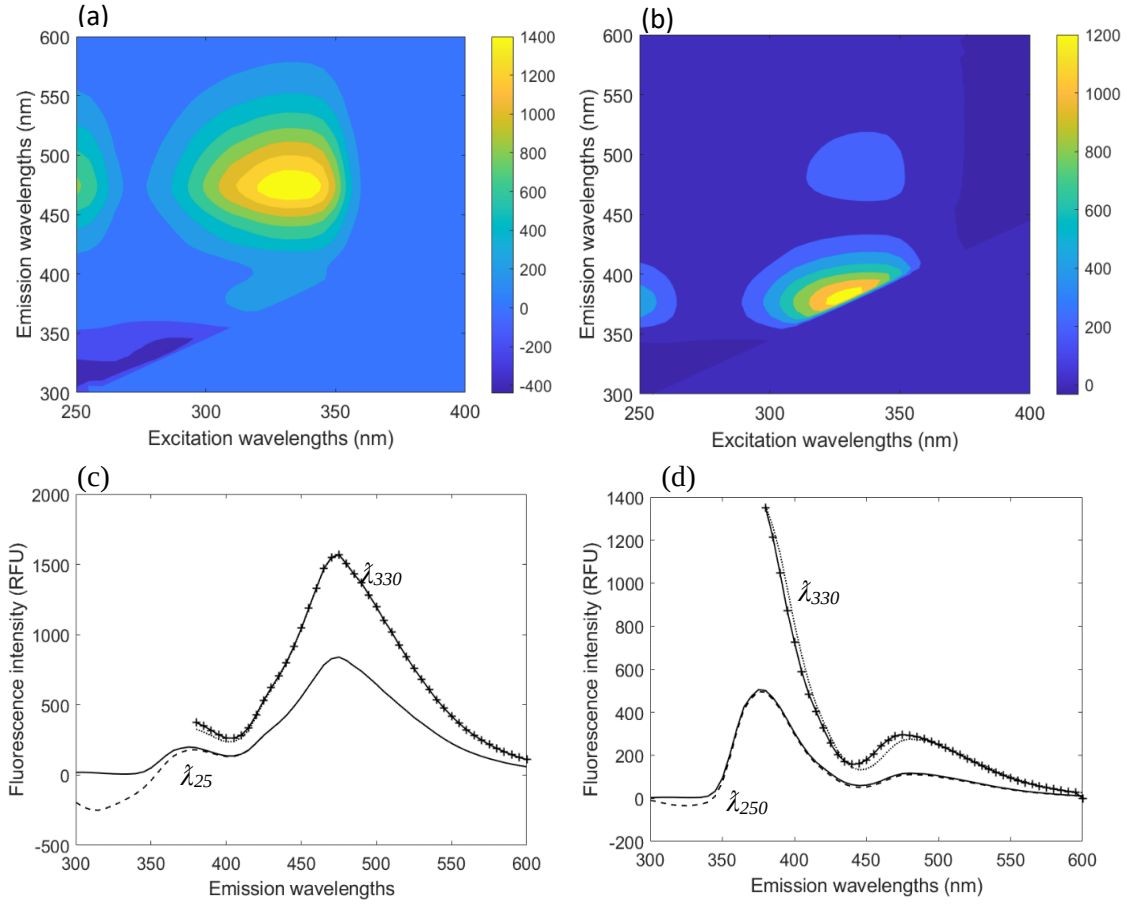

Figure 10.4. *Fluorescence excitation emission matrices after blank subtraction for 30 ppm Lepteridine™ diluted in Milli-Q water (a) & in dummy honey (b), and fluorescence emission spectra in Milli-Q water (c) and in dummy honey (d) at excitation bands 250 nm and 330 nm. At λ_{250} raw spectra (solid line) & after subtracting water spectrum (dashed-line). At λ_{330}, raw spectra (crossline) & after subtracting dummy honey spectrum (dotted-line)*

10.3.3. Fluorescence emission of diluted and undiluted honeys

Fluorescence excitation emission matrices of five diluted and undiluted honeys with different levels of Leptosperin and Lepteridine™ in the range of $\lambda_{ex/em}$ 250 - 400/300 - 600 nm are illustrated in Figure 10.5. The EEM of honey samples showed a fluorescence intensity difference between the measured and blank.

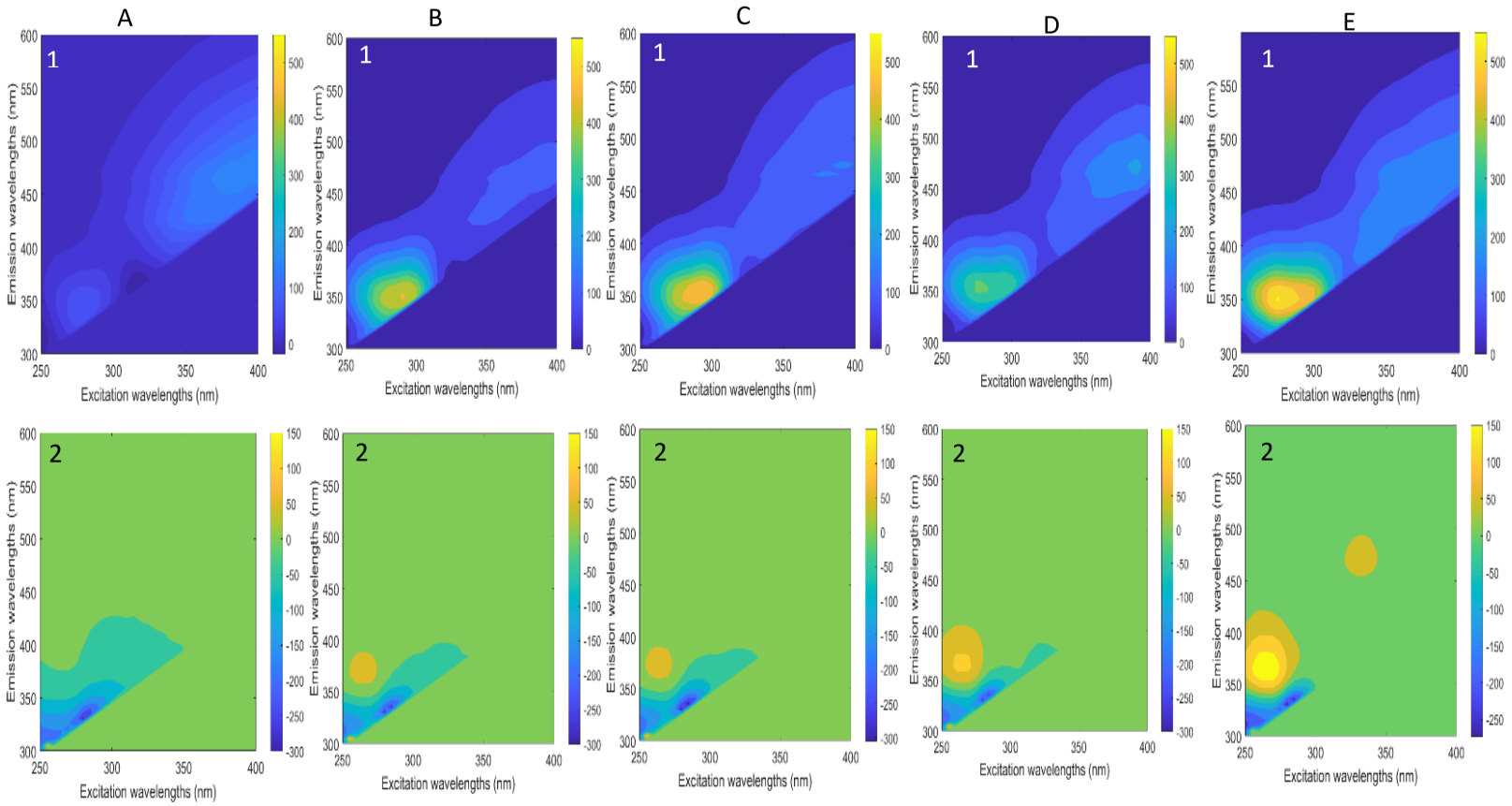

Figure 10.5. *Fluorescence excitation emission matrices (250-400/300-600 nm) of five undiluted (1) and 2 % (w/v) diluted (2) honey samples with different levels of Leptosperin (MM1) and Lepteridine™ (MM2): A (MM1:16 mg/kg & MM2:0.4 mg/kg); B (MM1: 179 mg/kg & MM2: 2.2 mg/kg); C (MM1: 302 mg/kg & MM2: 14 mg/kg); D (MM1: 460 mg/kg, MM2: 5.4 mg/kg) and E (MM1: 905 mg/kg & MM2:22.6 mg/kg). The measured fluorescence intensity was the intensity difference of sample and blank*

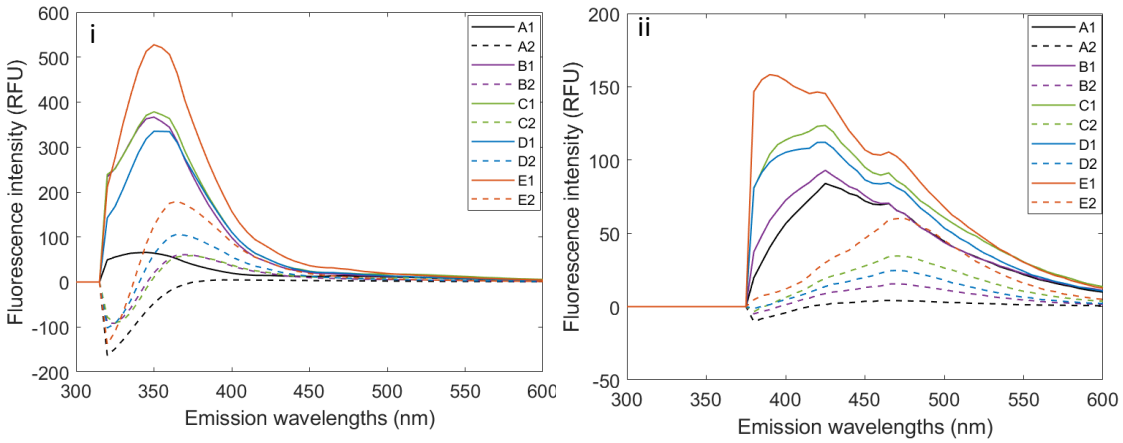

Figure 10.6. *Fluorescence emission spectra of the five honey samples in Figure 10.5: undiluted (solid line,1) and diluted (dashed line,2) at excitation 270 (i) and 330 nm (ii)*

As with pure standards, Leptosperin fluorescence emissions of four diluted honey samples (2 % (w/v)) were also detected at 350 - 400 nm for the excitation range of 260 - 270 nm except for a sample containing Leptosperin at 16 mg/kg (Figure 10.5-A2). In addition, Lepteridine™ fluorescence emission was found only in an EEM of $\lambda_{ex/em}$ 330 - 340/450 - 500 nm for a sample with a Lepteridine™ concentration of 22.6 mg/kg (Figure 10.5-E2). The fluorescence tail of Lepteridine™ at 320 - 340/350 - 400 nm did not show as with pure standards. Fluorescence emission of Lepteridine™ for excitation below 270 nm was also not observed on EEM. These could be due to weak signals compared to the intensity scale. However, on the raw EEM without blank subtraction small signals of Leptosperin and Lepteridine™ were found which were similar as those of standards. Negative intensity scales were sometimes found in EEM matrices of diluted honeys after blank deduction. This was likely due to the impact of Raman scatterings for honey samples containing small particles.

As with diluted samples, the Leptosperin signal of five undiluted honeys seemed apparent in EEM matrices. However, the signal ($\lambda_{ex/em}$ 270/365 nm) found in a sample with Leptosperin concentration 16 mg/kg could correspond to the background of the well-plate. Fluorescence emission of Leptosperin and polystyrene from the well-plate were merged due to inner filter effects for high absorbance samples. These signals were also detected for pure Leptosperin standard in dummy honey (section 10.3.2). The maximal fluorescence emission of Leptosperin in undiluted honey samples was at 350 nm meanwhile that of diluted samples was at 360 nm at excitation 270 nm (Figure 10.6 i). The highest signal of Lepteridine™ in undiluted honeys was discovered at 390 nm after exciting at 330 nm (Figure 10.6 ii). This was quite similar to

pure Lepteridine™ standard in dummy honey ($\lambda_{ex/em}$ 330/380 nm). Two different emission peaks (420 & 465 nm) were observed in the 400-500 nm range at excitation 330 nm in undiluted honeys. The peak at 465 nm could be relevant to Lepteridine™, but the peak at 420 nm is unknown.

10.3.4. PARAFAC analysis

The three-dimensional matrix of excitation emission fluorescence data of 100 diluted and undiluted samples was analysed using PARAFAC. For diluted honey data, two PARAFAC components were used that resulted in the core consistency ~1 (Figure 10.7 i). Two clear signals of fluorophores were identified in EEM (Figure 10.7 ii). The excitation-emission uniqueness at $\lambda_{ex/em}$ 265/365 nm was identified for Leptosperin and at $\lambda_{ex/em}$ 335/470 nm for Lepteridine™ (Figure 10.7 iii & iv). This was also in line with current pure standards and the results of Bong et.al (2018) (Bong et al., 2018).

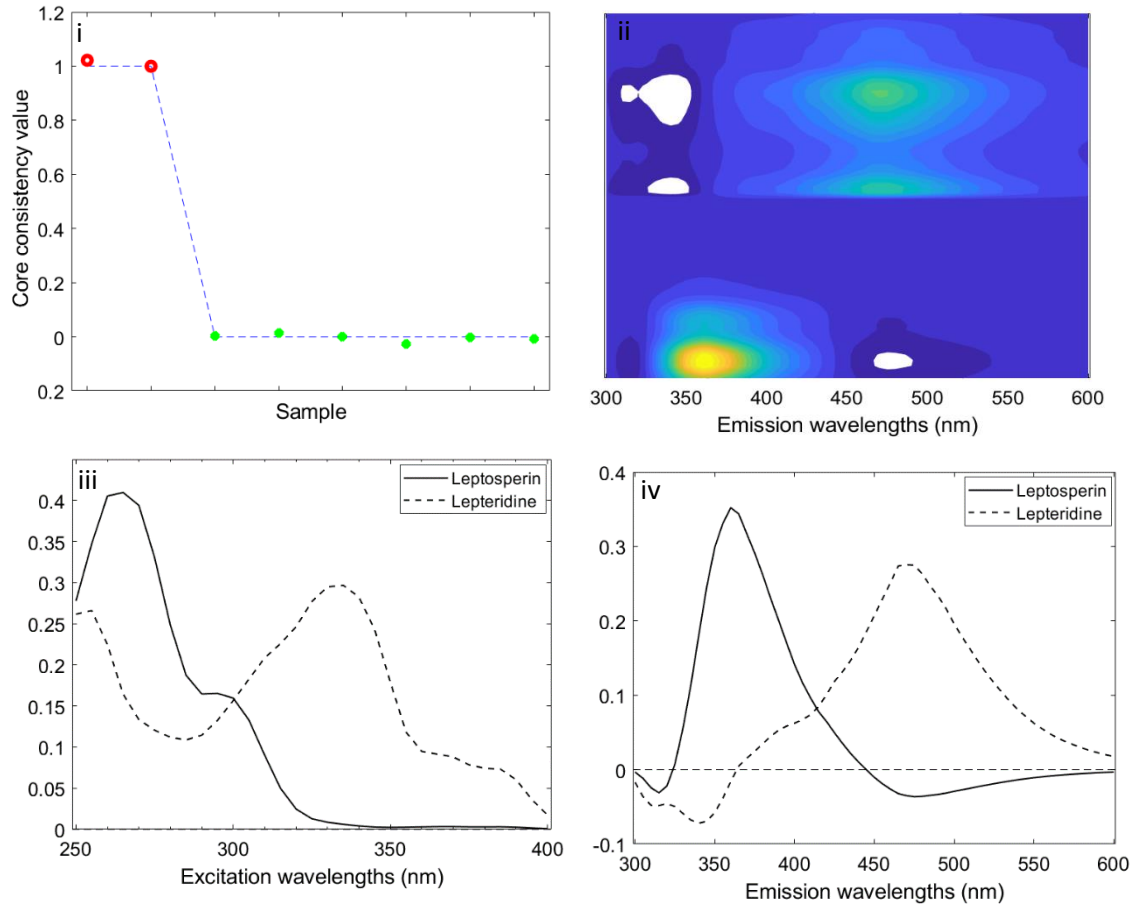

Figure 10.7. *PARAFAC results for 100-diluted honey samples in EEM of 250-400/300-600 nm: core consistency plot (i); fluorescence signals (ii); excitation (iii) and emission (iv) plots of Leptosperin and Lepteridine™ identified in a PARAFAC model*

For undiluted honey data, three PARAFAC components were chosen to obtain core consistency 0.98 (Figure 10.8 d). Three fluorophores seemed apparent on EEM (Figure 10.8 a, b & c). Component 2 had an excitation/emission range of 270 - 285/360 nm which could be relevant to Leptosperin because Leptosperin standard's signal in dummy honey was found in this spectral range. Meanwhile, components 1 and 3 gave fluorescence peaks in the ranges of 400 - 500 nm and 450 - 500 nm at excitation bands 390 and 345 nm. These components could correspond to the first and second fluorescence peaks of Lepteridine™, but PARAFAC apparently mixed these signals. Alternatively, only component 3 might relate to Lepteridine™ since its fluorescence emission aligned with that of pure standard in dummy honey and component 1 showed no equivalent in the standard in dummy honey system.

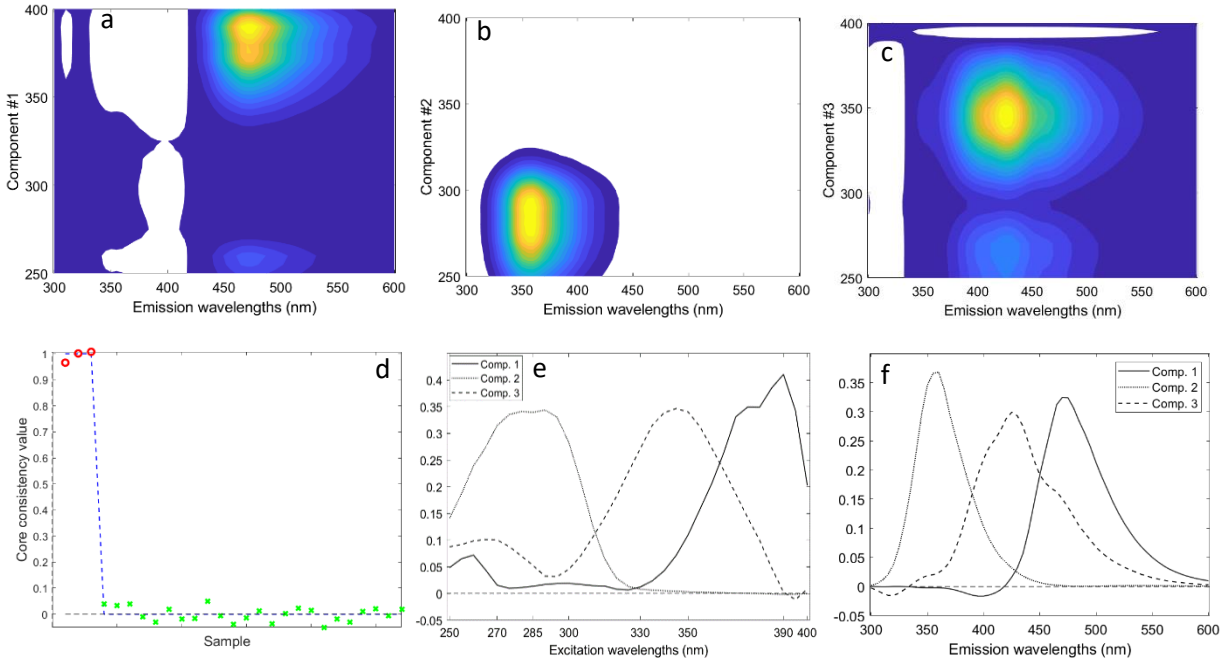

Figure 10.8. *PARAFAC results for 100-undiluted honey samples in EEM of 250-400/300-600 nm: fluorescence signals of component 1 (a), component 2 (b) and component 3 (c); core consistency plot (d); excitation (e) and emission (f) plots of three components identified in a PARAFAC model*

10.3.5. Estimation of chemical markers with standard PLS regression

Since Leptosperin and Lepteridine™ showed fluorescence signals at 270 and 330 nm respectively, the raw fluorescence spectral data of 100 diluted and undiluted honey samples at these excitation bands were used to predict Leptosperin, Lepteridine™ and UMF™ score using standard PLS regression (two-way PLS).

Table 10.2 shows standard PLS models of undiluted honeys compared with diluted honeys for prediction of fluorescence markers and UMF™ score at λ_{ex} 270 nm. Overall, fluorescence measurements of diluted honeys provide high linearity (R^2 ~ 1) for the concentrations of both fluorescence markers. By contrast, a non-linear relationship was observed for PLS models predicting fluorescence markers from undiluted honeys probably due to inner filter effects. Prediction of Leptosperin in undiluted honeys on the test set only gave 73 % accuracy which was much lower than prediction accuracy on diluted honeys at λ_{ex} 270 nm. Predictions of Lepteridine™ and UMF™ score from undiluted honey data on the test set were 61 % and 78 % respectively at λ_{ex} 270 nm, which were also lower by 7 - 20 percentage points than those predicted from diluted honey data. All models of undiluted honey data had prediction errors (RMSECV & RMSEP) higher than did models of diluted honey data.

Table 10.2. Standard PLS regression results for Leptosperin (MM1), Lepteridine™ (MM2) and UMF™ score obtained from diluted and undiluted honey data at excitation 270 nm

	Diluted honey data			**Undiluted** honey data		
PLS	MM1	MM2	UMF™	MM1	MM2	UMF™
Pre-processing	MC	MC	MC	MC	MC	MC
LVs	1	2	2	3	3	3
R^2CV	0.97	0.62	0.82	0.73	0.53	0.75
RMSECV	52.17	3.86	1.91	138.10	4.44	2.31
Bias CV	-0.06	0.01	0.02	-2.25	0.01	-0.03
R^2Pred	0.98	0.81	0.85	0.73	0.61	0.78
RMSEP	36.77	2.85	1.91	163.69	3.58	2.19
Bias Pred	-1.55	0.24	-0.02	-47.74	0.82	-0.04
Features (nm)	380, 385	330, 425, 435, 505	320, 325	320, 325	525, 530	465, 470

Note: MC means mean center

Table 10.3 illustrates the results of standard PLS models for undiluted and diluted honey data at λ_{ex} 330 nm. With the undiluted honey dataset, Lepteridine™ could be estimated with up to 82 % accuracy compared with 91 % accuracy for the diluted honey dataset. PLS models of Leptosperin and UMF™ score on undiluted honey data performed poorly on the cross-validation set, but the predictions on the test set reached 82 % accuracy. Prediction of Leptosperin in undiluted data at λ_{ex} 330 nm was of similar accuracy to that in diluted data. However, prediction of UMF™ score at λ_{ex} 330 nm in undiluted honey was still poorer than of diluted honey by 9 percentage points but looked good enough to be useful. Overall, undiluted models had higher prediction errors than diluted models.

Important features were selected for standard PLS models for both undiluted and diluted data. Those features were different for models with the same predictand. However, most selected features fell in the visible range (< 600 nm). Unsurprisingly, some important features from the UMF™ model were similar to those from the Leptosperin and Lepteridine™ models. This showed a high correlation between two fluorescence markers and the UMF™ scores as observed in the laboratory data (Figure 10.1).

Table 10.3. Standard PLS regression results for Leptosperin (MM1), Lepteridine™ (MM2) and UMF™ score obtained from diluted and undiluted honey data at excitation 330 nm

	Diluted honey data			**Undiluted** honey data		
PLS	MM1	MM2	UMF™	MM1	MM2	UMF™
Pre-processing	SNV	SNV	SNV	SNV	SNV	SNV
LVs	3	3	3	5	4	3
R^2CV	0.77	0.88	0.88	0.52	0.73	0.69
RMSECV	135.52	2.22	1.55	192.508	3.196	2.59
Bias CV	-0.01	0	0	1.99	-0.01	0.00
R^2Pred	0.81	0.91	0.92	0.83	0.82	0.82
RMSEP	119.42	1.9	1.33	160.12	3.10	2.25
Bias Pred	-40.34	0.09	-0.32	-83.70	-0.56	-1.07
Features (nm)	425, 430, 455, 460, 465	515, 520	405, 410, 530, 535	380, 385, 395, 400, 445, 450, 570, 580, 585, 595, 600	390, 395, 400, 405, 450, 455, 515, 520, 535, 540, 545, 550	380, 385, 420, 425, 435, 440

Note: SNV means standard normal variate

10.3.6. Multiway PLS (tri-PLS) analysis

A full three-dimensional EEM matrix of $\lambda_{ex/em}$ 250 - 400/300 - 600 nm was analysed with tri-PLS regression. Table 10.4 shows the prediction results of two fluorescence markers and UMF™ score for diluted and undiluted data. Overall, predictions from diluted data gave better accuracy than those from undiluted data by 5 - 15 percentage points. Compared to all standard PLS models at 270 and 330 nm, tri-PLS models on the full EEM improved prediction results for all predictands and the prediction errors also significantly reduced. In particular, with undiluted honey data, Leptosperin and Lepteridine™ could be estimated with 82 % accuracy and prediction of UMF™ score reach 86 % accuracy. Important features were identified in the 360 - 480 nm range. More features were needed for undiluted tri-PLS models than for diluted tri-PLS models. Selection of important features for Leptosperin and Lepteridine™ were close to their fluorescence peaks for both diluted and undiluted data which were not obvious in standard PLS models. This indicates that tri-PLS analysis on the full excitation emission matrix obtained better results than standard PLS of an emission fluorescence matrix at an excitation band.

However, in practice, fluorescence measurements at few excitation bands are more beneficial in terms of model stability than multiple bands. Therefore, sub-tri-PLS models of the combined fluorescence matrix at excitation bands 270 and 330 nm were examined (Table 10.5) since these bands engage the highest absorption and fluorescence emission of Leptosperin and Lepteridine™. The sub-tri-PLS models all resulted in predictions poorer than those of full-tri-PLS models and poorer than standard PLS models at 330 nm. This indicates that some other excitation bands were also important for analysis of full tri-PLS models.

Table 10.4. Tri-PLS regression results for prediction of Leptosperin (MM1), Lepteridine™ (MM2) and UMF™ score for both diluted and undiluted honey data operated on a full EEM matrix

	Diluted honey data			**Undiluted** honey data		
Tri-PLS	MM1	MM2	UMF™	MM1	MM2	UMF™
Pre-processing	MC	MC	MC	MC	MC	MC
LVs	3	3	3	4	7	5
R^2CV	0.97	0.88	0.85	0.83	0.7	0.79
RMSECV	49.40	2.18	1.17	106.77	3.44	2.08
Bias CV	-1.12	0.02	0.03	0.98	0.02	-0.02
R^2Pred	0.97	0.88	0.91	0.82	0.82	0.86
RMSEP	42.75	2.11	1.41	138.65	2.75	1.82
Bias Pred	11.66	0.00	-0.37	-33.31	0.83	0.01
Features (nm)	360, 365	475	360, 365, 460, 465	350, 355, 360, 450, 470, 475	385, 470, 475, 430, 440	350, 350, 360, 365, 430, 465, 470, 475

Note: MC means multi-way center

Table 10.5. Tri-PLS regression results for prediction of Leptosperin (MM1), Lepteridine™ (MM2) and UMF™ score for both diluted and undiluted honey data operated on a combined data matrix of excitation 270 and 330 nm

	Diluted honey data			**Undiluted** honey data		
Tri-PLS	MM1	MM2	UMF™	MM1	MM2	UMF™
Pre-processing	MC	MC	MC	MC	MC	MC
LVs	1	2	2	4	4	4
R^2CV	0.97	0.84	0.88	0.69	0.63	0.71
RMSECV	53.28	2.58	1.53	153.42	3.74	2.38
Bias CV	-0.50	-0.03	0.01	-3.94	-0.32	0.34
R^2Pred	0.97	0.9	0.91	0.77	0.68	0.77
RMSEP	50.85	1.82	1.40	141.47	3.54	2.56
Bias Pred	-0.85	0.29	-0.03	-3.23	0.19	-0.68
Features (nm)	320, 360	360, 470	360, 475	320, 340, 360, 370, 380	320, 360, 380, 465	320, 340, 380, 465

Note: MC means multi-way center

10.3.7. Multiblock PLS regression on fusion of NIR & fluorescence data of undiluted honeys

Multi-block analysis was investigated for the joined dataset of 100 undiluted honeys captured under fluorescence mode (by spectrofluorometer) and under NIR mode (by hyperspectral camera). Table 10.6 displays the prediction results at excitation 270 and 330 nm. Overall, multi-block regression models of the fluorescence and NIR datasets combined gave better prediction for both Leptosperin and Lepteridine™ than standard PLS models or tri-PLS models. However, prediction of UMF™ score did not improve compared to the tri-PLS output at both λ_{ex} 270 and 330 nm.

Multi-block PLS prediction of Leptosperin increased accuracy by ~ 10 and 5 percentage points compared to standard PLS at λ_{ex} 270 nm and tri-PLS models on a full EEM. Similarly, multi-block PLS prediction accuracy of Lepteridine™ was also slightly higher (by 0 - 6 %) than standard PLS at λ_{ex} 330 nm and than a tri-PLS model. Important features from multi-block models were similar to those identified from tri-PLS models. In general, all variables were in the visible range 320 - 535 nm.

Table 10.6. Multi-block PLS regression results for prediction of Leptosperin (MM1), Lepteridine™ (MM2) and UMF™ score for undiluted honey data at excitation wavelengths 270 and 330 nm

	λ_{ex} 270 nm			**λ_{ex} 330 nm**		
Tri-PLS	MM1	MM2	UMF™	MM1	MM2	UMF™
Pre-processing	MC	MC	MC	MC	MC	MC
LVs	2	2	2	2	2	2
R^2CV	0.8	0.56	0.69	0.58	0.76	0.71
RMSECV	125.21	3.75	2.54	186.03	2.89	2.57
Bias CV	3.45	0.04	0.01	1.61	-0.01	-0.01
R^2Pred	0.86	0.71	0.80	0.56	0.83	0.74
RMSEP	125.85	3.65	2.35	185.45	2.71	2.39
Bias Pred	54.83	-0.49	-0.13	-4.38	0.95	0.24
Features (nm)	380, 395	320, 335	360, 365, 370, 375	520, 535	470	470, 520, 535

Note: MC means mean center

10.3.8. Classification of three MPI honey classes

Fluorescence data of 100 undiluted honey samples at excitation bands 270 and 330 nm were used for classification of mono-mānuka, multi-mānuka and non-mānuka honeys using PLSDA (Table 10.7). Fluorescence data at excitation λ_{ex} 270 nm showed better classification than that at λ_{ex} 330 nm. The PLSDA model could classify non-mānuka honey with 100 % accuracy. In addition, PLSDA can also identify mono-mānuka and multi-mānuka honeys with 94 % and 89 % accuracy, respectively.

Table 10.7. The output of PLSDA model on the test set for classification of mānuka honeys on fluorescence undiluted honey data at excitation 270 and 330 nm

	λ_{ex} 270 nm				**λ_{ex} 330 nm**			
n = 30	Recall	Precision	F1	CA	Recall	Precision	F1	CA
Mono-mānuka	0.94	0.92	0.94	0.94	0.81	0.93	0.87	0.93
Multi-mānuka	0.89	0.95	0.89	0.89	0.55	0.79	0.57	0.60
Non-mānuka	1.00	1.00	1.00	1.00	0.67	0.85	0.44	0.33

10.4. Discussion

The fluorescence analysis of undiluted honeys was compared with 2 % (w/v) diluted honeys and their standards to assess whether fluorescence techniques might be applied to honey while still in the comb. Bong et al. (2017 & 2018) identified two unique fluorescence compounds Leptosperin & Lepteridine™ which could be used to help authenticate mānuka honey. By using 2 % (w/v) diluted honeys, these authors detected fluorescence signals at $\lambda_{ex/em}$ 270/365 nm for Leptosperin and at $\lambda_{ex/em}$ 330/470 nm for Lepteridine™ (Bong et al., 2018; Bong et al., 2017; Lin et al., 2020). The current study reconfirmed these fluorescence signals using both pure standards and 2 % (w/v) diluted honeys. However, in this work the fluorescence signal of Leptosperin maximally emitted at 360 nm instead of 365 nm at excitation 270 nm. Meanwhile, Lepteridine™ released a maximal signal at 475 nm with a tail at 375 nm at the default excitation 330 nm. The slight difference in the fluorescence peaks among studies could be due to the spectrofluorometer used.

As with pure standards, diluted and undiluted honeys also gave a fluorescence peak at $\lambda_{ex/em}$ 270/360 nm for Leptosperin and two fluorescence peaks at $\lambda_{ex/em}$ 330/375 and 330/475 nm for Lepteridine™ on EEM matrices (Figures 10.5 & 10.6). A PARAFAC model on the three-dimensional excitation-emission matrix of 100 undiluted honeys also reconfirmed these signals for Leptosperin and Lepteridine™ (Figure 10.8). According to Lambert-Beer's law, a high absorbance solution (Absorbance > 1) such as undiluted honey often experiences inner filter effects when measuring fluorescence emission. Both the emission and excitation spectra

could be distorted, and the measured fluorescence intensity becomes non-linear with the fluorophore concentration (Ceresa et al., 2021; Kimball et al., 2020). However, this study showed that the inner filter effects can be minimised. The use of in-line reflectance geometry fluorescence measurement on the black 96-well plate (clear bottom) under the LUX spectrofluorometer allowed capture of the internal reflectance fluorescence released from the sample within the well. According to the Thermo Scientific technical manual (2022), the LUX detector can detect fluorescence signals from a large angle across the upper surface of a sample within a well after the light beam excites the sample (ThermoScientific, 2022). The in-line geometry in this fluorescence configuration could be considered akin to the total internal fluorescence reflection cell configuration mentioned in the study of Kao et al. (1998). They stated that configuration systems of front-face, short path length and a total internal fluorescence in a reflection cell minimise the inner filter effects and provide approximate linearity for concentration in contrast to the right-angle configuration (Kao et al., 1998).

Thanks to this configuration, fluorescence peaks of Lepteridine™ in raw honey were similar to those of its pure standard and those in diluted honey. The maximal peak was at $\lambda_{ex/em}$ 330/375 nm and the small peak at $\lambda_{ex/em}$ 330/475 nm which was opposite to diluted honey's peaks, but similar to the pure standard in dummy honey (Figure 10.4). The change of maximal fluorescence peaks in undiluted honey and Lepteridine™ standard in dummy honey was known to be a second inner filter effect in which the fluorescence emission around the signal $\lambda_{ex/em}$ 330/375 nm could become the excitation for the second signal $\lambda_{ex/em}$ 330/475 nm (Ceresa et al., 2021). Mashhadi et al. (2022) reported that furosin and riboflavin release fluorescence signals at $\lambda_{ex/em}$ 405/485 and 405/540 nm, respectively. The current study did not scan honey above excitation 400 nm. However, it is likely that these compounds can also be detected in honey when scanning with the current in-line geometry spectrofluorometer.

Self-quenching was also discerned in the study. One of the key chemical markers, 2′-methoxyacetophenone (2'-MAP), currently used for measuring the purity of mono-floral mānuka honeys, produces a fluorescence signal at $\lambda_{ex/em}$ 320/410 nm. Fluorescence emission of 2'-MAP is close to the fluorescence emission of Lepteridine™ ($\lambda_{ex/em}$ 330/470 nm) (Liu et al., 2015). However, this study did not detect the 2'-MAP signals in the diluted honey EEM matrix, and PARAFAC models also did not identify the fluorescence signature of 2'-MAP. The fluorescence emission of 2'-MAP could possibly be quenched by Lepteridine™.

Prediction of Leptosperin and Lepteridine™ concentrations with two-way PLS models based on fluorescence intensity showed above 90 % accuracy for diluted honeys, but 70 - 80 % for undiluted honeys at both excitation wavelengths 270 and 330 nm. The predictive

accuracies improved by 1 - 9 percentage points when using tri-PLS for a full EEM of undiluted honeys (Table 10.4). These results confirmed that, despite high concentrations of undiluted honeys, fluorescence measurements in the 96-well plate under in-line geometry of the LUX spectrofluorometer provides sufficient linearity. Prediction of other key chemical markers of diluted and undiluted samples also performed acceptedly (results not reported here). The important features identified were present in the Vis range of 320 - 600 nm for two fluorescence markers, indicating its importance. This suggests that the Vis range is relevant for estimating chemical markers under fluorescence mode. Tri-PLS models for combining undiluted fluorescence matrices at two excitation bands 270 & 330 nm did not provide better predictive results for fluorescence markers (Leptosperin and Lepteridine^{TM}) than standard PLS models at each excitation band. However, tri-PLS for a full EEM significantly enhanced the prediction accuracies for undiluted data. Overall, multi-way analysis was a good approach for analysing high absorbance fluorescence data.

The use of fusion of NIR and fluorescence in multi-block PLS regression of undiluted honey data improved prediction of Leptosperin (λ_{ex} 270 nm) and Lepteridine^{TM} (λ_{ex} 330 nm) by up to 9 percentage points over standard PLS and tri-PLS for fluorescence data alone. This suggests that NIR data captured vibration signals that supported the prediction of these fluorescence markers. Multi-block approach is also good for industrial applications since honey data could be collected from different seasons or regions and with different optical instruments (Kohonen et al., 2008; Mishra et al., 2021). Combining NIR and fluorescence modes is suggested for evaluating the quality and purity signatures of mānuka honey. Schols et al. (2015) also suggested that the integration of near-infrared and fluorescence imaging has great potential for clinical practice (Schols et al., 2015).

In addition, fluorescence imaging could also be a useful system for application to assessment of mānuka honey quality. Fluorescence imaging has previously been studied for evaluation of food quality (Delwiche et al., 2019; Xiaohui et al., 2022). Delwiche et al. (2019) applied hyperspectral fluorescence imaging to shelf-life evaluation of fresh-cut Bell and Jalapeno pepper. They reported that using fluorescence imaging allowed detection of internal changes of pepper during storage. Similarly, Xiaohui et al. (2022) predicted pH value as an indicator for the detection of internal quality change of kiwifruit using hyperspectral imaging technology. They also found that machine learning used for the analysis of fluorescence imaging spectra allowed pH value to be predicted with an accuracy of 85 % (Xiaohui et al., 2022). These studies indicate that fluorescence imaging might offer potential for further

application to honey. Future research is suggested to investigate a fluorescence hyperspectral imaging system for prediction of mānuka honey quality and purity while still in the comb.

10.5. Conclusion

Although inner filter effects impact fluorescence measurement of undiluted honeys, the current study showed that an internal reflectance cell eliminated these effects for fluorescence measurements of undiluted mānuka honeys and provided sufficient linearity for prediction of concentrations of two fluorescence markers of identity and quality. Chemometrics can greatly assist in analysing and interpreting fluorescence signatures allowing quantitative estimation. Multi-way PLS regression (tri-PLS) on a full EEM performed well in predictions of Leptosperin, Lepteridine^{TM} and UMF^{TM} score, even for honeys without dilution, attaining accuracy above 80 %. A multi-block method for combined NIR and fluorescence data also enhanced predictions of two fluorescence markers at the excitation wavelengths 270 & 330 nm. In conclusion, fluorescence-based data could be useful for rapid evaluation of quality and purity of comb mānuka honey to be extracted from frames. Potentially, integration of NIR and fluorescence imaging, or fluorescence imaging alone could provide at-line or on-line application for quality assessment of mānuka honeys prior to bulk extraction.

Chapter 11
Quality assessment of honey frames using fusion of NIR and fluorescence methods

11.1. Introduction

So far in this research, spectral datasets of single composite honeys extracted from multiple frames have been used to evaluate the capability of NIR and fluorescence methods for assessment of honey's quality and purity. The results indicate that both NIR and fluorescence methods are independently applicable to full strength honey in reflectance mode and thus applicable to recently uncapped honey frames. Fusion of fluorescence with NIR data could enhance the predictability of the eight chemical markers, potency and purity further. The current chapter describes the assessment of honey in the frame using NIR and fluorescence methods together. It addresses research hypothesis 3 which postulates that in-frame quality of mānuka honey can be measured more accurately by combining NIR and fluorescence. This may also confirm findings and validate modelling methods used in previous chapters. In-frame assessment of potency (UMF^{TM} score/ UMF^{TM} buckets), purity (classification of MPI criteria) and eight chemical markers is directly relevant to the industrial level.

11.2. Materials and methods

11.2.1. Materials

Seven honey frames still capped by beeswax were provided Comvita®. They were harvested in Jan-Feb 2022 from seven geographic districts: Whanganui (WH), Wairarapa (WA), Hawkes Bay (HB), West Coast (MK), Waikato (WK), Panhandle-Ohura (PH) and BlueSky-National Park Mānuka (BS). A technique was developed for selective uncapping of sections of frame. NIR and fluorescence methods in combination with chemometrics were employed to assess mānuka honey quality while still in the frame.

Several sample areas per frame were selected for scanning by NIR and fluorescence sensors. Before scanning, each sample area was uncapped using a sliding knife (0.8 mm 304 stainless steel sheet) gauged to cut to a depth of 5 mm (Figure 11.1). By removing the wax, a sample area was formed as a square region 60 mm by 60 mm. We assumed that these sample areas represented the variability of a whole frame. Some frames could have six sample areas

while the others had two areas due to the availability of honey in the frame (Figure 11.2). Figure 11.2 illustrates the uncapped sample areas of seven frames (also from seven districts).

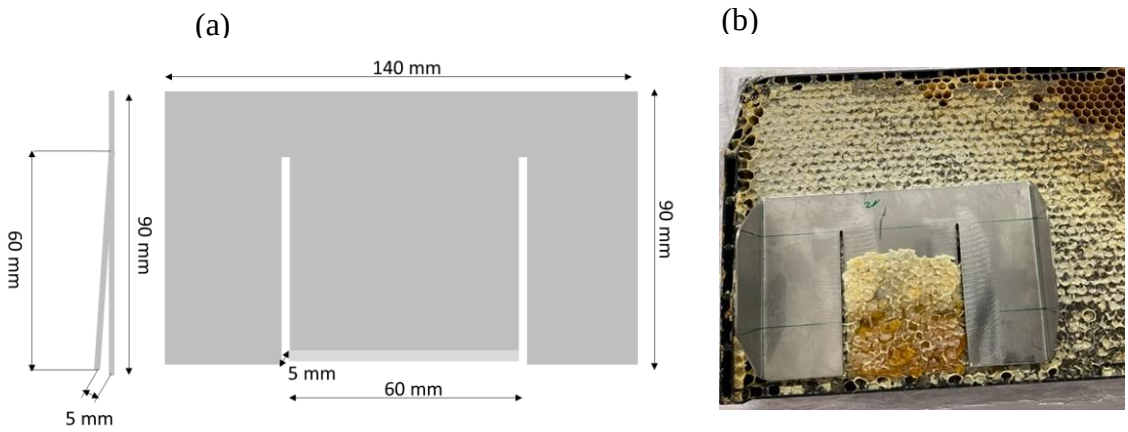

Figure 11.1. *The sketch of a designed knife (a) and (b) using knife to remove the cap wax*

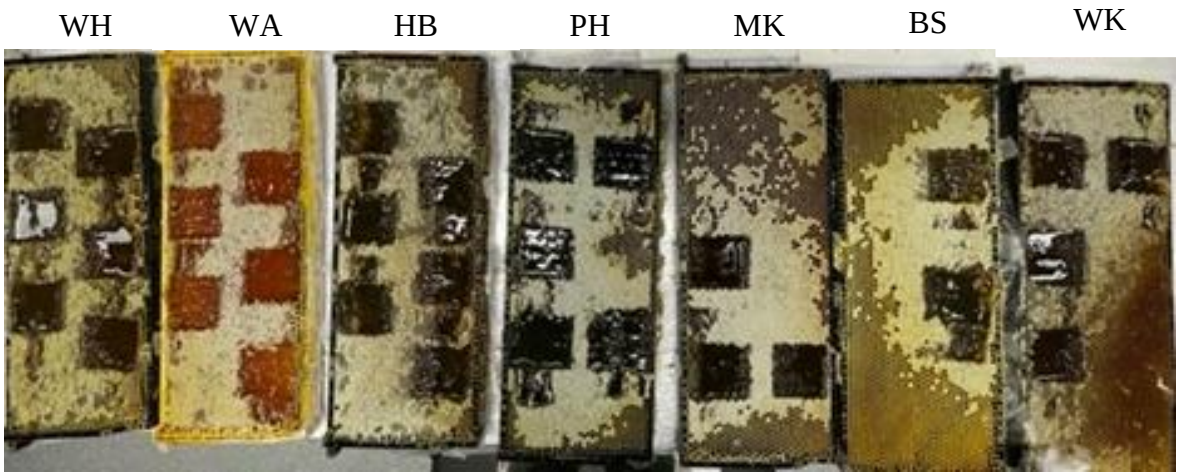

Figure 11.2. *Seven frames from seven geographic districts were uncapped at regions of interest before scanning*

11.2.2. Grading systems

Four UMF^{TM} buckets were suggested by Comvita for grading honey frames before bulk extraction (Table 11.1). These buckets were divided based on the amount of DHA, Leptosperin and Lepteridine^{TM}. The UMF^{TM} 20+ bucket captures the really high UMF^{TM} honey that contains a high level of DHA > 3500 ppm. The UMF^{TM} 10+ bucket covers a mid-range DHA (1500 - 3500 ppm) to capture honey with the UMF^{TM} between 10 - 20+. Then two subsequent

low UMF^{TM} buckets: <UMF^{TM} 10+ and << UMF^{TM} 10+ are established by using cut-off levels of Leptosperin and Lepteridine^{TM}. These current buckets are different from the five UMF^{TM} buckets developed in Chapter 7, but the whole bucket idea is quite similar to sort honey frames before the extraction.

Table 11.1. Four UMF^{TM} buckets used for grading honeys before bulk extraction

Levels/Buckets	UMF 20+	UMF 10+	<UMF 10+	<< UMF 10+
DHA (ppm)	≥ 3500	1500 - 3500	< 1500	< 1500
Leptosperin (ppm)	-	-	> 250	≤ 250
Lepteridine^{TM} (ppm)	-	-	> 5	≤ 5

11.2.3. Non-imaging systems

11.2.3.1. The integrated NIR and fluorescence spectroscopy settings

An integrated system of NIR and fluorescence modes was developed for scanning regions of interest of honey frames. These two modes work independently to capture reflectance and fluorescence signals of comb honey samples. The white reference (SG31514, R% 95, SphereOptics GmbH, Herrsching, Germany) was used in the integrated system before scanning. In the NIR mode, the halogen lamp illuminator (COFAN®, F-2510M128 II, DC12V_0.11A) was used as a light source to produce a broad range of spectrum incorporated with the FieldSpec spectroradiometer sensor (Model NIRLS408, ASD Inc., Boulder, CO, USA). The light source was placed 45 angular degrees to the frame at 210 mm distance (Figure 11.3). The light field diameter of this illuminator was 50 mm. The integration time to capture NIR reflectance signals was 36 ms. In the fluorescence mode, two UV LED illuminators at 265 nm (OceanOptics, L265A) and 310 nm (OceanOptics, L310A) were controlled by the external driver controller unit and were set with energy at 66 % to illuminate sample areas of honey to be scanned. The distance between the UV light and the frame surface was 70 mm. Each fluorescence measurement was integrated over 136 ms then recorded. The light field diameter of the UV illuminator was 30 mm. Scanning samples with UV light was implemented under the black carton box. Both reflectance NIR and fluorescence spectra were separately captured by the same non-imaging detector having the spectral range 350 - 2500 nm. The detector field of view was 60 mm. In Chapter 9, the results indicated wavelengths 270 and 330 nm were best fit for capturing signals of the two key fluorescent markers. However, the current study used two UV LED lights at 265 and 310 nm since these light sources were available in the market at purchasing time and would be available industrially.

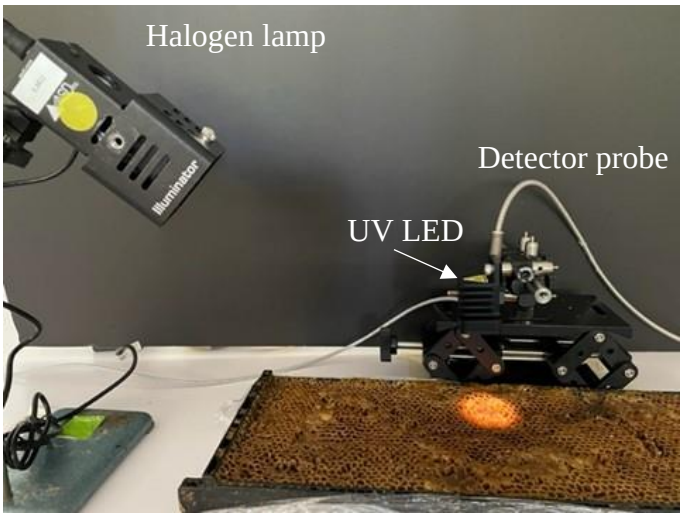

Figure 11.3. *The incorporation of NIR and fluorescence modes for scanning honey frames (the light circle on the frame shows the detector field of view 60 mm)*

11.2.3.2. The integrated NIR and fluorescence data

A total of 32 honey samples were scanned under the same sensor in the range 350 - 2500 nm to collect reflectance NIR and fluorescence data separately. Before scanning samples, the sensor was calibrated using dark and white references. The black cap covering the detector was used as dark reference and was scanned to account for instrument noise. The white reference panel (SG31514, R% 95, SphereOptics GmbH, Herrsching, Germany) with 95 % reflectance was scanned under the light source on allowing reflectance signals from samples to be correctly captured. This calibration was implemented separately for collecting both NIR and fluorescence data since the two modes used different light sources.

The NIR data of 32 honey samples covered the whole spectral range 350 - 2500 nm. However, only NIR data in the range 370 - 1600 nm were used (based on previous modelling study). This was because the spectral range below 370 nm and beyond 1600 nm did not give much information and was mostly discarded after using iPLS technique. So, these ranges were excluded to optimise modelling in the range of 370 - 1600 nm. The NIR spectra were normalised before modelling.

The fluorescence data of the same honey dataset (32 samples) were also collected in the spectral range 350 - 2500 nm after exciting each sample by illumination with UV light of 265 nm then 310 nm. Since the useful fluorescence emission was below 600 nm (e.g., fluorescence emission of Leptosperin and Lepteridine^{TM}), the fluorescence range of interest was in the 350-

600 nm range. Different pre-processing techniques and their combination (Normalisation, SNV, MSC) were employed on fluorescence data prior to modelling.

11.2.3.3. LUX fluorescence data

The same honey dataset of 32 samples was manually extracted from honey frames and placed in a 96-well plate, one set undiluted, another diluted to 2 %. These samples were then scanned with the LUX spectrofluorometer across the EEM range of $\lambda_{ex/em}$ 250 - 400/300 - 600 nm. In particular, fluorescence emissions collected at excitation wavelengths of λ_{ex} 265 and 310 nm were analysed carefully to compare with the integrated fluorescence data captured at these excitation wavelengths. Additional analysis was conducted on fluorescence data at excitation wavelengths 270 and 330 nm and compared with the results of Chapter 10. Pre-processing mean-center was used for LUX fluorescence data before modelling.

11.2.4. Hyperspectral imaging system

11.2.4.1. Hyperspectral acquisition settings

Seven honey frames containing 32 sample areas were scanned by line-scanning Hyperspec Vis-NIR camera (547 - 1701nm) (Model 1003B-10151, Headwall Photonics, Fitchburg, MA, USA). Hyperspectral acquisition was set to collect a clear hyperspectral image with working distance 650 mm; an aperture of 2.8 and scanning speed of hyperspectral acquisition 19.5 mm/s, and the translation speed of a mobile conveyor belt for carrying a honey frame at 19.5 mm/s. Each hyperspectral image gave a hypercube size of 700 x 320 x 235. The spatial dimension was dependent on the camera scanning and the conveyor belt speed which created a square unit of 0.78 x 0.78 mm per pixel under FOV 249.6 mm. A total of seven hyperspectral images were collected by the software (Headwall Hyperspec III, model E41211 vs 64, Headwall Photonics, Fitchburg, MA, USA).

11.2.4.2. Segmentation process

Three main stages were employed in the segmentation process to extract regions of interest (ROIs) in hyperpsectral images. First, multi-thresholding was used to segregate the pixels which have frame background, spectral noise and light saturation. Then, the morphological operation step was applied to remove unnessessary objects. Lastly, sample areas were labeled with centroid detection to extract ROIs representing honey samples (Figure 11.4). For each ROI extracted, all pixels from that ROI were averaged to obtain a spectrum which represented a honey sample.

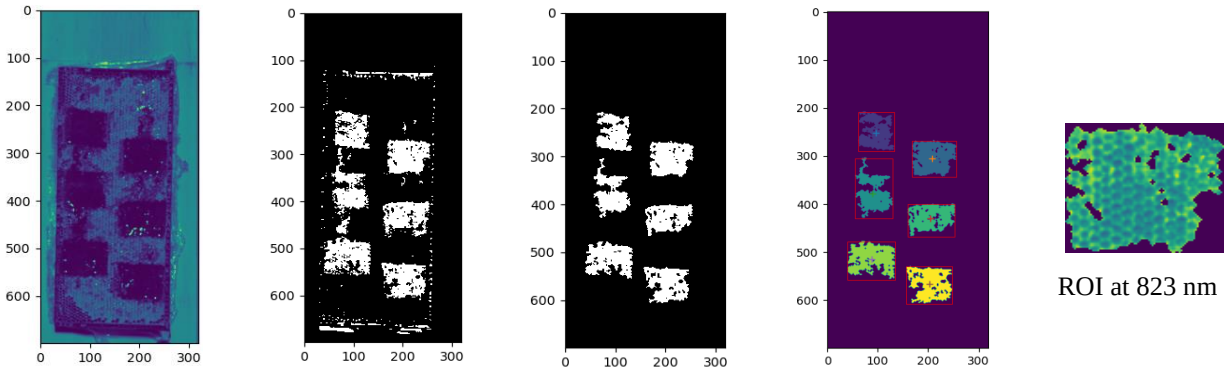

(1) Multi-thresholding (2) Morphological operation (3) Labelling with centroid detection

Figure 11.4. *Segmentation process to extract regions of interest (ROI) with three main steps: (1) multi-thresholding, (2) morphological operation and (3) labeling with centroid detection*

11.2.5. Modelling methods

Principal component analysis (PCA), partial least squares (PLS) regression and partial least squares discriminant analysis (PLSDA) were employed to analyse NIR non-imaging and hyperspectral imaging data, fluorescence at 265 & 310 nm and LUX fluorescence data. PCA was applied to all 32 samples to visualise the patterns and trends in the data. Then, PLS and PLSDA with venetian blind cross validation were employed to predict chemical markers, UMF^{TM} score and to classify into MPI honey classes and Comvita UMF^{TM} buckets. Before modelling, the Kennard-Stone technique was used to split each dataset into calibration and validation sets with ratio 70:30. In PLS models, the iPLS technique with one-interval band was used during modelling fluorescence data while 4-interval band was employed during modelling fluorescence and NIR hyperspectral combined to discard irrelevant wavelengths.

All pre-processing and chemometrics methods were run with PLS toolbox 8.8 (Eigenvector Research, Inc., WA 98831, USA) on MATLAB R2021a (The MathWorks, Inc., Massachusetts 01760, USA).

11.3. Results

11.3.1. Spectra of comb honeys

The spectra of 32 comb honey samples from seven geographic districts captured under NIR non-imaging sensor (350 - 2500 nm), NIR line-scanning HSI camera (547 - 1701 nm), the integrated fluorescence sensor ($\lambda_{ex/em}$ 265 & 310/350 - 2500 nm) and LUX spectrofluorometer at $\lambda_{ex/em}$ 265, 270, 310 & 330/300-600 nm are illustrated in Figures 11.5 - 11.8.

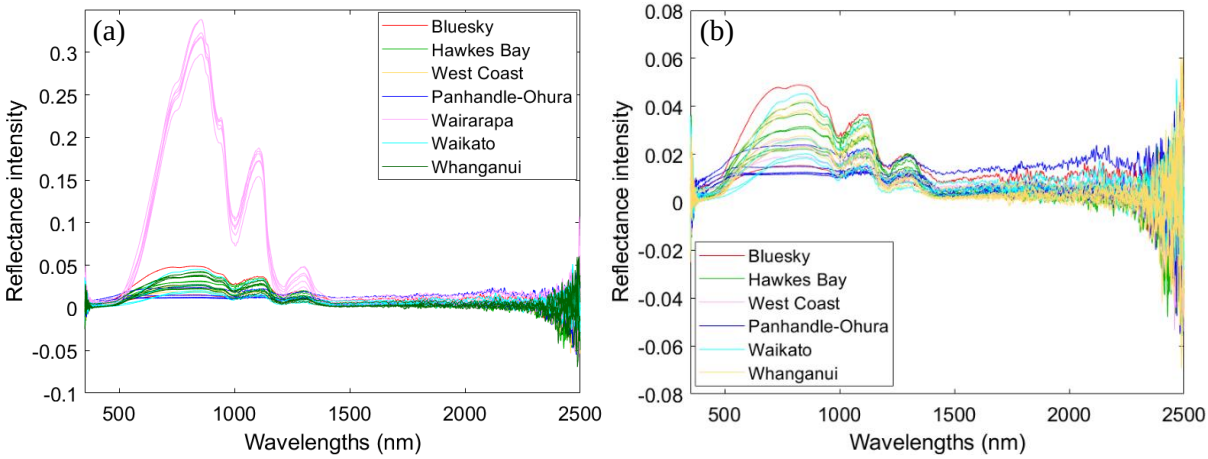

Figure 11.5. *NIR non-imaging spectra of 32 comb honey samples across seven geographic districts (a), across 6 districts without Wairarapa (b)*

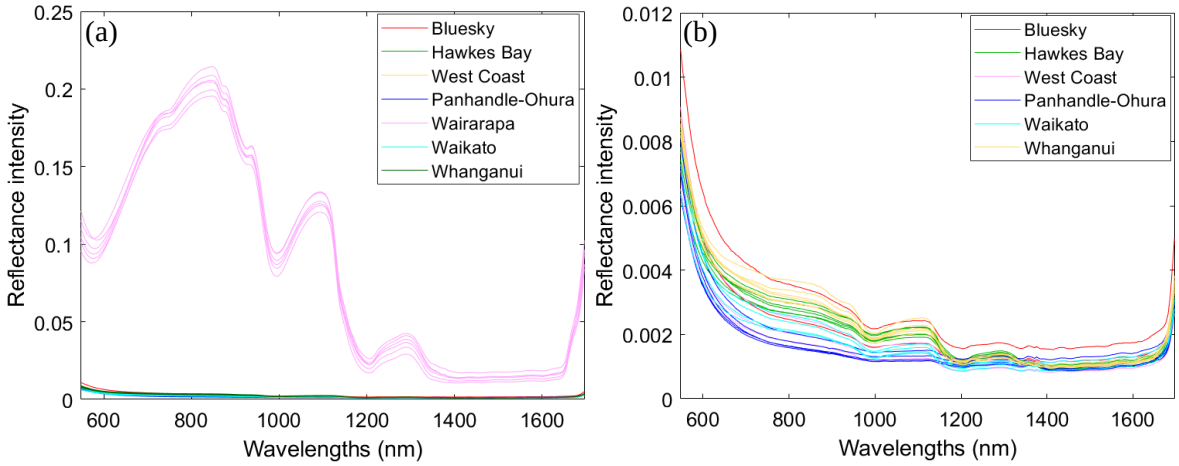

Figure 11.6. *NIR HSI spectra of 32 comb honey samples across seven geographic districts (a), across 6 districts without Wairarapa (b)*

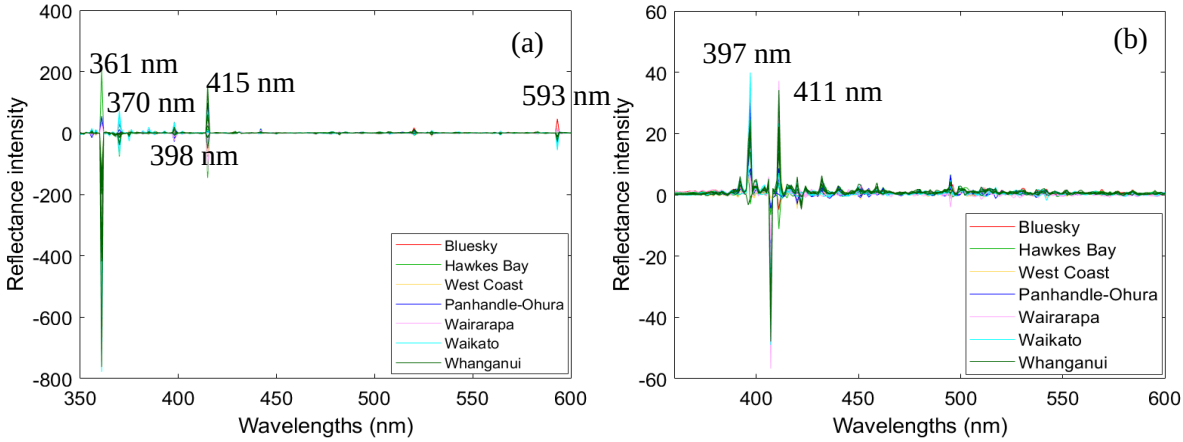

Figure 11.7. *Reflectance spectra obtained from the integrated fluorescence system of 32 comb honey (**undiluted**) samples across seven geographic districts at 265 nm (a), at 310 nm (b) after subtraction of the frame's signal*

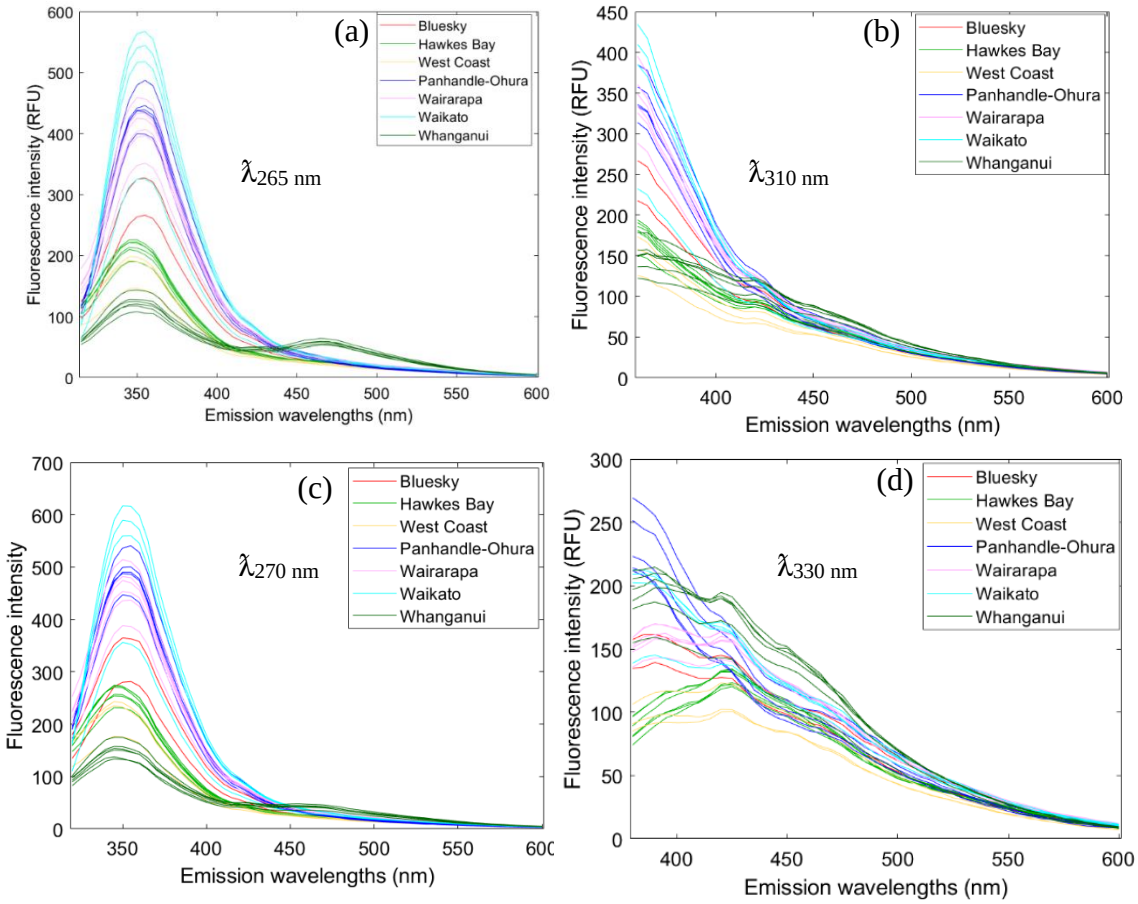

Figure 11.8. *Fluorescence spectra obtained from LUX spectrofluorometer system of 32 comb honey (**undiluted**) samples across seven geographic districts at 265 nm (a), at 310 nm (b), at 270 nm (c) and at 330 nm (d) after subtracting the signal of the black 96-well plate*

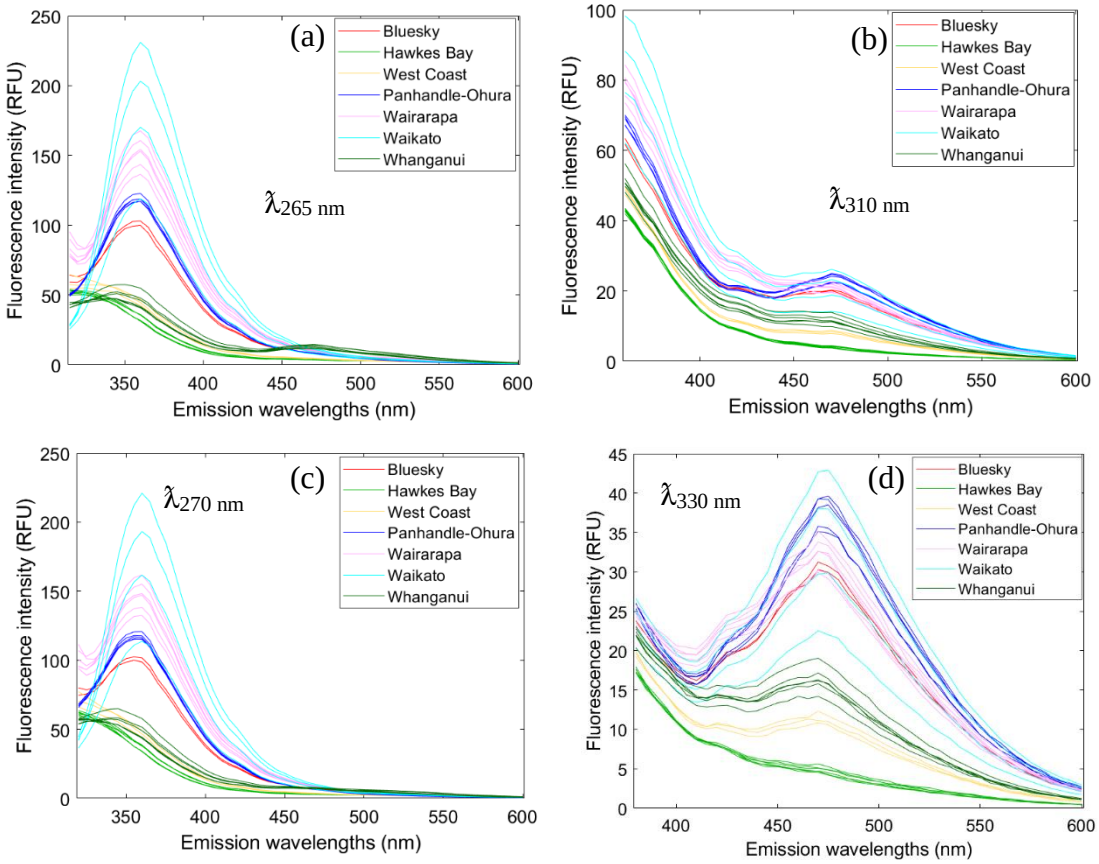

Figure 11.9. *Reflectance fluorescence spectra obtained from LUX spectrofluorometer system of 32 comb honey (**diluted**) samples across seven geographic districts at 265 nm (a), at 310 nm (b), at 270 nm (c) and at 330 nm (d)*

NIR non-imaging data (Figure 11.5) and HSI data (Figure 11.6) had high reflectance spectra from Wairarapa district compared to remaining districts. This was because Wairarapa honey spectra were collected from a yellow frame while honey spectra from other districts were collected from black frames. In general, NIR reflectance spectra of seven districts from both non-imaging and HSI reflected and absorbed similarly in the 547 - 1701 nm range. However, NIR non-imaging spectra gave higher reflectance intensity than NIR hyperspectral spectra.

Fluorescence signals of diluted and undiluted 32 honey samples at λ_{ex} 270 and 330 nm were captured under the LUX spectrofluorometer to check the results from the previous experiment (Chapter 10). Overall, fluorescence signals of some diluted comb honey samples were found maximally at $\lambda_{ex/em}$ 270/360 nm for Leptosperin and at 330/470 nm for

Lepteridine™ (Figure 11.9). This was similar to the study of Bong et al. (2017 & 2018) and the results of chapter 10. Similarly, fluorescence emission peaks of undiluted comb honey were found at $\lambda_{ex/em}$ 270/355 nm for Leptosperin (Figure 11.8c) and for Lepteridine™ at $\lambda_{ex/em}$330/380 nm and 330/465 nm (Figure 11.8d). These fluorescence signals also matched those identified in Chapter 10. However, fluorescence emission peaks of Leptosperin and Lepteridine™ captured from undiluted comb honey samples seemed to shift to the right by 5 nm. Honey samples from Wairarapa, Waikato, Panhandle-Ohura and Bluesky districts released higher fluorescence signals at $\lambda_{ex/em}$ 270/355 and $\lambda_{ex/em}$330/380 than those of honeys from other remaining regions (Figures 11.8). This implies concentrations of Leptosperin and Lepteridine™ were high in Wairarapa, Waikato, Panhandle-Ohura and Bluesky.

Fluorescence spectra of 32 comb honeys were captured at λ_{ex} 265 and 310 nm under the integrated system in the 350 - 2500 nm range. Each spectrum was automatically calibrated by dividing the raw spectrum by the spectrum of a white reference. Figure 11.7 illustrates the honey fluorescence spectra after subtracting the blank from the empty frame that carried that honey. The fluorescence spectra of honey show unusually sharp signals at both excitation wavelengths. This could be due to imperfect optical fiber or imperfect settings. The reflectance intensity at λ_{ex} 265 and 310 nm was also quite different due to unusual peaks. At λ_{ex} 265 nm, wavelengths 361, 370, 398, 415 and 593 nm were clearly identifiable in the spectra. Similarly, at λ_{ex} 310 nm wavelengths 397 and 411 nm were obvious in the reflectance spectra.

The fluorescence spectra of the 32 undiluted samples captured from the integrated system were compared with fluorescence spectra collected by LUX spectrofluorometer at excitation bands 265 and 310 nm. Leptosperin fluorescence signal was identified at $\lambda_{ex/em}$ 265/355 nm on LUX fluorescence spectra (Figure 11.8a), but it was not obvious in the spectra from the integrated system (Figure 11.7a). Similarly, a fluorescence signal could be expected at $\lambda_{ex/em}$ 310/360 nm (Figure 11.8b), but this signal was absent (Figure 11.7b). Since the fluorescence settings between the two systems are different, Leptosperin and Lepteridine™ 's signals might change somewhat under the integrated system. It would be useful to compare with pure Lepstoperin and Lepteridine™ standards captured with the integrated system, but all standards were used up in the previous experiment.

11.3.2. Preliminary analysis with PCA

Principal component analysis (PCA) was applied on each spectral dataset to check the distribution of honey samples from different geographic districts. Vis-NIR non-imaging data (370 - 1600 nm) and Vis-NIR hyperspectral data (547 - 1701 nm) were independently analysed

with PCA. Overall, PCA used two principal components (PC1 and PC2) to capture 95.8 - 99.3 % variance in both datasets (Figure 11.10a & 11.11a). Samples from Wairarapa and Panhandle-Ohura districts were nicely separated from other regional samples for both sets of spectral data. Whanganui, Hawkes Bay and two samples from Waikato were also separated in the PCA model from Vis-NIR non-imaging data. However, this was not obvious in the PCA model built from Vis-NIR hyperspectral data. Important variables identified in the loading plot of the non-imaging PCA model (Figure 11.10ii) were 522, 615, 854 and 1144 nm while 547, 853, 1095, 1135 and 1355 were dominant in the hyperspectral PCA model (Figure 11.11ii).

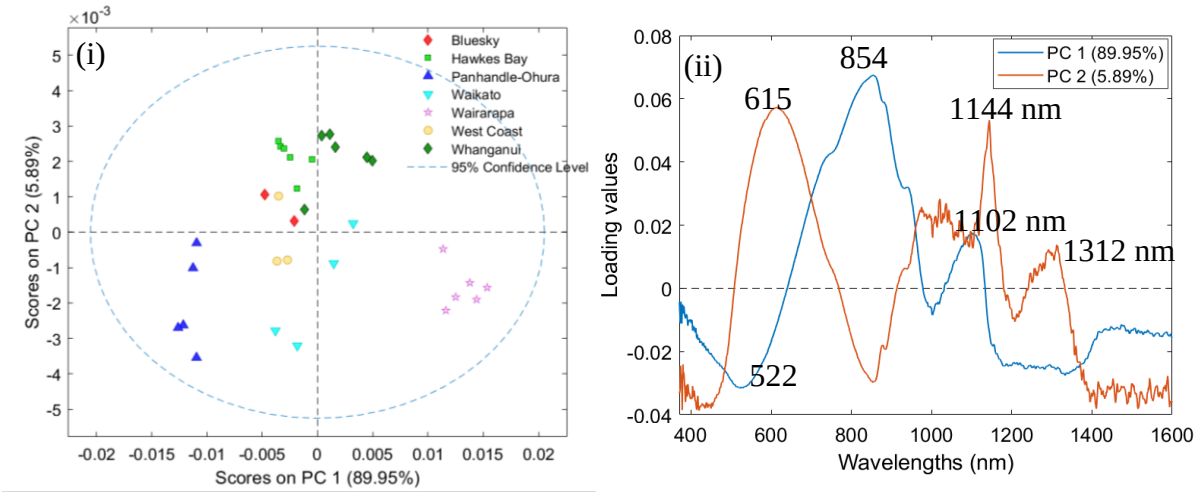

Figure 11.10. *The output of PCA analysis on NIR non-imaging data (370 – 1600 nm): (i) PC1 & PC2 score captured 95.8 % variance, (ii) loading plot of important*

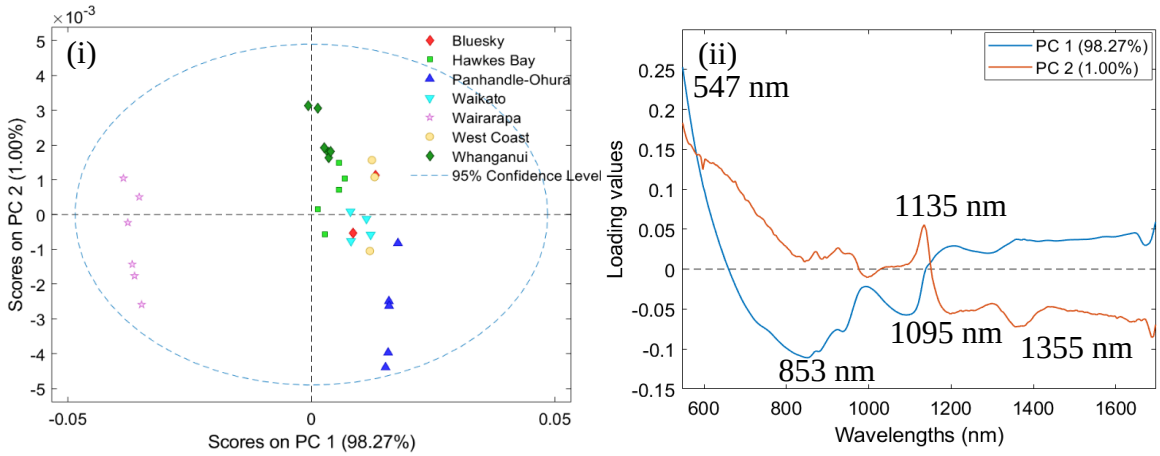

Figure 11.11. *The output of PCA analysis on NIR hyperspectral data (547 – 1701 nm): (i) PC1 & PC2 score captured 99.3 % variance, (ii) loading plot of important*

The LUX fluorescence data of undiluted comb honeys at λ_{ex} 270 and 330 nm were also analysed with PCA (Figures 11.12 & 11.13). Overall, using two first principal components (PC1 and PC2) can help visualise the distribution of samples from different geographic districts. The PCA model of LUX fluorescence data at λ_{ex} 270 nm separate samples from each district better than that of LUX fluorescence data at λ_{ex} 330 nm. The PCA score plots show some sample variation among districts, in particular at Waikato and West Coast. The PCA loading plot at λ_{ex} 270 nm indicates wavelength 355 nm is important which could be relevant to the Leptosperin footprint. Meanwhile the PCA loading plot at λ_{ex} 330 nm suggests 380, 435, 450 and 515 nm are important bands. The emission band 380 nm could correspond to Lepteridine™, but other bands may be relevant to other fluorophore signals (i.e., flavonoids or DHA/MGO brown pigments).

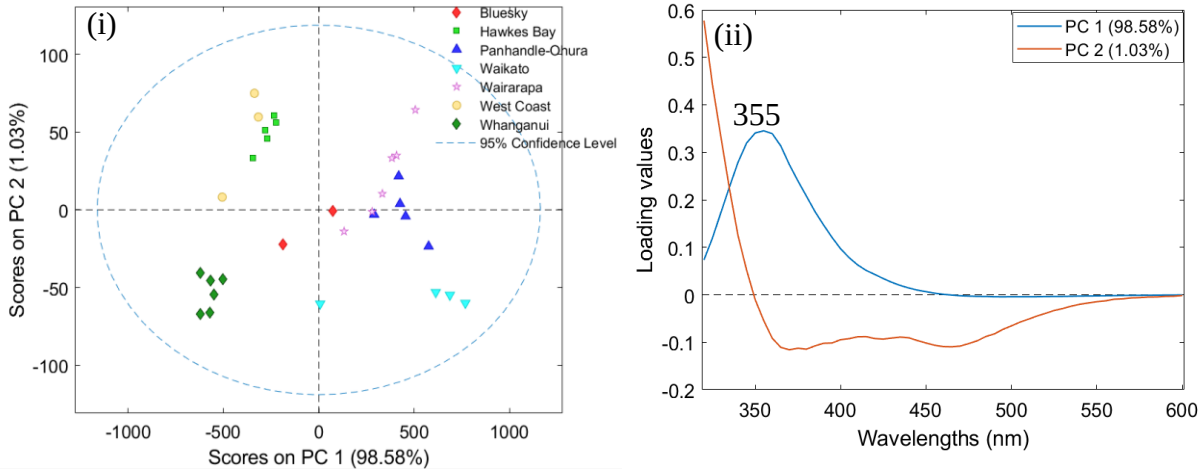

Figure 11.12. *The output of PCA analysis on LUX fluorescence data at excitation 270 nm: (i) PC1 & PC2 score captured 99.6 % variance, (ii) loading plot of important bands*

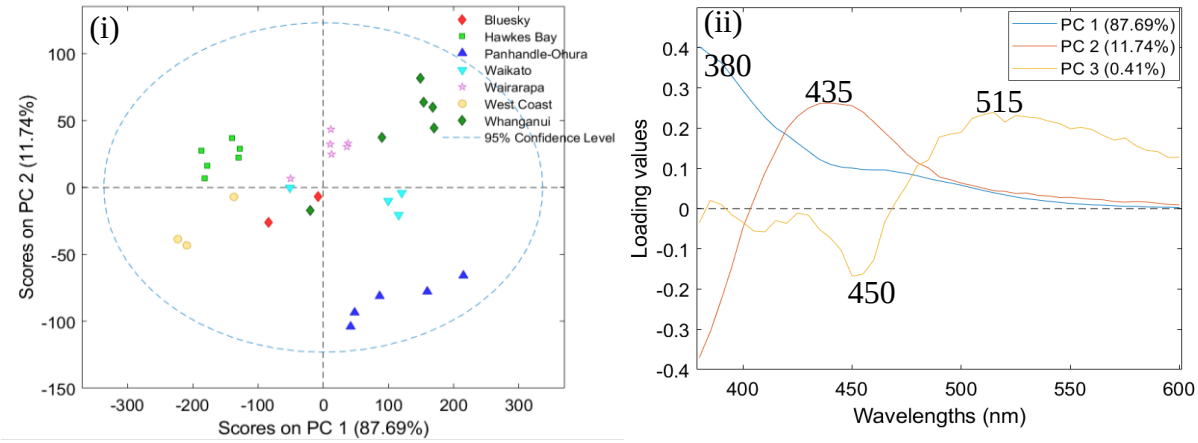

Figure 11.13. *The output of PCA analysis on LUX fluorescence data at excitation 330 nm: (i) PC1 & PC2 score captured 99.4 % variance, (ii) loading plot of important*

11.3.3. Prediction of chemical markers

11.3.3.1. NIR non-imaging and hyperspectral imaging data of in-frame honey

PLS regression was applied to NIR non-imaging (370 - 1600 nm) data to compare with hyperspectral imaging (547 - 1701 nm) data for prediction of eight chemical markers and the UMF^{TM} score (Tables 11.2 & 11.3). Overall, some imaging models performed better than non-imaging models. Imaging models of DHA, MGO, 3-PLA, 4-HPLA and UMF^{TM} score could predict between low and high levels (RPD > 1.5) while few non-imaging models could discriminate high from low concentrations (e.g., MGO, 3-PLA and UMF^{TM}). Although this study could not observe regional differences for prediction of chemical markers due to a small sample size for each district, intuitively regional variation of a dataset of 32 honey samples across seven geographic districts could impact on modelling performance.

Compared to results of the previous honey dataset (1656 samples), current results of non-imaging and hyperspectral imaging data shared similar trends for the prediction of eight key chemical markers. However, UMF^{TM} was well predicted for both the non-imaging and imaging dataset of 32 comb honeys (Tables 11.2 & 11.3) unlike the report in Chapter 6. This may have been because of the age of previous dataset (1656 samples) during storage. The frames used in Chapter 11 were fresh from the current seasons with few aging effects.

Table 11.2. PLS prediction models of eight chemical markers from NIR non-imaging data of 32-comb honey samples (calibration = 23, test = 9)

Models	Pre-processing	No. LVs	R^2 (CV)	RMSECV	Bias (CV)	R^2 (Pred.)	RMSEP	Bias (Pred.)	RPD
DHA	Normalize	1	0.48	625.99	8.39	0.19	598.05	-14.8	1.24
MGO	Normalize	4	0.65	111.74	-4.98	0.51	142.49	24.75	**1.51**
3-PLA	Normalize	3	0.75	195.37	-4.34	0.29	182.04	4.95	**1.82**
4-HPLA	Normalize	2	0.50	1.96	0.01	0.15	2.50	0.29	1.41
2'-MAP	Normalize	2	0.54	7.02	-0.18	0.24	8.82	3.29	1.49
2-MBA	Normalize	2	0.13	18.15	0.14	0.10	14.52	6.13	0.95
Leptosperin	Normalize	4	0.56	246.71	8.81	0.37	254.48	18.3	1.41
Lepteridine^{TM}	Normalize	3	0.41	6.27	0.30	0.38	5.45	-0.43	1.22
UMF^{TM}	Normalize	5	0.80	2.23	-0.21	0.79	4.90	4.24	**2.21**

Table 11.3. PLS regression models of eight chemical markers from NIR hyperspectral data of 32-comb honey samples (calibration = 23, test = 9)

Models	Pre-processing	No. LVs	R^2 (CV)	RMSECV	Bias (CV)	R^2 (Pred.)	RMSEP	Bias (Pred.)	RPD
DHA	Normalize	3	0.73	435.24	6.31	0.60	608.29	-323.07	**1.78**
MGO	Normalize	2	0.63	109.24	-2.70	0.72	107.42	-20.95	**1.55**
3-PLA	Normalize	3	0.77	186.70	-0.01	0.18	224.43	-57.92	**1.91**
4-HPLA	Normalize	4	0.63	1.74	-0.10	0.63	1.88	-0.95	**1.58**
2'-MAP	Normalize	3	0.55	7.59	-0.15	0.54	7.44	-4.52	1.38
2-MBA	Normalize	5	0.38	12.55	-0.16	0.01	22.33	-5.60	1.37
Leptosperin	Normalize	2	0.38	275.86	19.63	0.20	339.07	-81.51	1.26
Lepteridine^{TM}	Normalize	2	0.31	5.85	-0.17	0.81	6.60	-1.43	1.31
UMF^{TM}	Normalize	2	0.76	2.47	-0.09	0.80	3.55	-1.01	**1.99**

11.3.3.2. LUX fluorescence data

LUX fluorescence emission data of 32 undiluted honey samples at excitation bands 265, 270, 310 and 330 nm were modeled for prediction of Leptosperin, Lepteridine^{TM} and UMF^{TM} score (Figures 11.14 - 11.16). Overall, the fluorescence data at λ_{ex} 265 nm gave high prediction accuracy for the two fluorescence markers and for UMF^{TM} score, up to 90 % accuracy. Prediction of other chemical markers were also observed at 70 - 90 % accuracy at λ_{ex} 265 nm, better than at λ_{ex} 270 nm (results not shown in this chapter). The prediction results at λ_{ex} 310 nm also performed better than those at λ_{ex} 330 nm. The current chapter indicates that excitation wavelengths of 265 and 310 nm are important for prediction of the two fluorescence markers unlike previous results of 100-honey samples in Chapter 10. This could be due to the presence of small wax particles in the 32 comb honeys observed *in situ* that might shift fluorescence signals of these markers. The previous 100-undiluted honeys were all filtered. Overall, the prediction results of the 32 undiluted honey fluorescence dataset obtained higher accuracy than those of the 100-honey samples in Chapter 10.

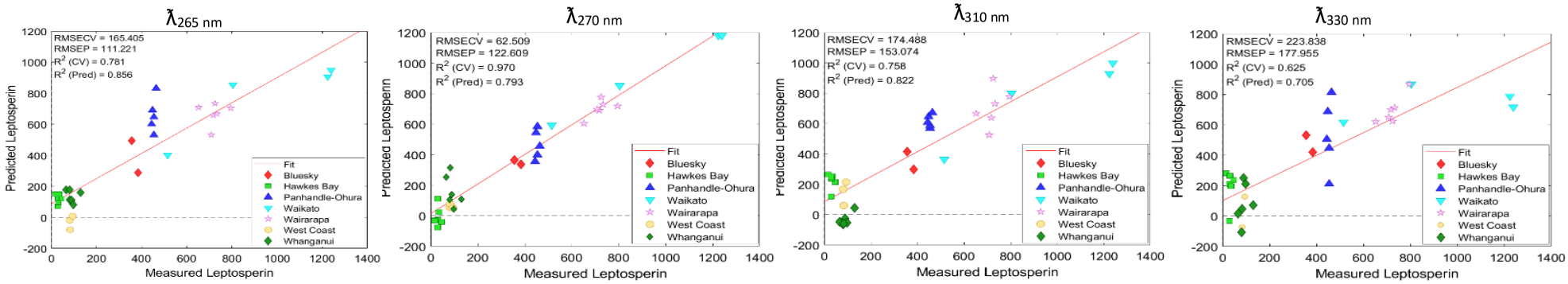

Figure 11.14. *PLS prediction of Leptosperin on fluorescence datasets at excitation bands 265, 270, 310 and 330 nm*

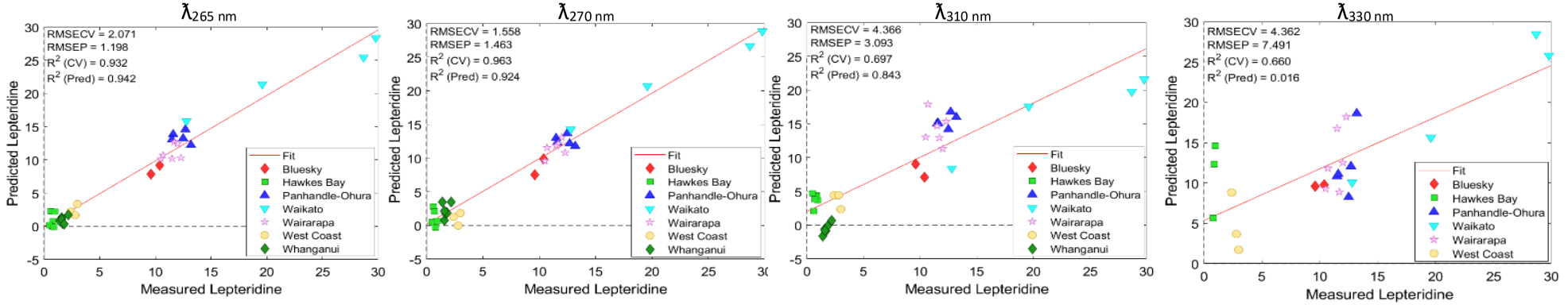

Figure 11.15. *PLS prediction of Lepteridine™ on fluorescence datasets at excitation bands 265, 270, 310 and 330* nm

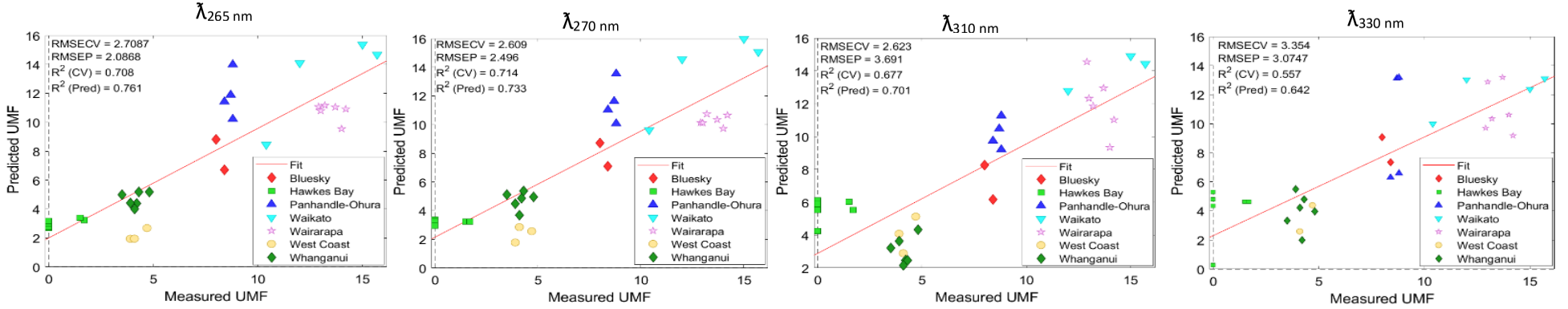

Figure 11.16. *PLS prediction of UMF™ on fluorescence datasets at excitation bands 265, 270, 310 and 330 nm*

Multi-way analysis using tri-PLS on the fluorescence EEM matrix across 250 - 400/350-600 nm of both diluted and undiluted honey data of 32 undiluted comb honey samples are illustrated in Tables 11.4 and 11.5). In contrast to diluted fluorescence data, the prediction of chemical markers from undiluted data was poor probably due to inner filter effects. However, all chemical markers from undiluted data could be predicted between high and low levels since 1.5 < RPD < 2.5, except for 2'-MAP and 2-MBA. Leptosperin was predicted with an RPD value > 2.5 indicating it has strong prediction capacity on the new dataset.

Table 11.4. Tri-PLS prediction of eight chemical markers from LUX fluorescence data of 32-*diluted* comb honey samples

Models	Pre-processing	No. LVs	R^2 (CV)	RMSECV	Bias (CV)	R^2 (Pred.)	RMSEP	Bias (Pred.)	RPD
DHA	Multiway center	3	0.95	151.38	5.87	0.99	89.87	-60.68	**5.13**
MGO	Multiway center	4	0.94	41.37	3.96	0.99	35.76	16.83	**4.10**
3-PLA	Multiway center	4	0.96	76.82	11.65	0.90	287.74	-228.64	**4.63**
4-HPLA	Multiway center	4	0.96	0.43	0.03	0.97	0.51	-0.13	**6.40**
2'-MAP	Multiway center	4	0.91	2.99	-0.11	0.98	4.17	-3.60	**3.50**
2-MBA	Multiway center	4	0.91	6.46	-0.16	0.10	4.82	2.85	**2.67**
Leptosperin	Multiway center	2	0.97	60.08	0.04	0.98	52.89	31.70	**5.79**
Lepteridine™	Multiway center	2	0.95	2.21	5.87	0.99	3.07	-60.68	**5.13**
UMF™	Multiway center	4	0.95	0.83	-0.07	0.71	3.75	2.41	**4.10**

Table 11.5. Tri-PLS prediction of eight chemical markers from LUX fluorescence data of 32-*undiluted* comb honey samples

Models	Pre-processing	No. LVs	R^2 (CV)	RMSECV	Bias (CV)	R^2 (Pred.)	RMSEP	Bias (Pred.)	RPD
DHA	Multiway center	6	0.76	332.53	73.02	0.74	671.27	362.93	**2.33**
MGO	Multiway center	3	0.67	85.82	4.97	0.93	156.03	106.86	**1.98**
3-PLA	Multiway center	6	0.79	171.27	9.58	0.49	303.16	175.83	**2.08**
4-HPLA	Multiway center	4	0.42	1.92	-0.00	0.25	3.70	2.60	1.43
2'-MAP	Multiway center	3	0.26	10.24	0.57	0.49	10.01	6.97	1.02
2-MBA	Multiway center	3	0.63	11.04	0.04	0.76	10.43	-2.59	**1.56**
Leptosperin	Multiway center	1	0.85	116.44	6.39	0.87	201.65	92.09	**2.99**
Lepteridine™	Multiway center	3	0.67	3.76	0.32	0.73	5.01	1.86	**2.03**
UMF™	Multiway center	3	0.67	2.03	0.11	0.91	6.29	4.86	**2.42**

11.3.2.3. Integrated fluorescence data at λ_{ex} 265 and 310 nm

Prediction of each chemical marker from the integrated fluorescence data at both λ_{ex} 265 and 310 nm gave poor accuracy (R^2 CV and Pred. < 0.4) (results not shown in this chapter). Overall, poor prediction of integrated fluorescence data was likely due to the imperfect integrated fluorescence system compared to the well-tuned LUX spectrophotometer. In addition, the plastic honey frame (Virgin Food Grade polypropylene) in black or yellow colour might also impact capture of fluorescence signals of honey under the integrated system. The polypropylene and colour pigments can absorb UV light which reduces the light flux absorbed

in honey (Boydağ et al., 2003). For this reason, fluorescence signals might be poorly detected by the detector. By contrast, measuring fluorescence emission of honey samples under the LUX spectrophotometer used the black polystyrene 96-well plate with clear bottom to minimise the influence of the plastic container's background and any fluorescence signals that might be detectable.

11.3.2.4. Fusion of LUX fluorescence and NIR hyperspectral data

LUX fluorescence data for undiluted honey samples at each excitation wavelength 265, 270, 310 and 330 nm were combined with NIR hyperspectral data (547 - 1701 nm) before multi-block PLS modelling. Prediction of all chemical markers was improved for all datasets (Tables 11.6 - 11.11). Prediction of DHA, MGO, 4-HPLA, Leptosperin and Lepteridine^{TM} in multiblock PLS models of fluorescence data at λ_{ex} 265 and 270 nm with HSI data obtained particularly high accuracy (> 88 % with RPD > 2.5). Prediction of UMF^{TM} score also gave R^2 CV = 0.88 and RPD > 2.5 on the joined dataset with the fluorescence data at λ_{ex} 270 nm, but not for the joined dataset at λ_{ex} 265 nm. Multi-block PLS prediction results of fusion of the fluorescence dataset at λ_{ex} 310 nm with HSI data performed better than those of the fluorescence dataset at λ_{ex} 330 nm. When combining two fluorescence datasets at λ_{ex} 265 and 310 nm in the fusion with HSI data all almost models significantly increased giving RPD > 2.5. In particular, prediction of Leptosperin and Lepteridine^{TM} gave accuracy > 90 % and RPD > 3 indicating the robustness of these models. However, when combining fluorescence datasets at λ_{ex} 270 and 330 nm with HSI data, results were poor. Overall, the multiblock PLS modelling enhanced prediction results of all chemical markers and of UMF^{TM} score.

Table 11.6. PLS prediction of eight chemical markers from multiblock data of undiluted LUX fluorescence at excitation 265 nm with HSI data

Models	Pre-processing	No. LVs	R^2 (CV)	RMSECV	Bias (CV)	R^2 (Pred.)	RMSEP	Bias (Pred.)	RPD
DHA	Mean center	5	0.90	252.60	4.57	0.92	122.24	30.27	**3.07**
MGO	Mean center	4	0.91	53.29	-2.61	0.84	26.91	7.20	**3.18**
3-PLA	Mean center	2	0.74	194.38	5.93	0.92	99.07	23.78	**1.83**
4-HPLA	Mean center	3	0.84	1.04	0.00	0.89	0.57	0.05	**2.65**
2'-MAP	Mean center	3	0.70	5.78	0.08	0.89	2.76	0.11	**1.81**
2-MBA	Mean center	5	0.88	6.77	-0.28	0.58	5.40	-2.31	**2.55**
Leptosperin	Mean center	4	0.84	138.82	-3.39	0.92	56.23	26.68	**2.51**
Lepteridine^{TM}	Mean center	4	0.88	2.71	-0.02	0.95	1.20	0.49	**2.82**
UMF^{TM}	Mean center	2	0.66	2.91	0.11	0.65	1.89	1.12	**1.69**

Table 11.7. PLS prediction of eight chemical markers from the multiblock data of undiluted LUX fluorescence emission data at λ_{ex} 270 with HSI data

Models	Pre-processing	No. LVs	R^2 (CV)	RMSECV	Bias (CV)	R^2 (Pred.)	RMSEP	Bias (Pred.)	RPD
DHA	Mean center	3	0.88	292.184	12.83	0.93	157.41	57.61	**2.65**
MGO	Mean center	5	0.94	42.69	-2.08	0.94	19.91	-2.22	**3.98**
3-PLA	Mean center	3	0.78	181.72	6.60	0.48	153.13	65.15	**1.96**
4-HPLA	Mean center	3	0.80	1.22	0.02	0.79	1.13	0.17	**2.26**
2'-MAP	Mean center	3	0.78	5.04	- 0.00	0.83	3.61	-0.79	**2.08**
2-MBA	Mean center	4	0.74	10.11	- 0.37	0.44	7.48	2.69	**1.70**
Leptosperin	Mean center	3	0.88	124.26	3.05	0.93	75.67	29.72	**2.80**
Lepteridine™	Mean center	3	0.87	2.81	0.03	0.94	1.68	0.60	**2.72**
UMF™	Mean center	3	0.88	1.67	0.02	0.64	1.70	0.56	**2.94**

Table 11.8. PLS prediction of eight chemical markers multiblock data of undiluted LUX fluorescence emission data at λ_{ex} 310 with HSI data

Models	Pre-processing	No. LVs	R^2 (CV)	RMSECV	Bias (CV)	R^2 (Pred.)	RMSEP	Bias (Pred.)	RPD
DHA	Mean center	2	0.85	315.6	-4.19	0.94	304.11	197.29	2.46
MGO	Mean center	2	0.77	83.54	-2.2	0.79	78.71	24.42	**2.03**
3-PLA	Mean center	3	0.69	207.0	1.90	0.82	136.58	43.64	**1.72**
4-HPLA	Mean center	4	0.72	1.38	0.07	0.99	0.63	0.60	**1.99**
2'-MAP	Mean center	4	0.65	5.86	0.28	0.89	3.56	0.80	**1.78**
2-MBA	Mean center	2	0.31	16.21	-0.55	0.10	10.29	-0.23	1.06
Leptosperin	Mean center	2	0.79	164.0	0.84	0.61	168.81	54.49	**2.12**
Lepteridine™	Mean center	3	0.77	3.86	-0.15	1.34	3.79	1.34	**1.98**
UMF™	Mean center	2	0.62	2.98	-0.06	0.69	3.14	1.14	**1.65**

Table 11.9. PLS prediction of eight chemical markers from the multiblock data of undiluted LUX fluorescence emission data at λ_{ex} 330 with HSI data

Models	Pre-processing	No. LVs	R^2 (CV)	RMSECV	Bias (CV)	R^2 (Pred.)	RMSEP	Bias (Pred.)	RPD
DHA	Mean center	3	0.78	376.36	21.00	0.84	384.87	2.74	**2.06**
MGO	Mean center	4	0.62	101.27	4.25	0.73	101.27	-6.86	**1.68**
3-PLA	Mean center	2	0.71	196.58	3.82	0.88	129.22	-10.15	**1.81**
4-HPLA	Mean center	3	0.73	1.40	0.01	0.95	0.73	0.15	**1.97**
2'-MAP	Mean center	3	0.66	5.74	-0.03	0.97	3.13	-0.65	**1.82**
2-MBA	Mean center	2	0.18	14.17	0.00	0.11	20.16	-2.24	1.22
Leptosperin	Mean center	3	0.46	239.79	7.88	0.61	297.11	-48.48	1.45
Lepteridine™	Mean center	3	0.55	4.76	0.06	0.68	5.85	-0.56	**1.61**
UMF™	Mean center	3	0.49	3.45	-0.15	0.19	5.38	-0.92	1.42

Table 11.10. PLS prediction of eight chemical markers from the multiblock data of undiluted LUX fluorescence emission data at λ_{ex} 265 & 310 nm with HSI data

Models	Pre-processing	No. LVs	R^2 (CV)	RMSECV	Bias (CV)	R^2 (Pred.)	RMSEP	Bias (Pred.)	RPD
DHA	Mean center	5	0.88	283.789	18.49	0.99	101.76	32.85	**2.73**
MGO	Mean center	5	0.91	53.05	-0.27	0.88	61.13	-1.61	**3.19**
3-PLA	Mean center	5	0.81	155.21	2.51	0.95	79.27	5.16	**2.29**
4-HPLA	Mean center	4	0.84	1.05	-0.01	0.97	0.58	-0.09	**2.63**
2'-MAP	Mean center	5	0.67	5.94	0.13	0.91	3.28	0.12	**1.76**
2-MBA	Mean center	5	0.84	7.85	-0.15	0.37	4.68	1.93	**2.19**
Leptosperin	Mean center	4	0.91	41.78	1.88	0.99	41.78	-8.61	**8.33**
Lepteridine™	Mean center	4	0.91	2.42	0.06	0.97	1.14	0.40	**3.16**
UMF™	Mean center	5	0.88	1.64	-0.03	0.64	3.22	0.66	**2.99**

Table 11.11. PLS prediction of eight chemical markers from the multiblock data of undiluted LUX fluorescence emission data at λ_{ex} 270 & 330 nm with HSI data

Models	Pre-processing	No. LVs	R^2 (CV)	RMSECV	Bias (CV)	R^2 (Pred.)	RMSEP	Bias (Pred.)	RPD
DHA	Mean center	4	0.86	288.87	12.92	0.94	270.57	130.59	**2.69**
MGO	Mean center	4	0.87	57.90	-0.74	0.98	29.01	4.14	**2.93**
3-PLA	Mean center	3	0.70	191.13	-0.83	0.78	188.12	60.86	**1.86**
4-HPLA	Mean center	5	0.76	1.31	-0.06	0.92	0.85	0.28	**2.11**
2'-MAP	Mean center	5	0.85	4.16	-0.10	0.77	6.48	3.01	**2.52**
2-MBA	Mean center	4	0.52	10.07	-1.07	0.92	6.83	-2.46	**1.71**
Leptosperin	Mean center	3	0.70	170.68	2.60	0.91	164.10	41.28	**2.04**
Lepteridine™	Mean center	2	0.57	4.36	0.26	0.94	4.16	-0.39	**1.75**
UMF™	Mean center	3	0.33	3.87	-0.20	0.76	3.38	1.49	1.27

11.3.4. Grading honey frames

11.3.4.1. Sorting honey frames into MPI honey classes

PLSDA was used to sort 32 comb honey samples (23 samples used for calibration and 9 samples for validation). Tables 11.12 & 11.13 show the cross-validated and predicted PLSDA results of three different datasets: NIR non-imaging, NIR hyperspectral imaging and LUX fluorescence data at $\lambda_{265\ nm}$ for separating mono-mānuka, multi-mānuka and non-mānuka honeys. Overall, the accuracy of these datasets exceeded 87 % on the calibration set and ≥ 78 % on the test set. Using fluorescence data at $\lambda_{265\ nm}$ gave 100 % cross-validated and predicted classification accuracy for all three honey classes. Following were NIR non-imaging and hyperspectral imaging data with > 90 % accuracy for mono-mānuka and non-mānuka honeys on the calibration set but only 67 - 80 % and 80 - 91 % accuracy on the test set. Multi-mānuka honey had a very small sample size (1 sample) on the test set. PLSDA models of LUX fluorescence and the imaging data could not detect multi-mānuka honeys but did so with non-imaging data at 89 % accuracy.

Table 11.12. Cross-validation PLSDA outputs of classification of mono-, multi- and non-mānuka honeys for three datasets (NIR non-imaging, NIR imaging and undiluted LUX fluorescence at $\lambda_{265\ nm}$)

Data	Recall			Precision			F1			OA
n = 23 samples	Mono	Multi	Non	Mono	Multi	Non	Mono	Multi	Non	
NIR non-imaging	1.00	0.80	1.00	0.91	1.00	1.00	0.95	0.89	1.00	0.96
NIR imaging	0.9	0.80	0.88	0.92	0.67	1.00	0.90	0.73	0.93	0.87
LUX fluorescence at $\lambda_{265\ nm}$	1.00	1.00	1.00	1.00	1.00	1.00	1.00	1.00	1.00	1.00

Table 11.13. Predicted PLSDA outputs of classification of mono-, multi- and non-mānuka honeys for three datasets (NIR non-imaging, NIR imaging and undiluted LUX fluorescence at $\lambda_{265\ nm}$)

Data	Recall			Precision			F1			OA
n = 9 samples	Mono	Multi	Non	Mono	Multi	Non	Mono	Multi	Non	
NIR non-imaging	0.67	1.00	0.80	0.80	1.00	0.76	0.67	1.00	0.80	0.78
NIR imaging	0.67	NaN	1.00	1.00	NaN	0.80	0.80	NaN	0.91	0.78
LUX fluorescence at $\lambda_{265\ nm}$	1.00	NaN	1.00	1.00	NaN	1.00	1.00	NaN	1.00	1.00

Note: NaN means that the model cannot pick up the information due to small dataset

11.3.4.1. Sorting honey frames into UMF™ buckets

A total of 32 comb honey samples were labeled with three UMF™ buckets of <<UMF10+, <UMF10+, UMF10+ based on the laboratory UMF™ score. There were few samples in the UMF 20+ bucket in the current dataset. Tables 11.14 & 11.15 display the classification results of three UMF™ buckets. Overall, all three buckets were well classified with the fluorescence data at λ_{ex} 265 nm. Samples in the <<UMF10+ bucket could be discriminated with 100 % accuracy for both fluorescence calibration and test sets. Samples in <UMF10+, UMF10+ zones could also be classified with 80 - 100 % accuracy.

The classification results of NIR imaging seemed better than those of NIR non-imaging. Samples in the <<UMF10+ bucket could be separated with 73 - 91 % accuracy for the two datasets. Samples in the < UMF10+ bucket could be discriminated with 60 - 100 % accuracy for NIR imaging data while those buckets were only classified with 53 - 73 % for NIR non-imaging data. Samples in the UMF10+ zone could not be recognized by PLSDA for both non-imaging and imaging test sets due to a small sample size (1 sample).

Table 11.14. Cross-validation PLSDA outputs of three UMF^{TM} buckets for three datasets (NIR non-imaging, NIR imaging and undiluted LUX fluorescence at $\lambda_{265\ nm}$)

Data n = 23 samples	Recall			Precision			F1			OA
	<<UMF 10+	<UMF 10+	UMF 10+	<<UMF 10+	<UMF 10+	UM F10+	<<UMF 10+	<UMF 10+	UMF 10+	
NIR non-imaging	0.90	0.80	0.88	0.92	0.88	1.00	0.90	0.73	0.93	0.87
NIR imaging	0.90	0.50	0.86	0.75	0.89	1.00	0.78	0.60	0.92	0.78
LUX fluorescence at $\lambda_{265\ nm}$	1.00	0.75	0.86	1.00	0.92	0.87	1.00	0.80	0.80	0.87

Table 11.15. Predicted PLSDA outputs of three UMF^{TM} buckets for three datasets (NIR non-imaging, NIR imaging and undiluted LUX fluorescence at $\lambda_{265\ nm}$)

Data n = 9 samples	Recall			Precision			F1			OA
	<<UM F 10+	<UMF 10+	UMF 10+	<<UMF 10+	<UM F10+	UMF 10+	<<UMF 10+	<UMF 10+	UMF 10+	
NIR non-imaging	0.80	0.50	NaN	0.62	0.71	NaN	0.73	0.57	NaN	0.67
NIR imaging	1.00	1.00	NaN	0.80	1.00	NaN	0.91	1.00	NaN	0.89
LUX fluorescence at $\lambda_{265\ nm}$	1.00	1.00	1.00	1.00	1.00	1.00	1.00	1.00	1.00	1.00

Note: NaN means that the model cannot pick up the information due to small dataset

11.3.5. Selection of important variables

PLSDA models of NIR imaging and LUX fluorescence data at λ_{ex} 265 nm were chosen to discover important variables for classifying three MPI honey classes (mono-mānuka, multi-mānuka and non-mānuka honeys) and three Comvita UMF^{TM} buckets (<<UMF 10+, <UMF10+, UMF10+). Table 11.16 shows important wavelengths contributing to the PLSDA classification results of both HSI imaging and LUX fluorescence data. Overall, important wavelengths identified for classification of MPI were quite similar to those characterised for classification of UMF^{TM} buckets for both datasets. For HSI data, important wavelengths were mostly relevant to water-OH 2nd overtone at 981 & 991 nm, C-H 3rd overtone at 992, 932 & 937 nm, 1st overtone of C-H combination at 1139 nm and C-H 2nd overtone at 1144 & 1154 nm (Xiaobo et al., 2010). For LUX fluorescence data at λ_{ex} 265 nm, wavelengths 325 and 340/355 nm corresponded to footprints of Lepteridine^{TM} and Leptosperin, respectively. Wavelengths 430/440 nm could be related to blue fluorescence emission of chlorophyll after exciting UV light (λ_{ex} 265 nm) (Schweiger et al., 1996), while wavelengths 590/600 nm could be relevant to fluorescence emission of DHA/MGO-brown pigments (Nguyen & Kochevar, 2003).

Table 11.16. Important wavelengths identified in PLSDA models of NIR imaging and LUX fluorescence at $\lambda_{265\ nm}$ for classification of MPI honey classes and Comvita® UMF™ buckets

PLSDA models	NIR imaging (nm)	LUX fluorescence at $\lambda_{265\ nm}$ (nm)
MPI classes	922 (-), 932 (+), 981 (-), 991 (+), 1139 (-), 1144 (+), 1154 (+)	325 (+), 330 (-), 340 (-), 430 (+), 440 (-)
Comvita® UMF™ buckets	927 (-), 937 (-), 981 (+), 996 (+), 1139 (-), 1154 (+)	325 (-), 355 (+), 590 (+), 600 (+)

Note: "+" & "-"marks indicate positive and negative contribution for classifying of mānuka honeys

11.4. Discussion

Honey frames can be assessed either by measuring concentration of chemical markers individually or by direct estimation of potency (UMF™ score) and purity (classification of MPI classes or Comvita® UMF™ buckets). Fluorescence could be applied at industrial scale to assess the quality and purity of honey frames before bulk extraction. Fluorescence with excitation at 265 nm can predict all chemical markers including two fluorescence markers Leptosperin and Lepteridine™. The same excitation wavelength could also estimate UMF™ score and sort honey frames into three MPI honey classes and Comvita® UMF™ buckets with 80 - 100 % accuracy. Fusion of fluorescence combined with NIR hyperspectral imaging using multi-block PLS modelling enhanced the prediction accuracy for all models. This indicates that the multi-block approach combining fluorescence and NIR methods has potential for online assessment of honey frames at the extraction processing line.

Sorting honey frames into different MPI honey classes or UMF™ buckets before bulk extraction also gives a degree of freedom for honey companies to decide how best to group honey frames into different quality buckets. This study shows that using fusion of fluorescence with NIR can separate honey frames with 90 - 100 % accuracy. Sorting honey frames into Comvita® UMF™ buckets is promising. Bad quality frames can be separated from good frames and high-quality frames may be sorted at different levels. This current study showed that three Comvita® UMF™ buckets were classified by PLSDA on fluorescence data at λ_{265nm} better than NIR hyperspectral data. Honey samples in UMF™ buckets of <<UMF10+, <UMF10+ and UMF10+ were separated with 100 % accuracy using fluorescence data alone. Future research should include samples from the UMF™ 20+ bucket in the dataset.

Four important wavelengths (325, 355, 590 and 600 nm) were characterized for classification of Comvita® UMF™ buckets using fluorescence method at λ_{265nm}. These bands are relevant to chemical footprints of Lepteridine™, Leptosperin and DHA/MGO brown

pigments. PLSDA classification of MPI classes also identified chemical footprints of Lepteridine^{TM}, Leptosperin, but do not point to footprints of DHA/MGO. Instead, chlorophyll (blue fluorescence emission at 430 and 440 nm for excitation 265 nm) seems important. In the NIR range, important wavelengths identified were similar between two classification models. The absorption of water molecules in interaction with other phytochemical markers, in particular DHA & MGO around 1000 nm, was identified as important for classification of MPI honey classes and UMF^{TM} buckets in the NIR range. Vibration of 1st overtone C-H combination at 1139 - 1154 nm relevant to CH_3- group was also found as important for classification results. The important wavelengths were line with the results from the previous chapters.

11.5. Conclusion

Quality assessment of honey in a real frame using fusion of NIR and fluorescence data was tested in the current chapter. The study proves that combining NIR and fluorescence modes offers great potential to assess the quality and purity of mānuka honey in an uncapped frame. This research provides the scientific basis for development of a rapid non-destructive system for online assessment of honey frames before bulk extraction. Multiple alternative ways of quality assessment of mānuka honey (measurement of eight chemical markers, potency (UMF^{TM} score) and purity (classification of MPI classes and UMF^{TM} buckets)) are also possible for application in industry where companies can balance the benefits of each implementation. Future research might be dedicated to applying this approach at a working extraction plant.

Chapter 12
General conclusions and future work

12.1. Introduction

Mānuka honey is a valuable, but limited resource. The value decreases when mānuka honey is diluted with others derived from non-*Leptospermum scoparium* nectars. Honey quality varies among geographic districts, across apiaries, within beehives and in a honey frame. Quality assessment of honey frames before lumped extraction is necessary to ensure the highest value can be recovered to benefit honey companies, beekeepers and landowners. But this is not current industrial practice. Qualitative and quantitative measurements of mānuka honey quality can be directly based on concentrations of eight key chemical markers or indirectly by estimating potency and purity mānukaness. The current research has employed non-destructive techniques such as NIR and fluorescence methods to assess honey quality while still in the frame. Data from these instruments were analysed using different chemometrics, machine learning and deep learning methods. The main research objective was to provide the scientific basis for a robust tool along with associated modelling methods to measure mānuka honey quality and identity which can be used for on-line and at-line automated assessment of honey frames at the extraction plant.

12.2. General conclusions

12.2.1. Quality assessment of mānuka honeys

The first two chapters describe the state-of-the-art of traditional and more recent methods that have been used to characterise mānuka honey. Traditional methods were unsuitable for on-line, and at-line uses to assess mānuka honey quality since they are destructive, expensive and slow to evaluate frame by frame. Various studies have employed NIR methods to detect fraud and to determine the botanical origin of mānuka honey (Yang et al., 2020; Zhang & Abdulla, 2022). Bong et al. (2017) and Lin et al. (2020) used fluorescence methods to identify two fluorescent markers Leptosperin and Lepteridine^{TM}, unique to mānuka honey when diluted to 2 % (w/v) with water. However, no prior study had attempted to use NIR or fluorescence methods to measure mānuka honey quality while still in the frame. And the fusion of NIR and fluorescence methods combined had not been reported before for assessment of mānuka honey.

Four research gaps for measurement of mānuka honey quality in the frame were identified earlier. This study successfully filled these gaps.

The current research first employed Vis-NIRS: non-imaging (350 - 2500 nm) & hyperspectral imaging (547 - 1701 nm) to assess mānuka honey quality and identity based on concentration of eight key chemical markers (Chapters 4 & 5). Prediction of key chemical markers using standard chemometrics and machine learning methods gave 60 % accuracy. The complexity of the honey matrix, due to variation in chemical compositions from different floral sources, heavily impacted measurement of chemical markers. Later, the study used alternative quality indicators based on potency and purity mānukaness to evaluate the quality of mānuka honey (Chapter 6). Overall, non-imaging or imaging methods combined with chemometrics, machine learning and deep learning show the potential to measure chemical markers, potency and purity. Global models built from the samples representing all geographic districts are strongly affected by variation in botanical source. Region-based models at some districts performed better than the others. This result implies that regional variation limits standard modelling methods (i.e., PLS & SVM) in which the relationships between spectral signals and responses (e.g., chemical marker's concentration) become non-linear due to the complex honey matrix, in particular when analysing hyperspectral data. Deep learning (i.e., 1D-CNN) showed capacity to interpret hyperspectral signals despite the complex honey matrix (Chapter 9). Prediction of potency and purity of mānuka honey gave above 70 % accuracy. Deep learning had not been applied to estimating chemical maker concentration. Developing such models can be a time-consuming process, but it appears that deep learning can deal with regional variation to enhance predictive accuracy further. Potentially, Vis-NIR hyperspectral imaging combined with deep learning could be used for automating on-line assessment of honey frames before bulk extraction. Overall, these findings have filled research gap 1: potency and purity mānukaness can be measured in a manner suitable for grading honeys at line.

The current study also calculated the dollar benefit of NIR methods when assessing honey frames into different quality buckets (e.g., UMF^{TM} buckets) for both non-imaging and imaging systems (Chapters 7 & 8). Generally, the results indicate that using UMF^{TM} buckets for sorting frames before bulk extraction enhances returns over the current method in which all frames are lumped together at extraction. The greatest benefit is found when the pricing UMF^{TM}/$$ curve is concave upward. When the pricing UMF^{TM}/$$ curve is concave downward, the benefit can be negative. Apiaries having a large quality variation between honey frames can get as much as 70 % revenue gain by when separating into different quality buckets.

This result covers research gap 3: economic benefit can be generated by sorting honey into different quality buckets before bulk extraction.

This study has also employed fluorescence methods to evaluate the quality of honey in the frame (Chapter 10). Internal reflectance fluorescence measurement allows high absorbance undiluted honeys to be measured and the inner filter effects to be minimised. Fluorescence-based prediction of key chemical markers gave > 80 % accuracy while prediction of potency and purity achieved 86 and 90 % accuracy, respectively. The current research proves that fluorescence can be used to assess honey quality while still in the frame. Moreover, fusion of NIR and fluorescence methods together significantly enhances assessment of mānuka honey quality (Chapters 10 & 11). These results cover research gaps 4 and 5 in which fluorescence signals of mānuka honey in undiluted mode can be measured despite the honey matrix effect and the predictability of all key markers increases when using fusion of fluorescence and NIR data.

Honey frames were scanned to evaluate honey while still in the frame using both NIR and fluorescence techniques (Chapter 11). This reconfirmed findings from the previous chapters (Chapters 6 - 10). Overall, these optical technologies combined can characterise mānuka honey in the frame immediately after uncapping. Measurements of eight key markers, potency and purity mānukaness of honey in the frame achieved above 80 % accuracy. The result fulfills research gap 2.

Different pre-processing techniques and modelling methods have been proposed to analyse spectral data. Mean center and SNV were mostly used on raw honey spectra before modelling. Standard chemometric methods PLS & SVM showed limitations in analysing hyperspectral data due to the complexity of the honey matrix. However, using 1D-CNN enhances modelling performance by up to 10 percentage points and minimises the impact of the regional variation. Multi-way analysis (e.g., tri-PLS, PARAFAC) shows higher capacity to analyse fluorescence signals than standard methods (e.g., two-way PLS) for high absorbance undiluted honey. Multi-block PLS approaches provide the capacity to model the fusion of fluorescence and NIR data combined. The multi-block PLS results show enhancement of prediction of all chemical markers, potency and purity up to 80 - 100 % accuracy when evaluating the quality of honey in the frame.

12.2.2. Key scientific contributions

The current PhD research has brought new knowledge of using in-line reflectance geometry spectrofluorometry to measure successfully high absorbance solutions. The study also addresses a novel approach of fusion of fluorescence and NIR data together to compensate for the limitations of each technique.

For assessment of mānuka honey quality, the current study contributes basic scientific guidance when using non-destructive NIR and fluorescence systems (Table 12.1). The quality of mānuka honey can be indicated via concentration of eight key chemical markers or by estimating potency and purity mānukaness. The signals of key chemical compounds can be captured in the Vis-NIR range and can be discerned within the complexity of the honey matrix. This research has provided a scientific basis for the industrial application of non-invasive assessment of honey in the frame.

Table 12.1. The contribution of the current research to new knowledge

New knowledge	Contribution
1	Assessment of NIRS for quantification of eight chemical markers, potency, and purity in undiluted honey.
2	Assessment of fluorescence for quantification of eight chemical markers, potency, and purity in undiluted honey.
3	Fusion of fluorescence and NIR is able to discriminate ‘x’ compound classes at ‘y’ level of concentration in the complex honey matrix.
4	Building advanced modelling such as 1D-CNN and multi-block which helps to counter the food matrix effect.
5	This study created the scientific basis for a non-invasive assessment of honey while still in the frame contributing to industrial application.

Important wavelengths for characterising mānuka honey quality were identified in both NIR and fluorescence methods (Table 12.2). In the NIR mode, wavelengths (666 - 740, 991, 1435 nm) identified were relevant to the presence of DHA, MGO, chlorophyl, flavonoids and to water molecules interacting with phytochemicals in the honey matrix (based on the results of NIR hyperspectral imaging combined with deep learning). In fluorescence mode, the assessment of undiluted honeys indicates that most important emission wavelengths were in present in the visible region. These bands were mostly relevant to the absorptions of Leptosperin, Lepteridine^{TM} and DHA/MGO (Chapters 10 & 11). Fluorescence emission at excitation wavelength 265 nm is of practical importance for modelling the quality of mānuka

honey in the frame since LEDs are readily available at 265 nm. In general, important wavelengths identified could be a guideline to choose the optimised sensor when commercialising the current technology.

Table 12.2. Summary of important variables identified to assess the quality and purity of mānuka honey while still in the frame

Dataset	Models	Prediction	Positive corelated (nm)	Negative correlated (nm)	Chemical footprints
NIR hyperspectral imaging (547-1701 nm)	PLSDA & 1D-CNN	MPI classes	932, 991, 1144, 1154	922, 981, 1139	Network of water + phytochemicals (e.g., DHA, MGO), carbohydrate groups
	PLSDA	Comvita® UMF™ buckets	981, 996, 1154	927, 937, 1139	Network of water + phytochemicals (e.g., DHA, MGO), carbohydrate groups
Fluorescence data at $\lambda_{265\ nm}$	PLSDA	MPI classes	325, 430	330, 340, 440	Lepteridine™, Leptosperin, chlorophyll
	PLSDA	Comvita® UMF™ buckets	355, 590, 600	325	Lepteridine™, Leptosperin, DHA-brown pigments
Fluorescence data at $\lambda_{265\ nm}$	PLS	DHA	415, 425	410, 430	DHA-brown pigments
	PLS	MGO	425	420	MGO-brown pigments
	PLS	3-PLA	315, 380, 385, 420, 425, 430	325	
	PLS	4-HPLA	315	325, 565, 570	
	PLS	2'-MAP	315, 395, 425	320, 525, 530, 550, 565	
	PLS	2-MBA	315, 355, 365, 390, 420	-	
	PLS	Leptosperin	400, 550	-	
	PLS	Lepteridine™	320	325, 595	
	PLS	UMF™	410, 425	320, 325	
Fluorescence EEM matrix (250-400/300-600 nm)	Tri-PLS	DHA	340, 360, 550	315, 395, 450, 470	
	Tri-PLS	MGO	390, 475	360, 470	
	Tri-PLS	3-PLA	315, 340, 355	360, 460, 475, 395. 550	

	Tri-PLS	4-HPLA	350, 355, 395	320, 360, 450, 475,
	Tri-PLS	2'-MAP	345	360, 450, 475
	Tri-PLS	2-MBA	355, 360, 395, 450, 470	320
	Tri-PLS	Leptosperin	355, 360, 380, 390, 395, 455, 475	330, 470, 525
	Tri-PLS	Lepteridine™	315, 355, 360, 470	
	Tri-PLS	UMF™	445, 550	360, 395, 470
Multi-block data (Fluorescence data at $\lambda_{265\ nm}$ + combined with HSI)	PLS	DHA	320, 420, 1267	325, 430, 435, 1415, 1642
	PLS	MGO	345, 920, 930, 1115, 1662	320, 420
	PLS	3-PLA	315, 355, 590, 1174, 1248, 1290	-
	PLS	4-HPLA	315, 375, 1465	325
	PLS	2'-MAP	375, 1450, 1465	360
	PLS	2-MBA	315, 345, 355, 445, 455	325, 390
	PLS	Leptosperin	335, 550, 1642	325, 430
	PLS	Lepteridine™	335, 1465	325, 455
	PLS	UMF™	420, 976, 991, 1090, 1135	315, 475
Multi-block data (Fluorescence data at $\lambda_{265\ \&\ 310\ nm}$ combined with HSI)	PLS	DHA	320, 375, 1149, 1262	325, 390, 420
	PLS	MGO	375, 415	380, 390
	PLS	3-PLA	315, 370, 610, 893, 932	460, 480, 570,
	PLS	4-HPLA	315, 385, 420,	335, 360, 545
	PLS	2'-MAP	370, 420, 1262	360, 450, 575,
	PLS	2-MBA	335, 375, 450, 505, 535, 550, 580, 590	325, 390
	PLS	Leptosperin	335, 360, 590, 730	320, 370, 495,
	PLS	Lepteridine™	335, 375, 630, 1617	320, 390
	PLS	UMF™	375, 415, 560	380, 585,

12.3. Future research suggestions

The current thesis provides a scientific foundation to support multiple types of technology: NIR non-imaging, NIR hyperspectral imaging, fluorescence, and their combination to be implemented in the honey industry. The choice is based on cost benefit (short & long term) and ability to operate at industrial scale. Early application may support quality control. In the long term, sophisticated implementation may involve the entire process being adjusted to maximise the benefit of each honey frame.

12.3.1. Improved models for on-line quality assessment of honey frames

On-line quality assessment of honey frames is promising since non-destructive technology allows honey frames to be sorted rapidly into different quality buckets. The current models, using fusion of NIR hyperspectral imaging (547 - 1701 nm) and fluorescence signals at excitations 265 and 310 nm, were developed from limited data from honey frames from seven geographic districts of the North Island. For industrial use current models need to be upgraded with a much larger dataset of honey frames covering multiple geographic districts across all New Zealand. This dataset should keep a balanced number of frames between districts. It is noted that New Zealand honey frame has black or yellow background. This also implies that frames with two different colours should be involved in balance to eliminate the effect of background noise. In addition, the future frame dataset should also contain sufficient high-quality frames to calibrate the upper reaches and sufficient low-quality frames to accommodate the multiple sources of variability there.

12.3.2. Continuous monitoring and validation of working models

Even the perfect model can lose utility if the reality of prediction changes. Honey quality could change every year due to prevailing weather and biennial bearing in some nectar sources. Models can easily be continuously monitored and validated against the laboratory data routinely collected by honey companies for each drum for payment and compliance purposes. Approximately 300 frames go into each drum and the spectra for each frame will be stored. When lab data become available, they can be compared with model predictions from the average of the relevant 300 stored spectra. When the systematic deviations become too great it is time to refresh the model. Building this monitoring system requires further work.

This continuous monitoring also allows checking of the on-line sensor used since sensor components (light source, camara lenses, fibre…) may be changed with time and therefore became the source of deviations.

12.3.3. Periodic upgrading of working models

Periodic updating of models is suggested, especially between seasons. Once sufficient frame-by-frame spectra and drum-by-drum laboratory data have been accumulated, this resource is available for periodic or even continuous, upgrading of working models.

12.3.4. Optimal design of hardware for industrial use

Hyperspectral and fluorescence sensors used in the current work are not cheap (US$ 45,000 - 50,000.). On-line processing aims to use cheap sensors, be easy to set up, be robust and use contactless measurement. For this, NIR hyperspectral imaging cameras show more advantages than fluorescence sensors. Previous results indicate both methods are good enough to predict UMF^{TM} score of honey in the frame. Fluorescence performs better but is difficult to measure without touching the frame. Since most fluorescence emission spectra fall in Vis, potentially hyperspectral imaging can also pick them up if the acquisition settings are good enough. Future work needs to identify the design of sensing technology that best suits on-line application. Rather than using continuous wavelengths, a multispectral sensor designed with selected bands may reduce the cost of the sensor.

12.3.5. Better modelling techniques

Deep learning shows the ability to deal with the complex honey matrix likely to be encountered industrially. This study employed only 1D-CNN architecture to analyse spectral information of honey. Future work might test 2D-CNN and 3D-CNN for modelling hyperspectral images of honey frames employing both spatial and spectral information for prediction of chemical markers, potency and purity mānukaness. The future models can be further updated over time.

12.4. Overall conclusion

NIR and fluorescence have been shown useful for estimating, at full strength, quality and purity (monoflorality) of mānuka honey when inspected in the frame before extraction. Under most circumstances this will offer the honey company significant economic benefit. For automated at-line application sufficiently good spectra can probably be obtained from a Vis-NIR hyperspectral camera (i.e., 300 - 1000 nm) plus LEDs at 265 and 310 nm. Future work is required to build and validate a prototype system including methods for on-going validation and periodic upgrade of the current working model.

This work was specific to New Zealand North Island mānuka honey but should be applicable to other honeys and has implications for grading of other wild harvest foods.

Appendices

A. Prediction of potency and purity mānukaness based on laboratory chemical data

A.1. Identifying important parameters

Principal component analysis (PCA) was applied on the lab-based data (1656 samples) of eight key chemical markers to identify important variables contributing on the identity of mono-mānuka honeys. With only two principal components (PCs), three honey classes were classified (Figure A.1a). PC1 is the key component capture 70.7 % variance in the dataset to differentiate mono-mānuka honeys from others. The PCA loading (Figure A.1b) also indicates positive correlation with all eight markers which means that their concentrations were higher in mono-mānuka honeys than multi-and non-mānuka honeys. In addition, PC2 helped separation of three types of honey. In addition, PC2 also separated two groups of mono-mānuka honey: samples from upper and lower quadrants on the right. Honey samples in the lower right quadrant had high levels of Leptosperin, Lepteridine^{TM}, 2-MBA while samples in the upper right quadrant got high levels of MGO, 2'-MAP, 3-PLA and 4-HPLA. This implies the chemical variation in mono-mānuka honeys.

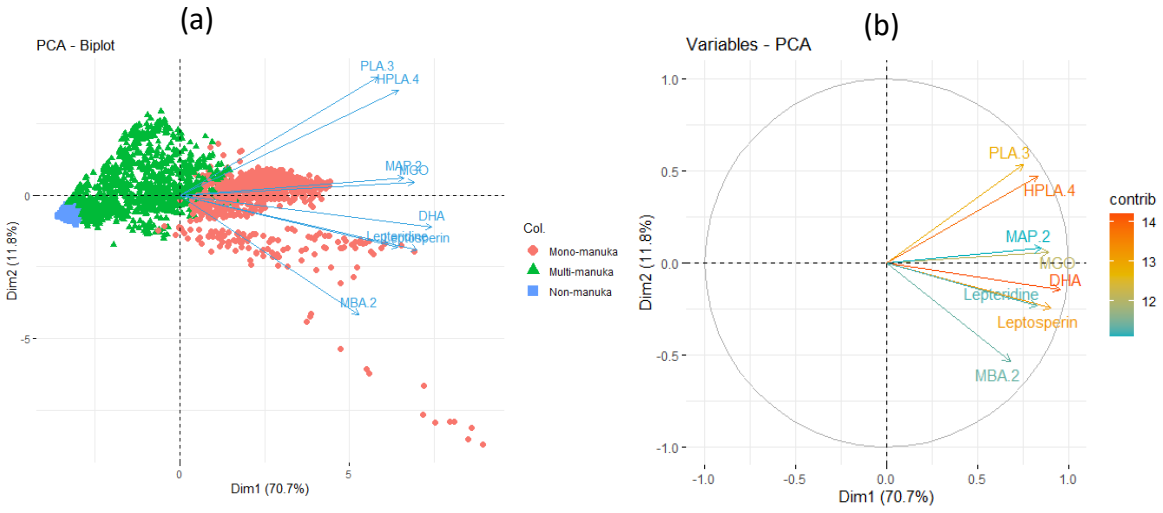

Figure A.1. *The PCA output of a matrix of eight chemical markers to classify mono-mānuka, multi-mānuka and non-mānuka. PCA biplot (a) and the loading of variables (b)*

DHA/MGO and Leptosperin contributes to UMF^{TM} values while other four chemicals (3-PLA, 4-HPLA, 2'-MAP, 2-MBA) are important to classify MPI honey classes (MPI, 2017b; UMFHA, 2022). A matrix of DHA, MGO and Leptosperin were built to predict UMF^{TM} score while a matrix of six chemical makers (3-PLA, 4-HPLA, 2'-MAP, 2-MBA, MM1 and MM2) were used to classify mono-mānuka, multi-mānuka and non-mānuka honeys.

A.2. Generalisation of potency mānukaness from lab-based data

Potency mānukaness was generalized from the linear PLS model. PLS regression was employed on the chemical lab-based data of the matrix of DHA, MGO and Leptosperin to estimate UMF^{TM} values. Prediction of UMF^{TM} gave 97 % accuracy (for UMF^{TM} 10 month) (Figure A.2). Then, the PLS regression coefficient was calculated and then the lab-based potency mānukaness for the whole population was estimated. Figure A.2 illustrates prediction of potency mānukaness of lab-based data with the accuracy 97 % (r^2 0.97). There was a non-linearity between lab-based potency predicted and the UMF^{TM} score measured from the laboratory. This non-linearity could not be explained by modelling.

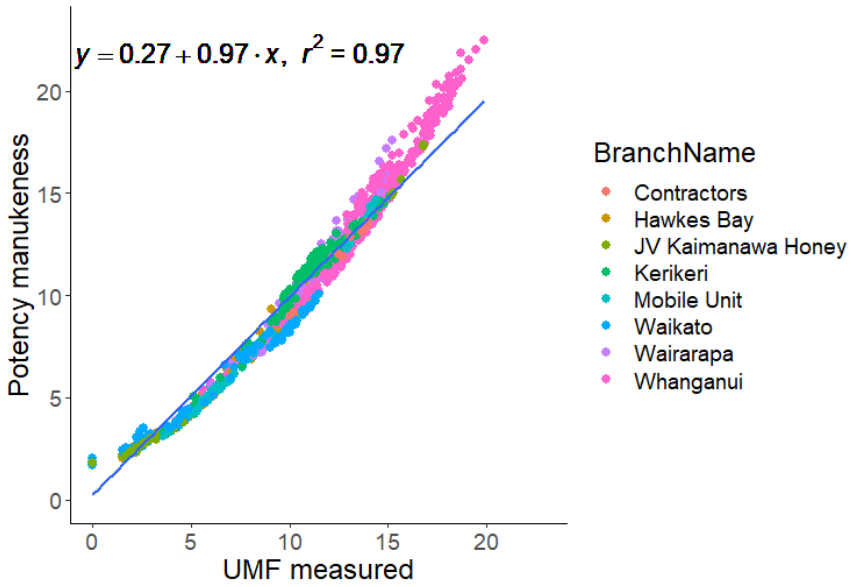

Figure A.2. *Potency mānukaness generated from the lab-based data of 1656 honey samples*

A.3. Generalisation of purity mānukaness from lab-based data

PLSDA and linear SVM were used to analyse the matrix of six key chemicals (3-PLA, 4-HPLA, 2'-MAP, 2-MBA, Leptosperin and Lepteridine^{TM}) to classify three MPI honey classes: mono-mānuka, multi-mānuka and non-mānuka honeys. The linear SVM classifier obtained higher classification accuracy than PLSDA. The SVM classification output obtained overall classification accuracy 97.5 %. The class accuracies of mono-mānuka, multi-mānuka and non-mānuka honeys were 100 %, 92.9 % and 96.9 %, respectively. So, the linear SVM model was chosen for generalisation of purity mānukaness.

Based on the linear classification model, the purity mānukaness was computed. Figure A.3 shows the violin plot distribution of mono-mānuka, multi-mānuka and non-mānuka honey samples. The 75 % population of the box indicates almost mono- mānuka honeys were separated from multi- and non-mānuka honeys. However, there was a little overlap at the distribution tail among these classes.

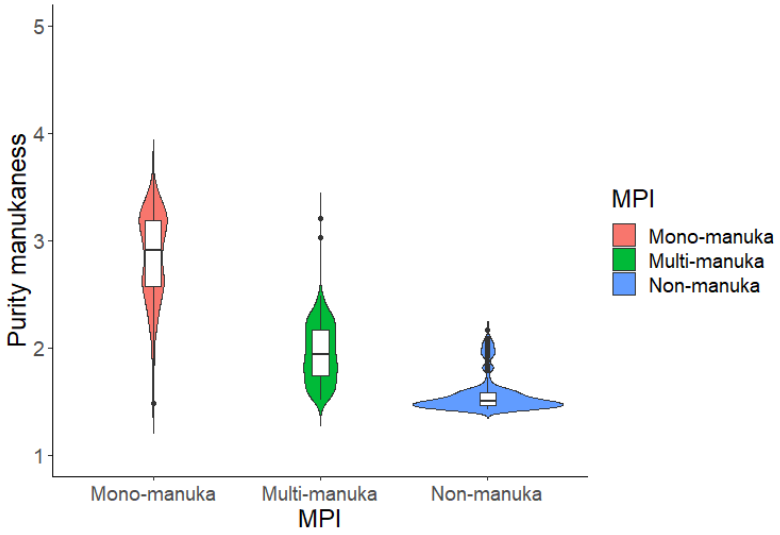

Figure A.3. *Purity mānukaness was generated from the lab-based six-chemical data of 1656 honey samples*

A.4. Plotting lab-based Potency and purity mānukaness plot

Potency and purity mānukaness were plotted against each other to check the linear relationship. Figure A.4 displays the linearity obtained between potency and purity with a correlation $r^2 = 0.85$. However, both parameters independently reflected the honey quality and identity, respectively. In general, each geographic district was relatively linear between potency and purity, but the lines of best fit differ somewhat between regions (Figure A.4b). Most honeys from Whanganui district possessed high potency values, but they quite vary in

purity values. Some honeys had high purity mānukaness. Kerikeri district had high homogeneity in both potency (UMF^{TM}: 10 - 15) and purity (3 - 3.5). Similarly, Wairarapa had potency (UMF^{TM}: 10 - 15) and purity (2.5 - 3). By contrast, Hawkes Bay and Waikato had a various level of potency (UMF^{TM} 5 - 5) and purity (1.5 – 3.5). JV Kaimanawa and Mobile Unit gave the lowest potency (UMF < 7.5) and purity < 2.5. Overall, variation in chemical profile from eight geographic districts were different and this generates the honey matrix effect when all honeys are combined together. This matrix effect was various for each geographic district.

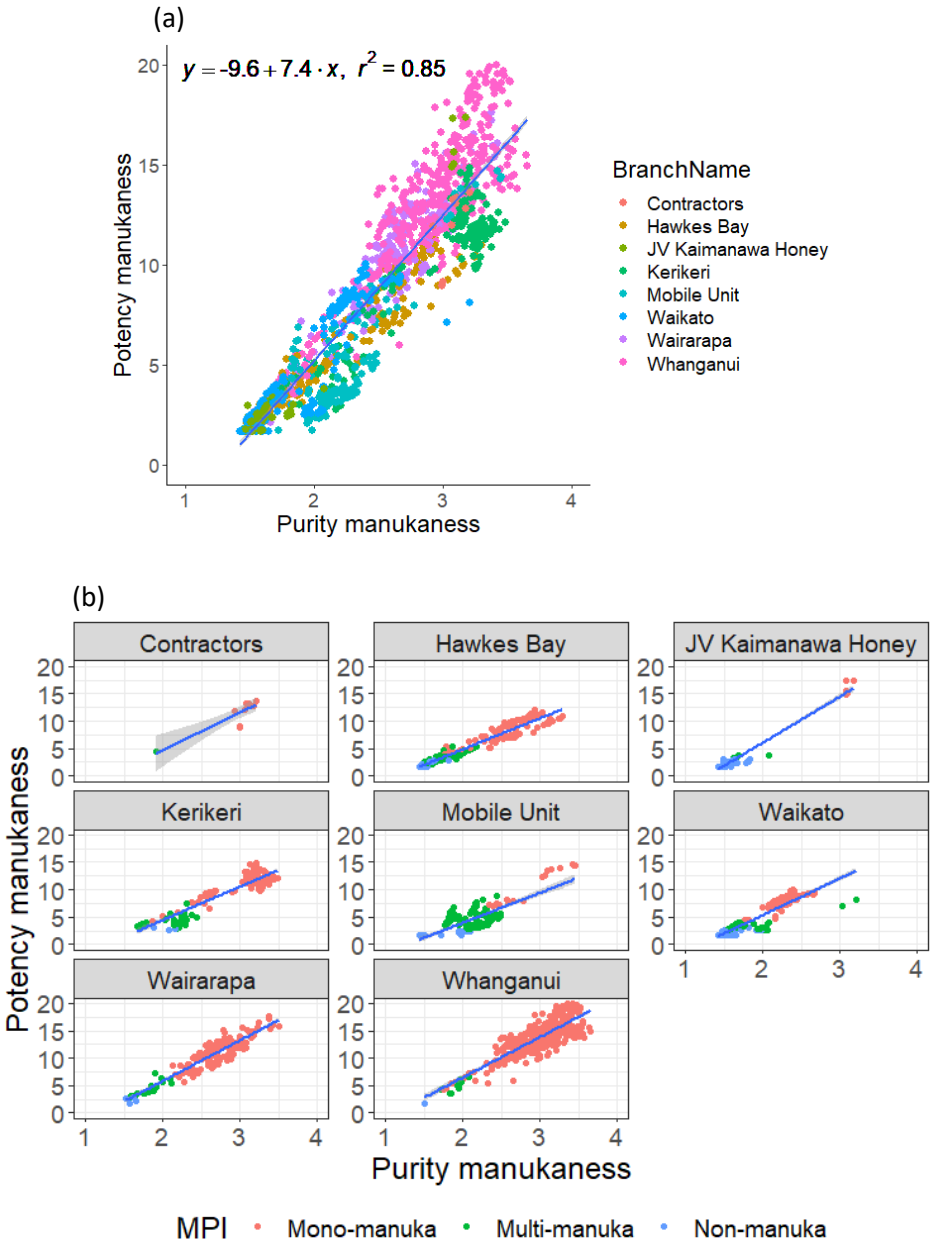

Figure A.4. *Lab-based potency and purity mānukaness plot for all districts (a) and for each district (b) grouping by three classes of MPI criteria. Note the blue line plotted is identical for each despite the changing axes and is the model line.*

A.5. Discussion and conclusion

Potency values formed from the lab-based data of the matrix of DHA, MGO and Leptosperin obtained 97 % accuracy compared to UMF™ score measured. Meanwhile, purity values developed from the lab-based matrix of 3-PLA, 4-HPLA, 2'-MAP, 2-MBA, Leptosperin and Lepteridine™ gave overall accuracy (OA) 97.48 % when classifying mono-mānuka, multi-mānuka and non-mānuka honeys. Measurements of potency and purity mānukaness based on the laboratory was not perfect, it still had a bias from the modelling in which the honey matrix effect could have played a role. In conclusion quality and purity of mānuka honey can be measured by potency and purity mānukaness but is impacted by the honey matrix effect.

B. Python code script for hyperspectral imaging segmentation

```
import numpy as np
import matplotlib.pyplot as plt
import skimage
from skimage import data
from skimage.feature import peak_local_max
from skimage import filters
from skimage import io
import os
import spectral.io.envi as envi
import matplotlib.patches as mpatches
from skimage.measure import label, regionprops
from scipy.ndimage import find_objects
from skimage import morphology
from scipy import ndimage as ndi
import pandas as pd
from skimage.color import label2rgb
import glob
import fnmatch

from skimage.morphology import dilation
from skimage.morphology import erosion
from skimage.morphology import binary_erosion
from skimage.morphology import binary_opening
from skimage.morphology import binary_closing
from skimage.morphology import disk, dilation, binary_erosion
import matplotlib.pyplot as plt
# PART 1: Correct dark and white balance & loading images
os.chdir("C:\\Users\\ttruong\\OneDrive - Massey University\\Data 2020& python co
# Read dark image
d=envi.open('C:/Users/ttruong/OneDrive - Massey University/Data 2020& python cod
Dark = d.load().astype("float64")
# calcualate the avergae of intensity of 350 number of lines in hypercubes
Ones=np.ones([350,1]) # create the array for dark
D=np.mean(Dark,axis=0)
Dhtarray=np.reshape(np.tensordot(Ones,D,axes=0),[350,320,235]) # reshape the dar

# Read white folder
w=envi.open('C:/Users/ttruong/OneDrive - Massey University/Data 2020& python cod
white=w.load().astype("float64")
# calcualate the avergae of intensity of 350 number of lines in hypercubes
Ones=np.ones([350,1])  # create the array for white
W=np.mean(white,axis=0)
Whtarray=np.reshape(np.tensordot(Ones,W,axes=0),[350,320,235]) # reshape the whi

# Read images containing in samples file
os.chdir("C:\\Users\\ttruong\\OneDrive - Massey University\\Data 2020& python co
image1 =envi.open('C:/Users/ttruong/OneDrive - Massey University/Data 2020& pyth
img1 = image1.load().astype("float64")
plt.imshow(img1[:,:,150])

# correction white and dark balance
Aaux=(img1-Dhtarray)
plt.imshow(Aaux[:,:,150]) # checking the Aaux
Baux=(Whtarray-Dhtarray)
plt.imshow(Baux[:,:,150]) # checking the Baux

# create the loop for the whole wavelength
tray1=np.zeros([350,320,235])
for i in range(0,234):
        tray1[:,:,i]=Aaux[:,:,i]/Baux[:,:,i]
```

```
# checking the plot at 1 wavelength
plt.imshow(Aaux[:,:,150]/Baux[:,:,150])
# or imshow like this
trayx=tray1[:,:,150]
plt.imshow(trayx)
# save the image
plt.imsave('C:/Users/ttruong/OneDrive - Massey University/Data 2020& python code
# PART 2: SEGMENTATION/SEGREGATION
# Thresholding for removing the background and keep honey
bina_img= tray1[:,:,32]<0.4
plt.imshow(bina_img)
# thresholding removing the straight line next to the image
bina_img2= tray1[:,:,154]<0.15
plt.imshow(bina_img2)
bina_img3= bina_img * bina_img2
plt.imshow(bina_img3)
# Thresholding for removing the shadow
bina_img4= tray1[:,:,52]>0.25
plt.imshow(bina_img4)
plt.show()
bina_img5 = bina_img3 * bina_img4
plt.imshow(bina_img5)
#checking after removing background
bina_img6=tray1[:,:,1] * bina_img5
plt.imshow(bina_img6)
# Remove small objects
img_clean = morphology.remove_small_objects(bina_img5,500)
plt.imshow(img_clean)
# Opening the image to remove small objects
pro=binary_opening(img_clean,selem=None, out=None)
plt.imshow(pro)
# Closing the image to remove small holes
cro=binary_closing(pro,selem=None, out=None)
plt.imshow(cro)
# Remove small objects second time
img_clean2 = morphology.remove_small_objects(cro,500)
plt.imshow(img_clean2)
plt.show ()
# final masking
bina_img7=bina_img5 *img_clean2
plt.imshow(bina_img7)
bina_img7x=bina_img7*tray1[:,:,57]
plt.imshow(bina_img7x)
# stacking images of the whole tray
list=[]
for i in range(235):
    bina_img8 =tray1[:,:,i]
    list.append(bina_img8)
bina_img8=np.stack(list,axis=2)
plt.imshow(bina_img8[:,:,57])
# Compute connected regions in the image; we're going to use this
from skimage import io, img_as_bool, measure, morphology
from skimage.segmentation import clear_border
# remove artifacts connected to image border
cleared = clear_border(bina_img7)
labels = measure.label(bina_img7,background = 0)
# measure objects and turn out the object size
props = measure.regionprops(labels)
fig,ax2=plt.subplots()
ax2.imshow(labels)
props[0]['Centroid'] # centroid of first labelled object
```

```
a=props[0].centroid
print(a)
for prop in props:
    print('Label: {} >> Object centroid:{}'.format (prop.label,prop.centroid))
# on the labeled image labels, regionprops is performed
fig,ax3=plt.subplots()
ax3.imshow(labels)#plot the labeled image on the previous plot
# Draw rectangle around honey regions.
for prop in props:
   minr, minc, maxr, maxc = prop.bbox
   rect = mpatches.Rectangle((minc, minr),
                             maxc - minc,
                             maxr - minr,
                             fill=False,
                             edgecolor='red',
                             linewidth=0.5)
   ax3.add_patch(rect)
for i in props:
    print (i['Centroid'][1],i['Centroid'][0]) # printing the x and y values of t
    plt.plot(i['Centroid'][1],i['Centroid'][0],'+')
plt.tight layout()
```

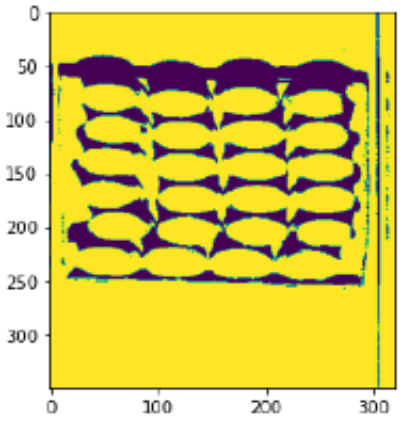

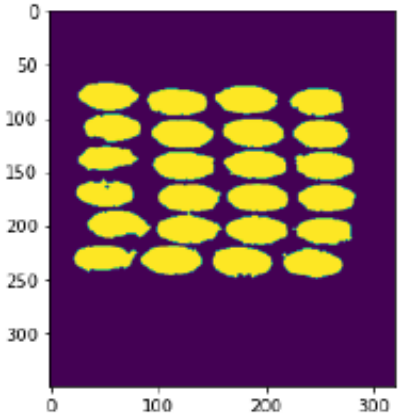

References

Al-Sarayreh, M., Reis, M. M., Yan, W. Q., & Klette, R. (2020). Potential of deep learning and snapshot hyperspectral imaging for classification of species in meat [Article]. *Food Control*, *117*. https://doi.org/10.1016/j.foodcont.2020.107332

Albani, J. R. (2004). In J. R. Albani (Ed.), *Structure and Dynamics of Macromolecules: Absorption and Fluorescence Studies* (pp. 141-192). Elsevier Science. https://doi.org/10.1016/B978-044451449-3/50004-6

Aleixandre-Tudo, J. L., Nieuwoudt, H., Olivieri, A., Aleixandre, J. L., & Du Toit, W. (2018). Phenolic profiling of grapes, fermenting samples and wines using UV-Visible spectroscopy with chemometrics [Article]. *Food Control*, *85*, 11-22. https://doi.org/10.1016/j.foodcont.2017.09.014

Algar, W. R., & Massey, M. (2019). Key Errors to Avoid in the Consideration of Fluorescence Quenching Data [Article]. *Spectroscopy*, *34*(8), 12-15. http://ezproxy.massey.ac.nz/login?url=https://search.ebscohost.com/login.aspx?direct=true&AuthType=ip,cookie,url,uid&db=aph&AN=138307856&site=eds-live&scope=site&authtype=sso&custid=s3027306

Alimova, A., Katz, A., Gottlieb, P., & Alfano, R. R. (2006). Proteins and dipicolinic acid released during heat shock activation of Bacillus subtilis spores probed by optical spectroscopy. *APPLIED OPTICS*, *45(3)*, 445–450. https://doi.org/10.1364/ao.45.000445

Alqarni, A. S., Owayss, A. A., & Mahmoud, A. A. (2016). Physicochemical characteristics, total phenols and pigments of national and international honeys in Saudi Arabia [Article]. *Arabian Journal of Chemistry*, *9*(1), 114-120. https://doi.org/10.1016/j.arabjc.2012.11.013

Alvarez-Suarez, J. M., Gasparrini, M., Forbes-Hernandez, T. Y., Mazzoni, L., & Giampieri, F. (2014). The Composition and Biological Activity of Honey: A Focus on Manuka Honey. *Foods*, *3*(3), 420-432. https://doi.org/10.3390/foods3030420

Amorati, R., Baschieri, A., Valgimigli, L., & Cowden, A. (2017). The antioxidant activity of quercetin in water solution [Article]. *Biomimetics*, *2*(3). https://doi.org/10.3390/biomimetics2030009

Ang, Z., Li, W., Cuiyun, W., Yulin, F., Guomin, H., Hua, L., Zhenwen, Z., & Hua, W. (2013). Simultaneous Determination of 14 Phenolic Compounds in Grape Canes by HPLC-DAD-UV Using Wavelength Switching Detection [article]. *Molecules*, *18*(11), 14241-14257. https://doi.org/10.3390/molecules181114241

Archer, R. (2022). *Plantation project* [Interview].

Arthur, A. M. (2016). *Hyperspectral Imaging*. Arthur,Alasdair Mac. https://media.ed.ac.uk/media/ATSC+2015+Lecture+3+Hyperspectral+Imaging/1_iczjc60u

Awad, M., & Khanna, R. (2015). *Efficient Learning Machines : Theories, Concepts, and Applications for Engineers and System Designers* [Book]. Apress. http://ezproxy.massey.ac.nz/login?url=https://search.ebscohost.com/login.aspx?direct=true&AuthType=ip,cookie,url,uid&db=nlebk&AN=985681&site=eds-live&scope=site&authtype=sso&custid=s3027306

Barnes, R. J., Dhanoa, M. S., & Lister, S. J. . (1989). Standard Normal Variate Transformation and De-Trending of Near-Infrared Diffuse Reflectance Spectra. *Applied Spectroscopy*, *43(5), 772–777*. https://doi.org/10.1366/0003702894202201

Bazar, G., Romvari, R., Szabo, A., Somogyi, T., Eles, V., & Tsenkova, R. (2016). NIR detection of honey adulteration reveals differences in water spectral pattern. *Food Chem*, *194*, 873-880. https://doi.org/10.1016/j.foodchem.2015.08.092

Beechem, J. M., & Brand, L. (1985). Time-resolved fluorescence of proteins. *Ann. Rev. Biochem.*, *54*, 43-71. https://doi.org/10.1146/annurev.bi.54.070185.000355

Beganović, A., Moll, V., & Huck, C. W. (2019). Comparison of Multivariate Regression Models Based on Water- and Carbohydrate-Related Spectral Regions in the Near-Infrared for Aqueous

Solutions of Glucose. *Molecules*, *24*(20), 3696. https://www.mdpi.com/1420-3049/24/20/3696
Betances-Salcedo, E., Revilla, I., Vivar-Quintana, A. M., & Inmaculada Gonzalez-Martin, M. (2017). Flavonoid and Antioxidant Capacity of Propolis Prediction Using Near Infrared Spectroscopy. *17*. https://doi.org/10.3390/s17071647
Bevilacqua, M., Rinnan, Å., & Lund, M. N. (2020). Investigating challenges with scattering and inner filter effects in front-face fluorescence by PARAFAC [Article]. *Journal of Chemometrics*. https://doi.org/10.1002/cem.3286
Bicknell, R., & Jaksons, P. (2018). Floral phenology and floral induction in Leptospermum scoparium [Article]. *New Zealand Journal of Botany*, *56*(4), 372-384. https://doi.org/10.1080/0028825X.2018.1492940
Bobis, O., MĂRghitas, L. A., Dezmirean, D. S., BĂRnułIu, L. I., MĂRgĂOan, R., Gherman, B., & Bonta, V. (2013). The Importance of Melissopalynology in Addition to Physical-Chemical Analysis on Botanical Authenticity Testing of Monofloral Honey. *Bulletin of the University of Agricultural Sciences & Veterinary Medicine Cluj-Napoca. Animal Science & Biotechnologies*, *70*(1), 24-30. http://ezproxy.massey.ac.nz/login?url=http://search.ebscohost.com/login.aspx?direct=true&db=edo&AN=91968977&site=eds-live&scope=site
Bogdanov, S., Ruoff, K., & Persano Oddo, L. (2004). Physico-chemical methods for the characterisation of unifloral honeys: a review. *Apidologie*, *35*(Suppl. 1), S4-S17. https://doi.org/10.1051/apido:2004047
Bong, J., Loomes, K. M., Lin, B., & Stephens, J. M. (2018). New approach: Chemical and fluorescence profiling of NZ honeys [Article]. *Food Chemistry*, *267*, 355-367. https://doi.org/10.1016/j.foodchem.2017.07.065
Bong, J., Loomes, K. M., Schlothauer, R. C., & Stephens, J. M. (2016). Fluorescence markers in some New Zealand honeys [Article]. *Food Chemistry*, *192*, 1006-1014. https://doi.org/10.1016/j.foodchem.2015.07.118
Bong, J., Prijic, G., Braggins, T. J., Schlothauer, R. C., Stephens, J. M., & Loomes, K. M. (2017). Leptosperin is a distinct and detectable fluorophore in Leptospermum honeys. *Food Chemistry*, *214*, 102-109. https://doi.org/10.1016/j.foodchem.2016.07.018
Boydağ, F. Ş., Mamedov, S. V., Alekperov, V. A., & Lenger Özcanli, Y. (2003). Optical characterization of weakly absorbing PP, PE, and PP/PE films. *Optics and Spectroscopy*, *95*(2), 225-229. https://doi.org/10.1134/1.1604429
Bro, R. (1996). Multiway calibration. Multilinear PLS [Article]. *Journal of Chemometrics*, *10*(1), 47-61. https://doi.org/10.1002/(SICI)1099-128X(199601)10:1<47::AID-CEM400>3.0.CO;2-C
Bro, R. (1997). PARAFAC. Tutorial and applications. *Chemometrics and Intelligent Laboratory Systems*, *38*(2), 149-171. https://doi.org/10.1016/S0169-7439(97)00032-4
Bro, R., & Gallagher, N. B. (2022). PARAFAC for Analysis of Fluorescence EEM Data. In E. R. incoporated (Ed.), (pp. 2). Eigenvector Research incoporated.
Bundit, T., Anothai, T., Pattaramart, P., Roongpet, T., & Chuleeporn, S. (2016). Comparison of Antioxidant Contents of Thai Honeys to Manuka Honey. *Malaysian Journal of Nutrition*, *22*(3), 413-420. http://ezproxy.massey.ac.nz/login?url=http://search.ebscohost.com/login.aspx?direct=true&db=ccm&AN=121510688&site=eds-live&scope=site
Burns, D. T., Dillon, A., Warren, J., & Walker, M. J. (2018). A Critical Review of the Factors Available for the Identification and Determination of Mānuka Honey [Original Paper]. *Food Analytical Methods*, *11*(6), 1561. https://doi.org/10.1007/s12161-018-1154-9
Centre for Remote Imaging, S. a. P. (2020). *Digital image*. https://crisp.nus.edu.sg/~research/tutorial/image.htm
Ceresa, L., Kimball, J., Chavez, J., Kitchner, E., Nurekeyev, Z., Doan, H., Borejdo, J., Gryczynski, I., & Gryczynski, Z. (2021). On the origin and correction for inner filter effects in fluorescence. Part II: secondary inner filter effect -the proper use of front-face configuration for highly

absorbing and scattering samples. *Methods and applications in fluorescence*, *9*(3). https://doi.org/10.1088/2050-6120/ac0243

Chan, C. W., Deadman, B. J., Manley-Harris, M., Wilkins, A. L., Alber, D. G., & Harry, E. (2013). Analysis of the flavonoid component of bioactive New Zealand mānuka (Leptospermum scoparium) honey and the isolation, characterisation and synthesis of an unusual pyrrole [Article]. *Food Chemistry*, *141*(3), 1772-1781. https://doi.org/10.1016/j.foodchem.2013.04.092

Chaudhari, s. (2016). Phenyllactic Acid: A Potential Antimicrobial Compound in Lactic acid Bacteria. *Journal of Bacteriology & Mycology Open Access*, *2*(5). https://doi.org/10.15406/jbmoa.2016.02.00037

Chen, S., Yu, Y.-L., & Wang, J.-H. (2018). Inner filter effect-based fluorescent sensing systems: A review [Review Article]. *Analytica Chimica Acta*, *999*, 13-26. https://doi.org/10.1016/j.aca.2017.10.026

Chin, N. L., & Sowndhararajan, K. (2020). *A Review on Analytical Methods for Honey Classification, Identification and Authentication*. https://doi.org/10.5772/intechopen.90232 (IntechOpen)

Clark, J. A., Demetriades-Shah, T. H., & Steven, M. D. (1990). High resolution derivative spectra in remote sensing. https://doi.org/10.1016/0034-4257(90)90055-Q

Claudia, J., & Giovanni Antonio, M. (2018). Methylglyoxal, the Major Antibacterial Factor in Manuka Honey: An Alternative to Preserve Natural Cosmetics? *Cosmetics*(1), 1. https://doi.org/10.3390/cosmetics6010001

Combarros-Fuertes, P., Estevinho, L. M., Teixeira-Santos, R., Rodrigues, A. G., Pina-Vaz, C., Fresno, J. M., & Tornadijo, M. E. (2019). Evaluation of Physiological Effects Induced by Manuka Honey Upon Staphylococcus aureus and Escherichia coli. *Microorganisms*, *7*(8). https://doi.org/10.3390/microorganisms7080258

Creasey, S. (2014). The great manuka honey swindle: lack of clarity around what constitutes a manuka honey has allowed some unscrupulous operators to make millions from the sale of fake manuka. Will new guidelines help put an end to this scandal? , (8161), 40. http://ezproxy.massey.ac.nz/login?url=http://search.ebscohost.com/login.aspx?direct=true&db=edsgsb&AN=edsgsb.A375370015&site=eds-live&scope=site

Daniels, B. J., Prijic, G., Meidinger, S., Loomes, K. M., Stephens, J. M., Schlothauer, R. C., Furkert, D. P., & Brimble, M. A. (2016). Isolation, Structural Elucidation, and Synthesis of Lepteridine From Manuka (Leptospermum scoparium) Honey. *J Agric Food Chem*, *64*(24), 5079-5084. https://doi.org/10.1021/acs.jafc.6b01596

Danila, C., Tamara Yuliett, F.-H., Sadia, A., Massimiliano, G., Patricia, R.-R., Piera Pia, M., Jiaojiao, Z., Leire Bravo, L., Susana Martínez, F., Pablo Agudo, T., José Luis, Q., Francesca, G., & Maurizio, B. (2018). Phenolic Compounds in Honey and Their Associated Health Benefits: A Review [article]. *Molecules*, *23*(9), 2322-2322. https://doi.org/10.3390/molecules23092322

De Ketelaere, B., Wouters, N., Kalfas, I., Van Belleghem, R., & Saeys, W. (2022). A fresh look at computer vision for industrial quality control. *Quality Engineering*, 1-7. https://doi.org/10.1080/08982112.2021.2001828

Deepa, P., & Thilagavathi, K. (2015). *Feature extraction of hyperspectral image using principal component analysis and folded-principal component analysis* 2015 2nd International Conference on Electronics and Communication Systems (ICECS),

Delwiche, S. R., Stommel, J. R., Kim, M. S., Vinyard, B. T., & Esquerre, C. (2019). Hyperspectral fluorescence imaging for shelf life evaluation of fresh-cut Bell and Jalapeno Pepper. *Scientia Horticulturae*, *246*, 749-758. https://doi.org/10.1016/j.scienta.2018.11.061

Dertat, A. (2017). *Applied Deep Learning-Part 4: Convolutional Neural Networks*. towards data science. https://towardsdatascience.com/applied-deep-learning-part-4-convolutional-neural-networks-584bc134c1e2

Dettori, A., Tappi, S., Piana, L., Dalla Rosa, M., & Rocculi, P. (2018). Kinetic of induced honey crystallization and related evolution of structural and physical properties [Article]. *LWT*, *95*, 333-338. https://doi.org/10.1016/j.lwt.2018.04.092

Dinç, E., Ertekin, Z. C., & Büker, E. (2017). Multiway analysis methods applied to the fluorescence excitation-emission dataset for the simultaneous quantification of valsartan and amlodipine in tablets [Article]. *Spectrochimica Acta Part A: Molecular and Biomolecular Spectroscopy*, *184*, 255-261. https://doi.org/10.1016/j.saa.2017.04.081

Dinkov, D. (2015). Quantitative melissopalynological analysis of bee honey using a bürker chamber [Article]. *International Food Research Journal*, *22*(4), 1538-1543. http://ezproxy.massey.ac.nz/login?url=http://search.ebscohost.com/login.aspx?direct=true&db=edselc&AN=edselc.2-52.0-84940208345&site=eds-live&scope=site

Dominguez, H. (2013). *Functional Ingredients From Algae for Foods and Nutraceuticals* [Book]. Woodhead Publishing. http://ezproxy.massey.ac.nz/login?url=http://search.ebscohost.com/login.aspx?direct=true&db=nlebk&AN=675921&site=eds-live&scope=site

Dramicanin, T., Ackovic, L. L., Zekovic, I., & Dramicaninn, M. D. (2018). Detection of Adulterated Honey by Fluorescence Excitation-Emission Matrices. https://doi.org/10.1155/2018/8395212

Elvira, M., Silvia, W., Gerold, B., & Thomas, H. (2008). Identification and quantification of methylglyoxal as the dominant antibacterial constituent of Manuka (Leptospermum scoparium) honeys from New Zealand. *Molecular Nutrition & Food Research*(4), 483. https://doi.org/10.1002/mnfr.200700282

Engelen, S., & Hubert, M. (2011). Detecting outlying samples in a parallel factor analysis model. *Analytica Chimica Acta*, *705*(1), 155-165. https://doi.org/10.1016/j.aca.2011.04.043

Engelen, S., Møller, S. F., & Hubert, M. (2007). Automatically identifying scatter in fluorescence data using robust techniques. *Chemometrics and Intelligent Laboratory Systems*, *86*(1), 35-51. https://doi.org/10.1016/j.chemolab.2006.08.001

Faber, N. M. (2015). Views on Multiway Calibration: Its Past and Future [Book Chapter]. *Data Handling in Science and Technology*, *29*, 1-5. https://doi.org/10.1016/B978-0-444-63527-3.00014-X

Faber, N. M., & Bro, R. (2002). Standard error of prediction for multiway PLS: 1. Background and a simulation study [Article]. *Chemometrics and Intelligent Laboratory Systems*, *61*(1), 133-149. https://doi.org/10.1016/S0169-7439(01)00204-0

Farrés, M., Platikanov, S., Tauler, R., & Tsakovski, S. (2015). Comparison of the variable importance in projection (VIP) and of the selectivity ratio (SR) methods for variable selection and interpretation [Article]. *Journal of Chemometrics*, *29*(10), 528-536. https://doi.org/10.1002/cem.2736

Fauzi, N., Farid, M., & Silva, F. (2014). High-Pressure Processing of Manuka Honey: Improvement of Antioxidant Activity, Preservation of Colour and Flow Behaviour [Article]. *Food & Bioprocess Technology*, *7*(8), 2299-2307. https://doi.org/10.1007/s11947-013-1204-7

Fearnley, L., Greenwood, D. R., Schmitz, M., Stephens, J. M., Schlothauer, R. C., & Loomes, K. M. (2012). Compositional analysis of manuka honeys by high-resolution mass spectrometry: Identification of a manuka-enriched archetypal molecule. *132*, 948-953. https://doi.org/10.1016/j.foodchem.2011.11.074

Flenley, J. (2013, 2022). About The Classifynder. https://www.veritaxa.com/wp-content/uploads/2014/09/classifynder_news_may2013-2-0.pdf

Fonin, A. V., Sulatskaya, A. I., Kuznetsova, I. M., & Turoverov, K. K. (2014). Fluorescence of Dyes in Solutions with High Absorbance. Inner Filter Effect Correction [Article]. *PLoS ONE*, *9*(7), 1-8. https://doi.org/10.1371/journal.pone.0103878

Frosch, S., Engelen, S., & Jørgensen, B. M. (2009). A fully robust PARAFAC method for analyzing fluorescence data [Article]. *Journal of Chemometrics*, *23*(3), 124-131. https://doi.org/10.1002/cem.1208

Gallagher, N. B. (2021). Savitzky Golay smoothing and differentiation filter. In *Eigenvector Research Incoporated*.

Gan, Z., Yang, Y., Li, J., Wen, X., Zhu, M., Jiang, Y., & Ni, Y. (2016). Using sensor and spectral analysis to classify botanical origin and determine adulteration of raw honey. *Journal of Food Engineering*, *178*, 151-158. https://doi.org/10.1016/j.jfoodeng.2016.01.016

Gannabathula, S., Skinner, M. A., Rosendale, D., Greenwood, J. M., Mutukumira, A. N., Steinhorn, G., Stephens, J., Krissansen, G. W., & Schlothauer, R. C. (2012). Arabinogalactan proteins contribute to the immunostimulatory properties of New Zealand honeys. *Immunopharmacol Immunotoxicol*, *34*(4), 598-607. https://doi.org/10.3109/08923973.2011.641974

Georgescu, M., Dobrea, M., & Dobrea, V. C. (2017). Antimicrobial effect of commercial Manuka honey and conventional local honey against gram-negative and gram-positive bacteria. *Scientific Works. Series C, Veterinary Medicine*, *63*(2), 133-136. http://ezproxy.massey.ac.nz/login?url=http://search.ebscohost.com/login.aspx?direct=true&db=aph&AN=128947818&site=eds-live&scope=site

Gerard, H. (2016). Manuka honey's golden future. *Nelson Mail*, 12. http://ezproxy.massey.ac.nz/login?url=http://search.ebscohost.com/login.aspx?direct=true&db=anh&AN=NEM160119001211109153 19-CD&site=eds-live&scope=site

Gerard, H. (2018). Partnership develops manuka plantations. 18. http://ezproxy.massey.ac.nz/login?url=http://search.ebscohost.com/login.aspx?direct=true&db=anh&AN=NEM181128001811466804 15-BV&site=eds-live&scope=site

Ghent, U. (Ed.). (2016). *Food chemistry handbook*. Ghent University.

Golic, M., Walsh, K., & Lawson, P. . (2003). Short-Wavelength Near-Infrared Spectra of Sucrose, Glucose, and Fructose with Respect to Sugar Concentration and Temperature. *Applied Spectroscopy, 57(2),*, 139–145. https://doi.org/10.1366/000370203321535033

Goss, C. H. A. (2009). *Indicators of Bioactivity and Floral Origin of New Zealand Honeys* The University of Waikato]. Hamilton, New Zealand.

Grainger, M. N. C., Manley-Harris, M., Fauzi, N. A. M., & Farid, M. M. (2014). Effect of high pressure processing on the conversion of dihydroxyacetone to methylglyoxal in New Zealand mānuka (Leptospermum scoparium) honey and models thereof [Article]. *Food Chemistry*, *153*, 134-139. https://doi.org/10.1016/j.foodchem.2013.12.017

Grainger, M. N. C., Manley-Harris, M., Lane, J. R., & Field, R. J. (2016a). Kinetics of conversion of dihydroxyacetone to methylglyoxal in New Zealand ma¯nuka honey: Part i - Honey systems [Article]. *Food Chemistry*, *202*, 484-491. https://doi.org/10.1016/j.foodchem.2016.02.029

Grainger, M. N. C., Manley-Harris, M., Lane, J. R., & Field, R. J. (2016b). Kinetics of the conversion of dihydroxyacetone to methylglyoxal in New Zealand ma¯nuka honey: Part II - Model systems [Article]. *Food Chemistry*, *202*, 492-499. https://doi.org/10.1016/j.foodchem.2016.02.030

Grainger, M. N. C., Owens, A., Manley-Harris, M., Lane, J. R., & Field, R. J. (2017). Kinetics of conversion of dihydroxyacetone to methylglyoxal in New Zealand mānuka honey: Part IV – Formation of HMF [Article]. *Food Chemistry*, *232*, 648-655. https://doi.org/10.1016/j.foodchem.2017.04.066

Gregory, H., & Nicholas, J. (2020). *Imaging Fundamentals*. Edmundoptics. https://www.edmundoptics.com/knowledge-center/application-notes/imaging/6-fundamental-parameters-of-an-imaging-system/

Guzelmeric, E., Ciftci, I., Yuksel, P. I., & Yesilada, E. (2020). Importance of chromatographic and spectrophotometric methods in determining authenticity, classification and bioactivity of honey [Article]. *LWT*, *132*. https://doi.org/10.1016/j.lwt.2020.109921

Hadi, A. S., Imon, A. H. M. R., & Werner, M. (2009). Detection of outliers. *WIREs Computational Statistics*, *1*(1), 57-70. https://doi.org/10.1002/wics.6

Hassoun, A., Sahar, A., Lakhal, L., & Aït-Kaddour, A. (2019). Fluorescence spectroscopy as a rapid and non-destructive method for monitoring quality and authenticity of fish and meat products: Impact of different preservation conditions [Review Article]. *LWT*, *103*, 279-292. https://doi.org/10.1016/j.lwt.2019.01.021

Hellwig, M., Rueckriemen, J., Sandner, D., & Henle, T. (2017). Unique Pattern of Protein-Bound Maillard Reaction Products in Manuka (Leptospermum scoparium) Honey. In (Vol. 65, pp. 3532-3540).

Huang, S., Wang, Y., Tang, J., & Dai, J. (2019). Signal status recognition based on 1DCNN and its feature extraction mechanism analysis [Article]. *Sensors (Switzerland)*, *19*(9). https://doi.org/10.3390/s19092018

Inoue, K., Murayarna, S., Seshimo, F., Takeba, K., Yoshimura, Y., & Nakazawa, H. (2005). Identification of phenolic compound in manuka honey as specific superoxide anion radical scavenger using electron spin resonance (ESR) and liquid chromatography with coulometric array detection. *85*, 872-878. https://doi.org/10.1002/jsfa.1952

Ishisaka, A., Ikushiro, S., Takeuchi, M., Araki, Y., Juri, M., Yoshiki, Y., Kawai, Y., Niwa, T., Kitamoto, N., Sakaki, T., Ishikawa, H., & Kato, Y. (2017). In vivo absorption and metabolism of leptosperin and methyl syringate, abundantly present in manuka honey. *61*. https://doi.org/10.1002/mnfr.201700122

Iwamoto, R. (2010). Infrared and Near-Infrared Study of the Interaction of Amide C═O with Water in Ideally Inert Medium. *J. Phys. Chem. A*, *114*(27), 7398–7407. https://doi.org/10.1021/jp102479t

Jeong, J. (2019). *The Most Intuitive and Easiest Guide for Convolutional Neural Network*. towardsdatascience. https://towardsdatascience.com/the-most-intuitive-and-easiest-guide-for-convolutional-neural-network-3607be47480

Jiang, Y., Li, C., & Takeda, F. (2016). Nondestructive Detection and Quantification of Blueberry Bruising using Near-infrared (NIR) Hyperspectral Reflectance Imaging. *Sci Rep*, *6*, 35679. https://doi.org/10.1038/srep35679

Johnston, M., McBride, M., Dahiya, D., Owusu-Apenten, R., & Nigam, P. S. (2018). Antibacterial activity of Manuka honey and its components: An overview [article]. *AIMS Microbiology*(4), 655. https://doi.org/10.3934/microbiol.2018.4.655

Juraj, M. (2011). Methylglyoxal—A Potential Risk Factor of Manuka Honey in Healing of Diabetic Ulcers [article]. *Evidence-Based Complementary and Alternative Medicine*. https://doi.org/10.1093/ecam/neq013

Kao, S., Asanov, A., & Oldham, P. (1998). A Comparison of Fluorescence Inner-Filter Effects for Different Cell Configurations. *Instrumentation Science & Technology*, *26*(4), 375-387. https://doi.org/10.1080/10739149808001906

Karoui, R., & Blecker, C. (2011). Fluorescence Spectroscopy Measurement for Quality Assessment of Food Systems—a Review [Review Paper]. *Food and Bioprocess Technology: An International Journal*, *4*(3), 364. https://doi.org/10.1007/s11947-010-0370-0

Kimball, J., Chavez, J., Ceresa, L., Kitchner, E., Nurekeyev, Z., Doan, H., Gryczynski, Z., Szabelski, M., Borejdo, J., Gryczynski, I., & Gryczynski, Z. (2020). On the origin and correction for inner filter effects in fluorescence Part I: Primary inner filter effect-the proper approach for sample absorbance correction [Article]. *Methods and applications in fluorescence*, *8*(3). https://doi.org/10.1088/2050-6120/ab947c

Kohonen, J., Reinikainen, S.-P., Aaljoki, K., Perkiö, A., Väänänen, T., & Höskuldsson, A. (2008). Multi-block methods in multivariate process control. *Journal of Chemometrics*, *22*(3-4), 281-287. https://doi.org/10.1002/cem.1120

Kretavičius, J., Račys, J., Čeksteryte, V., & Kurtinaitiene, B. (2010). Inactivation of glucose oxidase during heat-treatment de-crystallization of honey [Article]. *Zemdirbyste*, *97*(4), 115-122. http://ezproxy.massey.ac.nz/login?url=http://search.ebscohost.com/login.aspx?direct=true&db=edselc&AN=edselc.2-52.0-78751506164&site=eds-live&scope=site

Kruppa, B., & Strube, G. (1994). *Light Scattering. In: Mayinger F. (eds) Optical Measurements*. Springer. https://doi.org/10.1007/978-3-662-02967-1_9

Krzysztof, B. B., & Christian, W. H. (2019). Breakthrough Potential in Near-Infrared Spectroscopy: Spectra Simulation. A Review of Recent Developments [article]. *Frontiers in Chemistry*, *7*. https://doi.org/10.3389/fchem.2019.00048

Kumar Panigrahi, S., & Kumar Mishra, A. (2019). Inner filter effect in fluorescence spectroscopy: As a problem and as a solution [Review]. *Journal of Photochemistry and Photobiology C: Photochemistry Reviews*, *41*. https://doi.org/10.1016/j.jphotochemrev.2019.100318

Kwakman, P. H. S., te Velde, A. A., de Boer, L., Vandenbroucke-Grauls, C. M. J. E., & Zaat, S. A. J. (2011). Two Major Medicinal Honeys Have Different Mechanisms of Bactericidal Activity [Article]. *PLoS ONE*, *6*(3), 1-7. https://doi.org/10.1371/journal.pone.0017709

Kwon, S. J. (2011). *Artificial Neural Networks* [Book]. Nova Science Publishers, Inc. http://ezproxy.massey.ac.nz/login?url=http://search.ebscohost.com/login.aspx?direct=true&db=nlebk&AN=439593&site=eds-live&scope=site

Lakowicz, J. R. (2006). *Principles of fluorescence spectroscopy* (3rd ed.). Springer. http://ezproxy.massey.ac.nz/login?url=http://search.ebscohost.com/login.aspx?direct=true&db=cat00245a&AN=massey.b1894310&site=eds-live&scope=site

Larkin, P. (2018). *Infrared and Raman spectroscopy : principles and spectral interpretation* (Second edition ed.). Elsevier. http://ezproxy.massey.ac.nz/login?url=http://search.ebscohost.com/login.aspx?direct=true&db=cat00245a&AN=massey.b3998407&site=eds-live&scope=site

Latchoumane, L., Alary, K., Minier, J., Davrieux, F., Lugan, R., Chillet, M., & Roger, J.-M. (2022). Front-Face Fluorescence Spectroscopy and Feature Selection for Fruit Classification Based on N-CovSel Method [Original Research]. *Frontiers in Analytical Science*, *2*. https://doi.org/10.3389/frans.2022.867527

Lenhardt, L., Bro, R., Zeković, I., Dramićanin, T., & Dramićanin, M. D. (2015). Fluorescence spectroscopy coupled with PARAFAC and PLS DA for characterization and classification of honey [Article]. *Food Chemistry*, *175*, 284-291. https://doi.org/10.1016/j.foodchem.2014.11.162

Lewis, R. D., Tom, A. R., Ginny, M., John, M. W., & Jan-Peter, M. (2013). Fluorescence characterization of clinically-important bacteria [article]. *PLoS ONE*, *8*(9), e75270-e75270. https://doi.org/10.1371/journal.pone.0075270

Li, X., Prebble, J. G., de Lange, P. J., Raine, J. I., & Newstrom-Lloyd, L. (2022). Discrimination of pollen of New Zealand mānuka (Leptospermum scoparium agg.) and kānuka (Kunzea spp.) (Myrtaceae) [Article]. *PLoS ONE*, *17*(6), 1-24. https://doi.org/10.1371/journal.pone.0269361

Lin, B., Brimble, M. A., Bong, J., Stephens, J. M., Loomes, K. M., Middleditch, M. J., Daniels, B. J., & Furkert, D. P. (2020). Utility of the Leptospermum scoparium Compound Lepteridine as a Chemical Marker for Manuka Honey Authenticity [Article]. *ACS Omega*, *5*(15), 8858-8866. https://doi.org/10.1021/acsomega.0c00486

Lin, B., Loomes, K. M., Prijic, G., Schlothauer, R., & Stephens, J. M. (2017). Lepteridine as a unique fluorescent marker for the authentication of manuka honey. *Food Chemistry*, *225*, 175-180. https://doi.org/10.1016/j.foodchem.2016.12.099

Liu, L., Pilles, B. M., Reiner, A. M., Gontcharov, J., & Zinth, W. (2015). 2'-Methoxyacetophenone: An Efficient Photosensitizer for Cyclobutane Pyrimidine Dimer Formation. *ChemPhysChem*, *16*(16), 3483-3487. https://doi.org/10.1002/cphc.201500582

López, F. (2022). SHAP: Shapley Additive Explanations. *Towards Data Science*. https://towardsdatascience.com/shap-shapley-additive-explanations-5a2a271ed9c3

Lu, Y., Saeys, W., Kim, M., Peng, Y., & Lu, R. (2020). Hyperspectral imaging technology for quality and safety evaluation of horticultural products: A review and celebration of the past 20-year progress [Review Article]. *Postharvest Biology and Technology*, *170*. https://doi.org/10.1016/j.postharvbio.2020.111318

Luciani, X., Redon, R., & Mounier, S. (2013). How to correct inner filter effects altering 3D fluorescence spectra by using a mirrored cell [Article]. *Chemometrics and Intelligent Laboratory Systems*, *126*, 91-99. https://doi.org/10.1016/j.chemolab.2013.04.014

Lucília Carolina Vardenski, C., Elaine, K., Marise Bonifácio, Q., Mareci Mendes de, A., Ernesto, Q., & Leda Battestin, Q. (2015). Influence of temperature and homogenization on honey crystallization [article]. *Brazilian Journal of Food Technology*(2), 155. https://doi.org/10.1590/1981-6723.7314

Mashhadi, A., Bavali, A., & Mokhtari, F. (2022). Assay of honey freshness by a novel optical technique. *Scientific Reports*, *12*(1), 901. https://doi.org/10.1038/s41598-022-04920-w

McDonald, C. M., Keeling, S. E., Brewer, M. J., & Hathaway, S. C. (2018). Using chemical and DNA marker analysis to authenticate a high-value food, manuka honey. *npj Science of Food*, *2*(1). https://doi.org/10.1038/s41538-018-0016-6

Mildenhall, D. C., & Tremain, R. (2005). *Pollen analysis of New Zealand honey*. Institute of Geological and Nuclear Sciences. http://ezproxy.massey.ac.nz/login?url=http://search.ebscohost.com/login.aspx?direct=true&db=cat00245a&AN=massey.b1830937&site=eds-live&scope=site

Minaei, S., Shafiee, S., Polder, G., Moghadam-Charkari, N., van Ruth, S., Barzegar, M., Zahiri, J., Alewijn, M., & Kuś, P. M. (2017). VIS/NIR imaging application for honey floral origin determination [Article]. *Infrared Physics and Technology*, *86*, 218-225. https://doi.org/10.1016/j.infrared.2017.09.001

Ministry for Primary Industries. (2020). *2020 Apiculture Monitoring Programme*.

Mishra, P., Roger, J.-M., Jouan-Rimbaud-Bouveresse, D., Biancolillo, A., Marini, F., Nordon, A., & Rutledge, D. N. (2021). Recent trends in multi-block data analysis in chemometrics for multi-source data integration. *TrAC Trends in Analytical Chemistry*, *137*. https://doi.org/10.1016/j.trac.2021.116206

Moar, N. T. (1985). Pollen analysis of New Zealand honey [Article]. *New Zealand Journal of Agricultural Research*, *28*(1), 39-70. https://doi.org/10.1080/00288233.1985.10426997

Moller, M., & Denicola, A. (2002). Protein tryptophan accessibility studied by fluorescence quenching. *30*, 175-178. https://doi.org/10.1002/bmb.2002.494030030035

Motta, D., Santos, A. Á. B., Machado, B. A. S., Ribeiro-Filho, O. G. V., Camargo, L. O. A., Valdenegro-Toro, M. A., Kirchner, F., & Badaró, R. (2020). Optimization of convolutional neural network hyperparameters for automatic classification of adult mosquitoes. *PLoS ONE*, *15*(7), 1-30. https://doi.org/10.1371/journal.pone.0234959

MPI. (2017a). *Determination of Four Chemical Characterisation Compounds in Honey by Liquid Chromatography Tandem Mass Spectrometry (LC-MS/MS)*. (ISBN No: 978-1-77665-435-2). Chemistry Laboratory Method: MPI Technical – Paper No: 2017/30

MPI. (2017b). *Response to submissions on MPI's proposed definition for mānuka honey*. Ministry for Primary Industries. http://search.ebscohost.com/login.aspx?direct=true&db=cat00245a&AN=massey.b4193865&site=eds-live&scope=site

Murdoch, W. J., Singh, C., Kumbier, K., Abbasi-Asl, R., & Yu, B. (2019). Interpretable machine learning: definitions, methods, and applications [Working Paper]. https://doi.org/10.1073/pnas.1900654116

Murphy, K. R., Stedmon, C. A., Graeber, D., & Bro, R. (2013). Fluorescence spectroscopy and multi-way techniques. PARAFAC. *5*, 6557-6566. https://doi.org/10.1039/c3ay41160e

myFarm. (2022). *Waimarie Manuka Limited Partnership*. https://www.myfarm.co.nz/opportunity/waimarie-manuka-limited-partnership

Naes, T., Isaksson, T., Fearn, T., & Davies, T. (2004). *A User-friendly Guide to Multivariate Calibration and Classification*. NIR Publications.

Nagao, A., Ono, H., Kotake-Nara, E., Kobayashi, M., Tomita, T., & Maoka, T. (2015). A 3-hydroxy β-end group in xanthophylls is preferentially oxidized to a 3-oxo ε-end group in mammals [Article]. *Journal of Lipid Research*, *56*(2), 449-462. https://doi.org/10.1194/jlr.P055459

Negueruela, A. I., & Perez-Arquillue, C. (2000). Color measurement of rosemary honey in the solid state by reflectance spectroscopy with black background [Article]. *Journal of AOAC International*, *83*(3), 669-674. https://doi.org/10.1093/jaoac/83.3.669

News, F. W. (2019). Manuka Honey Market Growth to be Influenced by Rising Demand From Food Industries, & Increasing Usage for Medicinal Purposes by 2023:Radiant Insights, Inc. *Food Weekly News*, 182. http://ezproxy.massey.ac.nz/login?url=http://search.ebscohost.com/login.aspx?direct=true&db=edsghw&AN=edsgcl.585172092&site=eds-live&scope=site

Newswire, P. R. (2019). *Global Honey Industry*. http://ezproxy.massey.ac.nz/login?url=http://search.ebscohost.com/login.aspx?direct=true&db=bwh&AN=201902051712PR.NEWS.USPR.SP44338&site=eds-live&scope=site

Nguyen, B.-C., & Kochevar, I. E. (2003). Influence of Hydration on Dihydroxyacetone-Induced Pigmentation of Stratum Corneum [Article]. *Journal of Investigative Dermatology*, *120*(4), 655-661. https://doi.org/10.1046/j.1523-1747.2003.12089.x

Nickless, E. M. (2015). *Influential factors in nectar composition and yield in Leptospermum scoparium* Massey University, Palmerston North, New Zealand]. cat00245a. http://ezproxy.massey.ac.nz/login?url=http://search.ebscohost.com/login.aspx?direct=true&db=cat00245a&AN=massey.b3742005&site=eds-live&scope=site

Nilsson, J., De Jong, S., & Smilde, A. K. (1997). Multiway calibration in 3D QSAR [Article]. *Journal of Chemometrics*, *11*(6), 511-524. https://doi.org/10.1002/(SICI)1099-128X(199711/12)11:6<511::AID-CEM488>3.0.CO;2-W

Noviyanto, A., & Abdulla, W. H. (2020). Honey botanical origin classification using hyperspectral imaging and machine learning [Article]. *Journal of Food Engineering*, *265*. https://doi.org/10.1016/j.jfoodeng.2019.109684

Oelschlaegel, S., Graner, M., Pang-Ning, W., Boettcher, A., Koelling-Speer, I., & Speer, K. (2012). Classification and Characterization of Manuka Honeys Based on Phenolic Compounds and Methylglyoxal. *Journal of Agricultural & Food Chemistry*, *60*(29), 7229. https://doi.org/10.1021/jf300888q

Ohtani, K., Fujioka, S., Shimada, A., & Kimura, Y. (2011). Nematicidal Activities of 4-Hydroxyphenylacetic Acid and Oidiolactone D Produced by the Fungus Oidiodendron sp. *Zeitschrift für Naturforschung C*, *66*(1-2), 31-34. https://doi.org/doi:10.1515/znc-2011-1-205

Oroian, M., Ropciuc, S., & Paduret, S. (2017). Honey Adulteration Detection Using Raman Spectroscopy. *Food Analytical Methods*, *11*(4), 959-968. https://doi.org/10.1007/s12161-017-1072-2

Owens, A., Lane, J. R., Manley-Harris, M., Marie Jensen, A., & Jørgensen, S. (2019). Kinetics of conversion of dihydroxyacetone to methylglyoxal in New Zealand mānuka honey: Part V – The rate determining step [Article]. *Food Chemistry*, *276*, 636-642. https://doi.org/10.1016/j.foodchem.2018.10.039

Pascual-Mate, A., Oses, S. M., Fernandez-Muino, M. A., & Teresa Sancho, M. (2018). Methods of analysis of honey. *57*, 38-74. https://doi.org/10.1080/00218839.2017.1411178

Patel, S., & Cichello, S. (2013). Manuka honey: an emerging natural food with medicinal use [Review Paper]. *Natural Products and Bioprospecting*(4), 121. https://doi.org/10.1007/s13659-013-0018-7

Patrício, D. I., & Rieder, R. (2018). Computer vision and artificial intelligence in precision agriculture for grain crops: A systematic review. *Computers and Electronics in Agriculture*, *153*, 69-81. https://doi.org/10.1016/j.compag.2018.08.001

Pedersen, B., Bailey, D. G., Hodgson, R. M., Marsland, S., & Holt, K. (2018, 2018 / 07 / 03 /). Model and feature selection for the classification of dark field pollen images using the classifynder system.

Pedrós, R., Moya, I., Goulas, Y., & Jacquemoud, S. (2008). Chlorophyll fluorescence emission spectrum inside a leaf [Article]. *Photochemical and Photobiological Sciences*, *7*(4), 498-502. https://doi.org/10.1039/b719506k

Pu, Y.-Y., O'Donnell, C., Tobin, J. T., & O'Shea, N. (2020). Review of near-infrared spectroscopy as a process analytical technology for real-time product monitoring in dairy processing [Review Article]. *International Dairy Journal*, *103*. https://doi.org/10.1016/j.idairyj.2019.104623

PubChem. (2022). National Library of Medicine.

Pullanagari, R. R., Dehghan-Shoar, M., Yule, I. J., & Bhatia, N. (2021). Field spectroscopy of canopy nitrogen concentration in temperate grasslands using a convolutional neural network [Article]. *Remote Sensing of Environment*, *257*. https://doi.org/10.1016/j.rse.2021.112353

Qin, J. (2010). *Hyperspectral Imaging Instruments* (S. Da-Wen, Ed.). Elsevier.

Roberts, A. E. L., Brown, H. L., & Jenkins, R. E. (2015). On the antibacterial effects of manuka honey: mechanistic insights [article]. *Research and Reports in Biology*(default), 215. https://doi.org/10.2147/RRB.S75754

Rosendale, D. I. (2009). *Anitmicrobial activity of functional food ingredients focusing on manuka honey action against Escherichia coli : a thesis presented in partial fulfilment of the requirements for the degree of Doctor of Philosophy in Engineering and Technology at Massey University, Auckland, New Zealand* cat00245a.

Rueckriemen, J., & Henle, T. (2018). Pilot study on the discrimination of commercial Leptospermum honeys from New Zealand and Australia by HPLC-MS/MS analysis. *244*, 1203-1209. https://doi.org/10.1007/s00217-018-3036-1

Rueckriemen, J., Schwarzenbolz, U., Adam, S., & Henle, T. (2015). Identification and Quantitation of 2-Acetyl-1-pyrroline in Manuka Honey (Leptospermum scoparium). *63*, 8488-8492. https://doi.org/10.1021/acs.jafc.5b03042

Ruiz-Matute, A., Soria, A. C., Martinez-Castro, I., & Sanz, M. L. (2007). A New Methodology Based on GC−MS To Detect Honey Adulteration with Commercial Syrups. *Journal of Agricultural and Food Chemistry*, *55, 7264−7269*(Elsevier Ltd). https://doi.org/10.1021/jf070559j (AMER CHEMICAL SOC)

Ruoff, K., Luginbühl, W., Bogdanov, S., Bosset, J. O., Estermann, B., Ziolko, T., & Amadò, R. (2006). Authentication of the botanical origin of honey by near-infrared spectroscopy. *Journal of Agricultural and Food Chemistry*, *54*(18), 6867-6872. https://doi.org/10.1021/jf060770f

Ruoff, K., Luginbühl, W., Bogdanov, S., Bosset, J. O., Künzli, R., Amadò, R., Von Der Ohe, K., & Von Der Ohe, W. (2006). Authentication of the botanical and geographical origin of honey by front-face fluorescence spectroscopy. *Journal of Agricultural and Food Chemistry*, *54*(18), 6858-6866. https://doi.org/10.1021/jf060697t

Saeys, W. (2006). *Technical Tools for the Optimal Use of Animal Manure as a Fertiliser. On-line composition measurement and manure injection control* KU Leuven]. KU Leuven.

Saeys, W. (2018). Chemometrics. In K. Leuven (Ed.), (Course material ed.). Division of Mechatronics, Biostatistics and Sensors, KU Leuven.

Saeys, W., Nguyen Do Trong, N., Van Beers, R., & Nicolaï, B. M. (2019). Multivariate calibration of spectroscopic sensors for postharvest quality evaluation: A review [Review Article]. *Postharvest Biology and Technology*, *158*. https://doi.org/10.1016/j.postharvbio.2019.110981

Saeys, W., Xing, J., De Baerdemaeker, J., & Ramon, H. (2005). Comparison of transflectance and reflectance to analyse hog manures [Article]. *Journal of Near Infrared Spectroscopy*, *13*(2), 99-107. https://doi.org/10.1255/jnirs.462

Schols, R. M., Connell, N. J., & Stassen, L. P. (2015). Near-infrared fluorescence imaging for real-time intraoperative anatomical guidance in minimally invasive surgery: a systematic review of the literature. *World J Surg*, *39*(5), 1069-1079. https://doi.org/10.1007/s00268-014-2911-6

Schweiger, J., Lang, M., & Lichtenthaler, H. K. (1996). Differences in fluorescence excitation spectra of leaves between stressed and non-stressed plants [Article]. *Journal of Plant Physiology*, *148*(5), 536-547. https://doi.org/10.1016/S0176-1617(96)80073-3

Shafiee, S., Polder, G., Minaei, S., Moghadam-Charkari, N., Van Ruth, S., & Kuś, P. M. (2016). Detection of Honey Adulteration using Hyperspectral Imaging. *IFAC-PapersOnLine*, *49-16 (2016) 311–314*. https://doi.org/10.1016/j.ifacol.2016.10.057 (Elsevier Ltd.)

Shaikh, S., & O'Donnell, C. (2017). Applications of fluorescence spectroscopy in dairy processing: a review [Review Article]. *Current Opinion in Food Science*, *17*, 16-24. https://doi.org/10.1016/j.cofs.2017.08.004

Shalev-Shwartz, S., & Ben-David, S. (2014). *Understanding Machine Learning: From Theory to Algorithms*. Cambridge University Press.

Shen, Z., & Viscarra Rossel, R. A. (2021). Automated spectroscopic modelling with optimised convolutional neural networks. *Scientific Reports*, *11*(1). https://doi.org/10.1038/s41598-020-80486-9

Smallfield, B. M., Joyce, N. I., & van Klink, J. W. (2018). Developmental and compositional changes in Leptospermum scoparium nectar and their relevance to mānuka honey bioactives and markers* [Article]. *New Zealand Journal of Botany*, *56*(2), 183-197. https://doi.org/10.1080/0028825X.2018.1446450

Smeesters, L., Meulebroeck, W., Raeymaekers, S., & Thienpont, H. (2015). Optical detection of aflatoxins in maize using one- and two-photon induced fluorescence spectroscopy. *Food Control*, *51*, 408-416. https://doi.org/10.1016/j.foodcont.2014.12.003

Smith, C. B. (2017). *The Carbonyl Group, Part I: Introduction*. Spectroscopy. https://www.spectroscopyonline.com/view/carbonyl-group-part-i-introduction

Snow, M. J., & Manley-Harris, M. (2004). On the nature of non-peroxide antibacterial activity in New Zealand manuka honey [Article]. *Food Chemistry*, *84*(1), 145-147. https://doi.org/10.1016/S0308-8146(03)00258-9

Soni, A., Al-Sarayreh, M., Reis, M. M., & Brightwell, G. (2021). Hyperspectral imaging and deep learning for quantification of Clostridium sporogenes spores in food products using 1D-convolutional neural networks and random forest model. *Food Research International*, *147*. https://doi.org/10.1016/j.foodres.2021.110577

Sontag, D. (2020). *Support Vector Machines (SVMs)*. New York University. http://people.csail.mit.edu/dsontag/courses/ml14/slides/lecture2.pdf

SpectraBase. (2022). *4-Hydroxy-benzoic acid*. https://spectrabase.com/spectrum/JMvFXRaCjLq

Staffelbach, T. A., Orlando, J. J., Tyndall, G. S., & Calvert, J. G. (1995). The UV-visible absorption spectrum and photolysis quantum yields of methylglyoxal. *Journal of geophysical research:atmospheres*, *100*(D7), 14189-14198. https://doi.org/10.1029/95JD00541

Stephens, J. M. C. (2006). *The factors responsible for the varying levels of UMF®in mānuka (Leptospermum scoparium) honey* Waikato]. The University of Waikato, Hamilton, New Zealand.

Stephens, J. M. C., Loomes, K. M., Braggins, T. J., Bong, J., Lin, B., & Prijic, G. (2017). Fluorescence: A Novel Method for Determining Manuka Honey Floral Purity. In *Honey Analysis*. https://doi.org/10.5772/66313

Stephens, J. M. C., Molan, P. C., & Clarkson, B. D. (2005). A review of Leptospermum scoparium (Myrtaceae) in New Zealand. *New Zealand Journal of Botany*, *43*(2), 431-449. https://doi.org/10.1080/0028825X.2005.9512966

Stephens, J. M. C., Schlothauer, R. C., Morris, B. D., Yang, D., Fearnley, L., Greenwood, D. R., & Loomes, K. M. (2010). Phenolic compounds and methylglyoxal in some New Zealand manuka

and kanuka honeys [Article]. *Food Chemistry*, *120*(1), 78-86. https://doi.org/10.1016/j.foodchem.2009.09.074
Su, J., Yi, D., Liu, C., Guo, L., & Chen, W.-H. (2017). Dimension Reduction Aided Hyperspectral Image Classification with a Small-sized Training Dataset: Experimental Comparisons. *17*. https://doi.org/10.3390/s17122726
Sun, D.-W., & ElMasry, G. (2010). *Principles-of-Hyperspectral Imaging Technology* (D.-W. Sun, Ed. 1st ed.). Elsevier.
ThermoScientific. (2022). *Thermo Scientific Varioskan LUX Technical Manual*.
Thrasyvoulou, A., Tananaki, C., Goras, G., Karazafiris, E., Dimou, M., Liolios, V., Kanelis, D., & Gounari, S. (2018). Legislation of honey criteria and standards [Review]. *Journal of Apicultural Research*, *57*(1), 88-96. https://doi.org/10.1080/00218839.2017.1411181
Times, I. B. (2013). New Zealand Deals With Another Export Product Blow After UK FSA Issues Warning Against Kiwi Manuka Honey. http://ezproxy.massey.ac.nz/login?url=http://search.ebscohost.com/login.aspx?direct=true&db=bwh&AN=501263.20130825&site=eds-live&scope=site
Truong, H. T. D., Nguyen, D. T. N., & Saeys, W. (2021). Fluorescence-based discrimination of vegetative cells of bacillus strains from Escherichia coli and Saccharomyces cerevisiae [Article]. *Biosystems Engineering*, *209*, 232-245. https://doi.org/10.1016/j.biosystemseng.2021.07.007
Truong, H. T. D., Reddy, P., Reis, M. M., & Archer, R. (2022). Quality assessment of mānuka honeys using non-invasive Near InfraRed systems. *Journal of Food Composition and Analysis*, 104780. https://doi.org/10.1016/j.jfca.2022.104780
UMFHA. (2021). *UMF grading system*. https://www.umf.org.nz/grading-system-explained/
UMFHA. (2022). *What is UMF*. https://manukahoneyorganic.com/what-is-umf/
Van Eaton, C. (2014). *Manuka : the biography of an extraordinary honey* [Non-fiction]. Exisle. http://ezproxy.massey.ac.nz/login?url=http://search.ebscohost.com/login.aspx?direct=true&db=cat00245a&AN=massey.b3389062&site=eds-live&scope=site
Vandenabeele, P. (2013). *Practical Raman spectroscopy : an introduction*. John Wiley & Sons, Ltd. https://doi.org/10.1002/9781119961284
Waite, R. (2016). *Development of a model for predicting Manuka honey viscosity* (Vol. Bachelor). Massey University. http://ezproxy.massey.ac.nz/login?url=http://search.ebscohost.com/login.aspx?direct=true&db=cat00245a&AN=massey.b3742159&site=eds-live&scope=site
Wang, H. (2011). *The study of the antioxidant activity of phenolic components of manuka honey* The University of Waikato].
Wang, Q., Zhao, H., Zhu, M., Gao, L., Cheng, N., & Cao, W. (2020). Spectroscopy characterization, theoretical study and antioxidant activities of the flavonoids-Pb(II) complexes [Article]. *Journal of Molecular Structure*, *1209*. https://doi.org/10.1016/j.molstruc.2020.127919
Wang, S., Guo, Q., Wang, L., Lin, L., Shi, H., Cao, H., & Cao, B. (2015). Detection of honey adulteration with starch syrup by high performance liquid chromatography. *Food Chem*, *172*, 669-674. https://doi.org/10.1016/j.foodchem.2014.09.044
Wang, T., Zeng, L.-H., & Li, D.-L. (2017). A review on the methods for correcting the fluorescence inner-filter effect of fluorescence spectrum. *APPLIED SPECTROSCOPY REVIEWS*, *52*(10), 883-908. https://doi.org/10.1080/05704928.2017.1345758
Weik, M. H. (2001). diffuse reflectance. In *Computer Science and Communications Dictionary* (pp. 407-407). Springer US. https://doi.org/10.1007/1-4020-0613-6_5000
White, R. (2018). Letters. Manuka honey: the active antimicrobial ingredients. *Journal Of Wound Care*, *27*(12), 891-891. https://doi.org/10.12968/jowc.2018.27.12.891
Wikieigenvector. (2019). *Artificial Neural Network*. http://wiki.eigenvector.com/index.php?title=Ann
WikiEigenvector. (2020). Genetic Algorithms for Variable Selection. https://wiki.eigenvector.com/index.php?title=Genetic_Algorithms_for_Variable_Selection

Wikieigenvector. (2021). *Artificial Deep Learning Neural Network* https://www.wiki.eigenvector.com/index.php?title=Anndl
Wikieigenvector. (2022). *Using Cross-Validation*. https://wiki.eigenvector.com/index.php?title=Using_Cross-Validation
Wikieigenvector. (2023). *T-Squared Q residuals and Contributions*. https://wiki.eigenvector.com/index.php?title=T-Squared_Q_residuals_and_Contributions
Wilcox, R. R. (2019). Robust regression: Testing global hypotheses about the slopes when there is multicollinearity or heteroscedasticity [Article]. *British Journal of Mathematical & Statistical Psychology*, *72*(2), 355-369. https://doi.org/10.1111/bmsp.12152
Williams, S., King, J., Revell, M., Manley-Harris, M., Balks, M., Janusch, F., Kiefer, M., Clearwater, M., Brooks, P., & Dawson, M. (2014). Regional, annual, and individual variations in the dihydroxyacetone content of the nectar of Manuka (leptospermum scoparium) in New Zealand [Article]. *Journal of Agricultural and Food Chemistry*, *62*(42), 10332-10340. https://doi.org/10.1021/jf5045958
Williams, S. D., Pappalardo, L., Bishop, J., & Brooks, P. R. (2018). Dihydroxyacetone Production in the Nectar of Australian Leptospermum Is Species Dependent. *Journal of Agricultural and Food Chemistry*, *66*(42), 11133-11140. https://doi.org/10.1021/acs.jafc.8b04363
Woodcock, T., Downey, G., & O'Donnell, C. P. (2009). Near infrared spectral fingerprinting for confirmation of claimed PDO provenance of honey [Article]. *Food Chemistry*, *114*(2), 742-746. https://doi.org/10.1016/j.foodchem.2008.10.034
Workman, J., & Mark, H. (2016). How to Select the Appropriate Degrees of Freedom for Multivariate Calibration. *Spectroscopy*, *31*(6), 22–25.
Xiaobo, Z., Jiewen, Z., Povey, M. J. W., Holmes, M., & Hanpin, M. (2010). Variables selection methods in near-infrared spectroscopy [Review Article]. *Analytica Chimica Acta*, *667*(1), 14-32. https://doi.org/10.1016/j.aca.2010.03.048
Xiaohui, W., Lijia, X., Heng, C., Zhiyong, Z., Peng, H., & Bo, X. (2022). Non-Destructive Detection of pH Value of Kiwifruit Based on Hyperspectral Fluorescence Imaging Technology [article]. *Agriculture*, *12*(208), 208-208. https://doi.org/10.3390/agriculture12020208
Yang, X., Guang, P., Xu, G., Zhu, S., Chen, Z., & Huang, F. (2020). Manuka honey adulteration detection based on near-infrared spectroscopy combined with aquaphotomics [Article]. *LWT*, *132*. https://doi.org/10.1016/j.lwt.2020.109837
Yao, L., Datta, N., Tomás-Barberán, F. A., Ferreres, F., Martos, I., & Singanusong, R. (2003). Flavonoids, phenolic acids and abscisic acid in Australian and New Zealand Leptospermum honeys [Article]. *Food Chemistry*, *81*(2), 159-168. https://doi.org/10.1016/S0308-8146(02)00388-6
Yiuchung, C., Maninder, M., Xiaoming, Y., & Baojun, X. (2019). Phenolic acids and flavonoids profiles of commercial honey from different floral sources and geographic sources [article]. *International Journal of Food Properties*, *22*(1), 290-308. https://doi.org/10.1080/10942912.2019.1579835
Yukihiro Ozaki, C. W. H., Krzysztof B. Beć. (2018). *Chapter 2 - Near-IR Spectroscopy and Its Applications* (V. P. Gupta, Ed.). Elsevier. http://ezproxy.massey.ac.nz/login?url=https://search.ebscohost.com/login.aspx?direct=true&AuthType=ip,cookie,url,uid&db=cat09011a&AN=mul.oai.edge.massey.folio.ebsco.com.fs00001086.9f3e55fe.1a9b.56f6.a619.f1f394618389&site=eds-live&scope=site&authtype=sso&custid=s3027306
Zábrodská, B., & Vorlová, L. (2014). Adulteration of honey and available methods for detection – a review [Article]. *Acta Veterinaria Brno*, *83*, S85-S102. https://doi.org/10.2754/avb201483S10S85
Zhang, G., & Abdulla, W. (2022). New Zealand honey botanical origin classification with hyperspectral imaging. *Journal of Food Composition and Analysis*, *109*. https://doi.org/10.1016/j.jfca.2022.104511

Zhang, T. (2021). Deep Learning Model Interpretation Using SHAP. *Towards Data Science*. https://towardsdatascience.com/deep-learning-model-interpretation-using-shap-a21786e91d16

List of publications

Articles published in peer-reviewed journals

Truong, **H. T. D.**, Reddy, P., Reis, M. M., & Archer, R. (2023). Internal reflectance cell fluorescence measurement combined with multi-way analysis to detect fluorescence signatures of undiluted honeys and a fusion of fluorescence and NIR to enhance predictability. Spectrochimica Acta Part A: Molecular and Biomolecular Spectroscopy 2023 Vol. 290.

Truong, **H. T. D.**, Reddy, P., Reis, M. M., & Archer, R. (2022). Quality assessment of mānuka honeys using non-invasive Near InfraRed systems. *Journal of Food Composition and Analysis*, 104780.

Truong, H. T. D., Nguyen, D. T. N., & Saeys, W. (2021). Fluorescence-based discrimination of vegetative cells of bacillus strains from *Escherichia coli* and *Saccharomyces cerevisiae* [Article]. Biosystems Engineering, 209, 232-245. [Note: this article was from the master's thesis]

Manuscript currently submitted in peer-reviewed journals

Truong, **H. T. D.**, Al-Sarayreh M., Reddy, P., Reis, M. M., & Archer, R. (2022). Using deep learning to counter the matrix effect for *in situ* quality assessment of honey quality and monoflorality. [Submitted at Journal of Infrared Physics and Technology, currently in the review process].

MASSEY UNIVERSITY
TE KUNENGA KI PŪREHUROA
UNIVERSITY OF NEW ZEALAND

GRADUATE RESEARCH SCHOOL

STATEMENT OF CONTRIBUTION
DOCTORATE WITH PUBLICATIONS/MANUSCRIPTS

We, the candidate and the candidate's Primary Supervisor, certify that all co-authors have consented to their work being included in the thesis and they have accepted the candidate's contribution as indicated below in the *Statement of Originality*.

Name of candidate:	Hien Thi Dieu Truong
Name/title of Primary Supervisor:	Richard Archer
In which chapter is the manuscript /published work:	Chapter 6

Please select one of the following three options:

(●) The manuscript/published work is published or in press

- Please provide the full reference of the Research Output:

Truong, H. T. D., Reddy, P., Reis, M. M., & Archer, R. (2022). Quality assessment of mānuka honeys using non-invasive Near InfraRed systems. Journal of Food Composition and Analysis, 104780. https://doi.org/https://doi.org/10.1016/j.jfca.2022.104780

( ) The manuscript is currently under review for publication – please indicate:

- The name of the journal:
- The percentage of the manuscript/published work that was contributed by the candidate:
- Describe the contribution that the candidate has made to the manuscript/published work:

( ) It is intended that the manuscript will be published, but it has not yet been submitted to a journal

Candidate's Signature:	Hien Thi Dieu Truong — Digitally signed by Hien Thi Dieu Truong, Date: 2022.09.08 10:58:08 +12'00'
Date:	08-Sep-2022
Primary Supervisor's Signature:	Richard Archer
Date:	12 September 2022

This form should appear at the end of each thesis chapter/section/appendix submitted as a manuscript/ publication or collected as an appendix at the end of the thesis.

MASSEY UNIVERSITY
TE KUNENGA KI PŪREHUROA
UNIVERSITY OF NEW ZEALAND

GRADUATE RESEARCH SCHOOL

STATEMENT OF CONTRIBUTION
DOCTORATE WITH PUBLICATIONS/MANUSCRIPTS

We, the candidate and the candidate's Primary Supervisor, certify that all co-authors have consented to their work being included in the thesis and they have accepted the candidate's contribution as indicated below in the *Statement of Originality*.

Name of candidate:	Hien Thi Dieu Truong
Name/title of Primary Supervisor:	Richard Archer
In which chapter is the manuscript /published work:	Chapter 9

Please select one of the following three options:

○ The manuscript/published work is published or in press

- Please provide the full reference of the Research Output:

◉ The manuscript is currently under review for publication – please indicate:

- The name of the journal:
  Food Research International
- The percentage of the manuscript/published work that was contributed by the candidate: 75.00
- Describe the contribution that the candidate has made to the manuscript/published work:
  Methodology, data collection, data analysis and writing-original draft.

○ It is intended that the manuscript will be published, but it has not yet been submitted to a journal

Candidate's Signature:	Hien Thi Dieu Truong — Digitally signed by Hien Thi Dieu Truong, Date: 2022.09.08 11:25:27 +12'00'
Date:	08-Sep-2022
Primary Supervisor's Signature:	Richard Archer
Date:	12 September 2022

This form should appear at the end of each thesis chapter/section/appendix submitted as a manuscript/ publication or collected as an appendix at the end of the thesis.

GRS Version 5 – 13 December 2019
DRC 19/09/10

MASSEY UNIVERSITY
TE KUNENGA KI PŪREHUROA
UNIVERSITY OF NEW ZEALAND

GRADUATE RESEARCH SCHOOL

STATEMENT OF CONTRIBUTION
DOCTORATE WITH PUBLICATIONS/MANUSCRIPTS

We, the candidate and the candidate's Primary Supervisor, certify that all co-authors have consented to their work being included in the thesis and they have accepted the candidate's contribution as indicated below in the *Statement of Originality*.

Name of candidate:	Hien Thi Dieu Truong
Name/title of Primary Supervisor:	Richard Archer
In which chapter is the manuscript /published work:	Chapter 10

Please select one of the following three options:

○ The manuscript/published work is published or in press

- Please provide the full reference of the Research Output:

◉ The manuscript is currently under review for publication – please indicate:

- The name of the journal:

Spectrochimica Part A

- The percentage of the manuscript/published work that was contributed by the candidate: 75.00
- Describe the contribution that the candidate has made to the manuscript/published work:

Methodology, data collection, data analysis and writing-original draft.

○ It is intended that the manuscript will be published, but it has not yet been submitted to a journal

Candidate's Signature:	Hien Thi Dieu Truong — Digitally signed by Hien Thi Dieu Truong Date: 2022.09.08 11:27:56 +12'00'
Date:	08-Sep-2022
Primary Supervisor's Signature:	Richard Archer
Date:	12 September 2022

This form should appear at the end of each thesis chapter/section/appendix submitted as a manuscript/ publication or collected as an appendix at the end of the thesis.